Experimental Studies of Diode Lasers And Cold Atom Guiding

A Thesis submitted to the
University of St Andrews
in Application for the
Degree of Doctor of Philosophy

by

Gavin P. T. Lancaster

5th October 2001

As a human being, one has been endowed with just enough intelligence to be able to see clearly enough how utterly inadequate that intelligence is when confronted with what exists.

Albert Einstein 1879–1955

Abstract

This thesis is concerned with both the experimental development of diode lasers in the field of laser cooling and atom trapping and the use of light beams to guide cold atoms.

The characteristics of a novel, commercially available diode laser with a circular output were investigated. Extended mode-hop free tuning was observed and this, together with the spectrally narrowed linewidth, allowed Doppler-free spectroscopy to be taken of rubidium. This laser was included in atom trapping experiments both directly and when placed in an extended-cavity geometry. Apart from a simplification in the experimental setup, a degree of frequency stability was observed in the output enabling atoms to be trapped over a number of minutes with the laser unlocked. For reproducibility in any cold atom experiment a means of stabilizing a laser's frequency to a reference is required. A number of techniques for doing this have been investigated and compared. Further, the characterisation of a recently available gallium nitride diode laser in an extended-cavity geometry has been performed.

The second half of this thesis is concerned with experimental atom trapping and optical guiding. A number of magneto-optical traps (MOTs) have been constructed and tested with one novel trap in particular, the mirror MOT, allowing a cold atomic ensemble to be placed close to a mirrored surface while needing only four trapping beams in comparison to the six normally required. The generation of a low-velocity intense source (LVIS) of atoms has been obtained by one conventional and one novel method. Guiding a LVIS of cold atoms utilizing the optical dipole force has been investigated while the first experimental guiding of such an atomic beam with a blue-detuned Laguerre-Gaussian laser beam has been performed.

Acknowledgements

This thesis would not have been possible without the support and influence of a large number of people. I am especially indebted to my supervisor, Dr Kishan Dholakia. Both as a friend and as an academic mentor his boundless enthusiasm, frank honesty and cries of "Do you want to hear a crazy idea?" have inspired and encouraged me over the past 6 years.

In the beginning the group was small and at this time I was fortunate to work alongside Richard "Ricardo" Conroy who taught me a great deal on the practical aspects of working in a lab. His unnerving ability to fix just about anything and also his (equally!!) unnerving ability for remaining sober regardless of the quantity of alcohol being consumed makes you feel somewhat mortal! Of late, working with Daniel "Daniel-san" Rhodes (Are you going to do the "Crane" now?) and John "D'you want me to spell that for you?" Livesey has been a pleasurable and sometimes hilarious experience. Much of the work included in this thesis has been influenced and aided by these three and I would like to take this opportunity to thank them.

With the group encompassing optical tweezing of late, new faces have joined the more familiar and have made life in the office much more enjoyable. So thanks all the tweezing people, old and new: Jochen, Mike, Lynn, Veneranda and Karen. Many other people have passed through the group over the years, usually as summer or project students: Carol, William, Davina, Albert, Robert, Takashi, Sophie and Toni. All have provided new chat and a welcome diversion from life in a darkened room.

I would like to acknowledge those people who provided advice, support or help over the years, whether it be technical or otherwise. Aly, Fritz, Bob, Alan, Tony, Mark, Jim and all the guys in the Workshop...Cheers! I would also like to thank Jacqueline "Has anyone seen my keys?" Hewett for helping me to remain sane during writing-up. Her never-ending encouragement, support and "split-infinitive

radar" has truly helped and made the past 4 months memorable.

I would like to thank the Engineering and Physical Sciences Research Council for providing financial support during the period of these studies.

Finally, I would like to thank my family: my mum, my dad and my brother, for their unconditional love, encouragement and patience, without which none of this would have been possible. This thesis is dedicated to you.

Glossary of Acronyms

Abbreviations	Meaning
AlGaInN	Aluminium Gallium Indium Nitride
AOM	Acousto-Optic Modulator
AR	Anti-Reflection
BEC	Bose-Einstein Condensation
BNC	British Naval Connector
CCD	Charged Coupled Device
CW	Continuous Wave
DAVLL	Dichroic-Atomic Vapour Laser Lock
DBR	Distributed Bragg Reflector
DFB	Distributed Feedback
ECDL	Extended-Cavity Diode Laser
FSR	Free Spectral Range
FWHM	Full Width at Half Maximum
GaN	Gallium Nitride
GRINROD	Graded Refractive INdex ROD
InGaN	Indium Gallium Nitride
IR	Infrared
LG	Laguerre-Gaussian. A circularly symmetric laser mode that has a helical phase structure and a phase singularity at its centre.
LNA	$La_{1-x}Nd_xMgAl_{11}O_{19}$, Lanthanum Neodymium Magnesium Hexaluminate
LVIS	Low Velocity Intense Source (of atoms)
$MgAl_2O_4$	Spinel
MOCVD	Metal-Organic Chemical Vapour Deposition
MOT	Magneto-Optical Trap
MQW	Multiple Quantum Well
ND	Neutral Density

Glossary of Acronyms

Abbreviations	**Meaning**
OSA	Optical Spectrum Analyser
Nd:YVO_4	Neodymium Yttrium Vanadate
PZT	Piezoelectric Transducer
Rb	Rubidium
SiC	Silicon Carbide
TEM_{00}	Transverse electro-magnetic mode with no dark regions in both the vertical and the horizontal planes. This is a diffraction limited transverse mode with a single intensity lobe.
Ti:Al_2O_3	Titanium Sapphire
UHV	Ultra High Vacuum
UV	Ultra Violet
ZnO	Zinc Oxide
ZnSe	Zinc Selenide

Contents

1 Introduction **1**

1.1 Synopsis of Thesis 3

2 Diode Laser and Frequency Locking Theory **5**

2.1 Introduction 5

2.1.1 Realization of the Laser 6

2.1.2 Realization of the Semiconductor Laser 7

2.2 Semiconductor Diode Laser Characteristics 9

2.2.1 Spatial Characteristics 10

2.2.2 Linewidth Characteristics 11

2.2.3 Tuning Characteristics 12

2.3 Diode Lasers with Optical Feedback 14

2.3.1 Diffraction Grating Theory 16

2.3.2 Littman-Metcalf Geometry 18

2.3.3 Littrow Geometry 20

2.3.4 Comparison between Littman-Metcalf and Littrow Geometries 22

2.4 Frequency Locking Techniques 23

2.4.1 Servo Locking Systems 23

2.4.2 Doppler-Free Saturated Absorption Spectroscopy 25

2.4.3 Polarisation Spectroscopy 27

2.4.4 Dichroic-Atomic Vapour Laser Lock 29

2.4.5 Dual Current/PZT Locking 31

2.5 Summary 32

3 Experimental Diode Laser Systems and their Stabilization 40

3.1 Introduction 40

3.2 Laser Systems 41

3.2.1 Extended Cavity Diode Lasers 41

3.2.2 Guiding Laser 46

3.3 Frequency Stabilization Techniques 49

3.3.1 Polarisation Spectroscopy Lock 50

3.3.2 Dichroic-Atomic Vapour Laser Lock 55

3.3.3 Dual Current/PZT Lock 64

3.3.4 Comparison of Frequency Stabilization Techniques 69

3.4 Conclusions 70

4 A Circularized Laser Diode 73

4.1 Introduction 73

4.2 Free-Running Circulaser 74

4.2.1 Spatial Characteristics 76

4.2.2 Linewidth 78

4.2.3 Tunability 79

4.3 Circulaser in Extended-Cavity Geometry 84

4.3.1 Spatial Characteristics 87
4.3.2 Tunability 87
4.3.3 Linewidth 89
4.4 Injection Locking of a Circulaser 91
4.4.1 Introduction and Theory 91
4.4.2 Experimental Injection Locking of a Circulaser 94
4.5 Conclusions 96

5 Gallium Nitride-Based Extended-Cavity Diode Laser 100

5.1 Introduction 100
5.1.1 Background 101
5.2 GaN Diode Laser 103
5.2.1 Material Requirements 103
5.2.2 Diode Laser Structure 105
5.3 GaN Diode Laser in Extended-Cavity 105
5.3.1 Current-Power Characteristics 107
5.3.2 Tuning Characteristics 108
5.3.3 Linewidth Characteristics 111
5.4 Conclusions 112

6 Laser Cooling and Atom Trapping Theory 118

6.1 Introduction 118
6.1.1 Temperature 118
6.1.2 Historical Background 119
6.2 Primary Cooling Mechanisms 121

6.2.1 Radiation Pressure Force 121
6.2.2 The Cooling Cycle 122
6.2.3 Slowing of an Atomic Beam 123
6.2.4 Doppler Cooling 124
6.3 Further Cooling Mechanisms 127
6.3.1 Sub-Doppler Cooling 128
6.3.2 Sub-Recoil Cooling 134
6.4 Magnetically–Based Traps 135
6.4.1 Magnetic Trap 136
6.4.2 Magneto-Optical Trap 137
6.5 Atom Extraction from Magneto-Optical Traps 139
6.5.1 Atomic Funnel 140
6.5.2 Low-Velocity Intense Source of Atoms 141
6.6 Optical Dipole Traps 144
6.6.1 Optical Dipole Force 144
6.6.2 Red-Detuned Optical Dipole Trap 146
6.6.3 Blue-Detuned Optical Dipole Trap 147
6.7 Summary 149

7 Review of Atom Guiding Experiments 156

7.1 Introduction 156
7.1.1 Application to Atom Interferometry 157
7.2 Magnetic Field Guiding 158
7.2.1 Wire Guiding 159

7.2.2 Magnetic Atomic Beam splitters 162

7.2.3 Summary of Magnetic Field Guiding 164

7.3 Hollow fibre Light Beam Guiding 164

7.3.1 Red-Detuned Guiding 167

7.3.2 Blue-Detuned Guiding 169

7.4 Free-Space Light Beam Guiding 173

7.4.1 Red-Detuned Guiding 174

7.4.2 Blue-Detuned Guiding 175

7.4.3 All Optical Atomic Beam Splitters 178

7.5 Summary 181

8 Experimental Realization of Magneto-Optical Traps 187

8.1 Introduction 187

8.2 Prototype MOT 189

8.2.1 Construction 189

8.2.2 Bakeout 190

8.2.3 Trap Operation 192

8.2.4 Trap Characterisation 195

8.3 Mirror MOT 200

8.3.1 Motivation 200

8.3.2 Construction 200

8.3.3 Bakeout 202

8.3.4 Trap Operation and Characterisation 203

8.4 Ten-way Cross MOT 206

8.4.1 Construction 206
8.4.2 Bakeout 209
8.4.3 Trap Operation 209
8.5 Discussion and Summary 210

9 Experimental LVIS Generation And Cold Atom Guiding 214
9.1 Introduction 214
9.2 Generation of a Low-Velocity Intense Source of Atoms 215
9.2.1 Opaque Spot LVIS 216
9.2.2 Laguerre-Gaussian LVIS 218
9.2.3 Laser Detuning of LVIS 222
9.3 Guiding of a LVIS 228
9.3.1 Red-Detuned Gaussian Beam Guiding 228
9.3.2 Future Red-Detuned Guiding 231
9.3.3 Blue-Detuned Laguerre-Gaussian Beam 232
9.4 Future Work 240
9.5 Discussion and Summary 241

10 Conclusions 245
10.1 Summary of the Thesis 245
10.2 Future Work 248

A Laser Frequency Stabilization Electronics 250
A.1 Introduction 250
A.2 Circuit Description 251
A.3 Modifications 251

A.4 Experimental Locking of an ECDL and Circuit Diagrams 253

B MOT Field Gradient Modelling **262**

B.1 Introduction 262

C Publications And Publicity **280**

C.1 Publications 280

C.2 Conference Papers 281

C.3 Lectures 282

List of Figures

2.1 Schematic diagram of the double heterojunction in a GaAs-AlGaAs semiconductor diode laser. 8

2.2 Output power versus injection current for a typical AlGaAs laser. 10

2.3 The elliptical beam profile of a laser diode. 11

2.4 A typical wavelength versus temperature graph of a diode laser. 13

2.5 Diagram showing the grating angles and terms used in describing the physical properties of ruled diffraction gratings. 17

2.6 Schematic diagram indicating the diffracted orders seen when an incident beam diffracts from a ruled grating. 18

2.7 Schematic diagram of the Littman-Metcalf geometry when applied for use with diode lasers. 19

2.8 Schematic diagram of the Littrow geometry when applied for use with diode lasers. 20

2.9 A representation of competing processes present during optical feedback from a wavelength selective element, such as a diffraction grating. 21

2.10 Schematic diagram of a basic servo loop for stabilization of a laser. 24

2.11 Schematic diagram for a saturated spectroscopy setup. 26

2.12 Diagramatic explanation of the origin of atomic saturation absorption profiles. 27

2.13 A typical saturated absorption spectroscopy profile for the ^{85}Rb F=3→F' transition. 28

2.14 Schematic diagram for a polarisation spectroscopy setup. 29

2.15 Schematic diagram for Dichroic-atomic vapour laser lock. 30

2.16 Intensity signals measured from DAVLL experiment. 31

3.1 Schematic diagram of an extended-cavity diode laser 42

3.2 (Colour) A photograph of an extended-cavity diode laser. 43

3.3 A heterodyne experiment between two of the external cavity diode lasers. A linewidth of 135 kHz was inferred from the width of the peak. 44

3.4 Schematic diagram showing the operation of the Millennia laser head. 47

3.5 Schematic diagram showing the operation of the Ti:sapphire laser. 48

3.6 (Colour) Diagram of frequency selectivity of the intra-cavity elements. . . . 50

3.7 The polarisation spectrometer setup. 51

3.8 Expected locking signals from polarisation spectroscopy and saturated absorption spectroscopy of the $^{85}Rb\ ^5S_{1/2} \rightarrow\ ^5P_{3/2}$ transition. 53

3.9 (Colour) Experimental measurement of the saturated absorption spectra and polarisation spectrometer signals. 54

3.10 Schematic diagram of the experimental DAVLL setup. 56

3.11 A graph showing the B-field variation along the centre of the electromagnet. . 58

3.12 A typical DAVLL error signal. 58

3.13 Graph of theory (line) and experiment (points) for the photodiode intensity variation measured as a function of rotation of the quarter-wave plate. . . . 62

3.14 (Colour) The DAVLL locking signal measured for various magnetic fields. . . 63

3.15 (Colour) An enlargement of the circled section in Figure 3.14. 63

3.16 Tuning the frequency by adjusting the d.c. magnetic field applied to the vapour cell. 64

3.17 A simplified circuit diagram of the dual current/PZT locking electronics. . . 66

3.18 Schematic diagram of the acousto-optic modulator setup. 67

3.19 The energy diagram for ^{85}Rb. All values in brackets are frequencies in MHz. 68

4.1 Schematic diagram of the diode laser and microlens assembly. 75

4.2 (Colour) Beam profiles of (a) a normal, uncircularized Hitachi diode and (b) a circularized Hitachi diode from Blue Sky Research Inc.. 77

4.3 A scan from a 300MHz FSR Fabry-Perot interferometer of a free-running Circulaser showing single longitudinal mode operation. 80

4.4 A scan from a 300MHz FSR Fabry-Perot interferometer of a free-running Circulaser showing single longitudinal mode operation with a linewidth less than 4 MHz. 80

4.5 A frequency scan of 60 GHz showing the height differences in peaks due to the sampling rate of the digital oscilloscope. 82

4.6 A frequency scan of 10 GHz showing equal peak heights. 82

4.7 Graph of modehop free tuning verses current of a Circulaser. 83

4.8 Looking from left to right, the ^{87}Rb F=2→F', ^{85}Rb F=3→F'and ^{85}Rb F=2→F' transitions as seen using a free-running Circulaser. 84

4.9 The ^{85}Rb F=3→F' line as seen using a free running Circulaser. The hyperfine structure is visible clearly. 85

4.10 Current/Power curves for a Hitachi diode laser free-running and in an extended-cavity geometry. 86

4.11 Current/Power curves for a Sanyo diode laser free-running and in an extended-cavity geometry. 86

4.12 (Colour) Beam profile of (a) light incident on grating and (b) the Zeroth-order diffracted output. 87

4.13 Looking from left to right, the ^{87}Rb F=2→F', ^{85}Rb F=3→F', ^{85}Rb F=2→F' and ^{87}Rb F=1→F' transitions as seen using a Circulaser ECDL. 89

4.14 The ^{87}Rb F=2→F' and ^{85}Rb F=3→F' line as seen using a Circulaser ECDL. The hyperfine structure is clearly visible. 90

4.15 The beat note of two similar, unlocked, circularized ECDLs when heterodyned. 91

4.16 Regenerative gain versus input frequency ω_1 for a laser cavity oscillating at frequency ω_0. 92

4.17 (Colour) Diagram showing the locking range when injection locking a laser. . 93

4.18 Functional diagram of Circulaser injection locking setup. 95

5.1 (Colour) A photograph of a free-running GaN laser. 102

5.2 (Colour) A diagram showing the GaN layer arrangement in a Nichia diode laser and the MQW energy structure. 106

5.3 Output power of free-running and extended-cavity lasers as a function of drive current. 108

5.4 Discontinuous wavelength tuning of the GaN extended-cavity diode using both the HoloUV (circles) and HoloVIS (triangles) gratings. 109

5.5 Discontinuous wavelength tuning graphs for both 670 nm and 635 nm diode lasers in an extended-cavity geometry. 110

5.6 A measurement of the linewidth of the GaN ECDL using a home-built Fabry-Perot etalon. 112

6.1 (Colour) A map of the UK showing various temperatures measured in distance from the centre of Edinburgh. 120

6.2 (Colour) Graphical representation of the cooling cycle. 123

6.3 (Colour) Functional diagram for Zeeman slowing of a thermal atomic beam. . 124

6.4 One dimensional Doppler cooling. 125

6.5 The damping force in Doppler cooling. 126

6.6 Two counter-propagating linearly polarised laser beams produce a field whose polarisation changes every eighth of a wavelength between linearly polarised and circularly polarised. 129

6.7 The energy levels for an atom in a polarisation gradient. 129

6.8 The light induced energy shifts of the ground state of an atom placed in the polarisation gradient. 131

6.9 Sisyphus cooling in one dimension. 132

6.10 The damping force in polarisation gradient cooling. 133

6.11 The magneto-optical trap in one dimension. 137

6.12 Schematic diagram of a MOT. 138

6.13 Schematic diagram of the atomic funnel. 140

6.14 (Colour) Schematic of the low-velocity intense source (LVIS) of atoms system. 142

6.15 (Colour) Classical description of the dipole force. 145

6.16 Schematic of the blue-detuned optical dipole trap geometry. 148

6.17 Schematic of a blue-detuned optical dipole trap constructed from a Laguerre-Gaussian beam and two Hermite-Gaussian plug beams. 148

7.1 Configurations for magnetic guiding of neutral atoms. 160

7.2 Functional diagram of the wire guiding experiment. 160

7.3 Raw data from the experimental setup shown in Figure 7.2 with a current of 1 A and a bend of 0.5 mrad. 161

7.4 Experimental setup for magnetic guiding above the surface of a substrate. . . 162

7.5 Experimental realization of a substrate magnetic atom switch. 163

7.6 (Colour) Diagram illustrating light fields in hollow-core optical fibre guiding when (a) using red-detuned light and (b) blue-detuned light. 165

7.7 Experimental setup for red-detuned guiding in a hollow optical fibre. 167

7.8 Guided atom signal versus laser detuning from resonance. 168

7.9 Guided atom flux versus laser detuning from resonance for a high laser intensity of 50 MW m^{-2}. 169

7.10 Intensity dependence of the evanescent-wave-guided atom flux. 171

7.11 Detuning dependence of the guided atoms' internal states. 173

7.12 Schematic diagram of focusing of a thermal atomic beam using a red-detuned Gaussian beam. 174

7.13 The atomic beam flux at the detector as a function of transverse detector position. 175

7.14 Functional diagram for the guiding of cold Rb atoms directly from a MOT within the centre of a hollow light beam. 176

7.15 The guiding efficiency as a function of the detuning, δ_2, in the co-propagating (a) as well as the counter-propagating (b) scheme. 177

7.16 Experimental scheme for cold atom guiding using a far-off-resonance red-detuned laser. 179

7.17 Results gained from the experimental apparatus shown in Figure 7.16. . . . 180

8.1 (Colour) A photograph of the prototype atom trap. 190

8.2 Schematic of the MOT. 193

8.3 Captured image using an infrared sensitive CCD camera of trap centre showing a cloud of cooled and trapped rubidium atoms. 196

8.4 Diagram of the setup used to measure the number of atoms in the trap. . . . 197

8.5 (Colour) Number of trapped atoms verses time after the trap is turned on at 0.45s. 199

8.6 (Colour) Number of trapped atoms verses time after the trap is turned on at 0.43s. 199

8.7 (Colour) A photograph of the assembled mirror MOT. 202

8.8 A layout showing the polarisations and laser orientation requirements for trapping in the mirror MOT. 203

8.9 Schematic diagram of the mirror MOT. 204

8.10 A series of images showing the vertical translation of an atomic cloud within the mirror MOT. 207

8.11 (Colour) A functional diagram of the ten-way cross trap. 208

9.1 (Colour) A diagram showing the basic principle behind the formation of a low-velocity intense source (LVIS) of atoms. 216

9.2 An image captured using a CCD camera of a low-velocity intense source (LVIS) of atoms exiting the centre of a MOT 217

9.3 Experimental intensity profiles for Laguerre-Gaussian laser modes with the azimuthal index term, ℓ, shown for each. 220

9.4 An image captured using a CCD camera of a LVIS exiting the centre of a MOT produced by the insertion of a LG_{01} ($p = 0, \ell = 1$) beam as one of the six cooling and trapping beams. 221

9.5 Cloud shape seen when a LG_{03} was introduced as one of the six trapping beams. A ring of atoms can be seen orbiting the central cloud. 222

9.6 (Colour) On the left are seen false colour images of an opaque spot generated LVIS exiting the central region of a MOT. 224

9.7 (Colour) On the left are seen false colour images of a LG_{01} beam generated LVIS exiting the central region of a MOT. 225

9.8 (Colour) On the left are seen false colour images of a LG_{01} beam generated LVIS exiting the central region of a MOT. 226

9.9 (Colour) Composite data of unnormalised intensity profiles through a LVIS beam generated from (a) an opaque spot and (b) a LG_{01} beam. The different graphs refer to different laser detunings below resonance, as indicated in the legend. 1 pixel equals 100 μ m. 227

9.10 Captured images from one CCD camera of an atomic LVIS with (a) no guide beam present and (b) 700 mW of 7 GHz of red-detuned guide beam present. 229

9.11 (Colour) Intensity profiles measured along the LVIS axis are plotted in (a) after the subtraction of background scattering. Graph (b) is a subtraction of the "guide" and "no guide" plots from (a). 230

9.12 (Colour) Schematic diagram for an all-optical switch. 231

9.13 Results from the optical switch experiment using 550 mW of guide power detuned -12 GHz from resonance. 232

9.14 (Colour) Schematic diagram of co-linear blue-detuned Laguerre-Gaussian guiding of LVIS. 233

9.15 Experimental setup for the production of a Laguerre-Gaussian guide beam. . 234

9.16 (Colour) Captured images of LVIS with (a) no guide and (b) a co-linear LG_{02} guide beam present. 235

9.17 (Colour) Intensity profiles taken along yellow lines indicated in Figure 9.16. . 236

9.18 (Colour) Schematic diagram of the blue-detuned dark hollow beam guiding experiment conducted by Yan *et al.*. 238

9.19 Images of an atomic LVIS with (a) no guide beam present and (b) 180 mW of $\Delta = +5$ GHz blue-detuned LG_{03} oblique guide beam present. 238

9.20 (Colour) Diagram showing the formation of the two observable lines in Figure 9.19. 239

A.1 A block diagram of the laser stabilization electronics. 257

A.2 Circuit diagram of the oscillator board. 258

A.3 Circuit diagram of the tuned amplifier board. 259

A.4 Circuit diagram of the phase sensitive detection board. 260

A.5 Circuit diagram of the integrator board. 261

Chapter 1

Introduction

Laser cooling and atom trapping, since its birth in 1985, has had a considerable impact in atomic physics with important repercussions. Indeed, this was acknowledged with the Nobel Prize for Physics in 1997 being awarded jointly to William D. Phillips, Claude N. Cohen-Tannoudji and Steven Chu for their endeavours in reaching the lowest temperatures of any physical system in a laboratory. Crudely, the temperature of an object is determined by the kinetic energy of the constituent particles of that object on a microscopic level. Reducing the kinetic energy reduces the temperature. What the Nobel Prize Laureates achieved was to cool a dilute gas of alkali atoms from room temperature, where they are moving with a speed of a few hundred metres per second (the speed of a fast jet plane) , to a fraction of a degree above absolute zero, where they were moving at a few centimetres per second (the speed of a mosquito). This was achieved by selectively imparting momentum from photons to fast moving atoms, thereby slowing them down. Not only were the atoms slowed but they were confined spatially in a dense cloud.

So why was this considered important? First, experimentalists in atomic physics up until then had been forced to use either thermal atomic beams or vapour cells where atoms have high velocities. This allowed only short interaction times limiting the resolution of the atomic states being measured. Second, a possibility

of studying atom-atom interactions under such conditions, with many extraneous factors being omitted, was envisaged. Third, and probably the most important, was the quest for Bose-Einstein Condensation. This is a state predicted by Bose and Einstein in 1924 in which particles with sufficiently low temperatures and high densities have their de Broglie wavelengths overlapping. This state culminates in the particles loosing their fermionic properties, preferring to exist as bosons. A considerable amount of research had been conducted in attempting to realize BEC without success and although laser cooling and atom trapping did not produce BEC of its own accord, it was believed to be a significant step towards it. This was indeed true and in 1995 BEC was experimentally observed using other cooling methods to cool below the optical limit. The realization of both neutral atom traps and BEC has led to new areas in physics being created to accommodate new physical regimes. Cold atomic beams are now routinely available and the manipulation of these beams has paved the way for atom-optics. In much the same way that conventional optical elements reflect, split or combine light beams, atom-optics reflect, split or combine atomic beams. The most important use of these elements is in the fabrication of a compact atom interferometer and other precise measuring devices.

The characteristics of the lasers used in all cooling and trapping experiments have stringent requirements placed upon them. As such, this thesis is in two distinct halves. The first examines the characteristics required by these lasers and how one might achieve this in the experimental laboratory with ease and minimal expense. New and novel laser sources suitable for laser cooling are investigated including a laser diode producing a circular output directly from the laser can and the characterisation of a recently available gallium nitride diode laser that emits near 400 nm. The second half examines laser cooling and atom trapping as a basis from which the experimental generation and subsequent manipulation of a cold atomic beam can be performed.

1.1 Synopsis of Thesis

After this brief introductory chapter, Chapter 2 details the operating mechanisms of a semiconductor diode laser. Importantly, the influence of feedback is addressed and the manner in which selective feedback can be incorporated into a laser design is outlined. In laser cooling and atom trapping the laser frequency must be stabilized precisely to a reference. A number of techniques of how this can be done are detailed. Chapter 3 progresses by encompassing ideas and designs highlighted in Chapter 2 and bringing them experimentally to the laboratory. The construction of an extended-cavity diode laser is detailed as well as a comparison of three different frequency stabilization techniques employed during this research project. Chapter 4 investigates the characteristics of a novel diode laser that has had a small microlens attached close to its front facet. In addition to providing a circular output directly from the diode laser can, it has been found to possess improved characteristics suited for use in laser cooling. Chapter 5 is a characterisation of a gallium nitride diode laser placed in an extended-cavity geometry. The characteristics are related to the semiconductor structure peculiarities as have been reported in recent literature.

Chapter 6 describes the historical background leading to the advent of laser cooling and atom trapping. Theories of different cooling mechanisms are presented which led to the formation of BEC. Neutral atom traps are described, most importantly the magneto-optical trap (MOT). Two methods of extracting cold atoms directly from the centre of a MOT are outlined. The optical dipole force is introduced as a means of creating an atom trap but is fundamental with regard to the work presented in this thesis on the manipulation, notably guiding, of a cold atomic beam using light beams. A review of atom guiding experiments is presented in Chapter 7. The construction and operation characteristics of three different MOTs are detailed in Chapter 8. Within this chapter, a MOT enabling the placement of a cold cloud of atoms approximately 1 mm from a mirrored surface is described. Chapter 9 details how a cold atomic beam may be gener-

ated from the centre of a MOT experimentally. Further, preliminary experiments on the guiding of this beam using the optical dipole force is presented in Chapter 6. In particular, the first experimental guiding of a low-velocity intense source of cold atoms using a blue-detuned, co-linear, Laguerre-Gaussian laser beam is described.

Chapter 2

Diode Laser and Frequency Locking Theory

2.1 Introduction

Semiconductor diode lasers have had one of the most profound impacts in modern physics in recent decades. Their undisputed commercial success reflects this by being the principle functional component in every compact disc player, CD-ROM drive, laser pointer and laser printer. Many of the world's long and medium distance communication networks rely on pulses of light generated from semiconductor lasers reinforcing the need for these lasers to be manufactured in the largest quantities.

These lasers operate by the recombination of holes and electrons as they travel from one semiconductor material to another containing differing impurities (or dopants). On recombination, a photon is emitted with a characteristic energy determined by the structure of the energy bands for that particular material. Typical wavelengths are in the red and infrared regions of the spectrum although new-generation shorter wavelength diode lasers can access wavelengths in the blue and violet. Output powers can vary from a few milliwatts for a single mode

laser to kilowatt laser bar arrays. Diode lasers have, to a great extent, replaced titanium sapphire and dye lasers in atomic physics because of their low cost, ease of use, simplicity and reliability. However, they are not immune from problems and these need to be addressed before their full potential can be realized in atomic physics.

In this chapter, a brief historical background of the development of semiconductor diode lasers and their operating characteristics will be described. The effects and benefits obtained from implementing optical feedback to improve lasing characteristics, particularly with relevance to the area of spectroscopy and atom trapping, will be shown. Furthermore, in the field of laser cooling and atom trapping, it is a prerequisite that not only must the laser source be spectrally narrow but that it must be tuneable and stabilized to a precisely determined value. Therefore the methods and means of controlling the output frequency of these diodes and how the laser may be locked to a particular frequency reference will be discussed.

2.1.1 Realization of the Laser

In 1916, Albert Einstein published a paper based on his own proof of Planck's law and, through his use of statistical mechanics, introduced the concept of stimulated emission [1][1]. Ladenburg was close to proving experimentally Einstein's theory in 1933 through his work on negative dispersion in electrically excited gases [2] but it was not until 1953 that Weber demonstrated stimulated emission on a microwave transition [3]. Almost immediately a plethora of activity commenced in pursuit of an optical analogue with Maiman triumphing in 1960 with an experimental demonstration of a flash-lamp pumped ruby laser at 694 nm [4]. The first gas discharge laser was realized soon afterwards by Javan *et al.* in 1961 by achieving stimulated emission from a mixture of helium and neon [5].

[1] A translation of this paper into English can be found in "Sources of Quantum Mechanics" by B. L. Van Der Waerden, North-Holland Publishing Company, Holland, pages 63–77.

2.1.2 Realization of the Semiconductor Laser

The first indication that semiconductor materials could be used as a gain medium for the generation of stimulated emission came from Wantanabe and Nishizawa in 1957 [6] when they proposed that stimulated emission could result from the recombination of electron-hole pairs at a *p-n* junction. Work commenced on this appealing new idea which came to fruition when a semiconductor diode of GaAs exhibited laser characteristics once cooled to 77 K with liquid nitrogen and operated under pulsed conditions [7]. Two fundamental problems limited these so called *homojunction* lasers. Firstly, the charge carriers could recombine throughout the entire device. However, it was only very close to the *p-n* junction that current densities were sufficient to support lasing. The excess recombination led to heating of the semiconductor with the result that, without proper heat-sinking, the device would experience permanent and catastrophic breakdown very quickly. Secondly, a substantial fraction of the light generated in the active gain region was diffracted into the highly absorbing *p*-type and *n*-type semiconductor above and below the junction resulting in even more current being required to achieve threshold. Both these factors limited early semiconductor lasers to pulsed operation at cryogenic temperatures [7, 8].

To surmount the former of these problems and partially alleviate the latter, Kroemer, in 1963, proposed the *heterojunction* [9]. It was not until 7 years later, due to difficulties in material quality, that room temperature operation of a *n*-GaAs, *p*-GaAs and a *p*-AlGaAs layered structure was demonstrated [10]. Further refinement led to construction of the now common *double heterojunction*, an example of which is shown in Figure 2.1, which resulted in the first CW, room temperature laser diode [11]. From the simple but inefficient homojunction requiring as much as $5\text{x}10^4$ A cm^{-2} to operate, progress had led to current densities of only 100 A cm^{-2} being necessary to sustain lasing. The achievement of continuous lasing at room temperatures was the result of three main advantages of the double heterostructure over other designs, namely:

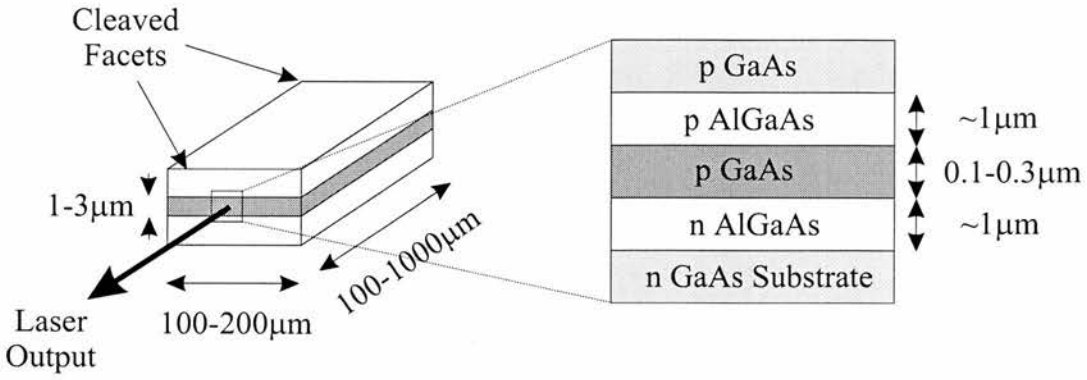

Figure 2.1: Schematic diagram of the double heterojunction in a GaAs-AlGaAs semiconductor diode laser.

(i) The refractive index, η, of $Al_xGa_{1-x}As$ was significantly less than that of GaAs ($\eta = 3.4$ for $x = 0.4$ while $\eta = 3.6$ for $x = 0$). This produced a natural gain-guided region for confinement of stimulated photons.

(ii) The bandgap energy of AlGaAs (1.3 eV - 2.2 eV) was significantly different from GaAs (~1.3 eV) allowing confinement of the injected holes and electrons in the active region. This increased carrier density gave a corresponding increase in optical gain which enabled a lower current to achieve laser threshold.

(iii) The different bandgap also gave a reduced absorption of light in the layers surrounding the active region, improving performance.

The thickness of the active layer in a typical double heterostructure laser ranged from 0.1 to 0.3μm. Advances in material growth techniques in the 1980s allowed the active layer thickness to be reduced to dimensions of 5 to 10 nm. In doing so, the energy levels exhibit quantum behaviour and the structure is referred to as a *quantum-well*. A number of such thin layers stacked above one another is named a *multi-quantum-well* (MQW). The quantisation of energy levels implies light is emitted over a narrower range of energies resulting in higher gain for lower threshold currents. Threshold currents as low as 0.5 mA cm^{-2} have been achieved in quantum-well lasers [12].

In 1996, Nakamura and colleagues reported room temperature operation of an indium gallium nitride (InGaN)-based MQW diode laser providing the shortest wavelength emission from a semiconductor laser at 417 nm at that time [13]. Further research yielded CW operation at room temperature and commercialisation of this diode [14]. Further details of this particular diode laser are given in Chapter 5.

2.2 Semiconductor Diode Laser Characteristics

The fundamental physics of semiconductors and diode lasers have been presented elsewhere [12, 15, 16, 17, 18, 19] and need not be reproduced here. However, it is pertinent to draw on several of the relevant features of diode lasers and these are summarised in this section.

A typical construction of a diode laser was shown in Figure 2.1. Laser light was generated by passing a current, the *injection current*, vertically through the gain region where electrons and holes recombined to produce photons. The emitted wavelength was determined by the bandgap energy of the particular semiconductor material and was broadband, typically $\Delta\nu = 20 - 50$ MHz, relative to atomic transitions, which are a few MHz. The active region was typically 0.1μm to 0.3μm thick, $\sim 4\mu$m wide with lengths ranging from 100μm to 1000μm. Transverse confinement of the laser mode can be achieved by two separate methods. The first method is known as *index-guiding* whereby growing lower refractive index material either side of the gain region, as well as above and below it, the light can be contained and guided along a narrow channel. The second, alternative method, known as *gain-guiding*, restricts the dimensions of the metal contact supplying the injection current to a thin stripe, thereby creating a narrow gain region in the active layer. The majority of atomic physics performed using diode lasers in the near infrared has been based on index-guided AlGaAs lasers. The output power of a typical semiconductor diode laser as a function of the injection current is shown in Figure 2.2. The abrupt onset of lasing can be seen at the threshold

current.

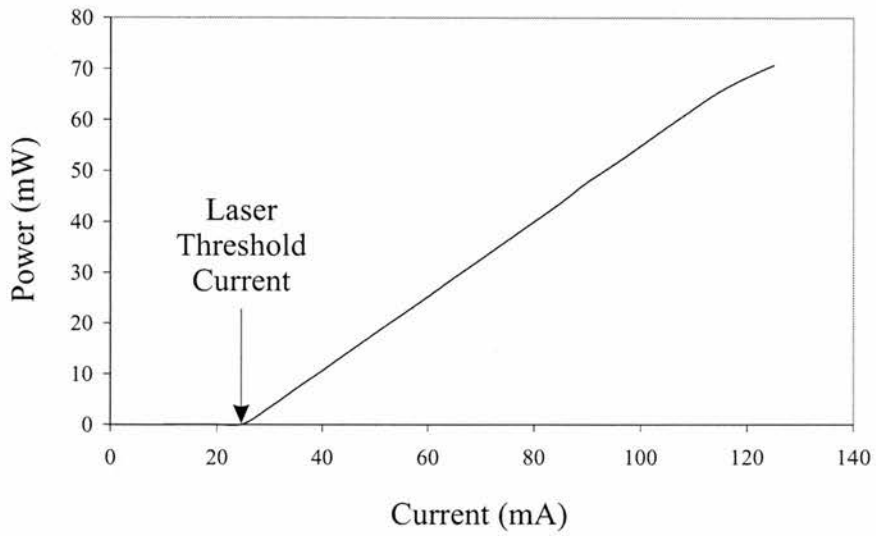

Figure 2.2: Output power versus injection current for a typical AlGaAs laser. The sudden change in slope when the threshold current is reached marks the onset of laser action.

2.2.1 Spatial Characteristics

Due to the output beam of the laser being emitted from a small rectangular aperture with dimensions of the same order as the wavelength of the light, diffraction occurs and the beam subsequently has a large divergence. A typical output beam has a divergence angle, full width at half maximum (FWHM), of 30^o in the direction perpendicular to the junction, $\theta_\perp$, and 10^o in the parallel direction, $\theta_\parallel$, as shown in Figure 2.3. The beam is then usually collimated, typically using a small f number lens to give an elliptical profile. If a circular profile is required, as is necessary in atom trapping experiments, then subsequent beam shaping by anamorphic prisms, cylindrical lenses or fibre coupling is needed.

The non-symmetric beam profile is one of all diode lasers' shortcomings when incorporated into atom trapping experiments. However, this limitation was addressed directly during this research and resolved without the need for extraneous beam shaping optics. Chapter 4 details the solutions implemented.

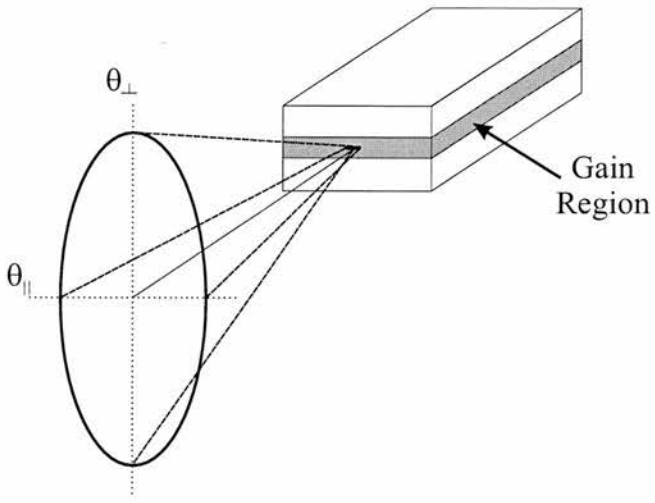

Figure 2.3: The elliptical beam profile of a laser diode is a result of emission from the rectangular gain region having dimensions of the same order as the emitted wavelength.

2.2.2 Linewidth Characteristics

The gain bandwidth of a diode laser will typically range over 20 nm although this reduces to approximately 5 nm in MQW lasers. A diode laser's mirrors, in most instances, are formed by simply cleaving the semiconductor wafer along the crystal axis perpendicular to the optical axis. This creates parallel reflecting surfaces which form the resonating cavity. Allowed longitudinal modes are defined by the free spectral range (FSR) of the cavity with the laser outputting one or more such modes. At low powers, just above threshold, it is common for the laser to run multi-mode but as competition effects mount with increasing current, one or two modes dominate. Diode lasers can be forced to run single mode by implementing one of a number of methods. Grooved or cleaved coupled cavities, distributed feedback (DFB) or distributed Bragg reflectors (DBR) achieve single mode operation although all of these methods result in reduced tuning ranges.

Because of the high index of refraction of the semiconductor (typically $\eta \sim 3.5$), the reflectivity at the cleaved interfaces is of the order of 30%. This low reflectivity (relatively speaking with respect to other laser cavities) in addition to very short cavity lengths leads to large laser mode linewidths defined by the modi-

fied Schawlow-Townes formula [16, 20, 21]. Linewidths of common commercially available diode lasers vary from 10 to 500 MHz, values somewhat larger than those defined by Schawlow and Townes but that are accounted for by fluctuations in charge carriers and temperature [22]. This linewidth is too large for probing atomic transitions whose linewidths are typically of the order of a few MHz. This is yet another weakness of the diode laser that must be addressed before use in atomic physics although selective optical feedback can ensure single longitudinal mode operation and narrow linewidths, as shall be discussed later in this chapter.

2.2.3 Tuning Characteristics

A diode laser's wavelength is primarily determined by the bandgap energy of the semiconductor material, with smaller changes occurring as a result of the diode's temperature [23, 24, 25] and current density [26, 27]. The bandgap energy is defined by the composition and structure of the device and, unfortunately, is outwith the control of the experimentalist in the laboratory. Commercial lasers show discontinuous tuning over typically 20 nm but if the laser is to be operated at or near room temperature, it is important to make a judicious choice of diode in the first instance.

Temperature Tuning

Tuning of the laser frequency is possible because both the optical path length and the wavelength dependence of the gain curve vary with temperature. Unluckily these dependencies are quite different. This results in a "staircase-like" tuning curve, as shown in Figure 2.4, where the slope of each step is the tuning of one mode and the jumps are caused by the hopping of one longitudinal mode to another. In this way it is possible to use the temperature dependency to observe atomic transitions and as a means of wavelength stabilization. However, the

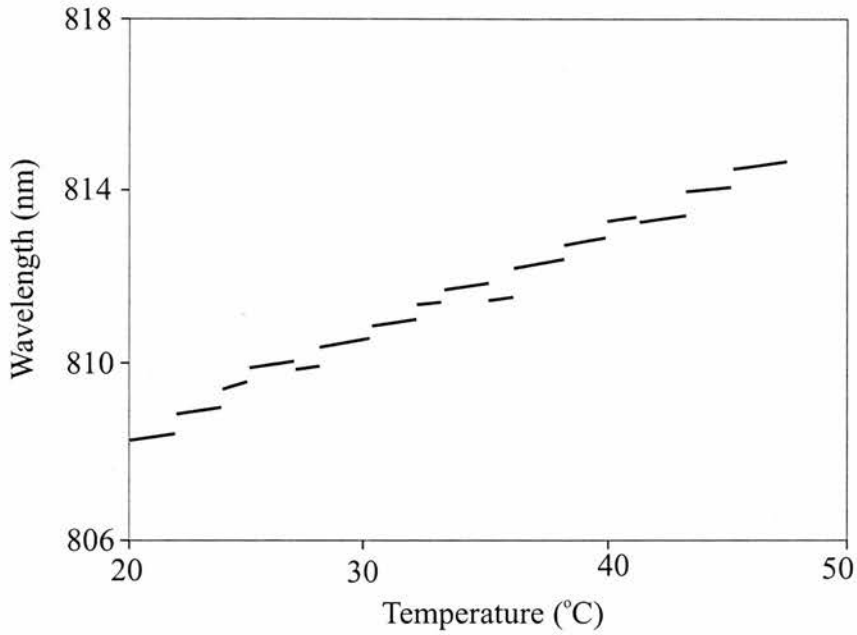

Figure 2.4: A typical wavelength versus temperature graph of a diode laser. The short continuous segments show the tuning of a single longitudinal mode due to the changing optical path length. The breaks occur when the peak of the gain bandwidth shifts too far and the laser jumps to another mode.

large spectral jumps are the main disadvantage to using diode lasers in atomic physics although there are methods to overcome this problem. A commercial laser quoted for operation at room temperature can lase typically ±30 K about this temperature. Problems exist when operating the laser at either ends of this temperature range. At high temperatures there is degradation in the laser's lifetime and at low temperatures care needs to be taken to ensure condensing water vapour does not come into contact with the semiconductor material causing the laser to cease operation.

Current Tuning

In addition to temperature tuning, the laser wavelength is also dependent on the injection current. In this case, the variation in current affects both the diode temperature and the carrier density. The temperature change is identical to that

described in the previous section while the change in carrier density results in a change of refractive index which in turn varies the wavelength. For time scales longer than $\sim$1 μs the change in current can be thought of as a quick method of changing the temperature of the diode since the index of refraction contribution is relatively small. The heating of the junction occurs through Joule heating and as a result the tuning curve shows the same characteristics as shown in Figure 2.4. Only on time scales shorter than 1 μs is the temperature rise small enough so that the change in refractive index has a noticeable effect. One of the great strengths of diode lasers over many of their contemporaries is their ability to tune rapidly in both amplitude and frequency by variation of the injection current.

2.3 Diode Lasers with Optical Feedback

It has been alluded to previously in this chapter that optical feedback affects the output from a diode laser. Feedback is achieved by creating a cavity external to the diode's own front and back facet by using an extraneous optical element to return a fraction of the output light back to the diode. The laser characteristics then take on those defined by the extended-cavity while the diode provides optical gain. Feedback has been reported using mirrors [28], GRINRODs [29, 30], etalons [31, 32] although the most dominant cavity design for diode lasers has been the Littman-Metcalf geometry [33, 34] and the Littrow geometry [22, 35, 36, 37]. Optical feedback can have both a detrimental and beneficial effect on a diode laser's characteristics. In most cases, unwanted reflections returning to the laser cavity can be eliminated successfully by the use of an optical isolator. Diode lasers are sensitive to optical feedback due to a combination of three main factors [38, 39, 40, 41, 42].

(i) The gain curve of the semiconductor is flat as a function of wavelength.

(ii) The cavity Q-factor is low.

(iii) The cavity is very short.

Because of the high gain, low Q cavity, there are only a small number of photons in the cavity at any one time. The lasing wavelength can therefore be perturbed easily by an external influence leading to a weak dependence of laser gain on wavelength. In addition, the laser acts as a photodiode when light is returned to the cavity. This affects the carrier densities in the active region thereby altering the net laser gain. The insensitivity of the laser gain to any preferred lasing wavelength can be used as an advantage in improving the laser's characteristics. Short laser cavities are more susceptible to optical feedback since the frequency shift is given by,

$$\omega - \omega_0 = \frac{c}{2\ell}\alpha', \tag{2.1}$$

where ℓ is the cavity length and α' is the combined phase shift from both output facet and the source of the feedback. Therefore for a given phase shift, the frequency shift is greater for shorter cavity lengths. The benefits one may achieve from employing selective optical feedback are, in general, fourfold. These are listed below with theoretical details being found in literature [28, 43].

(i) *Single Mode Operation*

Single mode operation from a diode laser may be brought about by implementing DFB, DBRs or coupled cavities. Unfortunately, associated with this improvement in longitudinal mode structure is a reduction in tuning of the laser wavelength.

(ii) *Increased Tunability*

By altering the extended-cavity length, the laser wavelength can be tuned mode-hop free, in some cases, across the entire gain bandwidth (~20 nm). However, this enhanced tunability requires careful alignment of optics and positioning of the optical feedback element.

(iii) *Linewidth Narrowing*

Since an oscillating mode's linewidth is inversely proportional to both the

cavity round-trip time and the cavity Q-factor, the mode oscillating within the extended-cavity experiences a spectral narrowing from these factors.

(iv) *Improved Frequency Stability*

Fluctuations in wavelength arise from the change in the refractive index-length product of the cavity. It can be shown mathematically that the variation in this product can be reduced by introducing optical feedback.

It is because of these characteristics that diode lasers placed in an extended-cavity geometry are now used extensively throughout the industrial and academic atomic physics community for detailed atomic and molecular spectroscopy. Two of the most popular geometries are known as the Littman-Metcalf geometry and the Littrow geometry. Both of these configurations rely on a diffraction grating as the means of providing selective optical feedback.

2.3.1 Diffraction Grating Theory

A diffraction grating is an optical element that spatially separates incident polychromatic light into its constituent wavelengths. It consists of a series of equally spaced parallel grooves etched onto the surface of a reflective substrate. The spacing between the grooves and the angle the grooves form with respect to the substrate influence the dispersion and efficiency of the grating. The spacing between grooves must be of the order of the wavelength of the incident light for diffraction to occur. Spacings too small or too large will not yield diffraction. There exist currently two types of diffraction gratings. One is known as a *ruled grating* where the grooves are physically cut into the substrate producing a sawtooth like profile. The other is called a *holographic* or *interference grating.* These are produced by using a photolithographic technique where an interference pattern is shone onto a light sensitive photoresist. After processing, the grating profile is sinusoidal in nature. The gratings used throughout this research were ruled gratings.

The general grating equation is:

$$n\lambda = d(sin\theta \pm sin\theta') \tag{2.2}$$

where n is the diffracted order, λ is the wavelength of light, d is the grating constant (the distance between successive grooves), θ is the angle of incidence of the light normal to the grating and θ' is the angle of diffraction measured normal to the grating, see Figure 2.5. A number of diffracted orders can be seen, as is shown mathematically by n in Equation 2.2. The number of orders is limited by the groove spacing and the angle of incidence (which cannot exceed 90^o) with higher orders having reduced efficiency but increased angular dispersion. A diagram of several diffracted orders generated from a grating are shown schematically in Figure 2.6.

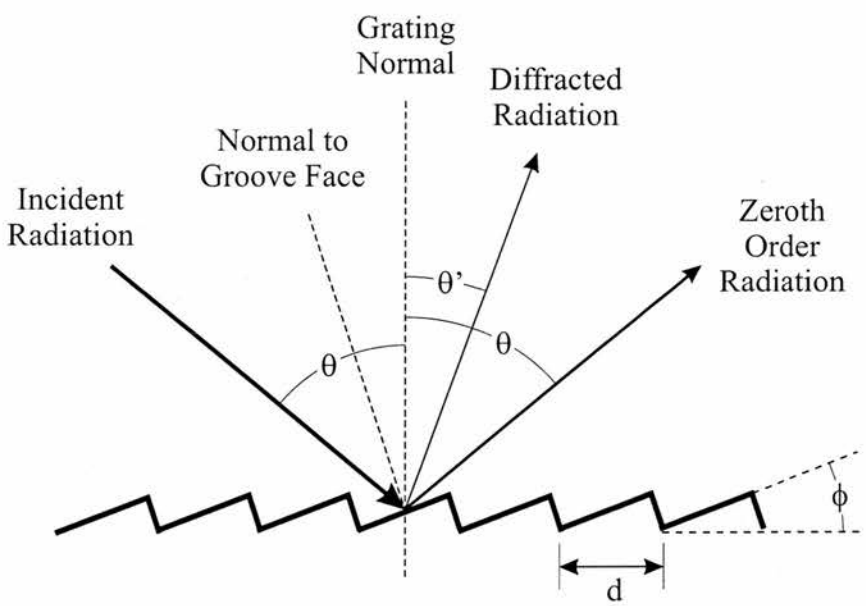

Figure 2.5: Diagram showing the grating angles and terms used in describing the physical properties of ruled diffraction gratings.

The angle ϕ defined by the longer side of the groove and the plane of the grating is the *blaze angle*. Changing the blaze angle diffracts preferentially more light into one specified order thereby increasing the efficiency in that order. The wavelength

at which maximum efficiency occurs is termed the *blaze wavelength.*

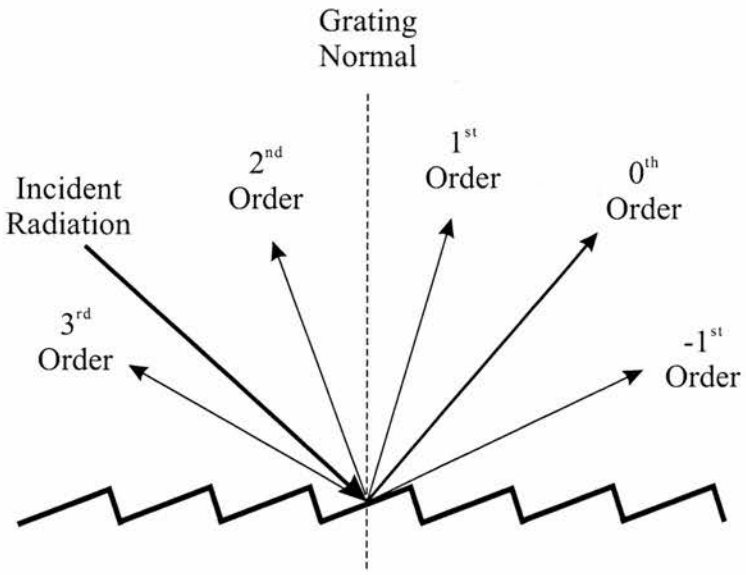

Figure 2.6: Schematic diagram indicating the diffracted orders seen when an incident beam diffracts from a ruled grating.

The experimental gratings used for the purposes of optical feedback throughout this work were ruled gratings with a grating constant of $8.3\text{x}10^{-7}$ m (1200 lines mm^{-1}) and a blaze wavelength of 300 nm into the first order. This blaze was chosen such that approximately 25–30% of incident light at 780 nm was diffracted into the first order thereby leaving the majority of the power in the zeroth order, and the output of the extended-cavity laser.

2.3.2 Littman-Metcalf Geometry

In the late 1970s Shoshan and co-workers [33] reported a nitrogen-laser-pumped dye laser that was tuneable with a spectrally narrow linewidth. A diffractive grating and a mirror gave a means of providing feedback. A diffraction grating was used because of its wavelength selective dispersion. Figure 2.7 shows a schematic diagram of the setup. Soon afterwards, Littman and Metcalf [34] published a

similar paper which rewarded them with the geometry being named after them[2]. As a direct result, several lasers emerged based on this geometry including pulsed dye lasers [44, 45, 46], pulsed CO_2 lasers [47] and diode lasers [48].

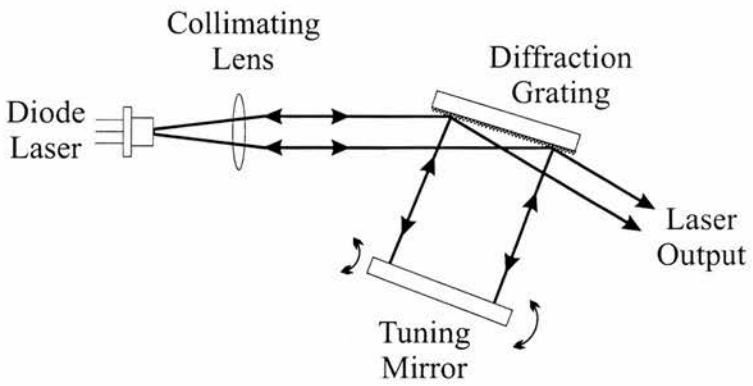

Figure 2.7: Schematic diagram of the Littman-Metcalf geometry when applied for use with diode lasers.

The output from the laser is collimated and directed towards the grating at grazing incidence. The zeroth order reflection becomes the output of the extended-cavity with the first order incident on a 100% reflection mirror. This is reflected back on itself before being diffracted once more at the grating and the first order being returned to the laser. The zeroth order at this point is lost from the cavity. The mirror angle acts as the tuning mechanism. When the cavity is tuned, the comb of extended-cavity modes shifts proportionally to the cavity length. The dispersion bandwidth also shifts but is proportional to the angle of the mirror. To achieve single mode tuning without mode-hops, the extended-cavity modes and the dispersion bandwidth must move in unison such that the same mode is preserved over the entire tuning range. In this way, the entire bandwidth gain of a diode laser can be accessed by a single, tuneable cavity mode. It should be noted however that high quality anti-reflection (AR) coatings (reflectivities lower than 10^{-3} and approaching 10^{-4}) are required for this type of performance while only limited tuning is observed when uncoated diodes are used. Coating performance is therefore crucial to the tunability of the laser.

[2]A excellent example that not only is life not fair in love and war, but in science also!

2.3.3 Littrow Geometry

In 1972, Hänsch reported the construction of a tuneable, pulsed dye laser using a grating mounted in, what has become to be known as, the *Littrow geometry* [35]. The design was incorporated into single-frequency, tuneable diode lasers in 1981 by Fleming and co-workers [20]. Figure 2.8 shows a schematic of the Littrow geometry when applied to a diode laser.

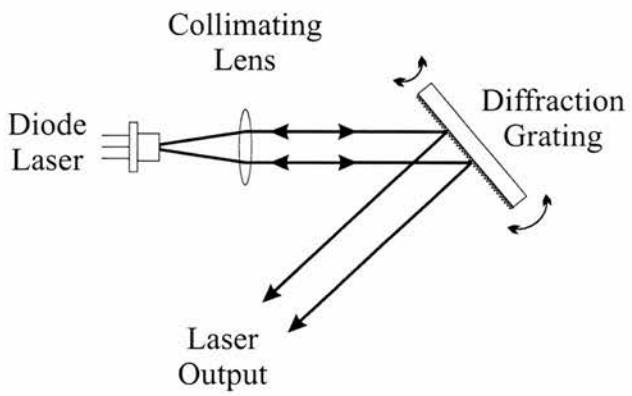

Figure 2.8: Schematic diagram of the Littrow geometry when applied for use with diode lasers.

Initially the output of the diode laser is collimated. It is then incident on a diffraction grating mounted at the *Littrow angle*. This is the angle at which the first diffracted order is returned to the diode to provide feedback whilst the zeroth order reflected beam becomes the output. The angle and distance of the grating relative to the diode determines the tuning. It is sometimes necessary to include an etalon within the cavity to obtain single-mode oscillation as it is often the case that the FWHM frequency bandwidth of the grating is larger than the diode laser's FSR. To obtain large, continuous tunability it is vital that the cavity length and gain dispersion should move synchronously, supporting the same mode at all wavelengths. The means by which a single, spectrally narrowed longitudinal mode is selected in the Littrow geometry is shown in Figure 2.9. The spectral gain profile of the semiconductor material extends over approximately 20 nm, as shown in Figure 2.9(a). The diffraction grating is spectrally selective

in nature and feeds back light only over a range of wavelengths. Longitudinal laser modes supported by both the diode laser cavity and the extended-cavity are shown in Figure 2.9(b). Single mode oscillation is obtained by having only one extended-cavity mode coinciding with one of the diode laser transmission peaks. Although in the figure there exists a number of modes that fulfill this requirement, indicated by ν_1, ν_2 and ν_3, only one will oscillate because only one lies within the grating selectivity bandwidth *and* at the highest point in the spectral gain profile, indicated by ν_2 in the figure.

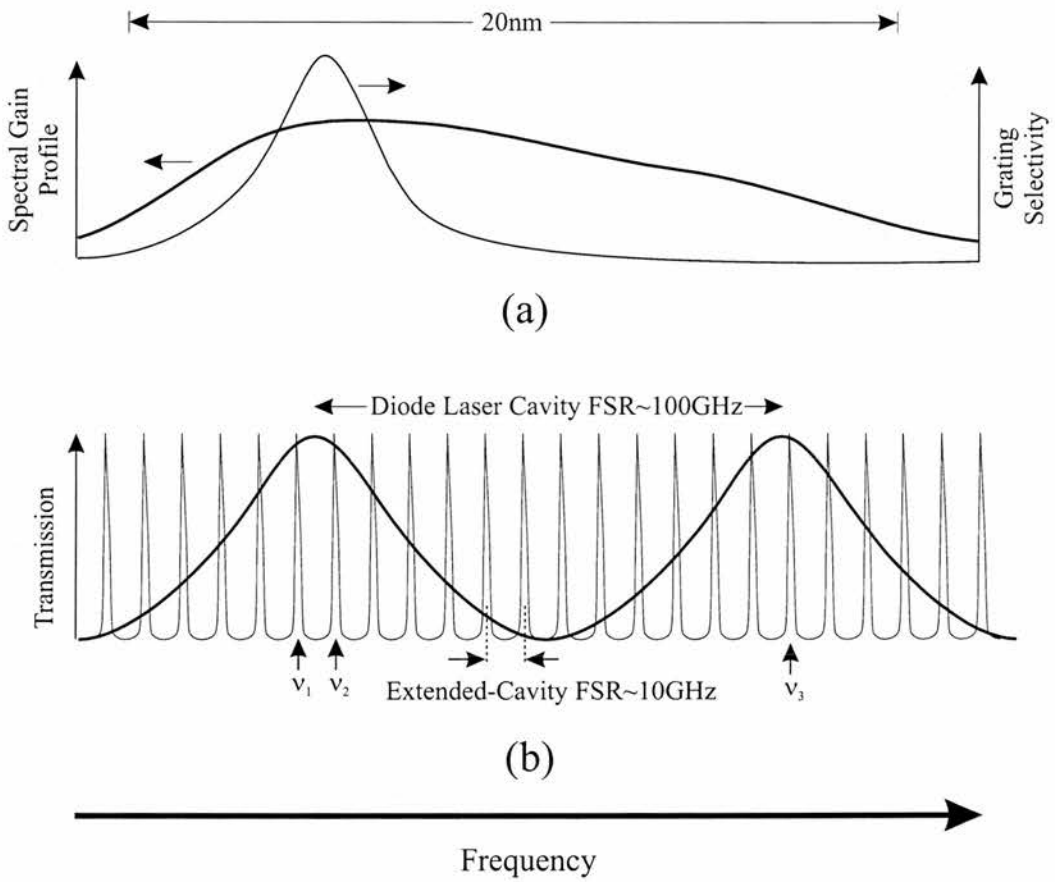

Figure 2.9: A representation of competing processes present during optical feedback from a wavelength selective element, such as a diffraction grating. The spectral gain profile of the diode laser (dark line) and the grating selectivity (light line) are shown in (a) whilst the modes that can be sustained in the diode laser (dark line) and extended-cavity (light line) are shown in (b). Although ν_1, ν_2 and ν_3 all lie within the transmission peaks of the laser diode cavity, only ν_2 lies within the grating selectivity *and* at the highest point in the spectral gain profile and therefore this is the *only* mode that will oscillate.

2.3.4 Comparison between Littman-Metcalf and Littrow Geometries

There are two main advantages of the Littman-Metcalf configuration over the Littrow geometry. Firstly, single-mode operation is usual due to the large wavelength dispersion obtained from the double pass diffraction. This generates a frequency bandwidth less than the FSR of the extended-cavity, forcing only one cavity mode to oscillate. However, single-mode operation can be achieved in the Littrow configuration by a number of additional methods. An intra-cavity etalon may be used that has high finesse and a FSR greater than the FWHM of the Littrow frequency bandwidth. This increases the complexity of the system as accurate tuning of this additional element at the same time as rotating the grating is necessary for mode-hop free tuning. Another solution is to use a single-mode commercial diode laser. Secondly, the output beam is not altered spatially by tuning which is the case with the Littrow geometry. However, the Littman-Metcalf geometry places stringent requirements on the quality of the grating because of the double pass diffraction scheme. Strong feedback is needed for wide tuning over the diode's entire gain bandwidth. A further disadvantage of the Littman-Metcalf geometry is the slight increase in complexity in alignment of the setup. Two optical elements need be positioned accurately in contrast to only one in the Littrow geometry.

If only a few GHz mode-hop free tuning is required at a specified wavelength then the Littrow geometry becomes attractive because of its simplicity and robustness. The Littman-Metcalf geometry is preferred if wide tunability is an important issue.

2.4 Frequency Locking Techniques

Not only must a laser output be single mode, tuneable and have narrow linewidth characteristics but in many instances the frequency must also be stabilized to a precisely determined value. Alternatively, a constant frequency difference between two lasers may be required to be maintained [49, 50, 51]. In general, this is accomplished by locking the laser frequency to a well known atomic or molecular transition frequency [52] or a mechanically stabilized, high finesse etalon [53, 54] by way of negative feedback.

2.4.1 Servo Locking Systems

A servo locking system, in this instance, describes a system which provides a means of negative feedback and stabilization of a laser to a particular frequency. A basic servo loop is shown in Figure 2.10. Some noise is present in the laser which causes its frequency to vary with time. The laser output is compared with a reference which, as mentioned, could take the form of an atomic transition or stable optical cavity. From this comparison an error signal is obtained which indicates how far the laser's frequency is from the reference frequency. This error signal is fed into compensation electronics to provide a negative feedback signal which is returned to the laser. The feedback is negative so as to cancel the effect of the noise and bring the laser's frequency back towards the reference. The error signal is inversely proportional to the gain of the electronics so in order to push the laser frequency as close to the reference frequency as possible it is necessary to have a gain as large as possible. In this manner, the laser's frequency is locked to the reference frequency.

An important point to consider when understanding servo locking is that there is always some form of time delay or lag in the system. A common method of feedback used in stabilizing an optical cavity is the use of a piezoelectric transducer (PZT) attached to one of the cavity mirrors. Since very small mechanical shifts

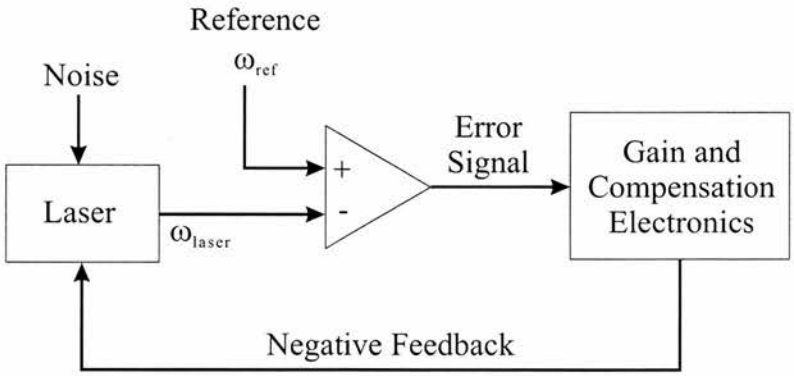

Figure 2.10: Schematic diagram of a basic servo loop for stabilization of a laser.

can lead to significant frequency deviations, on this scale, a PZT disc behaves like a classical spring. Since the mirror has a mass, the mirror/PZT ensemble acts like a harmonic oscillator. For low frequencies, below the ensembles' resonant frequency, the mirror will follow the error signal in phase and correct for the deviations in laser frequency. However, if corrections above the resonant frequency are rectified then there is a 180^o phase lag between the mirror and the error signal and the feedback becomes positive. This highlights the primary problem when implementing negative feedback in these types of systems, namely that if the same gain in the compensating electronics is employed across all frequencies then the system adjusts correctly for errors below the resonant frequency but becomes an oscillator for frequencies above this value.

One can increase the electronic gain at lower frequencies to improve d.c. response to the detriment of the bandwidth of the system and, vice versa, the bandwidth can be increased with a loss of gain at lower frequencies. Hence, a trade-off always exists between the bandwidth (fast transient response) and the d.c. gain (small steady-state errors) of any servo locking system.

In some laser locking scenarios it is possible to employ two servo systems simultaneously, one with a slow response and one with a fast response, to correct for noise across an increased frequency spectrum. An example of how this can be achieved in extended-cavity diode lasers is by using a PZT that corrects for slow drifts in

frequency and implementing the laser current to correct for high frequency noise. This is known as *dual current/PZT locking*. This particular locking scheme has been used successfully as part of this research.

Because this thesis is concerned with trapping and cooling neutral atoms, it was necessary to stabilize the experimental lasers relative to the atomic transitions of interest. All the systems discussed in the following subsections are specific applications of servo locking and are experimentally investigated in Chapter 3.

2.4.2 Doppler-Free Saturated Absorption Spectroscopy

The simplest method of locking a laser to an atomic hyperfine resonance is by Doppler-Free saturated absorption spectroscopy. This technique also serves as the basis for several other spectroscopic schemes, some of which are discussed in following sections. The technique was conceived in the early 1970s by Hänsch and co-workers [55, 56] as a method of gaining information from the spectra of atoms without the effect of Doppler broadening. The kinetic motion of an ensemble of thermal atoms in a vapour cell would tend to "wash out" the finer features of the atom's electronic structure and this method surmounted the problem by interacting solely with those atoms whose velocity along the direction of propagation of the laser was zero. This followed on from fundamental work carried out by themselves and others [57].

The experimental setup is shown in Figure 2.11. In this technique, two counter-propagating, overlapping laser beams of exactly the same frequency interact with atoms contained within a vapour cell. It is only those atoms that have zero velocity in the direction parallel to the passage of the laser beams that interact with both beams when the laser is tuned to the atomic resonant frequency, as shown in Figure 2.12. All other atoms have a velocity component in the direction of the laser beams and therefore experience a Doppler shift. The more intense *pump beam* saturates the transition so that the *probe beam* may pass unabsorbed

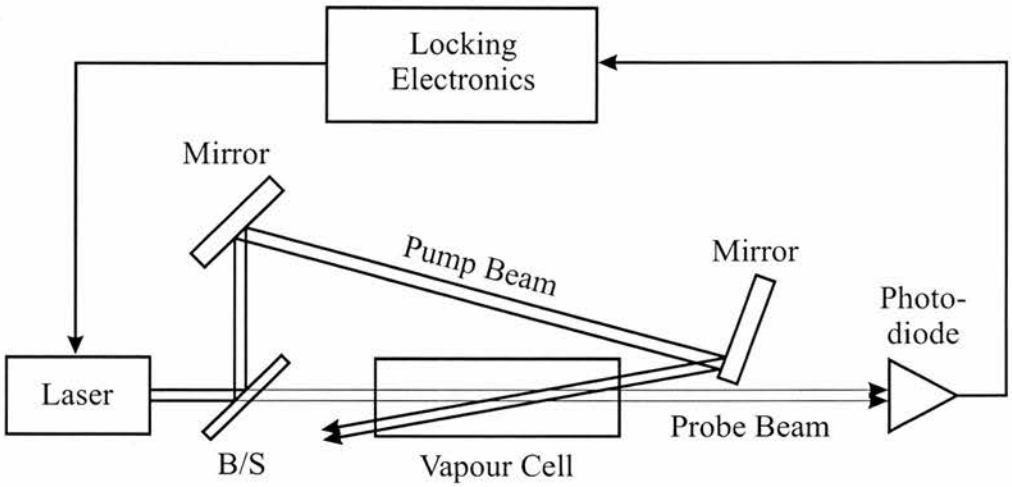

Figure 2.11: Schematic diagram for a saturated spectroscopy setup. B/S = Beam splitter.

through the vapour cell thereby creating a dip in the Doppler broadened absorption profile. These dips correspond to electronic transitions within the atom. As well as observing dips at frequencies coinciding with electronic transitions, so called *cross-over transitions* occur when the laser frequency is tuned exactly halfway between two electronic transitions. These dips can be explained by examining a sub-group of atoms with a specific velocity component parallel to the laser propagation direction. If the laser frequency is tuned to be exactly halfway between two electronic transitions then such a sub-group can interact with both laser beams simultaneously. An atom can be resonant with a laser frequency that has been Doppler shifted *up* to a particular transition whilst also being resonant with same laser frequency Doppler shifted *down* to a different transition. This only occurs when the Doppler shift is identical in both cases i.e. when the laser is tuned to be exactly halfway between two transition frequencies. A more thorough explanation of this phenomenon can be found in literature [58]. These cross-over transitions are important as they are used to provide a locking signal for experiments performed at St Andrews.

Depending on the experimental requirements, the laser frequency can be locked to either the peak, *peak locking*, or side of one of these transitions, *side-of-fringe locking*, as indicated on a rubidium saturated absorption signal shown in Fig-

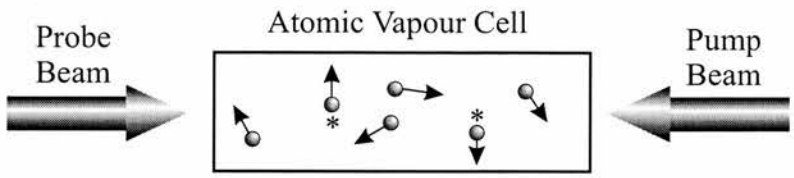

Figure 2.12: A cell contains a thermal atomic vapour. Two laser beams of the same frequency, a *pump beam* and a less intense *probe beam*, pass through the cell in a counter-propagating manner. When the laser frequency is tuned to an electronic transition within the atom then it is only those atoms with zero velocity along the direction of propagation of the laser beams (indicated by *) that can interact with both beams simultaneously. This creates a dip in the Doppler broadened absorption profile of the probe beam when the laser is tuned across an atomic transition.

ure 2.13. Side-of-fringe locking delivers a simple lock using elementary electronics while allowing a variation in the locking frequency over the width of the locking slope. Peak locking provides a stronger, more robust lock at the expense of more complicated electronics and being unable to vary the locking frequency without additional optics. Side-of-fringe locking was used as a means of frequency stabilization initially during this work because of simplicity although in the latter stages peak locking was incorporated to improve frequency stability. The following sections present the theory of each technique used in a chronological fashion as investigated during this research.

2.4.3 Polarisation Spectroscopy

While saturated absorption spectroscopy monitors the decrease in absorption of an atomic vapour, polarisation spectroscopy measures the polarisation state of a probe beam which passes through an atomic vapour. The technique has been utilized by the atomic physics community for a number of years with the first experimental observation being made by Wieman and Hänsch in 1976 [59]. It was applied to the stabilization of diode lasers in the early 1990s [60, 61] and later to applications in laser cooling and atom trapping [62]. The setup is very

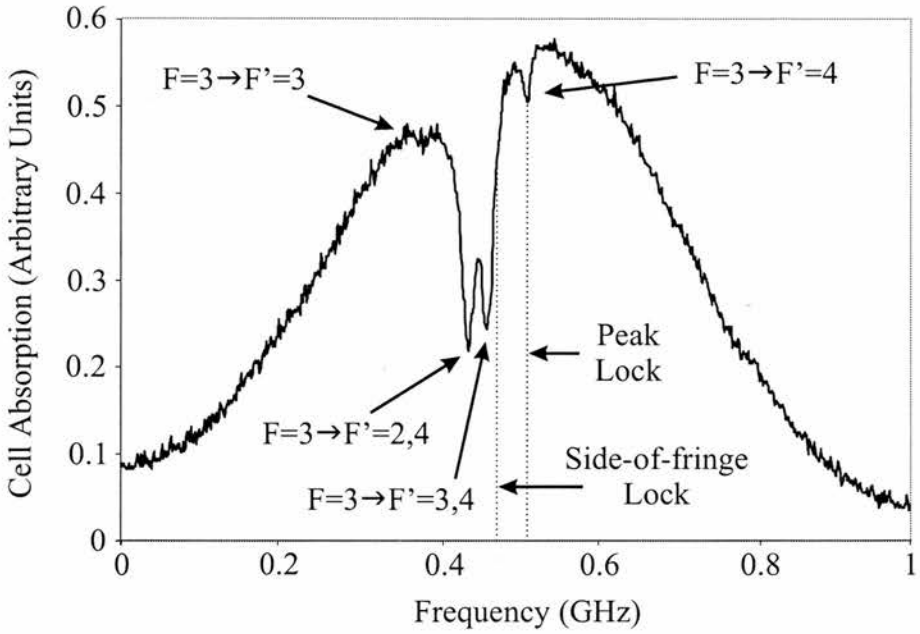

Figure 2.13: A typical saturated absorption spectroscopy profile for the ^{85}Rb F=3→F' transition. The vertical lines indicate the frequencies that a laser could be locked to using either a peak-locking or a side-of-fringe locking technique.

similar to that required for saturated spectroscopy but with the inclusion of a polariser, an analyser and a quarter-wave plate, as shown in Figure 2.14.

The output from a tuneable, monochromatic laser source is split into a weak probe beam and a stronger pump beam. The probe beam passes through a linear polariser, the vapour cell and a second linear polariser crossed with the first (known as an analyser) and is then incident on a photodiode. The pump beam passes through a quarter-wave plate before passing, in the opposite direction to the probe beam, through the vapour cell. The linearly polarised probe beam may be decomposed into two counter-rotating circularly polarised beams, one rotating in the same sense as the polarising beam and one rotating in the opposite sense. When tuned to an atomic resonance, the degenerate sublevels are unevenly pumped by the circularly polarised pump beam due to polarisation dependent selection rules. This anisotropy leads to two effects being seen on the linearly polarised probe beam. Firstly, the vapour becomes circularly dichroic making the probe beam elliptically polarised and, secondly, it becomes birefrin-

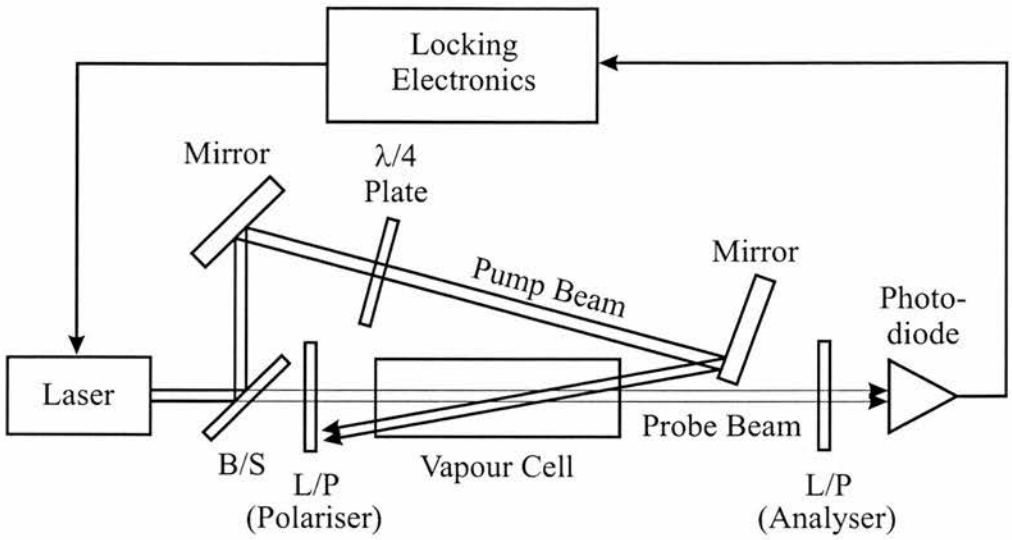

Figure 2.14: Schematic diagram for a polarisation spectroscopy setup. B/S = Beam splitter and L/P = Linear polariser.

gent which rotates the axis of polarisation [59]. Since it is only those atoms which interact with both laser beams at the same time that contribute to the effect, this technique is, like saturated absorption, Doppler-free. Therefore, when a laser is tuned across an atomic resonance, the probe beam polarisation adopts an elliptical nature and is rotated causing an increase in intensity being detected at the photodiode.

2.4.4 Dichroic-Atomic Vapour Laser Lock

Another technique that can be used to either side-of-fringe or peak lock a laser is known as dichroic-atomic vapour laser lock (DAVLL). Originally known as Zeeman locking, this technique was used to peak lock without the need for modulation of the laser frequency [63]. Instead the degenerate sublevel energies in an atomic vapour were made to oscillate by introducing an a.c. ripple to a solenoid placed around the vapour cell. This produced the desired absorption oscillation required for locking and was first shown in stabilizing an infrared stryrl-9 dye laser [64]. The method has been applied subsequently to a free-running diode

laser locked to a transition in caesium [65], a confocal-cavity locked diode laser using rubidium [66] and in stabilizing an ECDL in the Littrow geometry to potassium [67]. All of these experiments are Doppler-free in nature and lock the laser to one particular frequency. The second method of utilizing the Zeeman effect in an atomic vapour is shown in Figure 2.15. This describes a side-of-fringe locking scheme which was first proposed and demonstrated experimentally by Chéron *et al.* [68] on a diode pumped LNA laser in helium and later extrapolated for use by Corwin *et al.* [69] in rubidium using ECDLs.

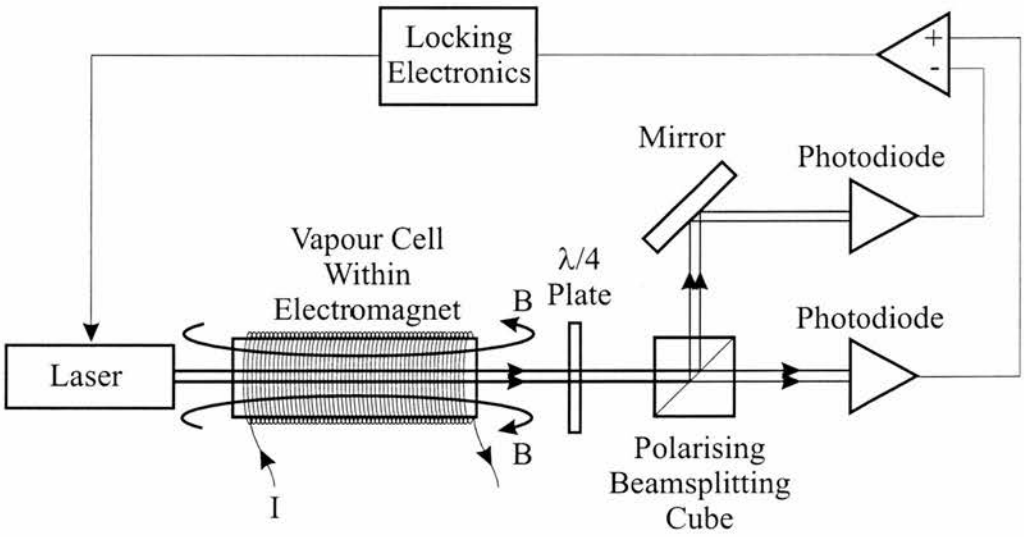

Figure 2.15: Schematic diagram for Dichroic-atomic vapour laser lock.

Linearly polarised radiation, resonant with an atomic transition, passes through an atomic vapour cell, parallel to the magnetic field. The linearly polarised beam can be thought of as a coherent sum of two orthogonal circular polarisation states, σ^+ and σ^- of equal intensities. The B-field separates the normally degenerate sublevels within the atoms causing the absorption line to be split into two Zeeman components, shifted in opposite directions. A quarter-wave plate produces two orthogonal, linearly polarised components which are then separated spatially at a polarising beam splitting cube and collected at individual photodiodes. The measured signals can be seen in Figure 2.16. If these signals are fed to a differential amplifier then a dispersive signal is obtained that can be used for locking

purposes. This dispersive signal has the same signal-to-noise ratio as saturation spectroscopy but because the signal is composed of Doppler broadened profiles, the capture range, i.e. the locking range, can be as large as 800 MHz [70].

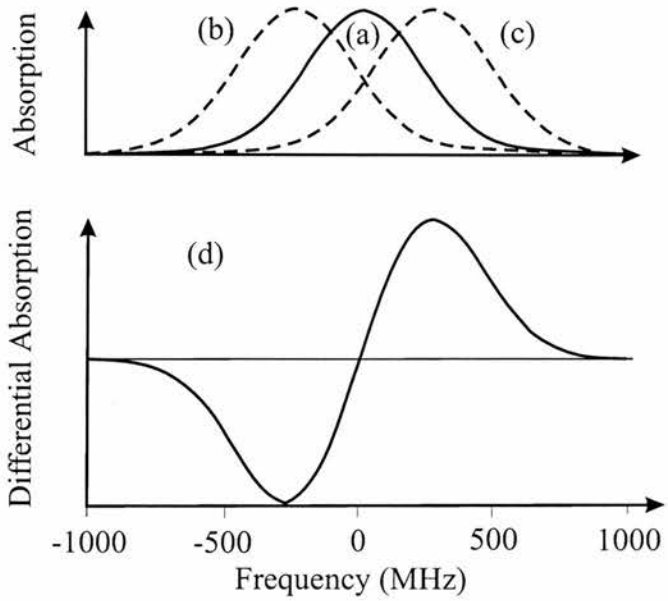

Figure 2.16: Intensity signals measured from DAVLL experiment. The Doppler broadened peak is shown when no magnetic field is present (a) along with the frequency shift associated with the σ^+ and σ^- polarisation peaks when present in a magnetic field of 100G, curves (b) and (c). When (b) and (c) are combined in a differential amplifier, (d) is generated giving the slope to which the laser is locked.

2.4.5 Dual Current/PZT Locking

All the the above techniques rely solely on feedback via the PZT resulting in high frequency noise not being corrected for. Incorporating a fast feedback loop via the diode laser's current increases the system's bandwidth thereby providing a stronger lock. One method of implementing two different feedback loops in a peak-locking scheme using a saturated absorption signal is dual current/PZT locking. The strength of this lock stems from the dual feedback providing both a slow and a fast response to frequency fluctuations. However, a disadvantage is that it requires the modulation of the laser frequency over the transition, usually

by applying a dither to the diode current driver, to generate a dispersive signal to which the frequency can be locked. This can impose sidebands on the laser output that may be unacceptable in a particular experiment. Chapter 3 outlines briefly the electronics required to generate the dispersive locking signal and also the experimental setup and performance of this scheme while Appendix A details the electronics and circuit diagrams. In the case of laser cooling, the laser must be detuned from the peak resonance frequency if dual current/PZT locking is employed. One method to do this is by incorporating additional optics, such as an acousto-optic modulator (AOM), into the setup which inevitably leads to a decrease in power and an increase in complexity of the laser system. However, the slight decrease in power is, in most cases, negligible with respect to the improvement in the frequency stability of the laser and robustness of the lock.

2.5 Summary

This chapter has provided an introduction to the operation of diode lasers. The characteristics of such lasers have also been discussed with respect to their use in laser cooling experiments. One crucial characteristic of any diode laser to be used in atom trapping is its ability to be tuned and stabilized effectively to a predetermined frequency, in this case the frequency corresponding to that of an atomic transition. This chapter has outlined three methods, namely polarisation spectroscopy, DAVLL and saturated absorption spectroscopy incorporating dual current/PZT feedback by which diode lasers can be locked. All three techniques have been implemented and evaluated and the results from these investigations will be presented in Chapter 3. Overall, this chapter highlights that diode lasers are inexpensive and rugged tools ideally suited for application in the field of laser cooling and atom trapping.

Bibliography

[1] A. Einstein, "Zur quantentheorie der strahlung," Mitteilungen der Physikalischen Gesellschaft Zürich **16,** 47 (1916).

[2] R. Ladenburg, "Dispersion in Electrically Excited Gases," Reviews of Modern Physics **5,** 243–256 (1933).

[3] J. Weber, Transactions of the IRE. Professional Group on Electron Devices **PGED-3,** 1 (1953).

[4] T. H. Maiman, "Optical maser action in ruby," British Communications and Electronics **7,** 674–675 (1960).

[5] A. Javan, J. W. R. Bennett, and D. Herriott, "Population inversion and continuous optical maser oscillation in a gas discharge containing a He-Ne mixture," Physical Review Letters **6,** 106–110 (1961).

[6] Y. Watanabe and W. Nishizawa, "Semiconductor Maser,", Japanese Patent no. 273217, 1957.

[7] R. N. Hall, G. E. Fenner, J. D. Kingsley, T. J. Soltys, and R. O. Carlson, "Coherent light emission from GaAs junctions," Physical Review Letters **9,** 366–368 (1962).

[8] M. I. Nathan, W. P. Dumke, G. Burns, J. F. H. Dill, and G. Lasher, "Stimulated emission of radiation from GaAs p-n junctions," Applied Physics Letters **1,** 62–64 (1962).

[9] H. Kroemer, "A proposed class of Heterojunction injection lasers," Proceedings of the IEEE **51,** 1782–1783 (1963).

[10] I. Hayashi and M. B. Panish, "GaAs-$Ga_xAl_{1-x}As$ heterostructure injection lasers which exhibit low thresholds at room temperature," Journal of Applied Physics **41,** 150–163 (1970).

[11] I. Hayashi, M. B. Panish, P. W. Foy, and S. Sumski, "Junction lasers which operate continuously at room temperature," Applied Physics Letters **17,** 109–111 (1970).

[12] W. T. Silfvast, *Laser Fundamentals*, 1st ed. (Cambridge University Press, The Pitt Building, Trumpington Street, Cambridge CB2 1RP, 1996).

[13] S. Nakamura, M. Senoh, S. Nagahama, N. I. abd T. Yamada, T. Matsushita, H. Kiyoku, and Y. Sugimoto, "InGaN-Based Multi-Quantum-Well-Structure Laser Diodes," Japanese Journal of Applied Physics **35,** L74–L76 (1996).

[14] S. Nakamura and W. Kaenders, "Market-ready blue diodes excite spectroscopists," Laser Focus World pp. 69–75 (1999).

[15] O. Svelto, *Principles of Lasers* (Plenum Press, 227 West 17th Street, New York, N. Y. 10011, 1976).

[16] A. E. Siegman, *Lasers* (University Science Books, 20 Edgehill Road, Mill Valley, CA 94941, USA, 1986).

[17] C. C. Davis, *Lasers and Electro-Optics, Fundamentals and Engineering*, 1st ed. (Cambridge University Press, The Pitt Building, Trumpington Street, Cambridge CB2 1RP, 1996).

[18] D. A. Neamen, *Semiconductor Physics and Devices* (Richard D. Irwin, Inc., 1992).

[19] J. Wilson and J. F. B. Hawkes, *Optoelectronics, An Introduction*, 2nd ed. (Prentice Hall International (UK) Limited, Campas 400, Maylands Avenue, Hemel Hempstead, Hertfordshire, HP2 7EZ, 1989).

[20] M. W. Fleming and A. Mooradian, "Spectral characteristics of external-cavity controlled semiconductor lasers," IEEE Journal of Quantum Electronics **QE–17,** 44–59 (1981).

[21] E. Patzak, A. Sugimura, S. Saito, T. Mukai, and H. Olesen, "Semiconductor laser linewidth in optical feedback configurations," Electronics Letters **19,** 1026–1027 (1983).

[22] C. Wieman and L. Hollberg, "Using diode lasers for atomic physics," Review of Scientific Instruments **62,** 1–20 (1991).

[23] E. Andreoni, J. H. Xu, S. Cartaleva, R. M. Celli, F. Mango, and S. Gozzini, "A simple system of thermal control and frequency stabilization of solitary diode lasers," Review of Scientific Instruments **71,** 3648–3652 (2000).

[24] C. M. Klimcak and J. C. Camparo, "Photothermal wavelength modulation of a diode laser," Journal of the Optical Society of America B **5,** 211–214 (1988).

[25] M. Nakamura, K. Aiki, N. Chinone, R. Ito, and J. Umeda, "Longitudinal-mode behaviors of mode-stabilized $Al_xGa_{1-x}As$ injection lasers," Journal of Applied Physics **49,** 4644–4648 (1978).

[26] A. Dandridge and L. Goldberg, "Current-induced frequency modulation in diode lasers," Electronics Letters **18,** 302–304 (1982).

[27] T. Sato, S. Yashima, and M. Shimba, "Frequency shift of a GaAlAs diode laser in a magnetic field," Electronics Letters **22,** 979–981 (1986).

[28] L. Goldberg, H. F. Taylor, A. Dandridge, J. F. Weller, and R. O. Miles, "Spectral characteristics of semiconductor lasers with optical feedback," IEEE Journal of Quantum Electronics **QE-18,** 555–563 (1982).

[29] K. Y. Liou, "Single-longitudinal-mode operation of injection laser coupled to a GRINROD external cavity," Electronics Letters **19,** 750–751 (1983).

[30] G. P. Barwood, P. Gill, and W. R. C. Rowley, "Longitudinal mode control in laser diodes," Measurement Science and Technology **3,** 406–410 (1992).

[31] P. B. Coates, "External cavity stabilisation of gain-guided laser diodes for metrological purposes," Journal of Physics E: Scientific Instrumentation **21,** 812–816 (1988).

[32] H. Hemmati, "Single longitudinal mode operation of semiconductor laser arrays with etalon feedback," Applied Physics Letters **51,** 224–225 (1987).

[33] I. Shoshan, N. N. Danon, and U. P. Oppenheim, "Narrowband operation of a pulsed dye laser without intracavity beam expansion," Journal of Applied Physics **48,** 4495–4497 (1977).

[34] M. G. Littman and H. J. Metcalf, "Spectrally narrow pulsed dye laser without beam expander," Applied Optics **17,** 2224–2227 (1978).

[35] T. W. Hänsch, "Repetitively pulsed tunable dye laser for high resolution spectroscopy," Applied Optics **11,** 895–898 (1972).

[36] K. B. MacAdam, A. Steinbach, and C. Wieman, "A narrow-band tunable diode laser system with grating feedback, and a saturated absorption spectrometer for Cs and Rb," American Journal of Physics **60,** 1098–1111 (1992).

[37] A. S. Arnold, J. S. Wilson, and M. G. Boshier, "A simple extended-cavity diode laser," Review of Scientific Instruments **69,** 1236–1239 (1998).

[38] P. J. Brannon, "Laser feedback: its effect on laser frequency," Applied Optics **15,** 1119–1120 (1976).

[39] R. Lang and K. Kobayashi, "External optical feedback effects on semiconductor infection laser properties," IEEE Journal of Quantum Electronics **QE–16,** 347–355 (1980).

[40] G. P. Agrawal, "Line narrowing in a single-mode injection laser due to external optical feedback," IEEE Journal of Quantum Electronics **QE–20,** 468–471 (1984).

[41] G. A. Acket, D. Lenstra, A. J. D. Boef, and B. H. Verbeek, "The influence of feedback intensity on longitudinal mode properties and optical noise in

index-guided semiconductor lasers," IEEE Journal of Quantum Electronics **QE–20,** 1163–1169 (1984).

[42] K. Peterman and G. Arnold, "Noise and distortion characteristics of semiconductor lasers in optical fiber communication systems," IEEE Journal of Quantum Electronics **QE–18,** 543–555 (1982).

[43] R. Wyatt and W. J. Devlin, "10 kHz linewidth 1.5 μm InGaAsP external cavity laser with 55 nm tuning range," Electronics Letters **19,** 110–112 (1983).

[44] M. G. Littman, "Single-mode operation of grazing-incidence pulsed dye laser," Optics Letters **3,** 138–140 (1978).

[45] K. Liu and M. G. Littman, "Novel geometry for single-mode scanning of tunable lasers," Optics Letters **6,** 117–118 (1981).

[46] G. Z. Zhang and K. Hakuta, "Scanning geometry for broadly tunable single-mode pulsed dye lasers," Optics Letters **17,** 997–999 (1992).

[47] F. J. Duarte, "Multiple-prism littrow and grazing-incidence pulsed CO_2 lasers," Applied Optics **24,** 1244–1245 (1985).

[48] K. C. Harvey and C. J. Myatt, "External-cavity diode laser using a grazing-incidence diffraction grating," Optics Letters **16,** 910–912 (1991).

[49] C. S. Edwards, G. P. Barwood, P. Gill, F. Rodríguez-Llorente, and W. R. C. Rowley, "Frequency-stabilised diode lasers in the visible region using Doppler-free iodine spectra," Optics Communications **132,** 94–100 (1996).

[50] R. B. M. Clarke, E. Riis, G. P. Barwood, P. Gill, G. Huang, and H. A. Klein, "A sideband-injection locked extended cavity diode laser for interrogating cold trapped Strontium ions," Optics Communications **158,** 36–40 (1998).

[51] U. Schünemann, H. Engler, R. Grimm, M. Weidemüller, and M. Zielonkowski, "Simple scheme for tunable frequency offset locking of two lasers," Review of Scientific Instruments **70,** 242–243 (1999).

[52] G. D. Rovera, G. Santarelli, and A. Clairon, "A laser diode system stabilized on the Caesium D_2 line," Review of Scientific Instruments **65,** 1502–1505 (1994).

[53] R. W. P. Drever, J. L. Hall, F. V. Kowalski, J. Hough, G. M. Ford, A. J. Munley, and H. Ward, "Laser Phase and Frequency Stabilization Using an Optical Resonator," Applied Physics B **31,** 97–105 (1983).

[54] A. Hemmerich, D. H. McIntyre, D. S. Jr., D. Meschede, and T. W. Hänsch, "Optically stabilized narrow linewidth semiconductor laser for high resolution spectroscopy," Optics Communications **75,** 118–122 (1990).

[55] P. W. Smith and T. Hänsch, "Cross–relaxation effects in the saturation of the 6328–Å neon–laser line," Physical Review Letters **26,** 740–743 (1971).

[56] T. W. Hänsch, I. S. Shahin, and A. L. Schawlow, "High–resolution saturation spectroscopy of the sodium D lines with a pulsed tunable dye laser," Physical Review Letters **27,** 707–710 (1971).

[57] N. Bloembergen, "Nonlinear optics and spectroscopy," Reviews of Modern Physics **54,** 685–695 (1982).

[58] D. Preston, "Doppler-free saturated absorption: Laser spectroscopy," American Journal of Physics **64,** 1432–1436 (1996).

[59] C. Wieman and T. W. Hänsch, "Doppler-Free Laser Polarization Spectroscopy," Physical Review Letters **36,** 1170–1173 (1976).

[60] M. Kozuma, M. Kourogi, and M. Ohtsu, "Frequency stabilization, linewidth reduction, and fine detuning of a semiconductor laser by using velocity-selective optical pumping of atomic resonance line," Applied Physics Letters **61,** 1895–1897 (1992).

[61] J. Maki, N. Campbell, C. Grande, R. Knorpp, and D. H. McIntyre, "Stabilized diode-laser system with grating feedback and frequency-offset locking," Optics Communications **102,** 251–256 (1993).

[62] G. P. T. Lancaster, R. S. Conroy, M. A. Clifford, J. Arlt, and K. Dholakia, "A polarisation spectrometer locked diode laser for trapping cold atoms," Optics Communications **170,** 79–84 (1999).

[63] R. A. Valenzuela, L. J. Cimini, R. W. Wilson, K. C. Reichmann, and A. Grot, "Frequency stabilisation of AlGaAs lasers to absorption spectrum of rubidium using Zeeman effect," Electronics Letters **24,** 725–726 (1988).

[64] A. Weis and S. Derler, "Doppler modulation and Zeeman modulation: laser frequency stabilization without direct frequency modulation," Applied Optics **27,** 2662–2665 (1988).

[65] T. Ikegami, S. Ohshima, and M. Ohtsu, "Frequency Stabilization of Laser Diodes to the Cs-D_2 Line with the Zeeman Modulation Method," Japanese Journal of Applied Physics **28,** L1839–L1841 (1989).

[66] T. P. Dinneen, C. D. Wallace, and P. L. Gould, "Narrow linewidth, highly stable, tunable diode laser system," Optics Communication **92,** 277–282 (1992).

[67] M. Gertsvolf and M. Rosenbluh, "Injection locking of a diode laser locked to a Zeeman frequency stabilized laser oscillator," Optics Communications **170,** 269–274 (1999).

[68] B. Chéron, H. Gilles, J. Hamel, O. Moreau, and H. Sorel, "Laser frequency stabilization using Zeeman effect," Journal de Physique III **4,** 401–406 (1994).

[69] K. L. Corwin, Z. Lu, C. F. Hand, R. J. Epstein, and C. E. Wieman, "Frequency-stabilized diode laser with the Zeeman shift in an atomic vapor," Applied Optics **37,** 3295–3298 (1998).

[70] M. A. Clifford, G. P. T. Lancaster, R. S. Conroy, and K. Dholakia, "Stabilization of an 852 nm extended cavity diode laser using the Zeeman effect," Journal of Modern Optics **47,** 1933–1940 (2000).

Chapter 3

Experimental Diode Laser Systems and their Stabilization

G. P. T. Lancaster, R. S. Conroy, M. A. Clifford, J. Arlt and K. Dholakia, "A polarisation spectrometer locked diode laser for trapping cold atoms"
Optics Communications **170**, 79–84 (1999).

M. A. Clifford, G. P. T. Lancaster, R. S. Conroy and K. Dholakia, "Stabilization of an 852 nm extended cavity diode laser using the Zeeman effect"
Journal of Modern Optics **47**, 1933–1940 (2000).

3.1 Introduction

In this chapter, the experimental laser apparatus used in the trapping experiments during the course of this research project is discussed. The chapter is divided into two sections, the contents of which are summarised below.

(i) Laser systems - The design details and operation of our in-house built extended-cavity diode lasers (ECDLs) used for atom trapping are shown in Section 3.2.1 and their characteristics compared and contrasted to other re-

ported ECDL geometries. Throughout the guiding experiments, a Ti:Sapphire laser was used to generate the required guiding power and the operating principle of this laser will be described briefly in Section 3.2.2.

(ii) Frequency stabilization techniques - Any ECDL used for laser cooling and trapping must be frequency stabilized to provide reproducible trapping and in this Chapter three locking schemes namely, polarisation spectroscopy, DAVLL and dual current/PZT will be evaluated. Each of these techniques will be described in turn and comparisons drawn on their respective strengths and weaknesses.

3.2 Laser Systems

3.2.1 Extended Cavity Diode Lasers

Laser cooling and trapping of rubidium (Rb) requires two tuneable, narrow linewidth lasers at 780 nm pumping both the required hyperfine cooling and repumping transitions. The experimental setup consisted of two commercially available diode lasers placed in the Littrow geometry giving the required narrow linewidths and tunability around the wavelengths of interest. Background theory and discussion on the Littrow geometry may be found in Chapter 2.

The laser system design was simple and straightforward, see Figure 3.1. A Hitachi 7851G single longitudinal mode diode laser operating at a nominal wavelength of 780 nm and 50 mW output power was used. The diode was mounted in a commercially available collimating tube (Thorlabs LT110P-B) and collimated over a distance of 2 to 3 metres. The collimating tube was then placed in a custom machined holder which in turn was affixed to a clear quadrant design mirror mount (Newport P100-AC). The mirror mount was then affixed to an aluminium baseplate and this assembly placed onto to a large cylindrical base (90 mm diameter, 40 mm high) via a peltier element. This was used to temperature stabilize the

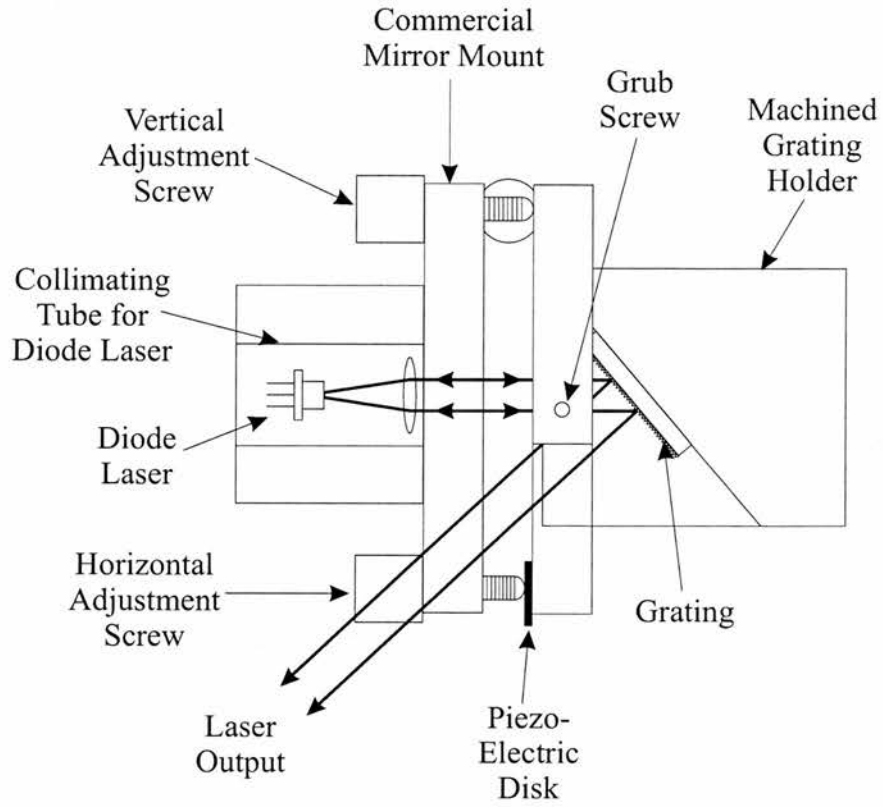

Figure 3.1: Schematic diagram of the extended cavity diode laser mounted in the Littrow geometry.

laser diode to between 5 and 10 mK. To provide optical feedback, a second custom machined holder was made to retain the diffraction grating and this second holder was placed onto the opposing side of the mirror mount. The gratings, either 1200 lines/mm or 1800 lines/mm (Optometrics UK), were retained by a small grub screw to facilitate replacement. The gratings fed back approximately 20% into the first diffracted order which was directed back to the diode forcing it to lase on the new cavity generated between the back facet of the diode and the grating. Details of gratings and the feedback mechanism are discussed in Chapter 2. This generated approximately 40 mW output from the ECDL. Coarse tuning was achieved by rotating the horizontal mirror mount screw giving typically 4 nm discontinuous tuning. Fine tuning was achieved by placing a piezoelectric transducer (PZT) beneath this screw. By applying a voltage to the PZT, continuous, modehop-free tuning of 8 GHz was measured [1]. A digital

photograph of the laser used throughout this study is shown in Figure 3.2.

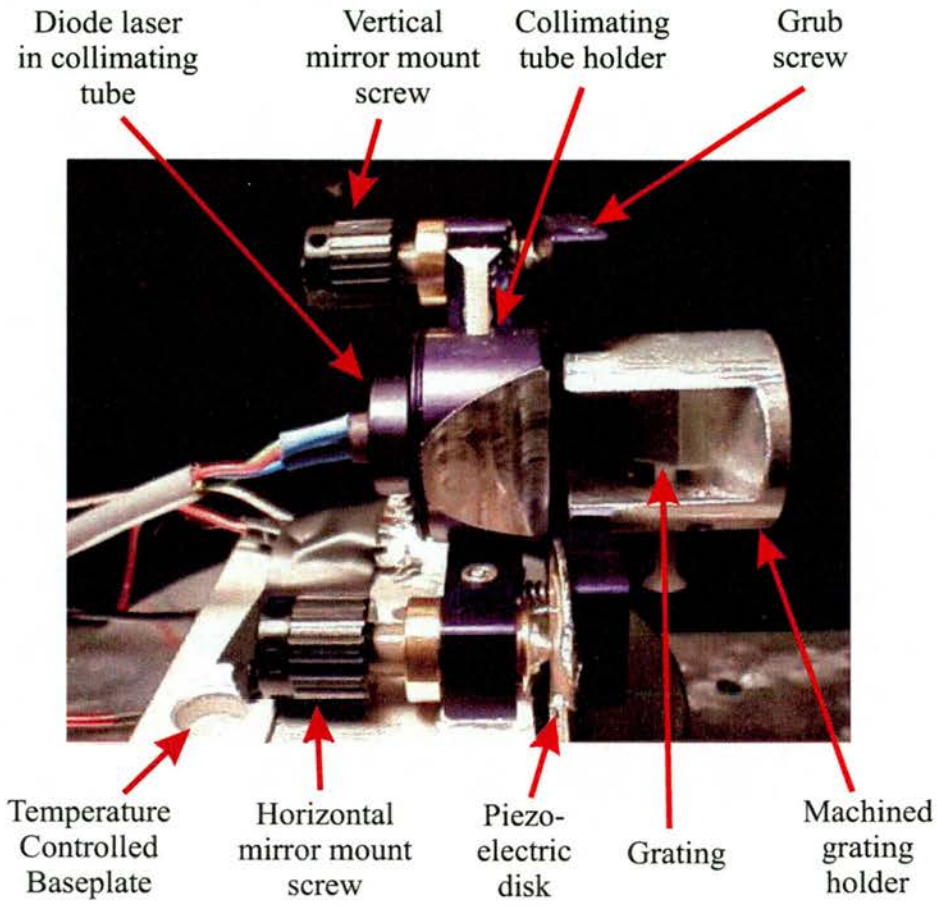

Figure 3.2: A photograph, taken from the side, of an extended-cavity diode laser used in trapping experiments.

Using a 300 MHz optical spectrum analyser (finesse > 300) the laser was found to run stably in a single longitudinal mode and an upper limit of 2 MHz was placed on the linewidth from the output of this device. By performing a heterodyne measurement using two similar lasers, a fast photodiode and a radio frequency spectrum analyser (Hewlett-Packard HP8566B), the linewidth of each external cavity diode laser could be measured in a 100 ms sampling time, Figure 3.3. The convoluted Lorentzian linewidth profile of both lasers was measured to be 135 kHz. This is sufficiently narrower than the natural linewidth of the hyperfine cooling transition in rubidium (6.1 MHz) and thus these lasers are suitable for cooling and trapping experiments. Two similar lasers were constructed and placed

in the configuration as described above and used subsequently in the trapping experiments discussed in Chapters 8 and 9.

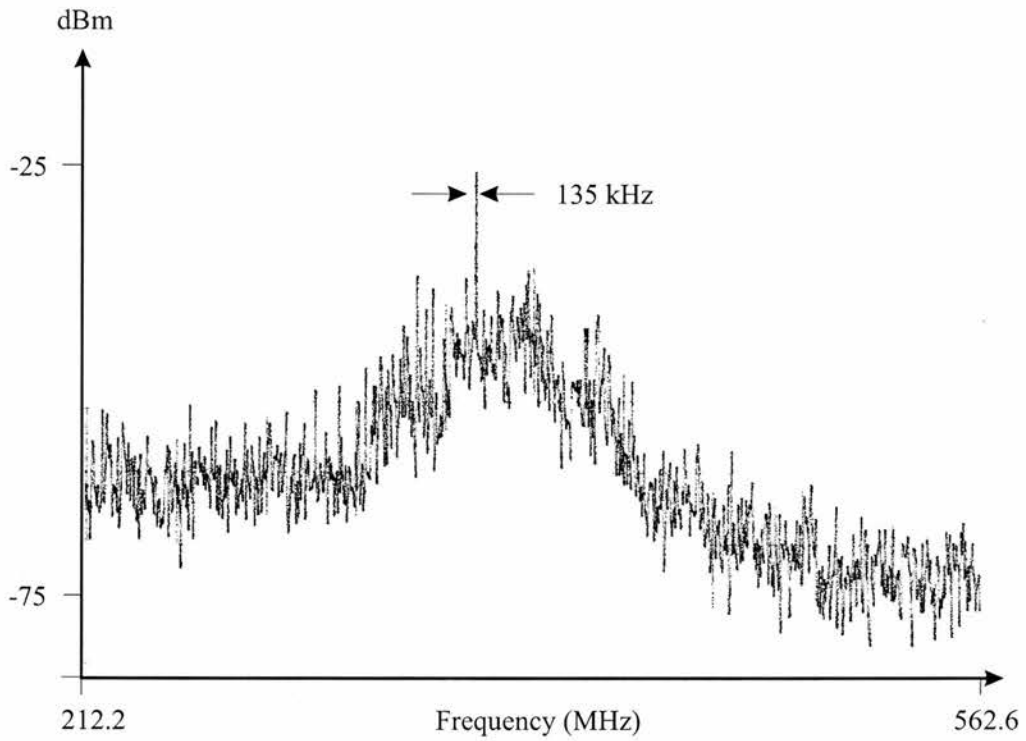

Figure 3.3: A heterodyne experiment between two of the external cavity diode lasers. A linewidth of 135 kHz was inferred from the width of the peak.

It is instructive at this point to describe the easiest way I have found by experience of how one aligns perfectly the first diffracted order back into the laser to force extended cavity operation. The laser and associated optics were setup as described above but which also incorporated a saturated absorption setup with a rubidium cell. The zeroth order output from the laser was directed through the Rb cell. The drive current was set so that the laser operated well above threshold (for the Hitachi diodes mentioned, this was typically ~80 mA). The grub screw retaining the machined grating holder onto the mirror mount was loosened and moved in small increments by hand while observing the zeroth order output with an infrared (IR) card. Careful alignment yielded a grating position which provided the zeroth order output spot and also a secondary, much fainter spot. This secondary spot is the result of the first order reflecting off the front facet

of the diode and back out onto the grating again. When these two spots were seen, the grub screw holding the machined grating holder was tightened. Both of these spots should be aligned on top of one another perfectly for feedback. The secondary spot could be moved by rotating the horizontal and vertical screws of the mirror mount. The spots were aligned to the best of one's ability by eye at this stage. A diode laser placed in an extended-cavity experiences a reduction in its lasing threshold current due to the increased optical feedback. By exploiting this fact, a simple method of obtaining extended-cavity operation can be followed which involves setting the drive current to just below threshold for the diode and visually observing the onset of lasing by altering the grating angle.

Experimentally, the drive current was then reduced to **just** below threshold (again, for the laser detailed above this was ~40 mA but varied depending on the actual diode). By observing the output on an IR card the sharp reduction in intensity when the current is set to such a value was found quite easily. While still observing the IR card, the mirror mount was carefully manipulated in the horizontal and vertical directions until the characteristic increase in intensity associated with the onset of lasing was found. The easiest way of doing this was to unscrew the horizontal screw past the position of maximum overlap between the spots, ensuring that the spots were well aligned vertically. Then using a thumb, rotate the mirror mount over the estimated optimal position while incrementally changing the vertical screw. Since the laser had been aligned by eye, it usually was not too long before the obvious jump in intensity was seen, indicating that the laser was operating on the extended-cavity. If some time was spent searching for the extended-cavity (for example, upwards of 10 minutes) then it was more beneficial to return to checking both spots were still lying close to one another and repeating the above procedure.

The procedure to tune the laser to the correct frequency required for trapping was slightly simpler but more time consuming. The diode drive current was increased to well above threshold (typically ~80 mA)while the output beam was directed through the Rb cell. A triangular wave form from a wave function generator

was placed on the PZT causing it to scan the laser frequency slightly. The peak to peak voltage depended on the specific PZT used with this setup requiring only 10 V peak to peak. The horizontal screw on the mirror mount was rotated slightly while watching the Rb cell through an IR viewer. When the laser was at the correct frequency, a line of fluorescence was seen in the vapour cell. An iterative method of changing the diode drive current slightly and then rotating the horizontal mirror mount screw was employed to find the correct operating parameters for the particular laser which gave the required wavelength.

A small fraction of the output of the beam (~2.5%) was split using a pellicle beam splitter and directed towards either a saturated absorption setup, a polarisation spectroscopy setup or a dichroic-atomic vapour laser lock (DAVLL) setup to provide frequency stabilization, all of these techniques shall be described in the second section of this chapter. The majority of the output was sent towards the trap.

3.2.2 Guiding Laser

Guiding experiments require a dipole force that can overcome the transverse motion of the majority of atoms so an appreciable flux can be guided. The transverse velocities of atoms in a *low velocity intense source* of atoms (LVIS), typically 3-5 ms^{-1}, are such that a guide beam of a few 100 mW can provide a sufficiently large potential barrier for atomic confinement. In this experiment a titanium doped sapphire (Ti:Sapphire or Ti:Al_2O_3) laser (Spectra-Physics, Model 3900S) is pumped using a diode pumped neodymium yttrium vanadate (Nd:YVO_4) laser (Spectra-Physics, Millennia Vs). A 1 W tuneable output around 780 nm in a TEM_{00} mode was obtained from the Ti:Sapphire. A brief description of each laser is outlined below.

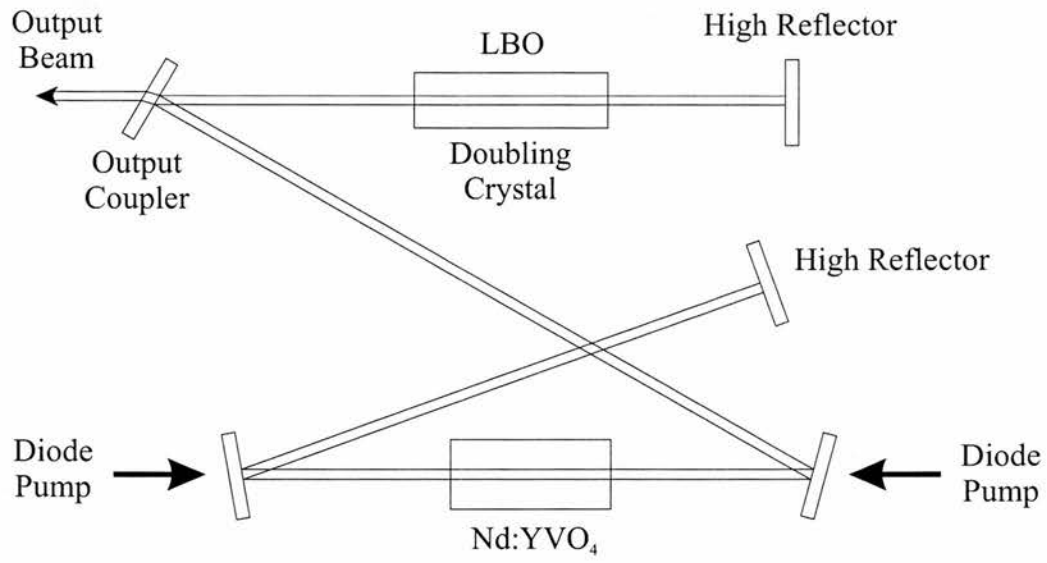

Figure 3.4: Schematic diagram showing the operation of the Millennia laser head.

Millennia Vs

A schematic diagram of this laser is shown in Figure 3.4. The Nd:YVO_4 crystal was pumped from either end by two fibre coupled diode laser bars, each capable of producing 20 W at approximately 815 nm. The bars were run below their maximum power output to extend lifetime [2] and after fibre coupling, 13 W was available from each laser bar to pump the crystal.

The 815 nm light excites the Nd^{3+} ions into pump bands where they quickly deplete to the relatively long lived ($\sim 60\mu s$) $^4F_{(3/2)}$ state. From there they can undergo stimulated emission to the $^4I_{(11/2)}$ level, emitting a photon at 1064 nm in the process. Since ions in this state quickly de-excite to the ground state, it is easy to obtain population inversion and hence low laser threshold. The resulting 1064 nm output was converted to the visible through frequency doubling (or second harmonic generation) in a nonlinear crystal of lithium triborate (LBO). This was placed intra-cavity where the high oscillating field increased conversion efficiency to the visible spectrum. The 532 nm light was extracted through a dichroic output coupler. A small fraction of this was split off and detected using

a photodiode. The voltage from this was then used as a feedback mechanism to alter the pump diode currents allowing the laser to operate in a constant power mode. Up to 5 W of stabilized power at 532 nm could be extracted from this Millennia laser to be used in the pumping of the Ti:Sapphire laser.

Titanium Sapphire

The output from the Millennia was used to pump a Spectra-Physics Model 3900S titanium sapphire laser (Ti:Al_2O_3). A schematic diagram of the Ti:sapphire is shown in Figure 3.5. The Ti^{3+} ion is responsible for the laser action. These ions replace a number of Al^{3+} ions in the sapphire crystal with the result that the electronic ground state of the titanium ion is split into two vibrationally broadened levels. Optical absorption occurs from 400 to 600 nm and emission from 650 to 1000 nm.

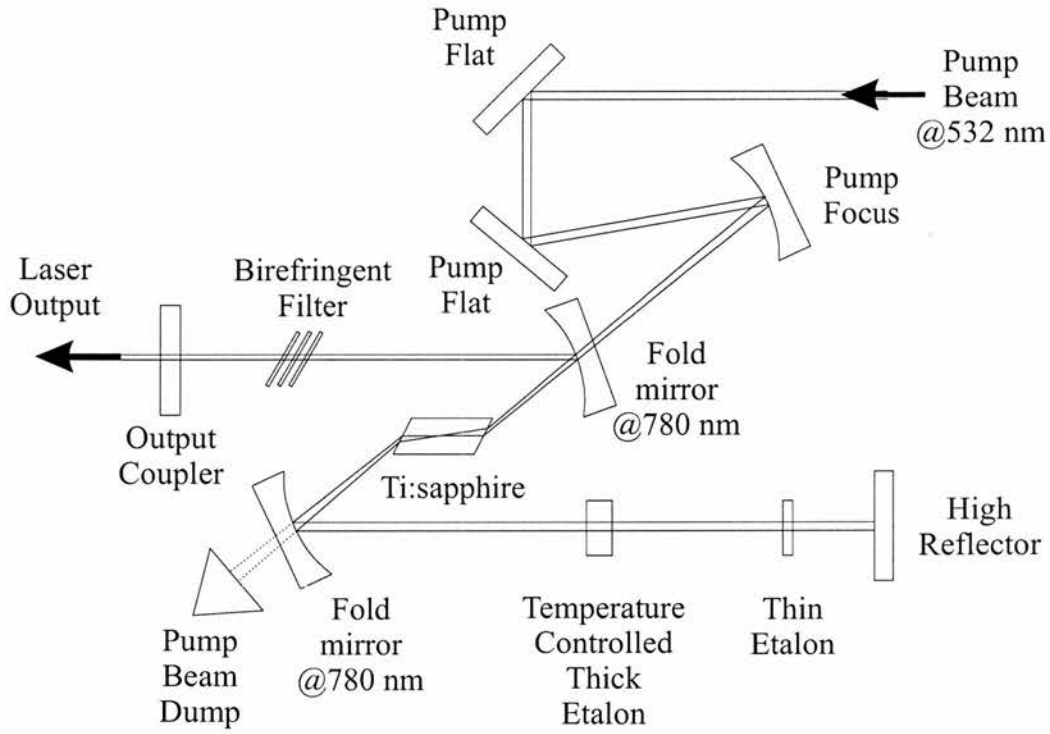

Figure 3.5: Schematic diagram showing the operation of the Ti:sapphire laser.

The pump beam was focused into one end of the Brewster angled titanium sap-

phire crystal. Similarly, the down converted oscillating field was focused to match the size of the pump inside the crystal. Any unabsorbed pump light was dumped after a single pass through the Ti:sapphire. As can be seen in the schematic, there are several intra-cavity elements that select the frequency at which the laser oscillates. The function of each of these elements will now be discussed briefly.

Firstly, the birefringent filter was the coarsest of the frequency selective elements in this cavity. It consisted of three crystalline quartz retardation plates orientated at Brewter's angle. On passing through these plates, the linear polarisation of the light field was changed into elliptically polarised light. There is only one frequency however that will have its polarisation unchanged on a single pass and see negligible loss when it next encounters the birefringent filter. The bandwidth of the birefringent filter was 100 GHz. Secondly, two intra-cavity etalons further refined the output frequency. The first was a thin etalon 0.5 mm thick with a free spectral range (FSR) of 200 GHz and a linewidth of 15 GHz. Tuning was achieved by tilting this etalon with tuning over 100 GHz possible [3]. The second etalon was 5 mm thick with a FSR of 20 GHz and a linewidth of 500 MHz. This allowed only two cavity modes separated by 200 MHz to lase. Tuning was accomplished by either angular adjustment of the etalon or by temperature control of the etalon housing. Figure 3.6 shows how the selectivity of the birefringent filter and etalons forces the laser onto only two of its cavity modes.

3.3 Frequency Stabilization Techniques

In this section, the experimental setup of the three frequency stabilization techniques mentioned previously in Chapter 2 will be described. All three methods have been evaluated and experimental results will be presented for polarisation spectroscopy in Section 3.3.1, DAVLL in Section 3.3.2 and dual current/PZT lock in Section 3.3.3.

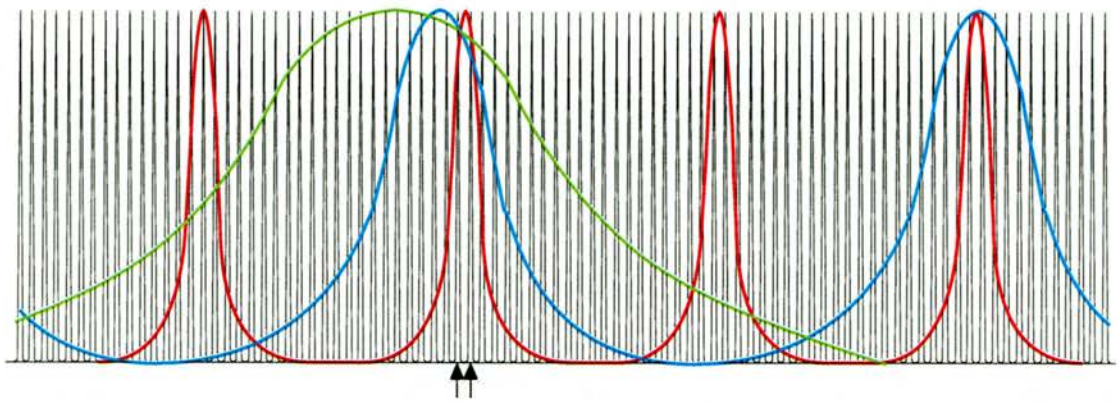

Figure 3.6: Diagram of frequency selectivity of the intra-cavity elements. The allowed cavity modes lie under the curves for the birefringent filter (green), the thin etalon (blue) and the thick etalon (red). The only 2 modes allowed with all three elements in place are indicated by the arrows.

3.3.1 Polarisation Spectroscopy Lock

Locking the ECDL to an atomic resonance is essential for stabilizing the laser frequency when trapping and cooling atoms. Widely used locking techniques employ feedback from Doppler-free signals to control the current and/or the PZT voltage to maintain the laser frequency at the desired value. Doppler-free signals can be generated using saturated absorption spectroscopy [4] and frequency modulation to generate a dispersive signal [5]. However, these techniques have disadvantages in terms of sensitivity for weak transitions and complexity respectively. Here, the use of polarisation spectroscopy is investigated as a simple, highly sensitive, alternative Doppler-free technique that generates an appropriate dispersive signal that has been used for stabilizing a laser.

Polarisation spectroscopy [6, 7] is a widely known technique in atomic spectroscopy. It is based on a light induced birefringence of an absorbing gas and is closely related to the widely used saturated absorption techniques. However, instead of monitoring the change in absorption of the probe beam due to a strong counter-propagating pump beam, the polarisation rotation of the probe is monitored. This technique is particularly attractive for providing a frequency refer-

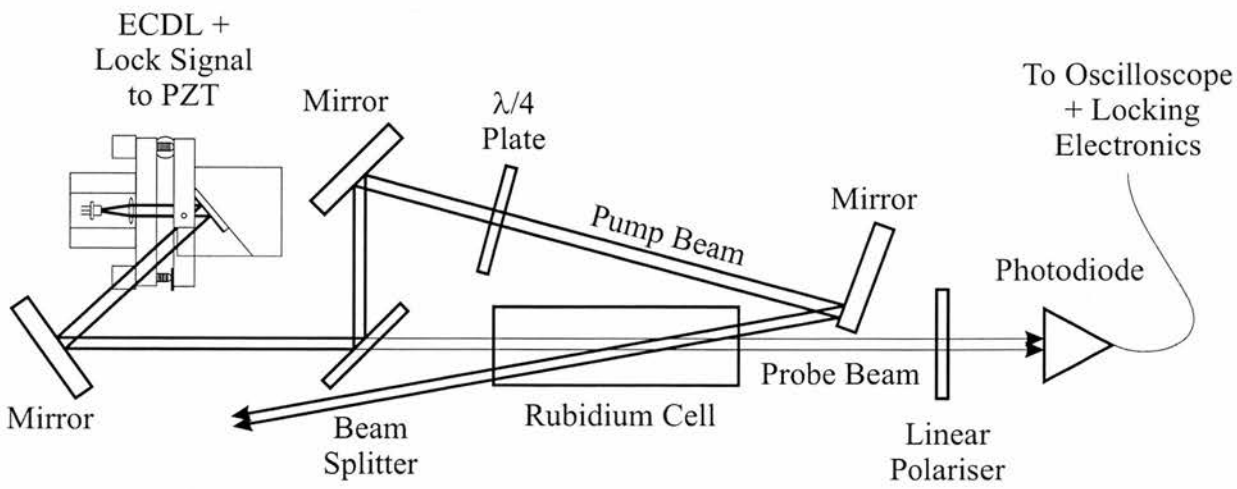

Figure 3.7: The polarisation spectrometer setup.

ence because it is typically 1-2 orders of magnitude more sensitive than saturated absorption and the dispersion profile of the polarisation allows stabilization without frequency modulation. Additionally, with a side-of-fringe locking technique the laser can be stabilized over a 100 MHz range around the cooling transition (F=3→F'=4 for ^{85}Rb). Optimum trapping occurs when the diode laser is red-detuned by 2 to 3 linewidths from line centre [8] and this is achieved easily by this system without the need for acousto-optic modulators.

Previous studies of polarisation spectroscopy have included its use for optical feedback to stabilize a free-running laser diode [9]. However, the systems used were more elaborate that the one discussed here. In comparison, this system stabilizes an ultra-compact extended cavity diode laser using a very simple polarisation spectrometer geometry.

Figure 3.7 shows the polarisation spectrometer used to generate a dispersive locking signal [10]. A linearly polarised probe beam passed through a 10 cm long rubidium cell. This beam then passed through a crossed polariser. Any induced anisotropy alters the transmission of light through this set of crossed polarisers resulting in an easily detectable signal. The anisotropy was introduced by means of a circularly polarised pump beam that counter-propagates through the rubidium

cell. The linearly polarised probe beam may be decomposed into two counter-rotating circularly polarised beams, one rotating with the polarising beam and one rotating in the opposite sense. The polarising beam introduced a difference in absorption and refractive index for each of these two beams because of the non-uniform pumping of the sublevels. On recombination after passing through the Rb cell, the plane of linear polarisation of the probe was rotated and may be detected as an increase in signal on the photodiode.

The intensity of the probe light at the photodiode of a polarisation spectrometer, ignoring cell window birefringence, can be modelled as Equation 3.1 [11]:

$$I_T = I_{BACK}\left[\varepsilon + \theta^2 + \frac{(\Delta\alpha L)^2 - 2\theta\left(\frac{\nu_0-\nu}{\gamma}\right)\Delta\alpha_0 L}{4\left(1+\left(\frac{\nu_0-\nu}{\gamma}\right)^2\right)}\right], \tag{3.1}$$

where $I_{BACK}(\varepsilon + \theta^2)$ is the constant background term caused by imperfect polarisers, with leakage ε, at a small misalignment θ, transmitting a fraction of the background saturated absorption. $\Delta\alpha_0 L$ is the change in absorption from saturated absorption at line centre, γ is the natural linewidth of the transition and $(\nu_0 - \nu)$ is the frequency detuning from line centre. No birefringence in the cell windows ($b = 0$) have been included because of cell window specifications in our experimental apparatus. With no constant background, the choice of angle θ between the crossed polarisers can lead to a dispersion shape (θ large) or Lorentzian shape ($\theta \sim 0$). The dispersion shape was desirable both in terms of allowing easy location of the correct hyperfine transition using the background absorption profile giving a zero crossing slope on which to lock and was achieved easily experimentally through slight misalignment of the polariser with respect to the polarisation of the laser.

The saturated absorption background can be expressed as Equation 3.2 [11]:

$$I_{BACK} = I_0 \left[exp\left(-\frac{M(\nu_0 - \nu)^2}{1.845 \times 10^{-13} \nu_0^2 T} \right) \right] \times \left[\sum_{F \to F' = 0 \pm 1} 1 - \frac{S_{F'}}{2} \left[1 + \frac{\left(\frac{\gamma_{F'}}{2}\right)^2}{(\nu - \nu_{F'})^2 + \left(\frac{\gamma_{F'}}{2}\right)^2} \right] \right] \quad (3.2)$$

where the first term represents the Doppler broadened profile of the transition at a given temperature, T, and the second term is the sum of the saturated lines for the allowed hyperfine transitions $F \to F'$ with a saturation parameter $S_{F'}$.

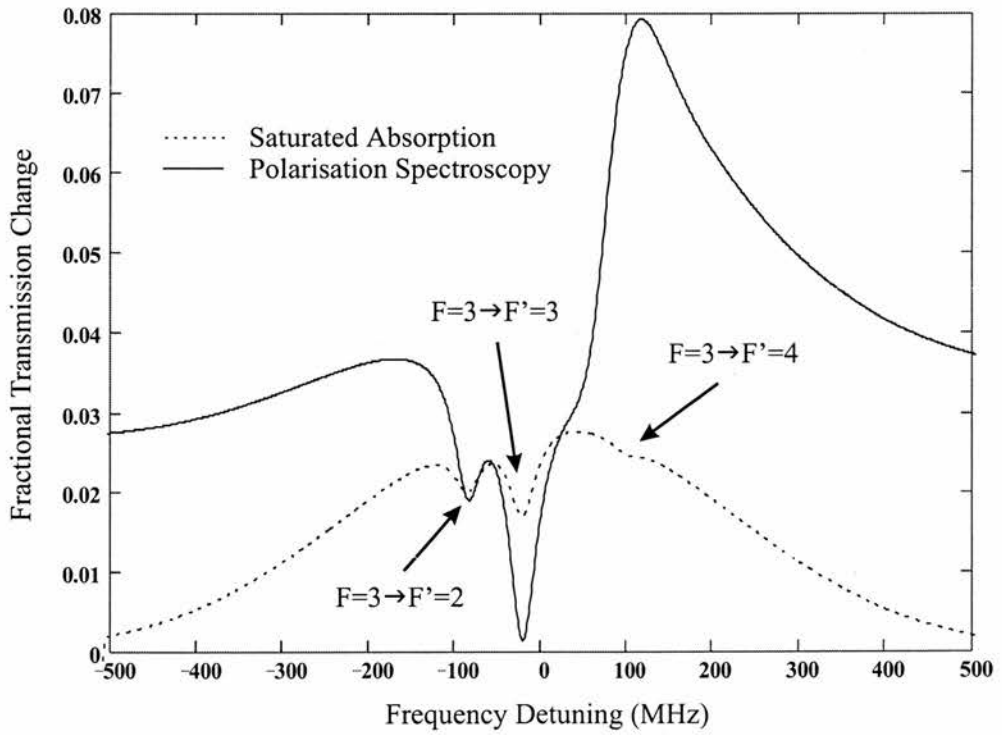

Figure 3.8: Expected locking signals from polarisation spectroscopy and saturated absorption spectroscopy of the ^{85}Rb $^5S_{1/2} \to {}^5P_{3/2}$ transition.

Figure 3.8 shows the difference in expected locking signal between saturated absorption and polarisation spectroscopy signals. The signal has been modelled with a 5^o angle between the polariser and the polarisation of the diode laser to show both the Lorentzian and dispersion line shapes. The polarisation signal was approximately seven times larger than the saturated absorption signal and had a broad range ($\sim$ 100 MHz) over which it could be locked and therefore used to access the optimum trapping frequency, some 10 to 15 MHz below the $^{85}Rb(F = 3 \rightarrow F' = 4)$ transition line centre.

Figure 3.9 shows the experimentally measured locking signals obtained from the setup for the $^{85}Rb\ ^5S_{1/2} \rightarrow\ ^5P_{3/2}$ transition in both saturated absorption mode and as a polarisation spectrometer. These results are in good agreement with the modelling from Figure 3.8 and illustrate the higher sensitivity offered by polarisation spectroscopy.

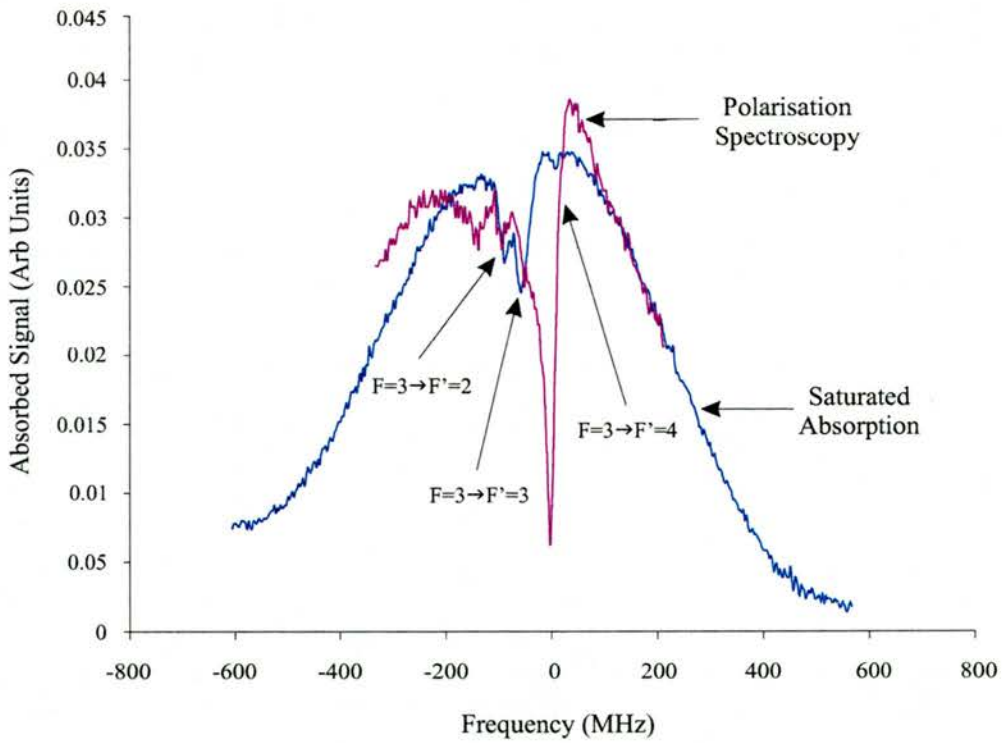

Figure 3.9: (Colour) Experimental measurement of the saturated absorption spectra and polarisation spectrometer signal from the experimental setup in Figure 3.8. The saturated absorption signal and the polarisation spectroscopy signal are shown in blue and red respectively.

This locking signal was fed into a simple and inexpensive electronic circuit, similar in design to that reported by MacAdam *et al.* [4]. This locking scheme was then used to stabilize the trapping laser in an atom trapping experiment and allowed for small changes, up to tens of MHz, in the position of the lock point using an electronic offset. It was noted however, that purely optical means cannot tune the laser while locked and electronic means must be employed. This was a limitation since optical offsets are more stable than those relying on electronics [12]. Atoms could be trapped continuously for over 2 minutes with the trapping time limited only by the background rubidium vapour pressure or the drift of the unlocked hyperfine pumping laser. The frequency drift of the laser while locked was measured to be less than 10 MHz. Locking the hyperfine laser was conducted using a similar scheme and this led to continuous trapping of up to 15 minutes being observed.

3.3.2 Dichroic-Atomic Vapour Laser Lock

One of the disadvantages of the polarisation spectrometer is that the locking range, although larger than simple saturated absorption, is still limited to approximately 100 MHz and any perturbing factor taking the laser beyond this range means the lock is lost. Also, fluctuations in beam alignment and intensity alter the lock point and lead to a drift in the laser frequency. An alternative frequency stabilization method known as Dichroic-atomic Vapour Laser Lock (DAVLL) [12] which utilizes the Zeeman effect and delivers a side-of-fringe locking signal with a locking range some eight times greater than polarisation spectroscopy has been investigated. The aforementioned drift mechanisms common to polarisation spectroscopy are overcome by the way the locking signal is generated. The tuning characteristics were studied using both optical offsets and by variation of the B-field yielding a new tuning technique while locked to the atomic transition of interest. This work has been carried out at a wavelength of 780 nm.

This technique uses a weak magnetic field to split the Zeeman components of an

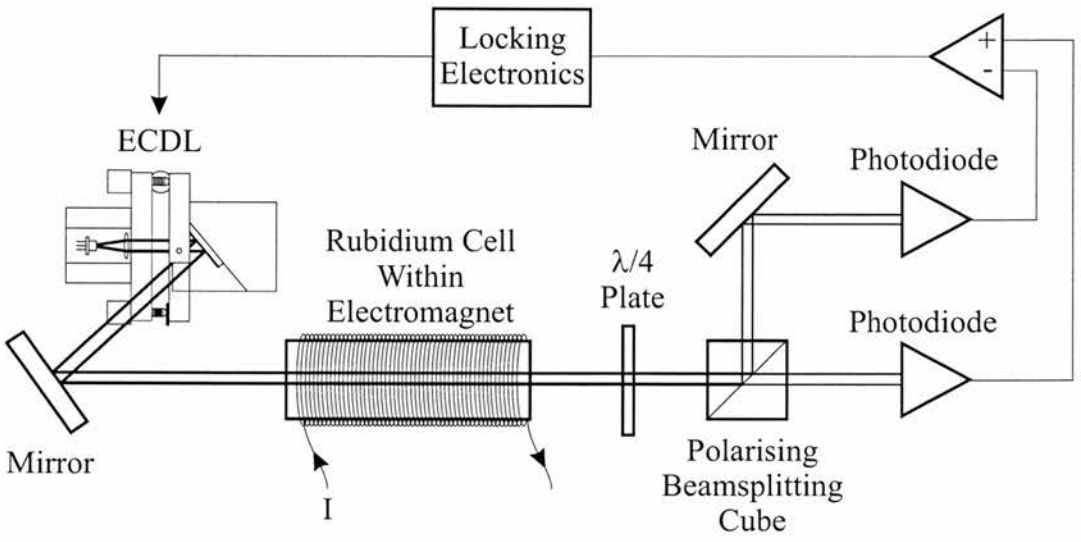

Figure 3.10: Schematic diagram of the experimental DAVLL setup.

atomic Doppler-broadened absorption signal and then generates an error signal dependent on the difference of these two signals. The technique was first demonstrated with a laser in helium [13] and then developed at 780 nm for rubidium [12]. A theoretical description of the method can be found in Chapter 2 where the origins of the locking signal are described. In the presence of a magnetic field, and when probed with circularly polarised light, the central absorption frequency of a Doppler-broadened lineshape is known to shift. For righthand circularly polarised light (σ^+) propagating in the z-direction and a B-field in the same direction, the central frequency of the absorption increases and for the opposite handedness of polarization (σ^-) this central frequency decreases. A dispersive error signal is required for locking. This was generated by subtracting the absorption profiles recorded for the two components of circularly polarized light, as was shown in Figure 2.16. The act of subtraction in this instance reduced any fluctuations in the locking signal from variations in lineshape or absorption. The experimental optical configuration utilized in this study is shown in Figure 3.10.

Pure linearly polarized light (which may be considered to consist of equal amounts of left and right handed components of circularly polarized light) was sent through a Rb vapour cell placed in a magnetic field. Two separate methods can be em-

ployed to generate the magnetic field:- (i) a standard electromagnet, which will be discussed here, and (ii) a series of magnetically impregnated rubber rings [12], the experimental details of which have been published previously [14]. The advantage of the electromagnet over the magnetically impregnated rubber rings is the flexibility it offers by allowing variation in the magnetic field, something which will be elaborated on later in this section. The electromagnet consisted of a thin wooden tube (14 cm long, 3 cm diameter) with wire wound round it generating a magnetic field of 35.8 GA^{-1} in the vapour cell. The variation in the magnetic field along the length of the vapour cell, when inserted within the electromagnet was less than 9%, see Figure 3.11. Immediately after passing through the vapour cell the light was incident on a quarter-wave plate orientated with both its fast and slow axes at 45^o to the plane of incidence of the incoming linearly polarized light. Following this, the light was separated into two components by a polarizing beam splitting cube and each orthogonal polarization component was incident on separate photodiodes. Subtraction of these photodiode signals led immediately to a dispersive signal that passes through zero. A typical dispersive DAVLL curve, which has been generated for rubidium, is shown in Figure 3.12. The capture range of the locking signal was large (~800 MHz) allowing the laser to recover from large perturbations in frequency.

Corwin *et al.* [12] stated that tuning of their lock frequency could be achieved by either using an electronic offset in their locking electronics or by rotating the quarter-wave plate. The latter optical method changed the frequency by weighting the relative intensities of the beams at each photodiode. This method generated a more appealing solution due to the insensitivity of the lock point to laser fluctuations however no details were given. To investigate these claims a theoretical and experimental investigation was begun on this aspect of the locking method as part of this research project and these findings are now presented.

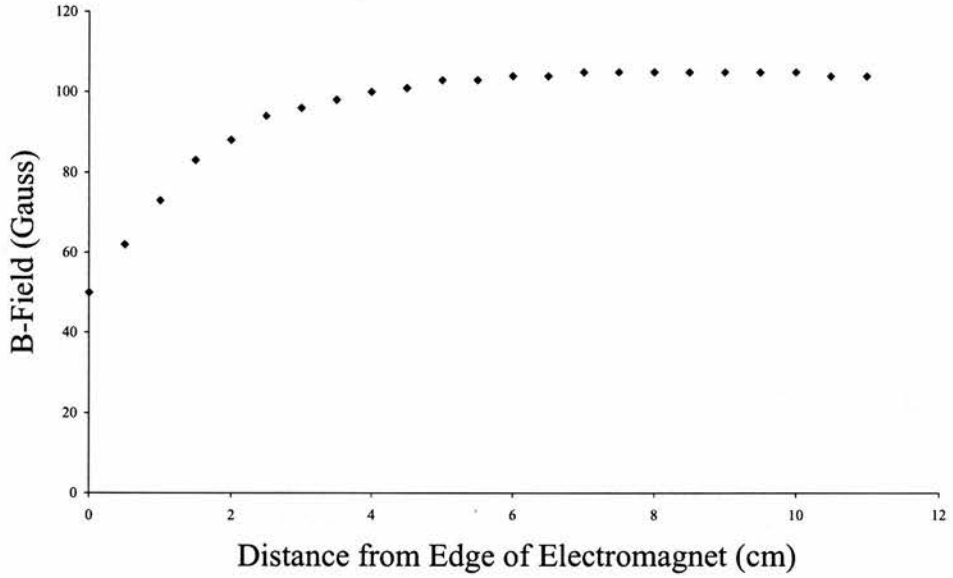

Figure 3.11: A graph showing the B-field variation along the centre of the electromagnet. A 9% variation was noted along the 10 cm length that the vapour cell occupies.

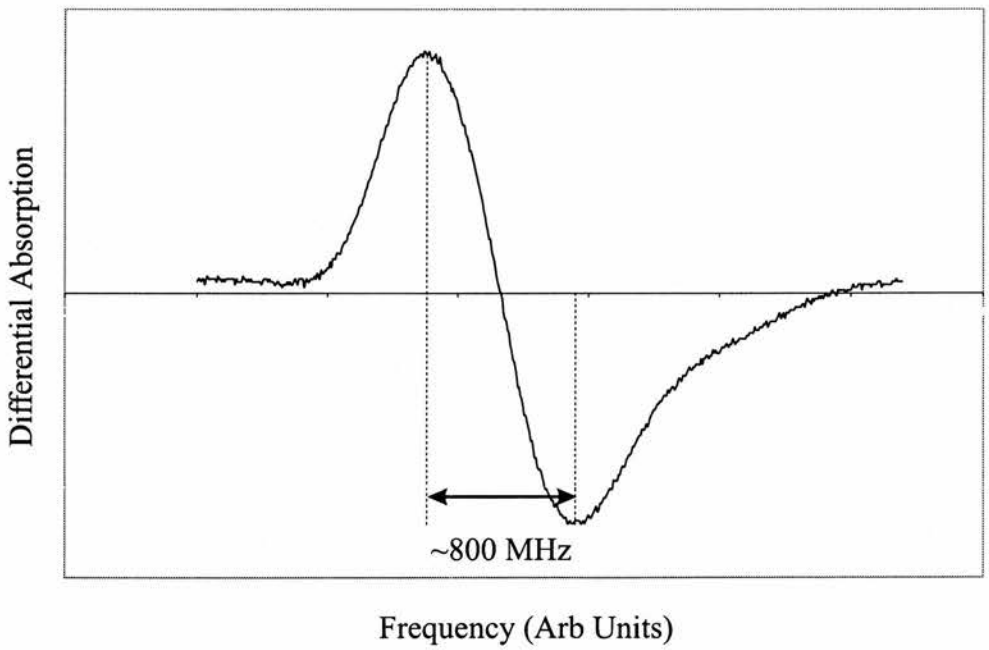

Figure 3.12: A typical DAVLL error signal. This example was observed in rubidium with a magnetic field of 162G.

Rotation of Quarter-Wave Plate – Theory

Let us assume that the quarter-wave plate has its fast axis horizontal, then the Jones Matrix for this optical element is:

$$\begin{pmatrix} 1 & 0 \\ 0 & i \end{pmatrix}$$

To rotate this element it is not sufficient to just use the rotation matrix:

$$\begin{pmatrix} cos\theta & sin\theta \\ -sin\theta & cos\theta \end{pmatrix}$$

For correct modelling of this problem, it must be imagined that the rotation matrix operates on the light and so rotating the waveplate is equivalent to rotating the light, having it pass through the quarter-wave plate and then rotating it the same angle back again. In this way the E-field vector after the waveplate is being measured in the same plane as it was before the plate. Therefore a rotation of a quarter-wave plate by angle θ is:

$$\underbrace{\begin{bmatrix} cos\theta & -sin\theta \\ sin\theta & cos\theta \end{bmatrix}}_{antirotation} \overbrace{\begin{bmatrix} 1 & 0 \\ 0 & i \end{bmatrix}}^{\lambda/4 Plate, Fast Axis Horizontal} \underbrace{\begin{bmatrix} cos\theta & sin\theta \\ -sin\theta & cos\theta \end{bmatrix}}_{Rotation}$$

$$= \begin{bmatrix} cos\theta & -sin\theta \\ sin\theta & cos\theta \end{bmatrix} \begin{bmatrix} cos\theta & sin\theta \\ -isin\theta & icos\theta \end{bmatrix}$$

$$= \underbrace{\begin{bmatrix} cos^2\theta + isin^2\theta & cos\theta sin\theta - icos\theta sin\theta \\ cos\theta sin\theta - icos\theta sin\theta & sin^2\theta + icos^2\theta \end{bmatrix}}_{\lambda/4 Plate Rotation Matrix}$$

Passing the light now through a polarising beam splitter produces a horizontal and a vertical component:

$$Horizontal = \begin{bmatrix} 1 & 0 \\ 0 & 0 \end{bmatrix} \begin{bmatrix} cos^2\theta + isin^2\theta & cos\theta sin\theta - icos\theta sin\theta \\ cos\theta sin\theta - icos\theta sin\theta & sin^2\theta + icos^2\theta \end{bmatrix}$$

$$= \begin{bmatrix} cos^2\theta + isin^2\theta & cos\theta sin\theta - icos\theta sin\theta \\ 0 & 0 \end{bmatrix}$$

$$Vertical = \begin{bmatrix} 0 & 0 \\ 0 & 1 \end{bmatrix} \begin{bmatrix} cos^2\theta + isin^2\theta & cos\theta sin\theta - icos\theta sin\theta \\ cos\theta sin\theta - icos\theta sin\theta & sin^2\theta + icos^2\theta \end{bmatrix}$$

$$= \begin{bmatrix} 0 & 0 \\ cos\theta sin\theta - icos\theta sin\theta & sin^2\theta + icos^2\theta \end{bmatrix}$$

If the input light incident on the quarter-wave plate is horizontally polarised then the horizontal and vertical components after passing through the polarising beam splitting cube become:

$$Horizontal = \begin{bmatrix} cos^2\theta + isin^2\theta & cos\theta sin\theta - icos\theta sin\theta \\ 0 & 0 \end{bmatrix} \begin{bmatrix} 1 \\ 0 \end{bmatrix}$$

$$= \begin{bmatrix} cos^2\theta + isin^2\theta \\ 0 \end{bmatrix}$$

$$Vertical = \begin{bmatrix} 0 & 0 \\ cos\theta sin\theta - icos\theta sin\theta & sin^2\theta + icos^2\theta \end{bmatrix} \begin{bmatrix} 1 \\ 0 \end{bmatrix}$$

$$= \begin{bmatrix} 0 \\ cos\theta sin\theta - icos\theta sin\theta \end{bmatrix}$$

Therefore, if we designate the horizontal direction to the x-axis and the vertical direction to the y-axis, we obtain Equations 3.3 and 3.4,

$$E_x = cos^2\theta + isin^2\theta \tag{3.3}$$

$$and \quad E_y = cos\theta sin\theta - icos\theta sin\theta \tag{3.4}$$

as the E-field components.

The intensity of each component is the square of the modulus of each E-field where the moduli for the x and y components are expressed as Equations 3.5 and 3.6:

$$| E_x | = \sqrt{(cos^2\theta)^2 + (sin^2\theta)^2} \tag{3.5}$$

$$and \quad | E_y | = \sqrt{(cos\theta sin\theta)^2 + (cos\theta sin\theta)^2} \tag{3.6}$$

Therefore giving Equations 3.7 and 3.8 as the intensity of light reaching each photodiode as a function of rotation angle of the quarter-wave plate for the both the x and y components respectively.

$$I_x = cos^4\theta + sin^4\theta \tag{3.7}$$

$$and \quad I_y = 2cos^2\theta sin^2\theta \tag{3.8}$$

Rotation of Quarter-Wave Plate – Experiment

Experimentally, a DAVLL signal was generated as described at the beginning of this section with the setup being illustrated in Figure 3.10. The waveplate was rotated incrementally and the intensity at each photodiode measured. Figure 3.13 shows the experimental values plotted as dots with the theoretical intensity values, modelled using the above matrices, as lines. The agreement between theory and experiment is excellent. The inclusion of this into the individual DAVLL

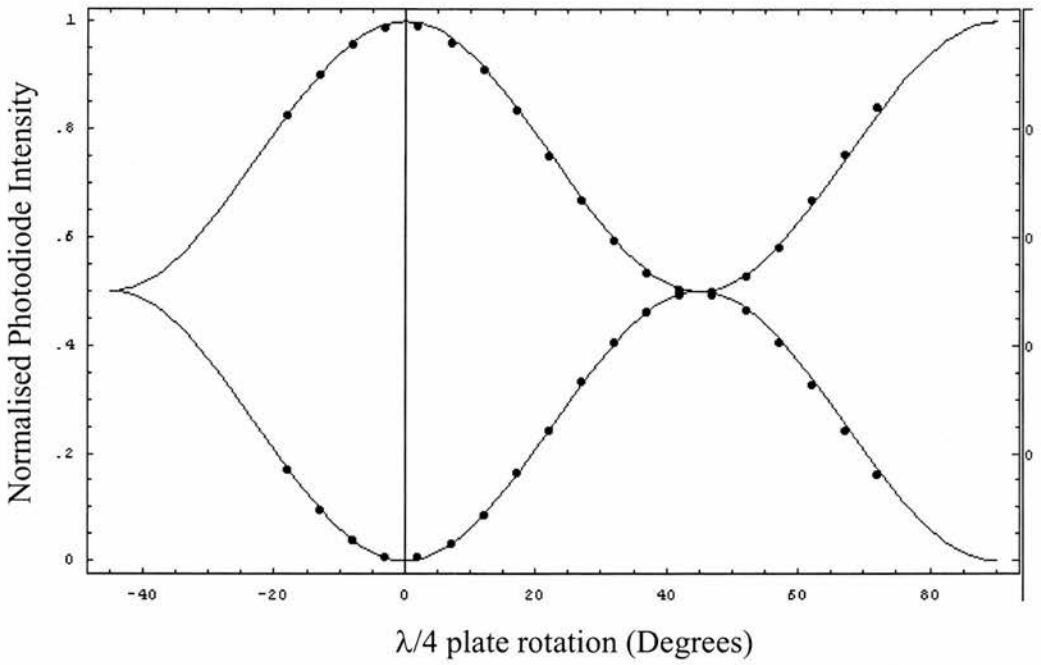

Figure 3.13: Graph of theory (line) and experiment (points) for the photodiode intensity variation measured as a function of rotation of the quarter-wave plate.

peak variations and subsequent lock point shift modelling was undertaken by my colleague, Mark Clifford. He also performed the experimentation to confirm this model.

Tuning of DAVLL Lock Point by B-Field Variation

The effect on the lock point of the DAVLL signal by the variation of the magnetic field was also investigated. The use of the electromagnet gave the flexibility to vary the magnetic field accurately and very easily. Typical data is shown in Figures 3.14 and 3.15 for various B-field values.

Several observations can be made from this experimental data. Firstly, the DAVLL signal gradient does not vary at fields between ~60 G and ~130 G. This means the slope of the error signal does not change with B-field. The data also shows the dependency of the cross-over point to magnetic field, something which has not been considered to date in literature. The causes of this effect were

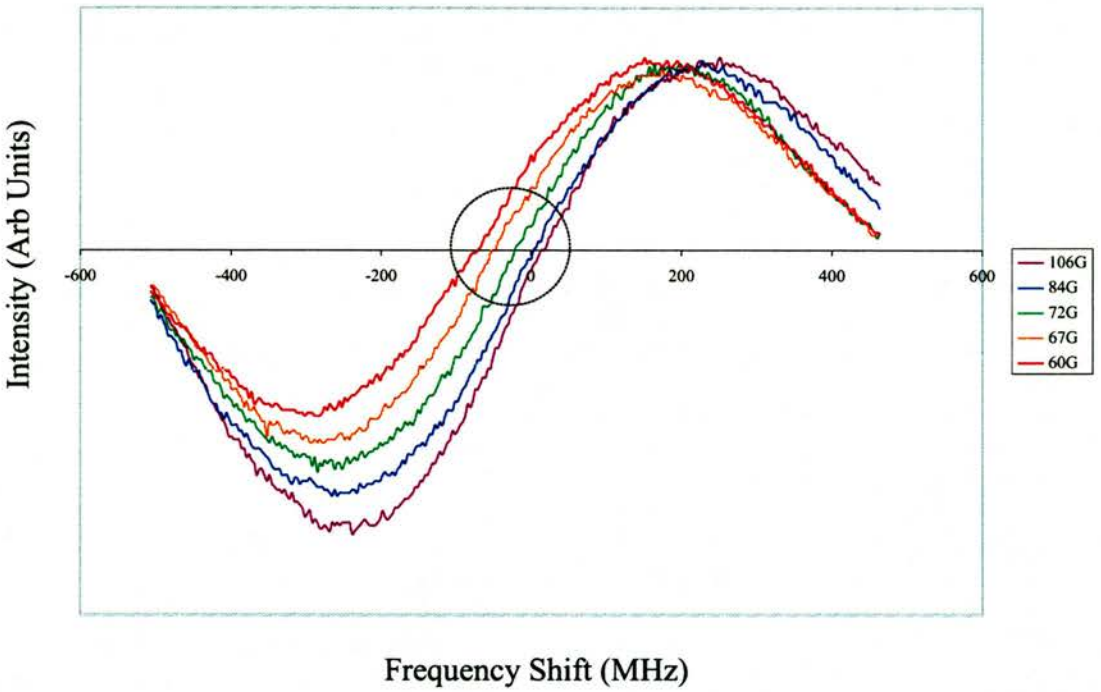

Figure 3.14: (Colour) The DAVLL locking signal measured for various magnetic fields. Note that the point of zero crossing alters.

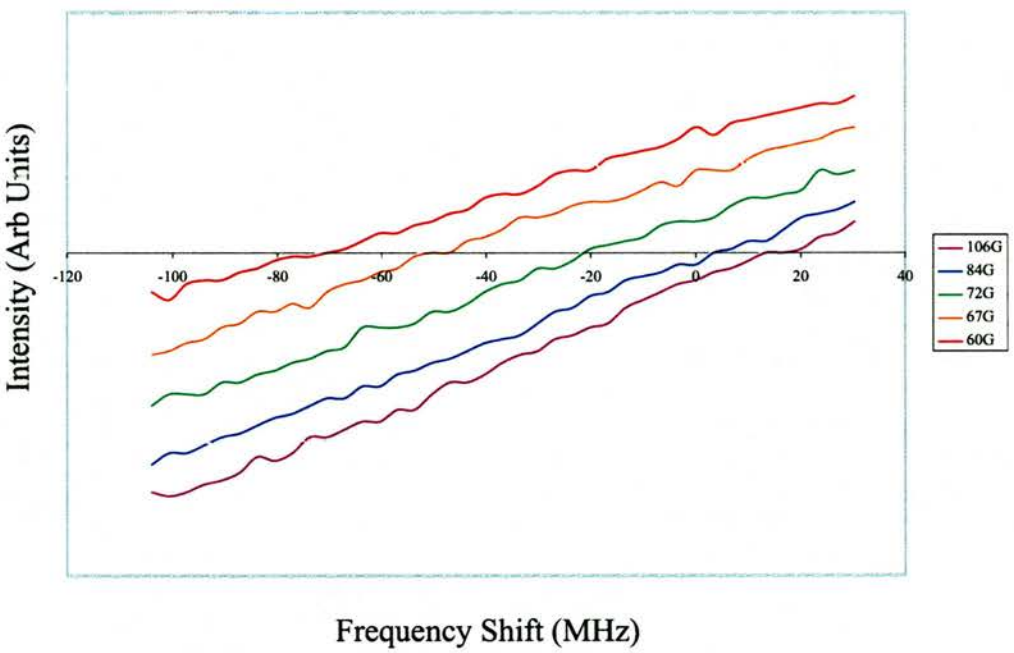

Figure 3.15: (Colour) An enlargement of the circled section in Figure 3.14.

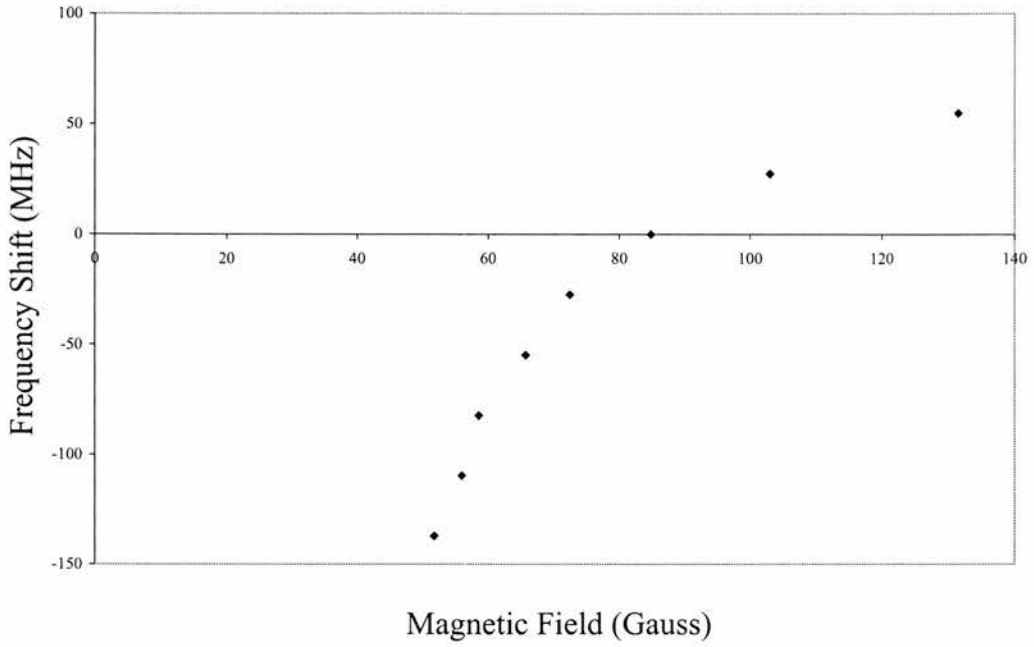

Figure 3.16: Tuning the frequency by adjusting the d.c. magnetic field applied to the vapour cell.

unknown but are most likely attributed to the non-symmetric circularly polarised lineshapes obtained from differing absorptions within the vapour cell [15]. This would cause an imbalance (that is B-field dependent) to appear between individual Doppler broadened peaks. Monitoring the frequency detuning of the lock point with B-field yields Figure 3.16. The use of an electromagnet in this way offers the possibility of varying the magnetic field and hence the lock point *in situ* in a controlled fashion. The data in Figure 3.16 show clearly that adjusting only the magnetic field gives a powerful and novel non-mechanical method for tuning a stabilized laser.

3.3.3 Dual Current/PZT Lock

Both systems mentioned in the previous sections improve the stability of the laser frequency but are limited in bandwidth due to the feedback loop relying on a mechanical system, i.e. the PZT. In this, the final area of frequency stabilization

that will be investigated, a dual feedback of PZT and drive current to the laser was employed to increase this bandwidth envelope to 100 kHz. Additional theory, limitations and background on feedback loops can be found in Chapter 2.

Here, a saturated absorption setup was used with the signal obtained being fed to a more complicated series of electronics than has been used previously. A simplified schematic diagram of the complete electronic circuit is shown in Figure 3.17. A triangular wave form was fed to the "Ramp In" socket to allow the modulation of the PZT in order to obtain the atomic transition of interest. A small sinusoidal dither was applied to the diode current (up to 100 kHz) from the oscillator board. This ramps the laser frequency back and forth over the peak of the hyperfine feature of interest. The saturated absorption signal obtained from the photodiode[1] was fed into a amplifier tuned to the dither frequency and then onto a phase sensitive detector. The dispersive signal subsequently generated can then be viewed via the "signal monitor" output. This signal was integrated over a short time base to provide a high frequency error signal which was fed to the current driver. A d.c. error term was created by integrating this fast error signal over a larger time scale. This second error signal was used to correct the PZT voltage in order to minimise the d.c. component of the diode driver error signal. In this way, the current could correct for any high frequency noise that occurred and the PZT corrected for lower frequency drifts due to air currents through the extended cavity or changes in temperature of the apparatus. The bandwidth of this scheme was limited only by the speed of the feedback loop i.e. the electronics or the electron/hole mobility in the diode laser. This technique resulted in the ability to continuously lock for several hours offering a very robust solution which is being used currently in all ongoing trapping experiments. A more detailed description of the electronics along with circuit diagrams are given in Appendix A.

This method is a peak-locking scheme and for laser cooling and trapping a tech-

[1]Note it is important that the photodiode and any associated electronics have a large enough bandwidth to detect and pass the signal at the dither frequency. This was an important consideration when 100 kHz dither was employed.

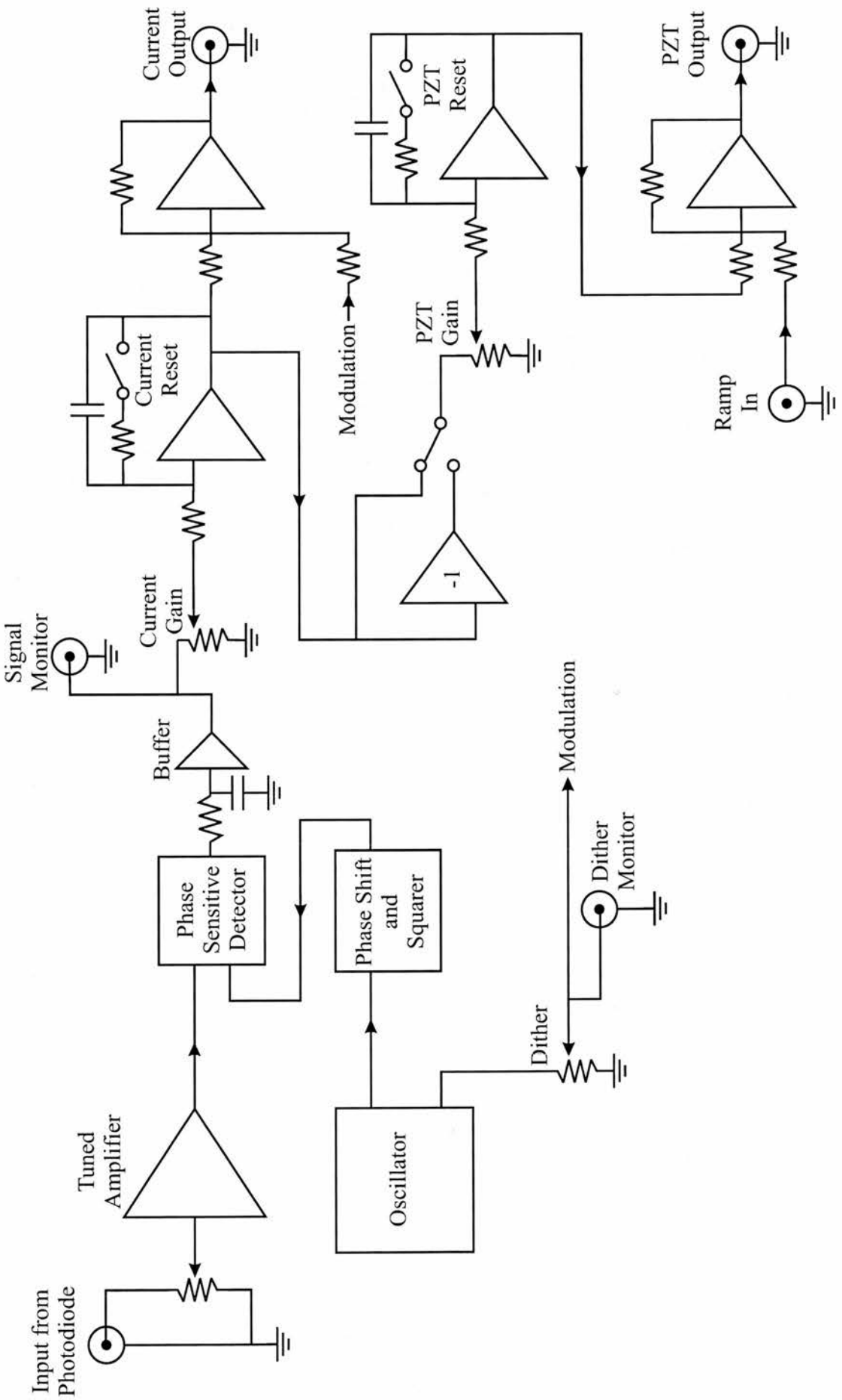

Figure 3.17: A simplified circuit diagram of the dual current/PZT locking electronics.

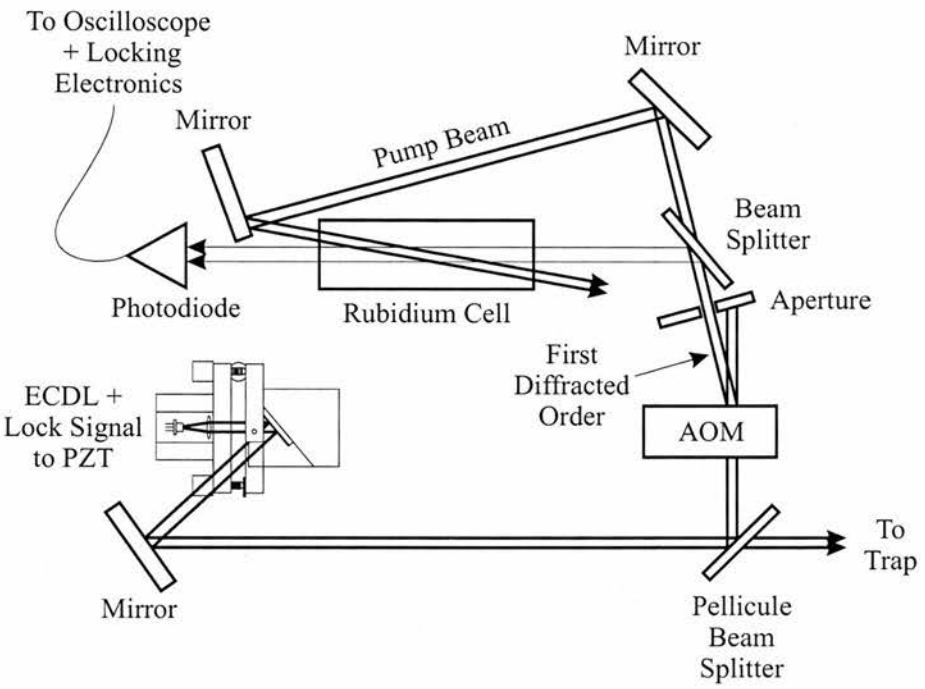

Figure 3.18: Schematic diagram of the acousto-optic modulator setup.

nique must be used to frequency offset the laser to the red side of the cooling transition. In this work, this was achieved using an acousto-optic modulator (AOM). The experimental inclusion of this to the laser apparatus is shown in Figure 3.18.

The AOM was originally placed in the trapping beam but this resulted in problems when tuning as with a frequency shift is an associated spatial shift of the beam. This has severe consequences in an atom trap where beam alignment can be critical. The setup in Figure 3.18 alleviates this problem by having the AOM in the saturated absorption arm.

The output from the ECDL was split by way of a pellicle beam splitter. The split light was directed through the AOM where the first diffracted order was passed into a saturated absorption setup. Our AOM (Model LM080, Isle Optics, UK) had a 80 MHz shift in frequency with 23 MHz tunability either side giving a possible offset from 57 to 103 MHz. This frequency was controlled by inputting a voltage ranging from 4.5 V (for 57 MHz) to 17.5 V (for 103 MHz) to the

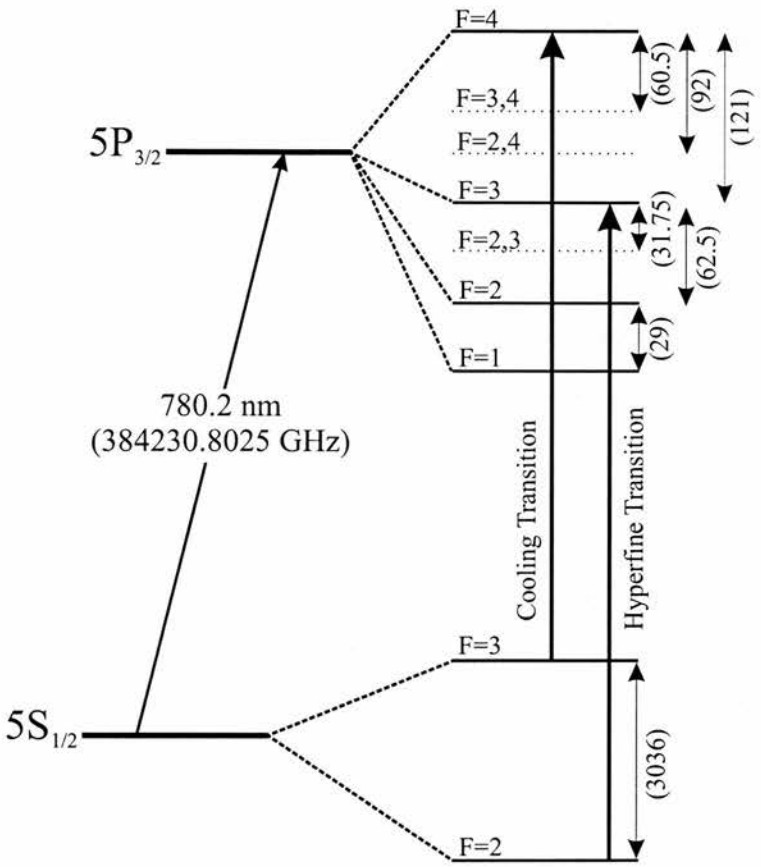

Figure 3.19: The energy diagram for ^{85}Rb. All values in brackets are frequencies in MHz.

appropriate socket on the AOM casing. Observing the energy diagram for ^{85}Rb, Figure 3.19, it can seen that there is only one transition which falls within this range, remembering that for trapping one needs to be approximately 12 MHz red-detuned of the cooling transition line centre. This transition is the $5S_{1/2}F = 3 \rightarrow 5P_{3/2}F' = (2,4)$ where the $F' = (2,4)$ refers to the cross-over transition between the $F' = 2$ and the $F' = 4$ transitions seen in saturated spectroscopy. In this manner, by locking the laser to the $5S_{1/2}F = 3 \rightarrow 5P_{3/2}F' = (2,4)$ transition with an 80 MHz shift due to the AOM, we obtain the laser frequency entering the trap at the correct 12 MHz red-detuned of the cooling transition. By changing the voltage offset we can tune the trapping frequency easily around this offset.

3.3.4 Comparison of Frequency Stabilization Techniques

Polarisation spectroscopy offered an improved locking scheme in comparison to a saturated absorption spectrometer with very little added complexity. Tuning while locked, meanwhile, was achieved by way of an electronic offset. This technique was a simple and inexpensive way of frequency stabilizing an ECDL to an atomic dispersive signal. Over short time periods the lock proved satisfactory but if an involved experiment required stabilization for longer then noise would inevitably cause the laser to "jump" out of lock.

This shortcoming of polarisation spectroscopy was relieved by DAVLL by providing a locking signal which had a larger capture range (typically 800 MHz in comparison to 100 MHz for polarisation spectroscopy), was insensitive to laser alignment and power fluctuations and provided a means by which a locked laser could be tuned non-electronically. These characteristics gave a more rugged lock with increased flexibility in having the ability to tuned the laser frequency by changing the current supplying the magnetic field generating solenoid.

However, both of these techniques were limited by the frequency response of the mechanical element providing corrective feedback, namely the PZT. Dual current/PZT gave the best lock of the three techniques by far. The bandwidth of the feedback was increased in relation to the two previous locking techniques and the laser lock was proven to be extremely robust. Noise in the form of speaking loudly, banging doors and hitting the optical table was unable to make the laser jump out of lock. However, sometimes the act of switching on other electronics in the vicinity, be it a power supply or a light, was enough to ruin locking. It is therefore advisable for electronic isolation measures to be introduced to stop this occurring. The electronics were significantly more complicated than those used in both polarisation spectroscopy locking and DAVLL. A further disadvantage was that further complications in the setup were needed as this technique locked to the peak of an atomic transition. Therefore, a method of offsetting the laser frequency for use in laser cooling experiments was necessary. The increase in

expense and time as a result of this complexity may be deemed unconscionable. However, these reservations about implementing the system are, I believe, greatly overshadowed by the improvement in the strength of lock. This point is supported by the experimental observation of continuous locking of an ECDL over a 24 hour period. Dual current/PZT lock is currently the locking technique of choice employed in all ongoing experiments in this field of research at the University of St Andrews.

3.4 Conclusions

Several ECDLs have been produced for laser cooling and trapping purposes. These have proven simple, robust and reliable tools tailored to the needs of any cooling and trapping experiments. Commercial diode lasers at 780 nm, 50 mW output power have been integrated into a Littrow geometry extended-cavity. These yielded approximately 40 mW single longitudinal mode output which was tuneable continuously over 8 GHz and discontinuously over 4 nm. Through a heterodyne experiment the linewidth of the laser in a 100 ms sampling time was measured to be 135 kHz.

Frequency stabilization of these lasers has been demonstrated by three different locking methods. Polarisation spectroscopy lock, dichroic-atomic vapour laser lock and dual current/PZT lock have all been implemented in the experimental setup and have been used to trap and laser cool rubidium atoms in a simple MOT. In the case of polarisation spectroscopy, the expected line shapes have been modelled and were shown to be in good agreement with the experimental results. Further, a means of altering the lock point whilst using the DAVLL system was investigated non-mechanically by changing the B-field. These system's relative strengths and weaknesses have been addressed with dual current/PZT found to be the most favourable.

Bibliography

[1] M. A. Clifford, J. Arlt, J. Courtial, and K. Dholakia, "High-order Laguerre-Gaussian laser modes for the studies of cold atoms," Optics Communications **156,** 300–306 (1998).

[2] "Millennia Vs Diode-Pumped, CW Visible Laser User's Manual," Spectra-Physics .

[3] "Model 3900S, CW Ti : Sapphire Laser User's Manual," Spectra-Physics .

[4] K. B. MacAdam, A. Steinbach, and C. Wieman, "A narrow-band tunable diode laser system with grating feedback, and a saturated absorption spectrometer for Cs and Rb," American Journal of Physics **60,** 1098–1111 (1992).

[5] G. D. Rovera, G. Santarelli, and A. Clairon, "A laser diode system stabilized on the Caesium D_2 line," Review of Scientific Instruments **65,** 1502–1505 (1994).

[6] J. Maki, N. Campbell, C. Grande, R. Knorpp, and D. H. McIntyre, "Stabilized diode-laser system with grating feedback and frequency-offset locking," Optics Communications **102,** 251 256 (1993).

[7] C. Wieman and T. W. Hänsch, "Doppler-Free Laser Polarization Spectroscopy," Physical Review Letters **36,** 1170–1173 (1976).

[8] K. Lindquist, M. Stephens, and C. Wieman, "Experimental and theoretical study of the vapor-cell Zeeman optical trap," Physical Review A **46,** 4082–4090 (1992).

[9] M. Kozuma, M. Kourogi, and M. Ohtsu, "Frequency stabilization, linewidth reduction, and fine detuning of a semiconductor laser by using velocity-selective optical pumping of atomic resonance line," Applied Physics Letters **61,** 1895–1897 (1992).

[10] G. P. T. Lancaster, R. S. Conroy, M. A. Clifford, J. Arlt, and K. Dholakia, "A polarisation spectrometer locked diode laser for trapping cold atoms," Optics Communications **170,** 79–84 (1999).

[11] W. Demtröder, *Laser Spectroscopy* (Springer-Verlag, 1981), Vol. 5.

[12] K. L. Corwin, Z. Lu, C. F. Hand, R. J. Epstein, and C. E. Wieman, "Frequency-stabilized diode laser with the Zeeman shift in an atomic vapor," Applied Optics **37,** 3295–3298 (1998).

[13] B. Chéron, H. Gilles, J. Hamel, O. Moreau, and H. Sorel, "Laser frequency stabilization using Zeeman effect," Journal de Physique III **4,** 401–406 (1994).

[14] M. A. Clifford, G. P. T. Lancaster, R. S. Conroy, and K. Dholakia, "Stabilization of an 852 nm extended cavity diode laser using the Zeeman effect," Journal of Modern Optics **47,** 1933–1940 (2000).

[15] N. Beverini, E. Maccioni, P. Marsili, A. Ruffini, and F. Sorrentino, "Frequency stabilization of a diode laser on the Cs D_2 resonance line by the Zeeman effect in a vapor cell,", Applied Physics B Online Journal, 2001.

Chapter 4

A Circularized Laser Diode

G. P. T. Lancaster, W. Sibbett and K. Dholakia, "An extended-cavity diode laser with a circular output beam"
Review of Scientific Instruments **71**, 3646–3647 (2000).
G.P.T. Lancaster, W. Sibbett and K. Dholakia, "A circularized laser diode for high-resolution spectroscopy of rubidium"
To be submitted.
UK Patent no. C455.00/U.

4.1 Introduction

Semiconductor diode lasers are now firmly established as important tools in spectroscopy. They offer compact, inexpensive light sources that provide advantages over more conventional Ti-Sapphire and dye laser systems in high-resolution atomic physics experiments.

As mentioned previously in Chapter 2, standard diode lasers have several undesirable characteristics for spectroscopy including poor tuning characteristics and large linewidths but by taking advantage of the susceptibility of these lasers to op-

tical feedback, one can convert the diode laser into an improved spectroscopic light source. Feedback is usually introduced by a dispersive optical element (diffraction grating) external to the diode [1, 2]. In the simplest form of this, the Littrow geometry [3], the diode laser linewidth is reduced to less than 1 MHz and continuous tuning of up to 8 GHz can typically be realized. This leads to a laser source which has the required spectral characteristics and which can be tuned smoothly around the frequency of interest. Such laser systems were discussed extensively in Chapter 3 and their specifications highlighted.

Another drawback of diode lasers is their elliptical output. The spatial beam profile is important in laser cooling and atom trapping [4], where non-spherical beams can cause distortions of the atom-cloud shape. This is corrected by either using anamorphic prisms, cylindrical lenses or by coupling the laser output into a single mode optical fibre. All these conventional methods require additional optics thereby increasing the complexity of the experiment and, in some cases, at the expense of a substantial loss in power. In this chapter the characteristics of a diode laser that has a small, cylindrical microlens placed close to the output facet are investigated. This procedure, known as *circularization*, results in a circular output and was evaluated both free-running and in an extended-cavity geometry. Further, such a diode laser was injection locked from a second similar laser mounted in the Littrow geometry. The locked laser was used subsequently to cool and trap neutral rubidium atoms.

4.2 Free-Running Circulaser

Commercial diode lasers were obtained (Blue Sky Research Inc., San José, CA), part Nos. PS026-00 and M000-703009 respectively for the Hitachi HL 7581G, 50 mW and Sanyo DL-7140-201, 70 mW circularized laser diodes. Both diodes have had a small cylindrical, virtual point microlens placed close ($\sim$30 μm) to the diode's output facet, see Figure 4.1. These diode lasers have been named *Circulasers*. It should be emphasized that the lasers detailed above operate at

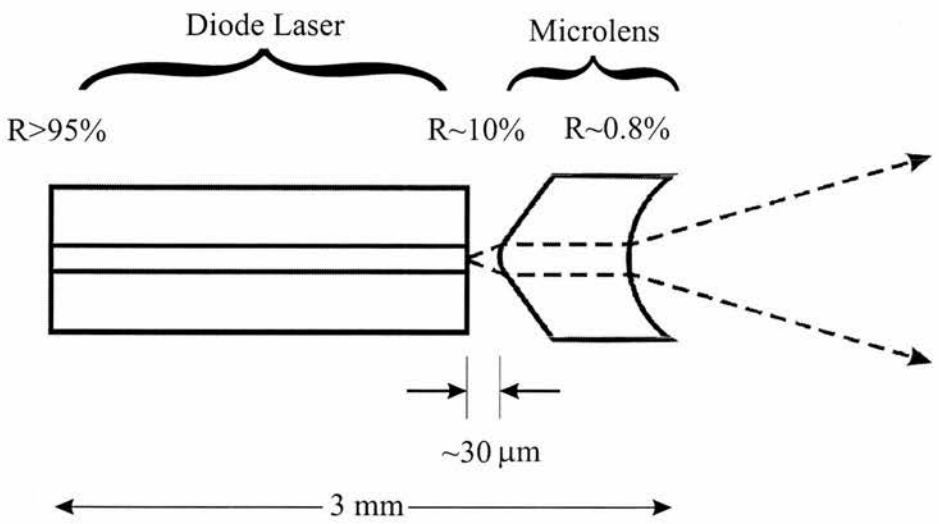

Figure 4.1: Schematic diagram of the diode laser and microlens assembly.

780 nm which is a wavelength hitherto unexplored with respect to circularized diode lasers.

The primary function of the ~250 μm thick microlens is to provide a circular output beam directly from the laser package. In addition however, even though the lens is anti-reflection (AR) coated with reflectivity of ~0.8%, the outer surface of the lens reflects a small fraction of the light back to the laser. The effect of the microlens is to create a three mirror cavity. The effective reflectivity (amplitude coefficient R')of the facet nearer the lens is modified, becoming a periodic function of the microlens to diode facet distance, ℓ. This effective reflectivity can be shown to be a function of the wavelength of light emitted λ, the unmodified front facet reflectivity R, and the lens reflectivity r, as shown in Equation 4.1 [5].

$$R'^2 = R^2 + [2R(1 - R^2)r]cos(4\pi\ell/\lambda) \tag{4.1}$$

The periodicity of the reflectivity results in a wavelength dependent loss and this allows the laser to oscillate preferentially on a single longitudinal mode [5]. The modified cavity formed between the back facet of the diode and the lens acts like

a 3 mm long cavity with an internal etalon which has a length defined by the distance between the front facet of the diode and the microlens.

There is some ambiguity over whether the photon lifetime is increased thereby narrowing the laser linewidth solely as a result of the microlens. Talvitie *et al.* [6] reported in October 1997 that a narrowing of a free-running diode laser at 635 nm had been recorded due to the inclusion of such a microlens, but in early 1998 the same group published findings suggesting that, due to the feedback being extremely weak, no such linewidth narrowing took place [7]. In both studies the same diode laser was investigated (a modified SDL-7501-G1, part number PS010 from BlueSky Research). The discrepancy in these findings may be accounted for by different microlenses having slightly differing reflectivities, although the exact effect the microlens has on the laser linewidth remains unclear. Without a lengthy and detailed study of several diodes it is impossible to predict the exact effect the microlens has on the laser's linewidth at this time but previous studies on diode lasers conclude that feedback from an external reflective element resulted in narrowing of the laser linewidth [5, 8]. It was proposed, with reasonable certainty, that the circularized diode lasers used in this research would show a similar narrowing in linewidth due to feedback from an external reflective element.

4.2.1 Spatial Characteristics

The spatial characteristics of the output beam from a free-running circularized diode were investigated initially. The circularized diode was placed in a commercially available collimating tube (Thorlabs Part No. LT110A or LT230P5-B depending on whether the 9 mm diameter can Hitachi was used or the 5.6 mm can Sanyo respectively). This was then placed in a custom machined holder which was temperature stabilized using two peltier elements. A Newport model 505 diode driver was used enabling an external modulation of up to 500 kHz to be added onto the drive current. A beam profiler (Photon Inc., model 2350) was

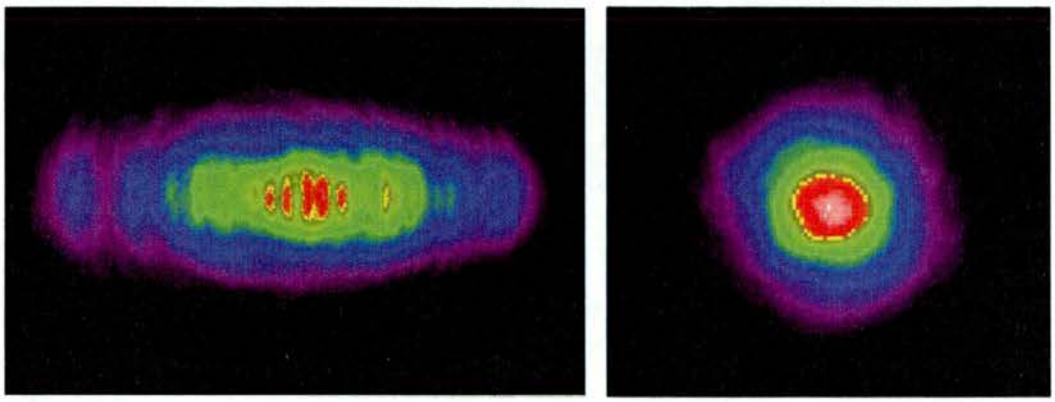

(a) (b)

Figure 4.2: (Colour) Beam profiles of (a) a normal, uncircularized Hitachi diode and (b) a circularized Hitachi diode from Blue Sky Research Inc..

used to compare the profile of a normal, unaltered Hitachi HL 7581G diode to a circularized diode. A f=+100 mm focal length lens was used to decrease the size of the beam onto the profiler but care was needed in alignment to ensure the beam passed centrally through the lens minimizing the effect of aberrations. Typical profiles of a non-circularized laser are shown compared to a Circulaser, see Figure 4.2.

The aspect ratio of beam height to beam width of the circularized beam was 1 : 1.1 in comparison with the normal, non-circularized beam of 1 : 2.4. Aspect ratios of beams used to trap atoms have been measured to be as large as 1 : 1.2 and hence such a laser as detailed here should show no apparent distortions in cloud shape. Therefore it is concluded that the observed spatial profile of this laser is adequate for atom trapping purposes.

A measurement of the divergence was taken by measuring the M^2 value of the beam. The M^2 parameter, derived from the product of waist size and far-field divergence angle, measures how closely a beam approaches the theoretical perfection represented by a Gaussian TEM_{00} beam [9]. It is a useful way of comparing a beam's quality with the universal absolute minimum of unity. This was done using the "k Factor Wizard" program incorporated within the previous mentioned

beam profiler. M^2 values for the circularized laser were measured to be less than 1.2. This is close to the value expected from measuring a normal diode laser and with confidence it can be stated that there is negligible deterioration in the beam quality.

4.2.2 Linewidth

Recently, Talvitie and co-workers used a commercially available circularized diode laser at 633 nm for Doppler-free studies of iodine [7]. Such a system employs weak feedback from an aforementioned integral microlens allowing the diode to run in a single longitudinal mode.

As part of the work undertaken at St Andrews, a measurement was taken of the free-running Circulaser linewidth. The laser beam was collimated and directed into a 300 MHz Free Spectral Range (FSR) Fabry-Perot etalon, Finesse=400, and a trace recorded on a Tektronix TDS360 oscilloscope. The scan shown in Figure 4.3, highlights that the laser operates on a single longitudinal mode although it was found that at operating currents higher than 124 mA the laser switched to multimode output. The four narrower peaks seen in the scan are the result of the flyback of the optical spectrum analyser (OSA) due to the saw-tooth ramp applied to the one of the cavity mirrors. The laser linewidth was measured to be <4 MHz from the FSR of the etalon, as shown in Figure 4.4. The laser at this point was not locked to a frequency standard and so no account is made of drift in frequency. To measure long term frequency drift of this laser, an integration method using a digital oscilloscope was implemented.

A beam splitter was used to send a portion of the output of a Circulaser to a 300 MHz FSR Fabry-Perot interferometer via a 40dB optical isolator with the signal being read on a Tektronix TDS360 digital oscilloscope. Because the laser frequency was sensitive to current noise and the Newport diode driver used was mains driven, an ultra low noise diode driver (ILX, model LDX–3620) was

obtained. This operated from batteries with a noise of $\leq$ 850 nA r.m.s.. The apparatus was switched on for a minimum of one hour to allow all components to reach thermal equilibrium. The experiment was carried out on a Saturday when noise in the vicinity of the laboratory was at a minimum and the heating supply had been turned off[1]. The oscilloscope was set to integrate and the drift of the laser measured over several time frames. Over a 5 minute period the laser fluctuated by 49 MHz whilst over 1 hour the laser drift was 130 MHz. With no active feedback to the laser in any form, these values represent the drift when only temperature stabilization of the diode housing was employed. This is in contrast with unlocked drift measurements of uncircularized diode lasers which fluctuate typically by twice this value. The inclusion of the microlens produces an inherent improvement of stability of the circularized laser compared to its uncircularized counterpart. Later in this chapter it will be shown that this increase in stability is observed when the Circulaser is placed in an extended-cavity resulting in a laser system that can cool and trap atoms for a number of minutes without the need for locking to a frequency reference.

The high frequency variations in frequency around the central value as a result of the laser's sensitivity to current are somewhat large if the free-running laser were to be used as the cooling laser but such a laser has been used, unlocked, as a hyperfine repumping laser on the ^{85}Rb F=2$\rightarrow$3 transition for atom trapping. The correct frequency was obtained by tuning the driving current, the details of which are now discussed.

4.2.3 Tunability

Talvitie and colleagues [7] also discovered that the circularized diode had the ability to tune modehop free simply by tuning the drive current. This feature was investigated using our diode lasers operating at 780 nm.

[1] At this time there was no air conditioning in the laboratory and so experiments sensitive to temperature changes were timed to coincide with periods where least fluctuation would occur.

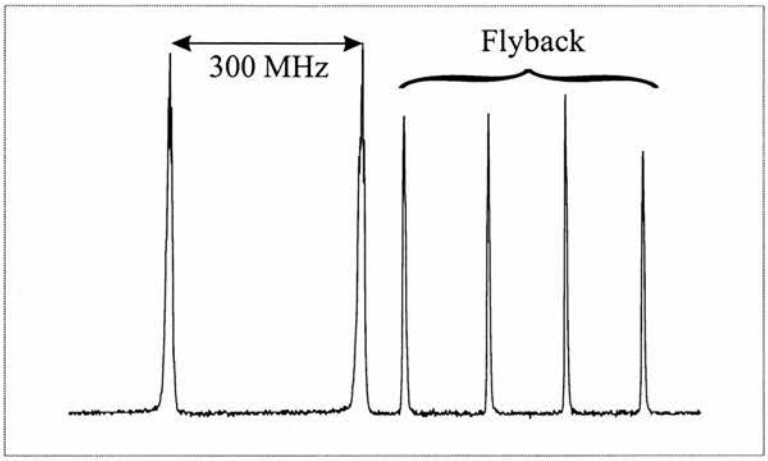

Figure 4.3: A scan from a 300MHz FSR Fabry-Perot interferometer of a free-running Circulaser showing single longitudinal mode operation at 80 mA drive current. The smaller peaks are a feature created by the non-symmetric wave driving the interferometer's cavity mirror, known as flyback.

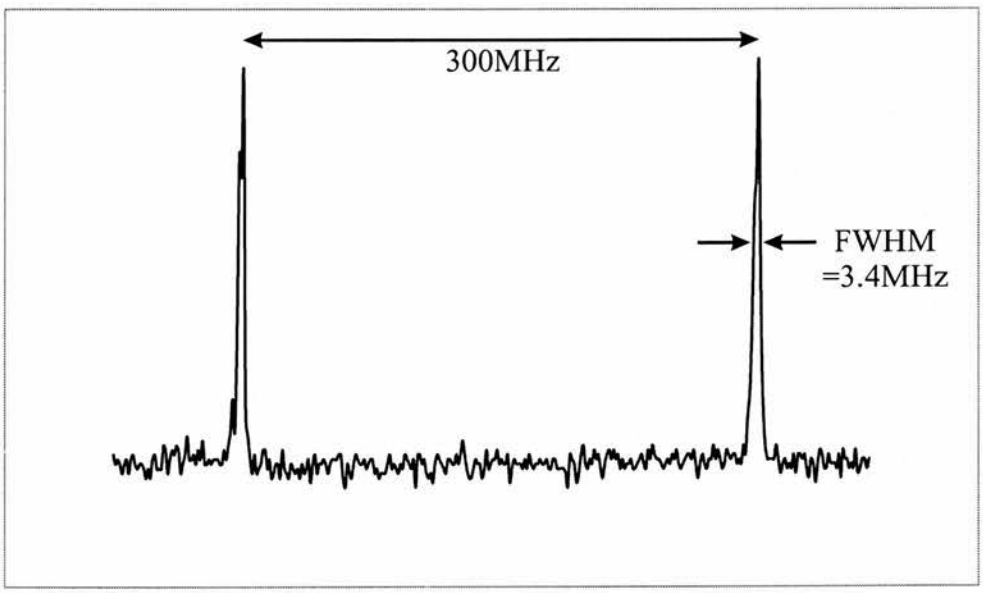

Figure 4.4: A scan from a 300MHz FSR Fabry-Perot interferometer of a free-running Circulaser showing single longitudinal mode operation with a linewidth less than 4 MHz.

A wavefunction generator (Thurlby Thandar Instruments TG210) was connected to the modulation input of a Newport model 505 laser diode driver. The peak-to-peak voltage of the saw-tooth wave varied depending on the range over which the laser was to be tuned but the maximum was typically 4.5 V. This allowed a complete scan from just above lasing threshold to maximum current (40 mA to 125 mA). The frequency of the wave generator was not critical but less than 100 Hz was used for all of the experiments. It was necessary to reduce the frequency to sub-Hertz when measuring the tuning of the laser for reasons that will be explained later.

The laser was collimated and a fraction split off by way of a beam splitter. This was directed into a 300 MHz FSR Melles Griot spectrum analyser of Finesse=400. When the current was increased and the laser frequency tuned, the peaks moved in one direction. By counting the passage of these peaks and knowing the frequency spacing between them, the tuning could be calculated. The frequency of the wave generator was decreased to a minimum of $2\text{x}10^{-4}$ Hz to facilitate possible observation of a discontinuous jump. From any jump, a modehop could be inferred. Difficulty was encountered tracking the moving peaks when the laser tuning exceeded ~50 GHz since the wave generator was, at this stage, outputting its lowest frequency yet the peaks were moving too quickly to be counted reliably. The 300 MHz FSR spectrum analyser was replaced with a 1.5 GHz spectrum analyser, allowing the peaks to be monitored easily. A typical scan of over approximately 60 GHz can be seen in Figure 4.5.

The difference in peak heights was due to the sampling rate of the oscilloscope. This was corroborated by scanning over ~10 GHz, shown in Figure 4.6, where the sampling was sufficiently rapid to measure each peak accurately. Using this method, a continuous, mode-hop free scan of 110 GHz was measured. A tuning curve for a Circulaser diode is shown in Figure 4.7, and from this graph a tuning of 2.17 GHz mA^{-1} was obtained, highlighting the importance of an ultra stable current diode driver.

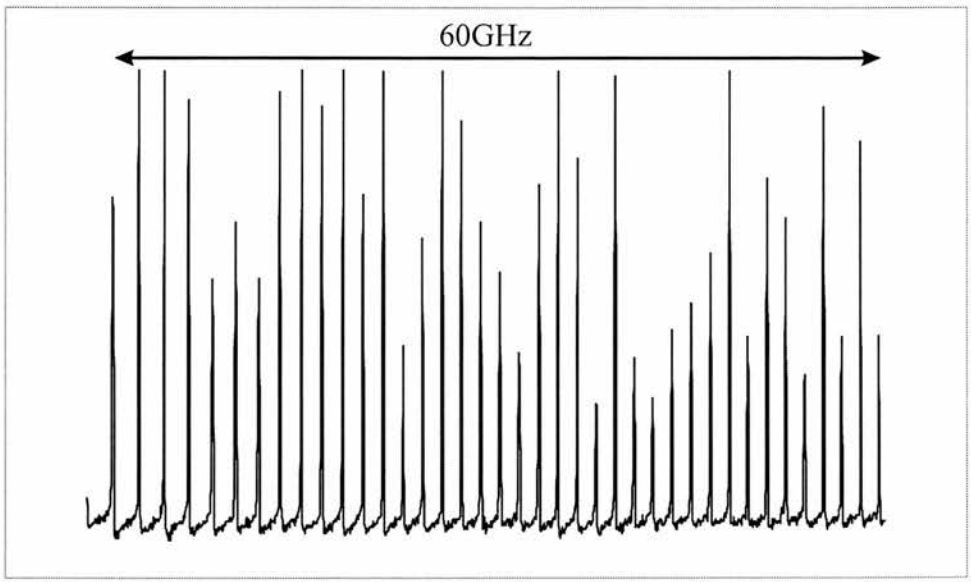

Figure 4.5: A frequency scan of 60 GHz showing the height differences in peaks due to the sampling rate of the digital oscilloscope.

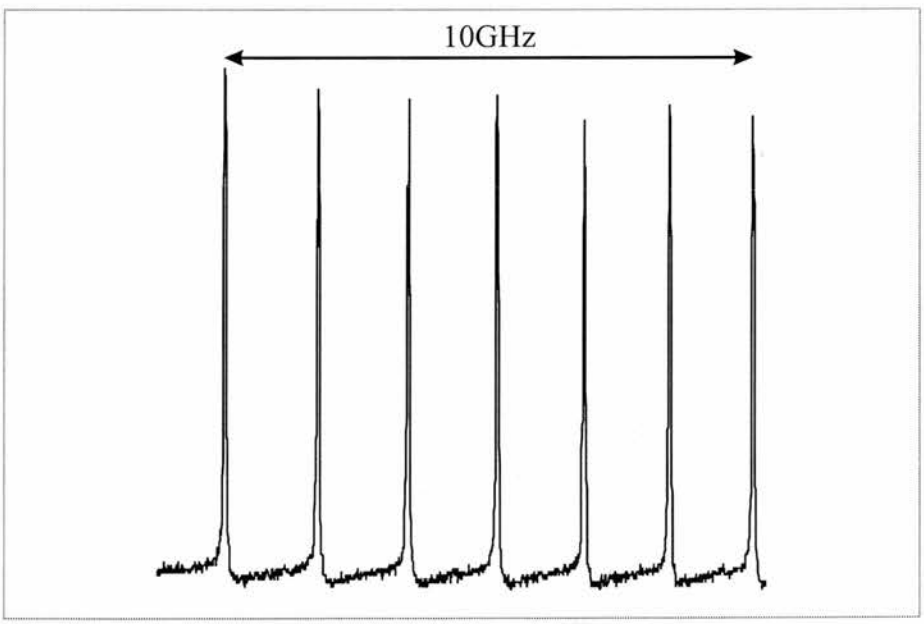

Figure 4.6: A frequency scan of 10 GHz showing equal peak heights.

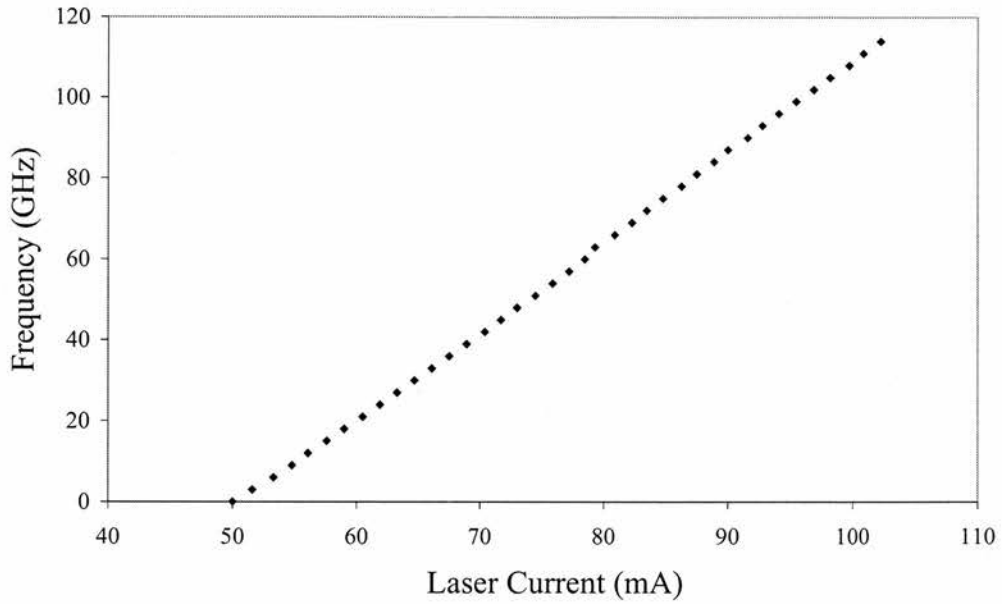

Figure 4.7: Graph of modehop free tuning verses current of a Circulaser.

An experiment was conducted to verify if the laser could be used as a spectroscopic tool. A small fraction of the output beam was directed towards a visible spectrometer (IST–REES E201) and the temperature of the diode set to 23.2C to enable the laser to operate with a nominal wavelength of 780 nm with a current[2] of ~60 mA. The remainder of the output was used in a saturated absorption spectroscopy setup and the current and temperature varied in a systematic way until fluorescence was seen in the vapour cell. The laser was then scanned across the rubidium transition and the trace in Figure 4.8 typifies what was obtained. As can be seen from this scan, three rubidium lines can be scanned continuously with the hyperfine features clearly visible on a reduced scan over just one of the lines, shown in Figure 4.9. It should be noted that since the hyperfine features of rubidium can be resolved, the laser must have a linewidth of $\leq$10 MHz. Uncircularized lasers have linewidths typically ranging from 10 to 500 MHz [1] and it is concluded that although the full extent of linewidth narrowing is not known, there is sufficient narrowing taking place due to the microlens to lend

[2]This current was chosen to give an output power sufficient to be used in subsequent trapping experiments.

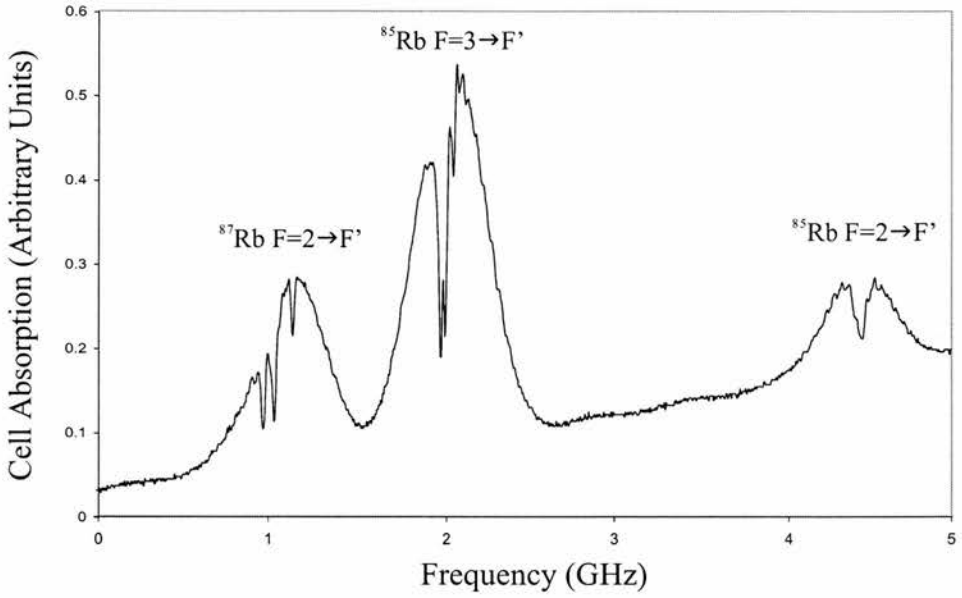

Figure 4.8: Looking from left to right, the ^{87}Rb F=2→F', ^{85}Rb F=3→F'and ^{85}Rb F=2→F' transitions as seen using a free-running Circulaser. The hyperfine structure can be seen clearly, indicating that the laser linewidth is narrower than the atomic linewidth.

this laser suitable for investigation of the hyperfine structure of atoms, giving an extremely simple spectroscopic tool. There are no mechanical elements to the system, except the lens itself but this is aligned and then epoxied in place by BlueSky Research, thereby giving a robust and stable diode with characteristics and simplicity not matched by any other diode based spectroscopic tool without the need for expensive or complicated locking electronics.

4.3 Circulaser in Extended-Cavity Geometry

The laser was then placed in an extended-cavity geometry identical to the one reported in Chapter 3 with all mechanical and electrical parts being the same.

A measurement of the output powers of the diodes in the Littrow geometry was made. The current/power characteristics for a circularized Hitachi diode are shown in Figure 4.10. The two extended-cavity curves relate to the orientation

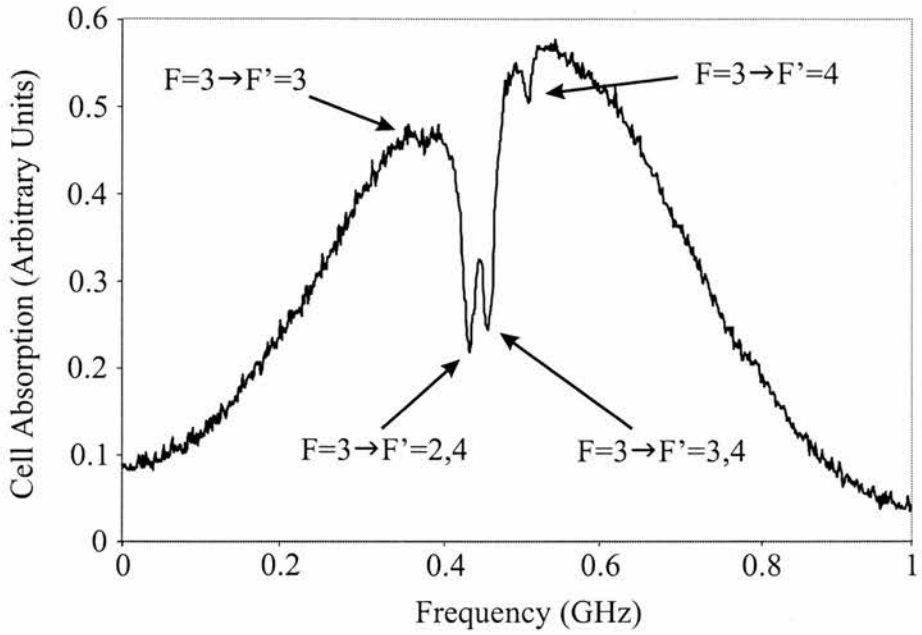

Figure 4.9: The ^{85}Rb F=3→F' line as seen using a free running Circulaser. The hyperfine structure is visible clearly.

of the polarised light incident on the grating. The gratings were obtained from Optometrics, UK with 1200 lines/mm and were blazed for 300 nm. Due to the grating reflectivity being polarisation dependent, it was important to orientate the laser diode relative to the grating for maximum output power. It was simpler to do this with an uncircularized diode since the output polarisation is perpendicular to the most divergent axis of the output beam. There was no such visual cue with a Circulaser and so the only method of ensuring the diode was orientated correctly was to monitor the output power while rotating the diode in its mount.

A similar set of curves for a circularized Sanyo laser are shown in Figure 4.11 with the diode orientation in the extended-cavity being optimised for maximum output power. From these it can be seen that approximately 30 mW and 60 mW single mode, narrow linewidth, tuneable output was obtained from the circularized Hitachi and Sanyo diodes respectively in a Littrow geometry extended-cavity.

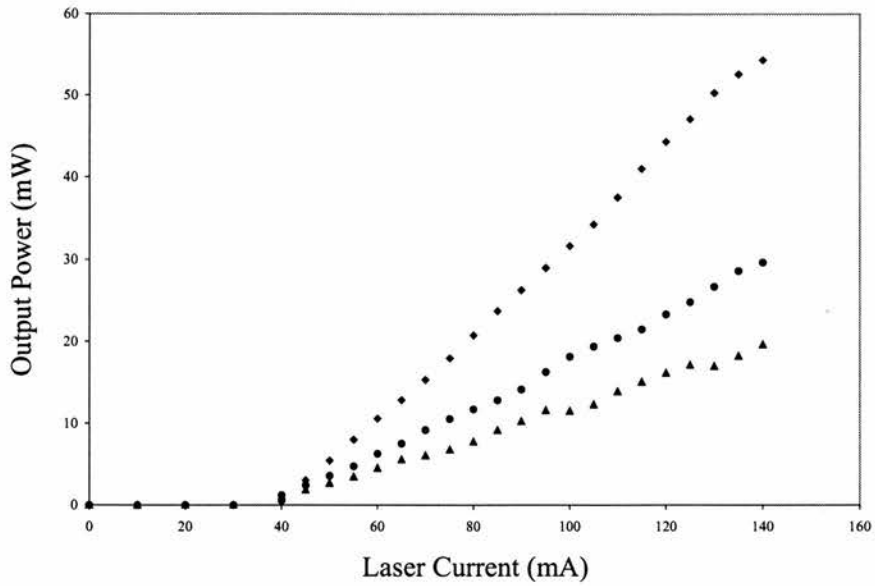

Figure 4.10: Current/Power curves for a free-running Hitachi diode laser (diamonds), in an extended-cavity with the laser rotated for maximum power in the zeroth diffracted order output (circles), and in a extended-cavity with the laser rotated for maximum power in the first diffracted order (triangles).

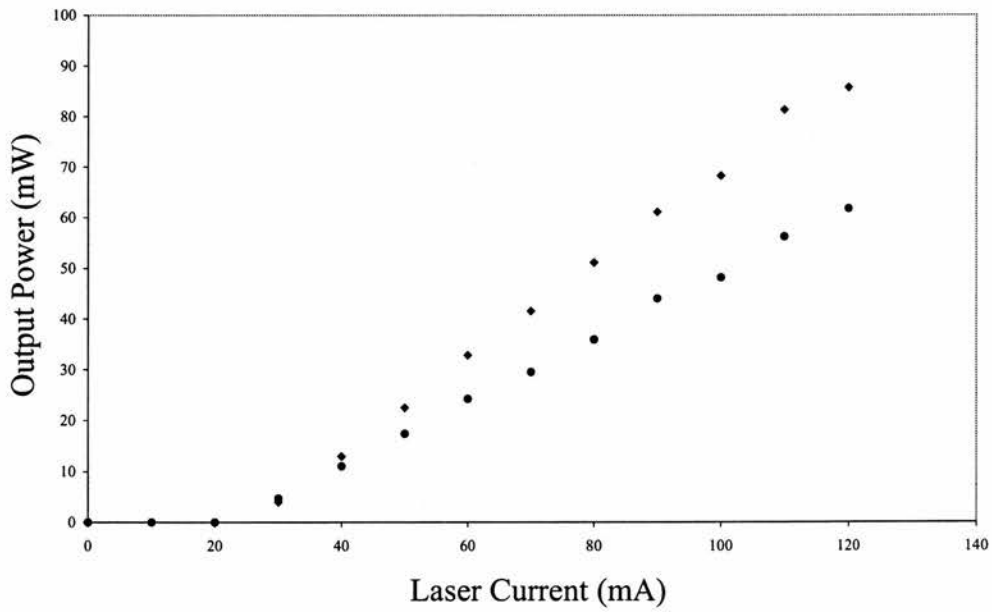

Figure 4.11: Current/Power curves for a free-running Sanyo diode laser (diamonds), and in an extended-cavity with the laser rotated for maximum power in the zeroth diffracted order output (circles).

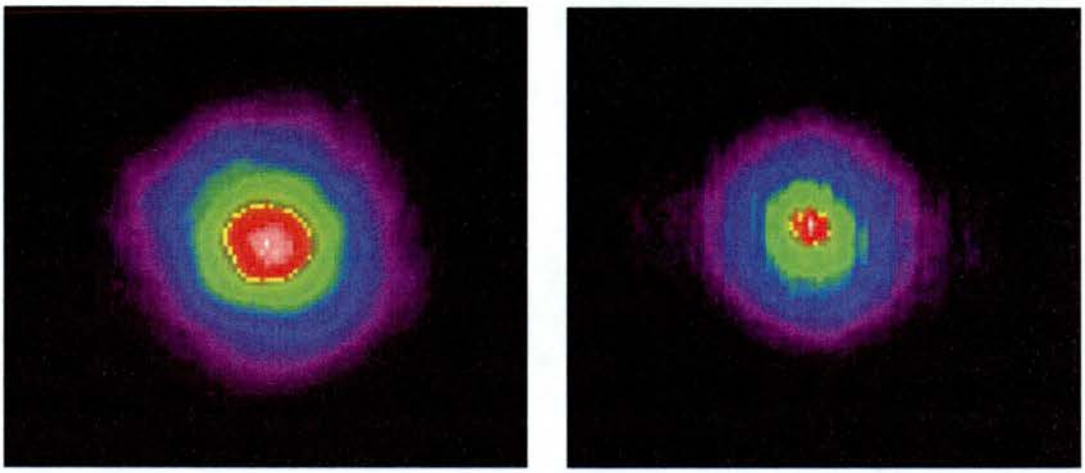

(a) (b)

Figure 4.12: (Colour) Beam profile of (a) light incident on grating and (b) the Zeroth-order diffracted output.

4.3.1 Spatial Characteristics

The spatial quality of the beam was measured both before and after the laser was incident on the diffraction grating using the same technique as in Section 4.2.1. No noticeable degradation in the beam quality was observed with the aspect ratio of beam height to width remaining at 1:1.1, see Figure 4.12. Again, this is in comparison with 1 : 2.4 for the standard 780 nm Hitachi laser diode. The M^2 value of the Circulaser beam after the grating was measured to be less than 1.2.

4.3.2 Tunability

Tuning of the laser frequency was achieved by altering the external cavity length. This was done coarsely by rotating the horizontal mirror mount adjustment screw while the fine tuning was achieved by applying a voltage to a piezoelectric transducer (PZT) disk placed beneath this screw. Discontinuous tuning was possible over 5 nm, from 779 to 784 nm and continuous, modehop-free tuning of $\sim$5 GHz was achieved. It is informative to note here that the range of continuous tuning

varied and depended on the external-cavity alignment. The continuous tuning range was also less than measured previously for elliptical diodes in the same configuration (these typically being ~8 GHz [10]). This was probably due to mode competition effects between the cavities and warrants further study but since atom cooling studies require only ~1 GHz tuning around the frequency of interest, it was thought inappropriate to spend extensive periods of time investigating this. It can be commented however, that slightly more care is required in current selection in order to obtain a smooth frequency scan over the frequency of interest. It is worth remarking here also that the feedback from the grating is sufficient to pull the laser output to the desired wavelength and any dual cavity effects due to the presence of the AR-coated microlens are restricted only to a slight reduction in the continuous tuning range of the ECDL. Importantly, during these studies it has been possible to bring a number of extended-cavity diode lasers (EDCLs), using Circulaser diodes, to the rubidium D2 line. Further, the addition of the microlens to the laser diode has an obvious beneficial effect on the stability of the laser frequency, as will be discussed subsequently in this section.

Although the reduced modehop-free tuning should not lead to problems when the lasers are used for cooling, in some instances a large tuning range is desired. To extend tunability further, synchronous current/PZT scanning was employed [11]. A fraction of the saw-tooth wave driving the scanning PZT was used as a modulation input to the diode driver. The modehop-free tuning range was then measured to be 26 GHz. This occurred when the transfer function between the modulation current and PZT voltage was 0.248 mA V^{-1} for the given apparatus. With this setup a continuous, uninterrupted scan of the D2 rubidium lines was taken, shown in Figure 4.13. The detail in this scan was depleted due to the resolution of the digital oscilloscope but by reducing the amplitude of the scan the detailed hyperfine levels of two of the lines could be seen clearly, Figure 4.14.

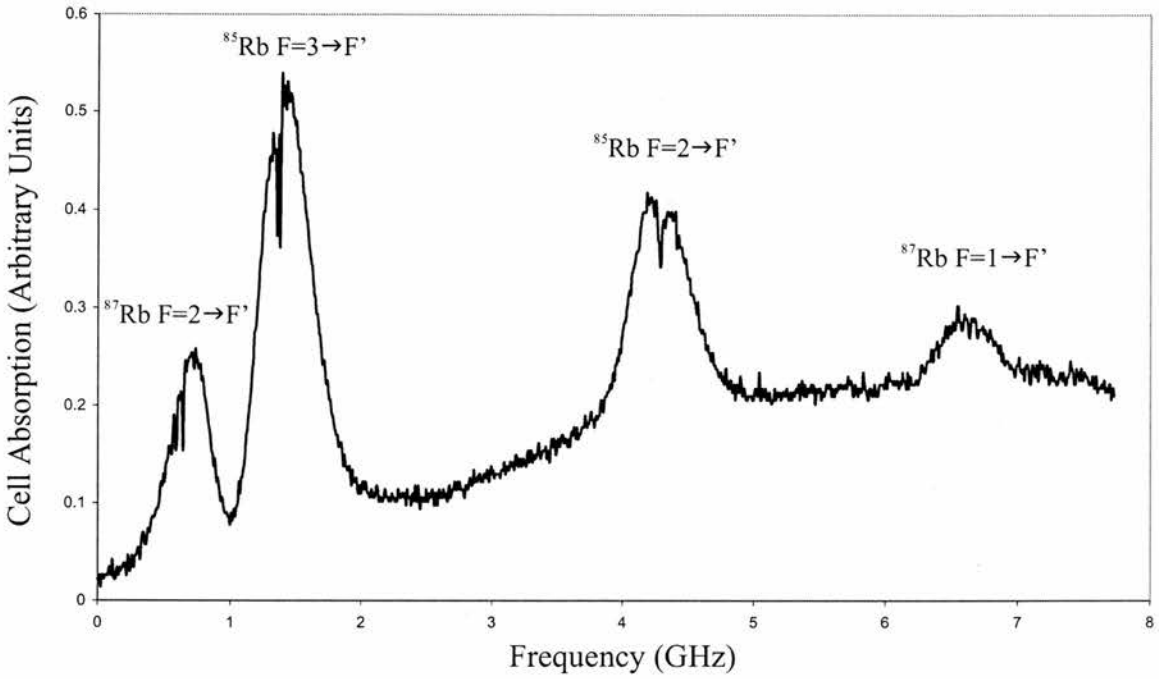

Figure 4.13: Looking from left to right, the ^{87}Rb F=2→F', ^{85}Rb F=3→F', ^{85}Rb F=2→F' and ^{87}Rb F=1→F' transitions as seen using a Circulaser ECDL.

4.3.3 Linewidth

A heterodyne experiment was conducted to measure the beat note between two circularized ECDLs. The outputs from two similar unlocked ECDLs were heterodyned together and the beat note recorded using a fast photodiode and a radio frequency spectrum analyser, see Figure 4.15.

The beat note linewidth was measured to be < 300 kHz in a 50 ms sample time. The ECDL linewidth was therefore sufficiently narrow for use in laser cooling and atom trapping of ^{85}Rb and both lasers were used subsequently for this purpose. The zeroth-order output was then directed through an expanding telescope to produce a beam of diameter $\sim$1.5 cm before being split to provide the three pairs of orthogonal beams needed to operate a magneto-optical trap. In comparison to the previous standard ECDL used in the initial experiments [10], a small increase in the power available at trap centre due to the absence of any beam shaping optics within the trapping apparatus was obtained. As mentioned briefly before,

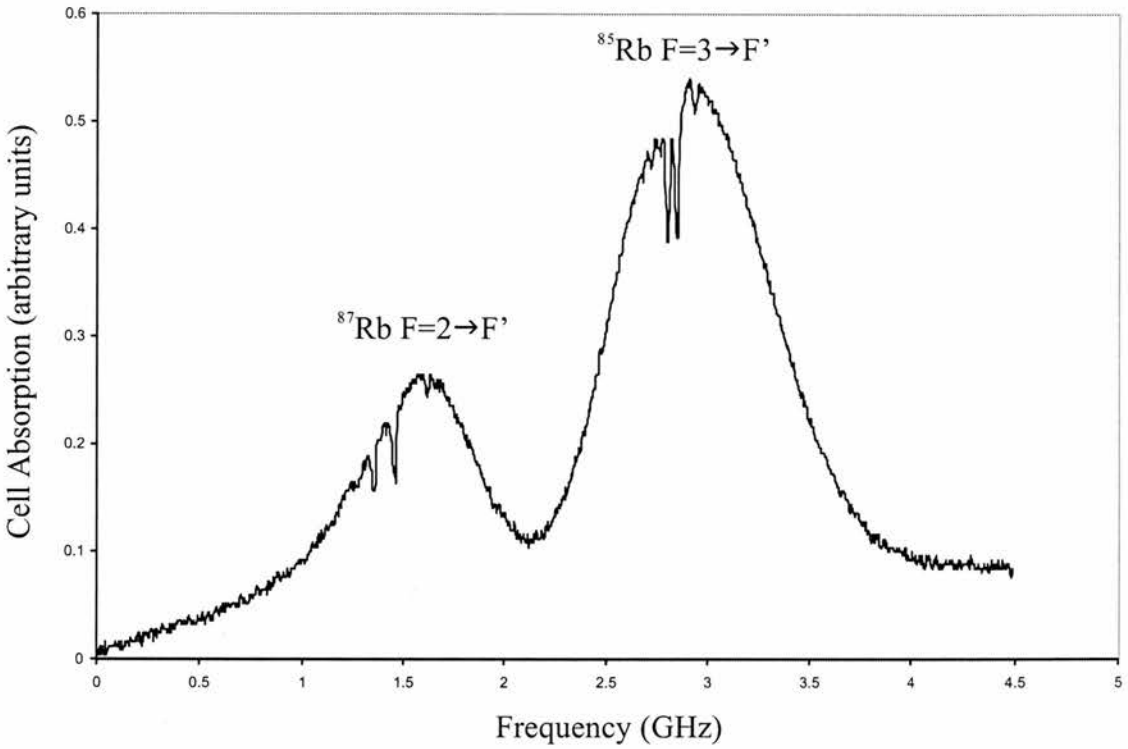

Figure 4.14: The ^{87}Rb F=2→F' and ^{85}Rb F=3→F' line as seen using a Circulaser ECDL. The hyperfine structure is clearly visible.

the inherent stability of the laser frequency was observably better and this was believed to be due to the additional etalon effect caused by the microlens [6]. Continuous trapping of ^{85}Rb atoms was observed over a number of minutes with an unlocked Circulaser ECDL, demonstrating the long term frequency stability of this simple yet powerful system [12]. This is in contrast with the standard 7851G diode laser in a very similar ECDL geometry where trapping could only be observed for a few seconds with the lasers unlocked. For long-term reproducibility, the circularized ECDLs were stabilized using using polarisation spectroscopy with rudimentary and inexpensive electronics to allow reliable and consistent trapping where cost and simplicity are paramount [13].

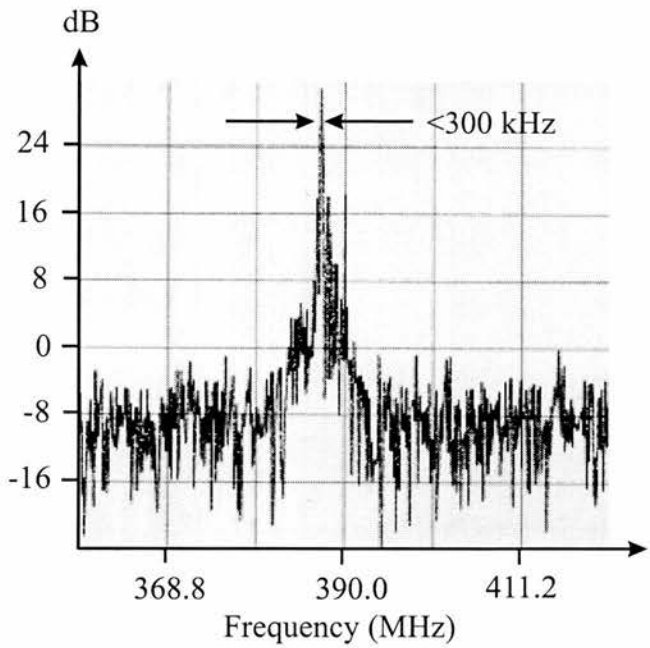

Figure 4.15: The beat note of two similar, unlocked, circularized ECDLs when heterodyned.

4.4 Injection Locking of a Circulaser

4.4.1 Introduction and Theory

In 1865 Christiaan Huygens noticed, while bedridden for a number of days, that when two clocks were placed close together in his room, their pendulums locked into synchronism and when moved further apart they returned to being free-running. He later traced the effect to vibrations being transmitted through the wall between them, but this coupling of two separate oscillators was the first recorded observation of injection locking [14, 9]. Later, in 1907, the coupling between two tuning forks placed on a table top was observed by Rayleigh. Oscillator synchronization is not limited to purely physical systems such as the many examples in optics, electronic oscillator circuits and phase-locked loops but transcends to other areas such as biology. A number of striking examples exist in nature which show such coupling including the synchronized flashing of entire trees full of tropical fireflies and the synchronization of the female human being menstrual

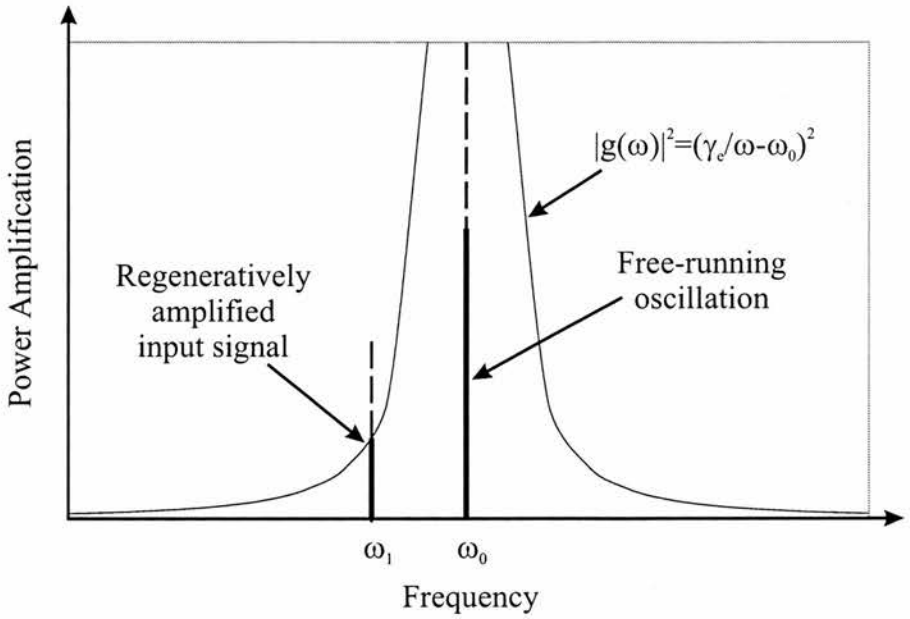

Figure 4.16: Regenerative gain versus input frequency ω_1 for a laser cavity oscillating at frequency ω_0.

cycle through pheremonal communication [15].

In lasers, the same effect can be utilized to "lock" one laser's frequency (slave laser) to that of another (master laser) by injecting a weak signal from the master to the slave. For locking to occur, the master frequency, ω_1, and the free-running oscillating slave frequency, ω_0, must be within, what is known as, the *locking range*. This range is dependent upon the external decay rate[3], γ_e, of the laser cavity which is due to external coupling. The regenerative gain experienced by a weak signal at frequency ω input to a cavity oscillating at ω_0 where $\omega \neq \omega_0$ is given by

$$| \tilde{g}(\omega) |^2 \approx \frac{{\gamma_e}^2}{(\omega - \omega_0)^2}, \tag{4.2}$$

with Figure 4.16 showing this equation graphically.

[3]Also known as the frequency bandwidth.

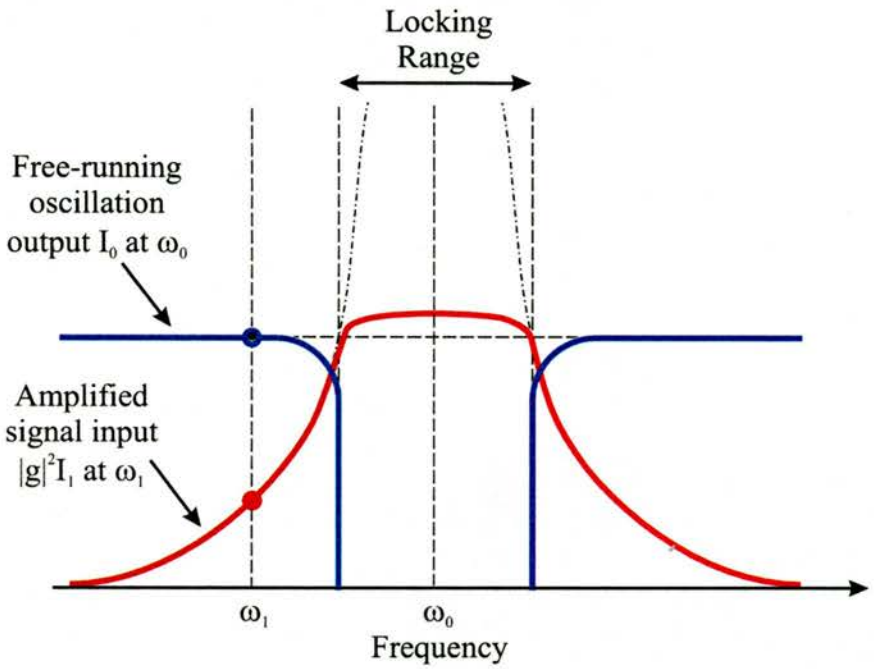

Figure 4.17: (Colour) When an injected signal is tuned outside the locking range on either side, the output from the laser consists of both the amplified and the free-running oscillation signal. When the injected signal is tuned inside the locking range, only single output wave with the injected frequency is present.

If a weak signal at frequency ω_1 and of amplitude I_1 is injected into an oscillating cavity whose natural cavity resonance is at a frequency ω_0 with an output amplitude I_0, with ω_1 being far from ω_0, then the signal at ω_1 will experience regenerative gain at the same time ω_0 is oscillating. Because ω_1 is small and the gain it experiences is also small, no effect on the free-running oscillation signal at ω_0 is seen. However, if ω_1 approaches ω_0 then from Equation 4.2, the gain experienced at ω_1 increases sharply. The amplified output intensity becomes $|\,\tilde{g}(\omega_1)\,|^2 I_1$, which is the power extracted from the gain medium. If this value approaches and passes the free-running oscillation output, I_0 at ω_0, then there is not enough gain in the medium to support both frequencies and the signal at ω_0 is suppressed. Figure 4.17 shows how the output powers of both signals at ω_0 and ω_1 change with tuning of the master frequency. Therefore, the laser now oscillates with an output power equal or slightly above that which it oscillates with naturally, but at the injected frequency ω_1.

The first experimental demonstration of injection locking of one laser to another was carried out in 1966 by Stover and Steier [16] at the Bell Telephone Laboratories using two single-frequency helium neon lasers. Each laser had a piezoelectric transducer (PZT) mounted behind one of the cavity mirrors to allow tuning. In this experiment, a small fraction of one laser was injected into the other (from the master to the slave). An optical isolator was employed in order to avoid unwanted feedback from the slave laser to the master. The outputs from both lasers were overlapped via a beam splitter and directed towards a photodiode which detected the beat note frequency by way of a radio frequency spectrum analyser. The beat frequency was then displayed on an oscilloscope. To prove injection locking was taking place two experiments were performed. Firstly, the injection signal was blocked and the frequency of the master laser was scanned using a linear PZT scan. As a function of the PZT scan, the beat note frequency was seen to decrease as the two laser frequencies converged and then increase as the frequencies passed one another, as was expected. Next, the injection signal from the master laser was allowed to enter the slave cavity. When the experiment was repeated it was seen that when the master laser was within the locking range, a d.c. component was observed in the beat signal clearly proving that both lasers were oscillating with the same frequency.

4.4.2 Experimental Injection Locking of a Circulaser

A further extension of work performed on a circularized diode lasers was to use a Circulaser in an extended cavity geometry (master) to injection lock a free-running Circulaser (slave) successfully. The experimental setup is shown in Figure 4.18.

Both lasers were collimated and approximately 8 mW was split from the output of a circularized ECDL lasing on one of the rubidium D2 lines using a beam splitter. One of the split beams was passed through two 35dB optical isolators, one having crossed polarizing beam splitters which output any returning orthog-

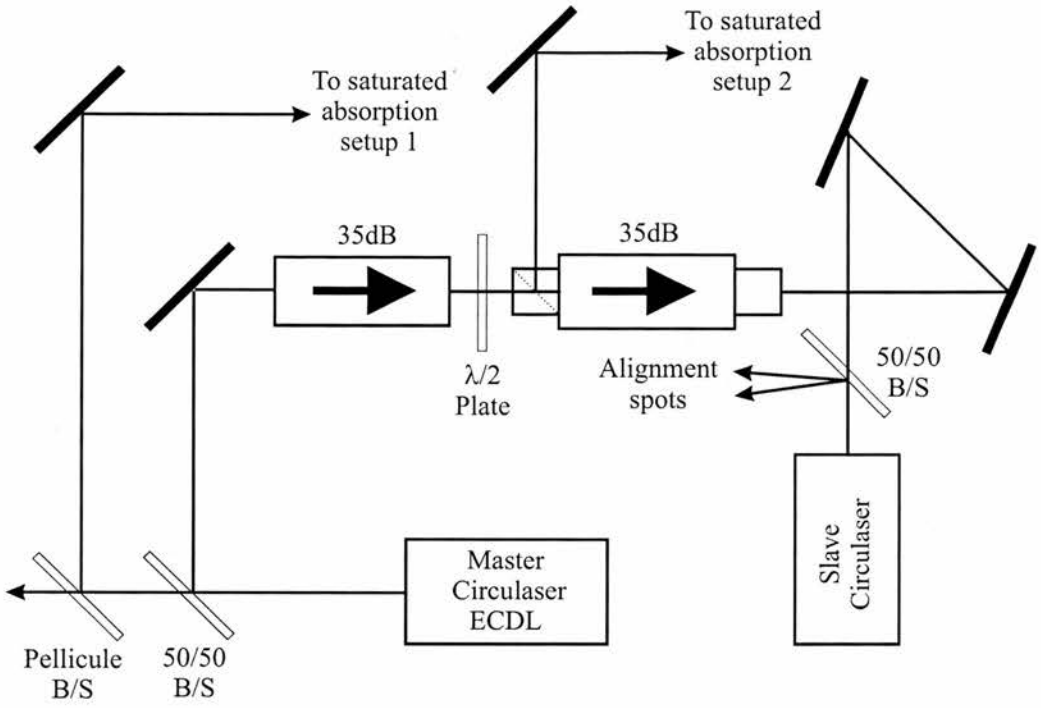

Figure 4.18: Functional diagram of Circulaser injection locking setup.

onal polarization in a direction perpendicularly to that of the input beam. A half-wave plate was inserted between the isolators which allowed the polarization of the master laser to match that of the slave laser. Alternatively, the slave laser could be rotated in its mount. The beam was manœuvred using beam steering mirrors and directed along the output path of the slave laser. A 50/50 beam splitter was placed in front of the slave laser to aid in the alignment process but this could be removed after the locking had been achieved. Between 1% and 2.5% of the slave power was experimentally found to be required from the master to lock the slave laser. In practice this was measured to be between 0.5 mW and 2 mW for 80 mW slave output. This gave 60 mW usable trapping power once the beam had been enlarged and steered towards the trap. Less than 6 nW of slave power was measured to be returned to the master. This leads to a rejection of 71dB through both isolators. Monitoring the slave output through a rubidium cell, it could be seen clearly, using an infrared viewer, when the slave was locked successfully to the master by the increase in fluorescence through the cell.

The output from the slave laser was used in a second saturated spectroscopy setup and the master ramped over the ^{85}Rb F=3→F' line. The slave output was expanded using a telescope and directed towards the trapping region to be used as the cooling beams in a standard MOT experiment.

4.5 Conclusions

Circularized laser diodes make a welcome addition to the area of spectroscopy and laser cooling. The weak feedback from the integral microlens causes a narrowing of the lasing linewidth and also enables smooth tuning across the majority of the gain bandwidth. Hyperfine structure of rubidium atoms have been observed using such a circularized laser with no other optical elements in place. This is in stark contrast to normal, free-running uncircularized diodes that are used for spectroscopy whose linewidths are greater than the atomic features of interest and whose tuning with current is step-like in nature. To overcome these disadvantages it is usual that the diode be placed in an extended-cavity geometry, which complicates the setup considerably. The extreme simplicity of the Circulaser lends itself to areas of research and teaching where spectroscopy is investigated on a regular basis but where adjustment of extended-cavities is not preferred, such as in an undergraduate teaching laboratory. Once the wavelength of interest is found for a particular Circulaser, all that need be done on subsequent occasions to find the desired wavelength is set the diode temperature and laser drive current. This has been found to be true for operation of such a diode over months of experimentation.

The benefits of using Circulasers over conventional uncircularized diodes in an ECDL for use in atom trapping experiments are also apparent: a reduction in the number of optical components leads to a simplification of the experimental system; there is an increase in trapping power available because of this and inherent frequency stability means some cold atom experiments may be conducted with unlocked lasers. It is also noted here that ECDLs, with their tuneable, single

mode, circular outputs, will be very useful in other applications, for example, the pumping of an optical parametric oscillator without the need for cylindrical telescopes or other beam shaping optics [17].

There are many more avenues that could be followed in investigating the possibilities of these simple but effective lasers: investigating in detail the effect the microlens has on the laser linewidth; if the same effects are seen at other laser wavelengths, particularly in the blue/near UV region; and evaluating whether stabilization of the free-running diode would lead to it being suitable for use as the cooling beam in a MOT experiment. In this chapter the work performed has brought a new and novel laser system to the current atom trapping configuration. In St Andrews, all previous laser cooling ECDLs in the laboratory have been replaced with the new circularized design and it is unlikely that in the future the former design will be used. Much work could still be done investigating the properties of these particular lasers, in fact I suspect an entire Ph.D. could be completed in doing so. It was not the aim of this study to investigate these diodes exhaustively, but rather to ascertain and evaluate their possible inclusion into the experiment for means of improvement and simplification. I believe this has been completed successfully.

Bibliography

[1] C. Wieman and L. Hollberg, "Using diode lasers for atomic physics," Review of Scientific Instruments **62,** 1–20 (1991).

[2] R. S. Conroy, A. Carleton, and K. Dholakia, "A compact, high-performance extended-cavity diode laser at 635nm," Journal of Modern Optics **46,** 1787–1791 (1999).

[3] L. Ricci, M. Weidemüller, T. Esslinger, A. Hemmerich, C. Zimmermann, V. Vuletic, W. König, and T. Hänsch, "A compact grating-stabilized diode laser system for atomic physics," Optics Communications **117,** 541–549 (1995).

[4] C. Wieman, G. Flowers, and S. Gilbert, "Inexpensive laser cooling and trapping experiment for undergraduate laboratories," American Journal of Physics **63,** 317–330 (1995).

[5] G. P. Barwood, P. Gill, and W. R. C. Rowley, "Longitudinal mode control in laser diodes," Measurement Science and Technology **3,** 406–410 (1992).

[6] H. Talvitie, A. Seppänen, A. Äijälä, and E. Ikonen, "Continuous-wave light source at 317nm based on frequency doubling of a diode laser," Applied Physics B **66,** 397–400 (1998).

[7] H. Talvitie, M. Merimaa, and E. Ikonen, "Frequency stabilization of a diode laser to Doppler-free spectrum of molecular iodine at 633nm," Optics Communications **152,** 182–188 (1998).

[8] L. Goldberg, H. F. Taylor, A. Dandridge, J. F. Weller, and R. O. Miles, "Spectral characteristics of semiconductor lasers with optical feedback," IEEE Journal of Quantum Electronics **QE-18,** 555–563 (1982).

[9] A. E. Siegman, *Lasers* (University Science Books, 20 Edgehill Road, Mill Valley, CA 94941, USA, 1986).

[10] M. A. Clifford, J. Arlt, J. Courtial, and K. Dholakia, "High-order Laguerre-Gaussian laser modes for the studies of cold atoms," Optics Communications **156,** 300–306 (1998).

[11] T. Nayuki, T. Fujii, K. Nemoto, M. Kozuma, M. Kourogi, and M. Ohtsu, "Continuous Wavelength Sweep of External Cavity 630 nm Laser Diode without Antireflection Coating on Output Facet," Optical Review **5,** 267–270 (1998).

[12] G. P. T. Lancaster, W. Sibbett, and K. Dholakia, "An extended-cavity diode laser with a circular output beam," Review of Scientific Instruments **71,** 3646–3647 (2000).

[13] G. P. T. Lancaster, R. S. Conroy, M. A. Clifford, J. Arlt, and K. Dholakia, "A polarisation spectrometer locked diode laser for trapping cold atoms," Optics Communications **170,** 79–84 (1999).

[14] M. Sargent, M. O. Scully, and W. E. Lamb, *Laser Physics*, 3rd ed. (Addison-Wesley Publishing Company, 1977).

[15] M. K. McClintock, "Menstrual synchrony and suppression," Nature **229,** 244–245 (1971).

[16] H. L. Stover and W. H. Steier, "Locking of laser oscillators by light injection," Applied Physics Letters **8,** 91–93 (1966).

[17] I. D. Lindsay, G. A. Turnbull, M. H. Dunn, and M. Ebrahimzadeh, "Doubly resonant continuous-wave optical parametric oscillator pumped by a single-mode diode laser," Optics Letters **23,** 1889–1891 (1998).

Chapter 5

Gallium Nitride-Based Extended-Cavity Diode Laser

R. S. Conroy, J. J. Hewett, G. P. T. Lancaster, W. Sibbett, J. W. Allen and K. Dholakia, "Characterisation of an extended cavity violet diode laser" *Optics Communications* **175**, 185–188 (2000).

5.1 Introduction

In this chapter, the work carried out on a recently available commercial gallium nitride (GaN) diode laser when placed in an extended-cavity geometry will be described. The laser emits in the ultraviolet and during the course of this chapter its characteristics will be compared to those of diodes in the same geometry but operating at the more usual red wavelengths. Its viability for use in areas of spectroscopy and laser cooling are also discussed.

5.1.1 Background

Since the launch by Nichia Chemical Industries Ltd. (Kaminaka, Japan) of a commercial diode laser emitting in the blue/violet region of the visible spectrum, operating continuous wave (CW) and at room temperature [1], there has been much excitement regarding the potential of these devices in several areas of science and industry. However, reducing the wavelength of diode lasers into the blue has not been an easy step to take. Several materials including ZnSe [2, 3], ZnO [4] and III-V nitrides such as GaN [5] have been investigated intensively. Until recently it had been impossible to achieve room temperature operation from a CW diode laser at this wavelength. The foremost reason for this in the case of ZnSe was excessive non-radiative recombination because of high crystal defect densities in the semiconductor material. While in nitride materials, it was the low carrier concentrations. High defect densities result in heating and the eventual failure of the device. Low carrier concentrations made it impossible to obtain a population inversion to initiate and sustain lasing. As a result, much effort was expended on refining the growth techniques to reduce these defects and increase carrier concentrations. Nichia Chemical Industries Ltd. achieved the first current-injection nitride based laser [6] and then also the first room temperature, CW operation for over 10,000 hours[1] in the latter half of 1997.

The rapid development of GaN diode lasers has led to the recent commercial availability of CW blue/violet diode lasers having practical lifetime characteristics. The main market for these devices is acknowledged to be optical data storage but such developments also afford exciting possibilities in atomic physics and chemistry by offering a low cost, compact, turnkey source as an alternative to upconversion fibre lasers or frequency-doubled diode, dye or Ti:Sapphire lasers, which are used traditionally to access wavelength regions around 400 nm. Recently, a commercial product applicable to the field of atomic physics utilizing these diodes has been advertised [1] and this confirms their market potential.

[1]This is defined by laser manufacturers as the "burn-in time" and denotes the minimum time a laser diode must be able to operate for before failure.

Visible diode lasers have typical linewidths in the tens of megahertz range. For some applications this is sufficient, but for high-resolution spectroscopy a continuously tuneable, sub-megahertz linewidth output is desirable to locate and resolve spectroscopic features. One particularly attractive way of achieving this with a conventional diode laser is to use a diffraction grating in an extended-cavity to feedback the first order and use the zeroth order as the output (Littrow geometry). This is known as an extended-cavity diode laser (ECDL). Such an arrangement can narrow the linewidth of a visible diode laser dramatically to the order of several hundred kHz or below. It provides discontinuous tuning over the entire gain bandwidth and continuous tuning over several gigahertz on altering the length and angle of the diffraction grating [7]. Further details of this geometry and other feedback mechanisms can be found in Chapters 2 and 3.

The characterisation of a GaN diode laser operating in a Littrow geometry around 393 nm giving a tuneable, single frequency output in excess of 3.5 mW is detailed in this chapter. The output was tuned smoothly over 6 GHz and discontinuously over 2.7 nm. An upper limit of 5 MHz was placed on the linewidth. A photograph of the free-running violet diode is shown in Figure 5.1.

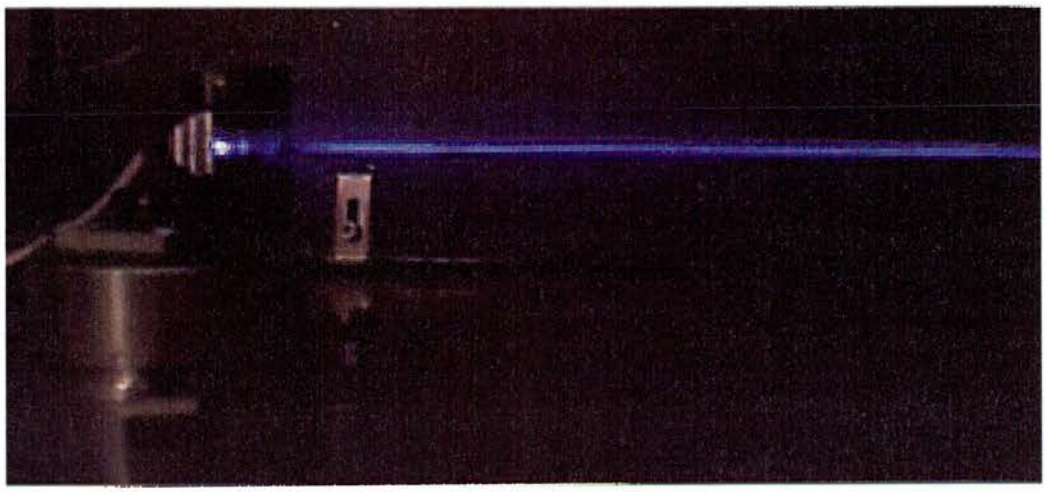

Figure 5.1: (Colour) A photograph of a free-running GaN laser.

This violet ECDL was around $\sim 1/10$ of the cost of the commercial system developed recently [7] when component costs were compared to the retail price.

Furthermore, the performance of violet diodes was compared to visible diodes in similar extended-cavity geometries and it was found that important differences need to be taken into consideration by spectroscopic users. The use of violet diode lasers in extended-cavity geometries have been reported previously. At the time of writing applications included sum-frequency generation of light for spectroscopy of mercury at 254 nm [8] and spectroscopy of potassium at 404 nm [9]. A characterisation of a commercially packaged extended-cavity diode system has also been conducted [10] however, this was somewhat limited due to the inability to alter cavity parameters. The work presented here overcomes this restriction by allowing the cavity elements to be changed.

5.2 GaN Diode Laser

The bandgap energy of AlGaInN can vary between 6.2 eV and 1.95 eV depending of the composition of the semiconductor alloy. Therefore, these III-V semiconductors make for useful light-emitting devices at all wavelengths over the visible spectrum. GaN has a bandgap of 3.4 eV at room temperature which produces a stimulated photon wavelength of 365 nm if used in an optoelectronic device.

5.2.1 Material Requirements

Substrate

A substrate is required to commence growth for all semiconductor devices. This is a thin wafer of high quality material on which subsequent layers of semiconductor material can be deposited. GaN is grown usually on a substrate of sapphire (Al_2O_3), (0001) orientation (C-face) at temperatures of about 1000^oC by metal-organic chemical vapour deposition (MOCVD). Although both GaN and sapphire possess the same hexagonal symmetry, sapphire has a lattice constant which is 13% [5, 11] larger and a thermal expansion coefficient almost double that of GaN.

Nakamura *et al.* [11] experimentally grew GaN structures on a substrate of spinel ($MgAl_2O_4$), which has only a 9.5% lattice mismatch to GaN, but found that it gave no increase in crystal quality. To grow a device on such a mismatched substrate requires a buffer layer. This is a soft layer of GaN grown at a relatively low temperature of 550^oC which helps reduce the number of defects occurring during growth. Ideally a substrate of GaN would be used to eliminate all mismatch but these are not commercially available. A substrate of SiC could be used since the lattice constant mismatch is only 3.5% but at the time these were extraordinarily expensive [12] and also have differing thermal expansion coefficients to GaN.

n-type GaN

Grown GaN layers usually exhibit *n*-type conduction characteristics without doping. This is thought to be due to nitrogen vacancies or residual oxygen in the structure, these atoms being present during the MOCVD process. To obtain carrier concentrations high enough to sustain lasing either Si or Ge is used as a dopant. These species are implanted at concentrations between $1x10^{17}$ and $1x10^{20}$ cm^{-3}.

p-type GaN

Formerly, it was impossible to *p*-type dope GaN with high carrier concentrations and this was the factor limiting further progress in this field. However, in 1989, Amano *et al.* [13] discovered that by irradiating a Mg-doped sample of GaN with a low energy electron beam, *p*-type material could be manufactured. This was stumbled across by accident when the researchers were observing a Mg-doped sample under an electron microscope and when testing the characteristics afterwards found that it had become *p*-type. Later, in 1992, Nakamura *et al.* [14] discovered that low resistivity *p*-type GaN could also be obtained by post-thermal annealing of Mg-doped GaN in a N_2 ambience.

5.2.2 Diode Laser Structure

The structure of the Nichia diode laser including the indium gallium nitride (InGaN) multi-quantum-well (MQW) gain region is shown in Figure 5.2. The ternary semiconductor InGaN is used as the active region because, depending on the indium mole fraction, the bandgap varies between 1.95 eV and 3.4 eV equating to stimulated photon emission between 636 and 365 nm in bulk InGaN. However, in MQW structures it is the confinement of electronic states in the quantum wells and in indium concentration fluctuations which has a larger and more pronounced effect on the lasing wavelength [15], as shall be discussed later. The MQW structure consists of four 35 Å-thick undoped $Ga_{0.85}In_{0.15}N$ well layers separated by 70 Å-thick undoped $Ga_{0.98}In_{0.02}N$ barrier layers. The four wells form the gain region.

The layers surrounding the MQW gain region minimise defects in the crystal and confine the carriers and stimulated photon emission. The buffer layer is 300 Å-thick of GaN. The 0.1 μm-thick n-type and p-type GaN layers directly above and below the MQWs are used for light guiding while the 0.5 μm thick n-type and p-type $Al_{0.08}Ga_{0.92}N$ layers act as cladding for confinement of the carriers and light from the active region. The mirror facets for the laser cavity were formed by etching due to difficulties in cleaving the (0001) C-face sapphire substrate. After polishing, the facet surface had a roughness of approximately 50 Å [5]. Three pairs of quarter-wave TiO_2/SiO_2 dielectric multilayers (70% reflecting) were used to reduce the threshold current. This work led to the first current-injection III-V Nitride diode laser demonstrating the lowest recorded wavelength generated from an electrically pumped semiconductor diode laser (417 nm) [6].

5.3 GaN Diode Laser in Extended-Cavity

The diode laser used for this work was a Nichia Corporation NLHV500 device, with the manufacturer's specifications giving a nominal CW output power of

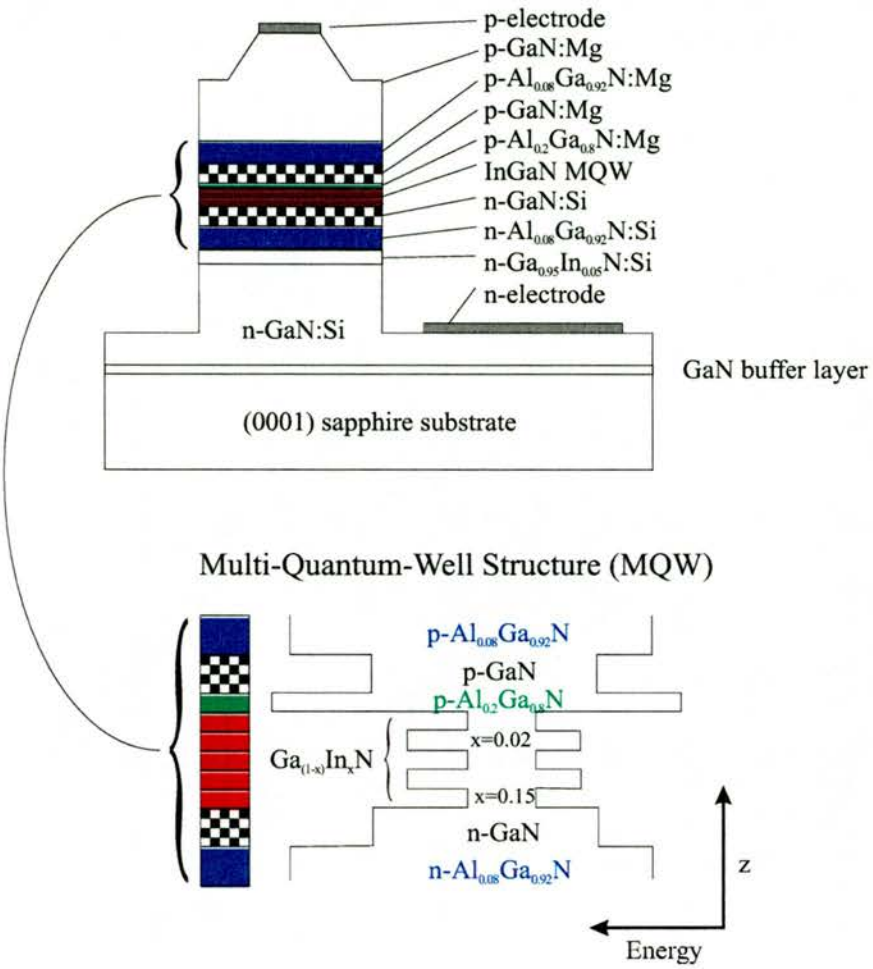

Figure 5.2: (Colour) A diagram showing the GaN layer arrangement in a Nichia diode laser and the MQW energy structure. Reproduced from [16].

5 mW at 393 nm[2]. The threshold current was measured to be 27 mA with a maximum operating current of 33 mA. The increased resistance of the semiconductor material dictated that a higher than normal operational voltage of 4.5 V was required when compared to red or near infrared diode lasers. The slope efficiency above threshold was 68%. Using a Fabry-Perot etalon, the output of the laser was measured to be composed of several longitudinal modes, which showed an average tuning rate of 16 GHz/mA.

[2]It is noted that at the time of writing, commercial diode lasers with output powers of 30 mW were available from the same source.

5.3.1 Current-Power Characteristics

The violet diode laser was placed in an extended-cavity configuration in the Littrow geometry. The design of which has been discussed extensively in Chapter 3 and is based upon a standard 25 mm mirror mount. The diode laser was placed in a collimating tube (Thorlabs LTP110B) and centred automatically with respect to the accompanying aspheric collimating optic. This tube was held in a holder attached to the main body of the mirror mount. The length of the extended-cavity was adjustable between 20 and 30 mm. This resulted in a low cost, compact, simple geometry which offered high performance [17]. This high-performance was attributed mainly to the stability and construction of the mirror mount. The performance of the violet ECDL was assessed with two gratings both having 2400 lines/mm. The reduction in the grating constant[3] compared to gratings used at red or infrared wavelengths allowed the zeroth order output to leave the grating at a sensible angle. One was blazed with 30% efficiency into the first order (HoloUV) and the other was 55% efficient (HoloVIS) both at 392 nm. The standard output characteristics of this laser operating with either grating are shown in Figure 5.3. The reflected first-order component provided the feedback necessary for the extended-cavity, with the output coupling provided by the zeroth-order reflection from the grating. It was expected that the cavity having the HoloVIS grating would give a lower slope efficiency than the HoloUV grating but with a wider tuning range due to the increased feedback accessing more of the gain spectrum of the diode laser. The front facet of the GaN diode was not anti-reflection (AR) coated, normally a hindrance for low power extended-cavity visible diode lasers [18], but, notably, this did not prevent good performance of this system. The collimating lens used was AR coated for 350-450 nm with less than 0.5% reflection and was not observed to cause etalon effects within the 20 mm-long extended-cavity.

From Figure 5.3 it can be seen that the HoloUV grating, with lower diffraction

[3]This is defined to be the distance between successive grooves on the grating. Theory on diffraction gratings can be found in Section 2.3.1.

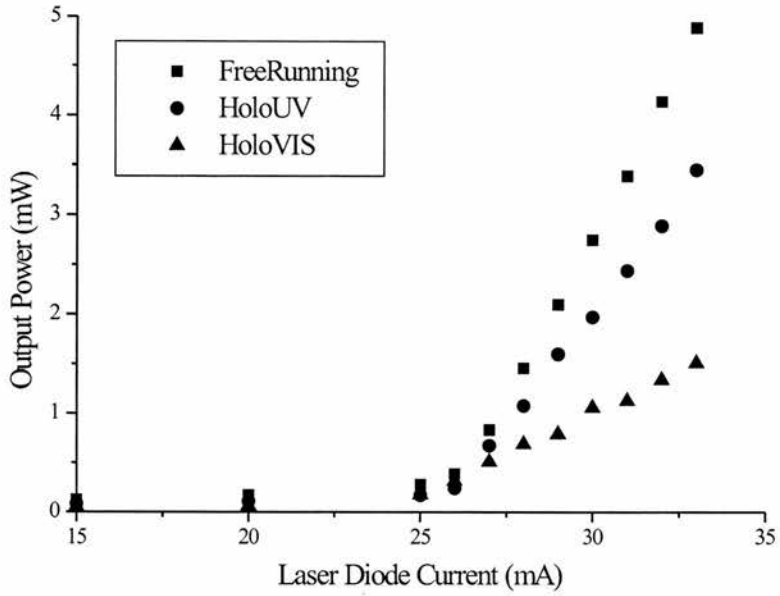

Figure 5.3: Output power of free-running and extended-cavity lasers as a function of drive current.

efficiency, gave a larger slope efficiency of 46%. A maximum of 3.5 mW of single frequency power was produced. The more efficient HoloVIS grating gave a reduced threshold but with a lower slope efficiency of 17%, thereby limiting the maximum available single frequency power to 1.5 mW.

5.3.2 Tuning Characteristics

The tuning range of the extended-cavity can be seen in Figure 5.4 as the angle and position of the mount holding the diffraction grating was changed manually. The HoloUV grating was limited to a tuning range of 1.3 nm, beyond which the diode no longer operated in a single axial mode. The greater feedback from the HoloVIS grating permitted a tuning range of 2.7 nm which approached the quoted value of 3 nm from a similar system commercialised by TuiOptics Ltd (Munich, Germany).

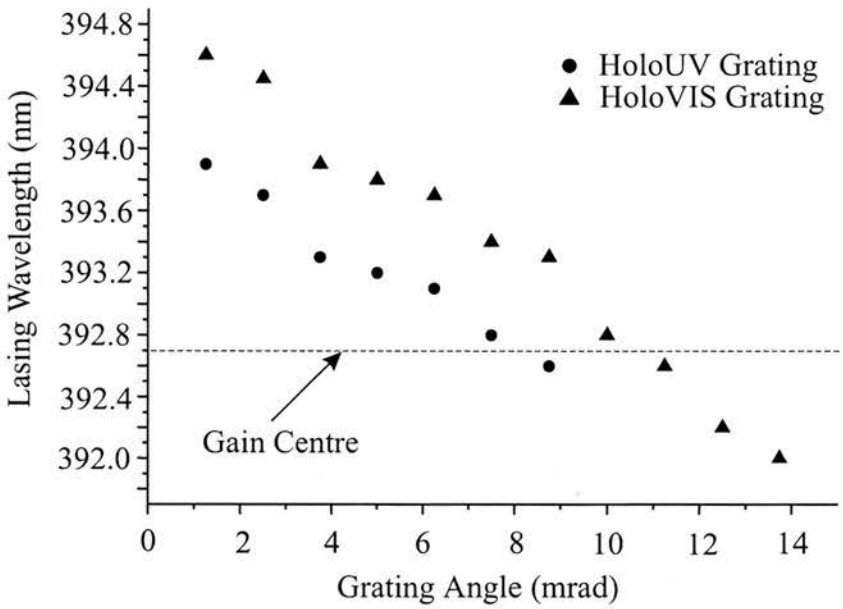

Figure 5.4: Discontinuous wavelength tuning of the GaN extended-cavity diode using both the HoloUV (circles) and HoloVIS (triangles) gratings. The gain centre of the free-running diode was 392.7 nm.

To compare this tuning behaviour, the compact ECDL configuration was operated with both a 635 nm (SDL-7501-G1) and 670 nm (Hitachi 6712G) diode laser. ECDLs in the red region of the visible spectrum are well established in high-resolution spectroscopy and as such set a benchmark against which this novel laser system can be compared. Both lasers were AR coated with a reflectivity of less than 0.001%. Data for discontinuous tuning of these devices had been recorded previously and it was found that tuning of up to 12 nm was possible in the compact geometry, see Figure 5.5.

The output could also be tuned continuously by means of a low voltage PZT element placed beneath the horizontal screw in the mirror mount to change the grating angle and its distance from the diode. For a voltage of 10 V peak-to-peak, the output could be tuned over 6 GHz without mode-hopping and this is sufficient for many high resolution spectroscopic purposes. With greater PZT extension, or concurrent grating and current tuning, greater continuous tuning ranges should be possible [19].

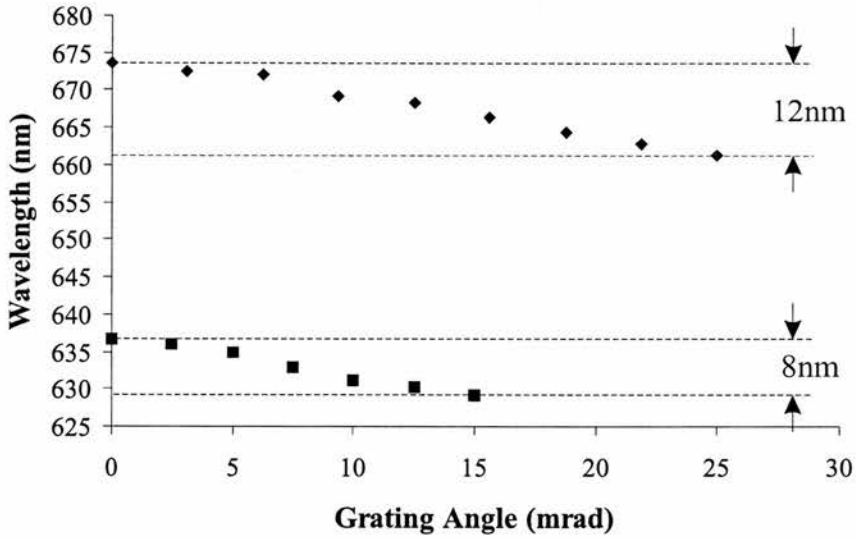

Figure 5.5: Discontinuous wavelength tuning graphs for both 670 nm and 635 nm diode lasers in an extended-cavity geometry. Note that the tuning range achieved is dramatically larger than that for the violet ECDL.

It was believed that this reduced tuning when compared to red and infrared diode lasers in similar geometries arose from compositional fluctuations within the InGaN wells. These manifest themselves in the form of self-forming indium-rich quantum dots during the MOCVD growth process. These dots have been verified experimentally using tunneling electron microscopy to be between 2 to 5 nm in diameter with an areal density of $\sim$ 5x10^{11} cm^{-2} [20]. Additionally, it was believed by the academic community that the light emission energy of these devices was largely determined by the indium fraction in the quantum well, however Kiesielowski [15] concluded that it was a confinement in the electronic states that governed the photon energy to a greater extent. It was also proposed recently by Chichibu *et al.* [21] that excitons play an important role in the lasing process at room temperature of $In_xGa_{1-x}N$ MQWs. Moreover, these excitons have been thought to be localised at deep traps in the quantum well structure. The role of excitons and their locality dependence has been confirmed experimentally by measuring the Stokes shift between excitation and emission in InGaN MQW structures [22]. The measured shifts were as large as 100 meV to 250 meV at room

temperature. At present it is considered that the main radiative recombination is attributable to excitons localised at the In-rich regions in the well acting as quantum dots. Subsequently, these localised excitons cause locally-enhanced carrier radiative recombination and an increase of the inhomogeneous spontaneous emission linewidth below the lasing threshold. Particular spatial regions therefore contribute to specific spectral regions. During tuning, the different spectral regions become dominant in turn and this produces the observed jumps in wavelength. These compositional fluctuations are believed to limit the discontinuous tuning of the violet ECDL and give rise to discontinuities in the gain spectrum causing wavelength jumps in the coarse tuning of the ECDL. Notably, wavelength jumps of about 0.4 nm have been reported by Nakamura and Fasol [23] for current tuning of the single-mode emission of free-running InGaN MQW laser. This behaviour is in contrast to that of near-infrared or red diode lasers in which strong compositional fluctuations do not arise. The limited discontinuous tuning of GaN diode lasers in an extended-cavity is thus a disadvantage in their use for high-resolution spectroscopy. In any experiment, therefore, a judicious choice of violet device must be made to ensure access to the desired wavelength range.

5.3.3 Linewidth Characteristics

A scanning etalon was constructed to determine the laser linewidth. The measured linewidth was 5 MHz which was at the practical limit of available mirrors, see Figure 5.6. It was believed that the instantaneous linewidth of the laser was in the region of 1 MHz, as reported for the commercial system developed recently [1] and for visible diode lasers running extended-cavity [7]. The stability of the laser was better than 20 MHz over five minutes with no pronounced drift.

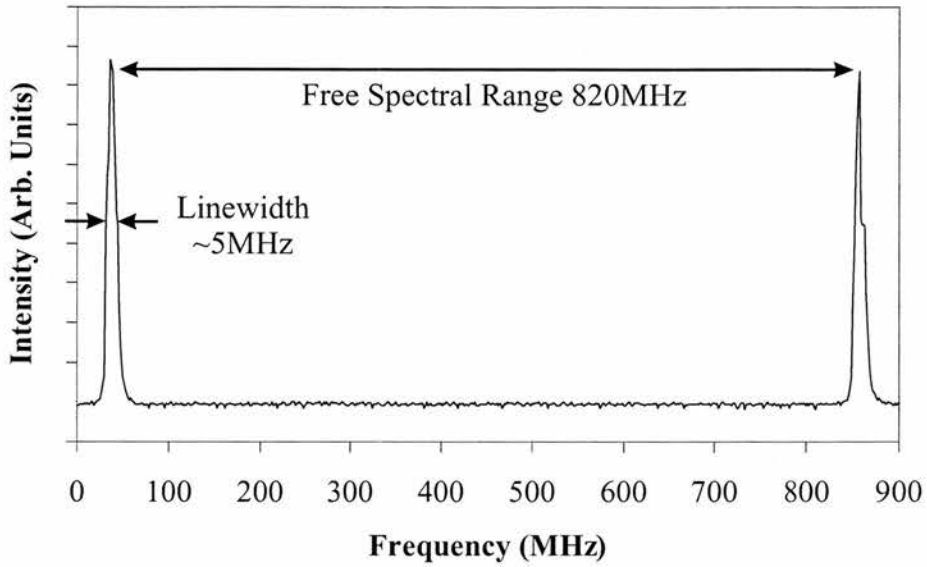

Figure 5.6: A measurement of the linewidth of the GaN ECDL using a home-built Fabry-Perot etalon. The etalon had a FSR of 820 MHz and a finesse of around 200. The upper limit on the linewidth is measured to be 5 MHz with this value being instrument limited.

5.4 Conclusions

A commercially available Nichia diode laser, placed in an extended-cavity, has been characterised. Either 3.5 or 1.5 mW of tuneable, single frequency light was extracted depending on the particular reflective grating used in the system. An upper limit to the linewidth of 5 MHz was measured for the laser. The emitted wavelength, centred around 392 nm, was tuneable continuously over 6 GHz and discontinuously over 2.7 nm. The tunability of a GaN-based extended-cavity diode laser was less than observed for red and near-infrared diode lasers in the same geometry and it was believed this was due to compositional fluctuations of the indium content within the MQW structure. If such a violet laser was to be used at a specific wavelength, for example in high-resolution spectroscopy, then a considered choice of diode must be made to ensure that the region of interest can be accessed by the extended-cavity. This is not true in the case of longer wavelength diodes in the visible and near-infrared, where it has been possible to force

several diode lasers, some with their gain centre several nanometres away from the region of interest, to the desired wavelength. Even with this initial inconvenience in having to choose a tailored laser, the ability to scan the frequency of this laser with ease makes it attractive for a number of spectroscopic applications. With a suitable choice of violet diode, for example, it would be possible to laser cool Ca^+ ions at 397 nm, which are of direct interest in quantum computing [24]. The ECDL established during this research can access the strong Al transition at 394.4 nm, which can be used to monitor vapour concentrations of aluminium [25]. Free-running GaN-based lasers are already being used in practical applications, such as tumour identification and demarcation for types of skin cancer [26].

Looking to the future, it is clear that the next few years will reveal much about the physics behind GaN light emitters. Reliable working examples of devices in this field have only been commercialised in the past 4 years. As alluded to in this chapter, much vital information is still not known about the devices and the details behind their operation. Indeed, Nichia Chemical Industries Ltd. are currently the sole manufacturer and supplier to the world's blue/violet diode laser marketplace highlighting the requirement for understanding of how these semiconductors operate in detail. Here, characterisation of a diode laser in the Littrow geometry was conducted and no attempt was made at investigating the Littman geometry. This would be an obvious step to take in the future. Using UV designed optics and gratings would improve output power but would also result in a reduction in tuning. An additional interesting investigation would be to obtain a diode laser with an AR coating on its front facet. AR coated lasers in the red or near infrared have delivered larger tuning ranges when compared to their uncoated counterparts and whether this would hold true at near-UV wavelengths is an unclear and intriguing question.

Bibliography

[1] S. Nakamura and W. Kaenders, "Market-ready blue diodes excite spectroscopists," Laser Focus World pp. 69–75 (1999).

[2] D. B. Eason, Z. Yu, W. C. Hughes, W. H. Roland, C. Boney, J. J. W. Cook, and J. F. Schetzina, "High-brightness blue and green light-emitting diodes," Applied Physics Letters **66,** 115–117 (1995).

[3] W. Xie, D. C. Grillo, R. L. Gunshor, M. Kobayashi, H. Jeon, J. Ding, A. V. Nurmikko, G. C. Hua, and N. Otsuka, "Room temperature blue light emitting *p-n* diodes from Zn(S,Se)-based multiple quantum well structures," Applied Physics Letters **60,** 1999–2001 (1992).

[4] D. M. Bagnall, Y. F. Chen, Z. Zhu, T. Yao, S. Koyama, M. Y. Shen, and T. Goto, "Optically pumped lasing of ZnO at room temperature," Applied Physics Letters **70,** 2230–2232 (1997).

[5] S. Nakamura, M. Senoh, S. Nagahama, N. Iwasa, T. Yamada, T. Matsushita, H. Kiyoku, and Y. Sugimoto, "Characteristics of InGaN multi-quantum-well-structure laser diodes," Applied Physics Letters **68,** 3269–3271 (1996).

[6] S. Nakamura, M. Senoh, S. Nagahama, N. I. abd T. Yamada, T. Matsushita, H. Kiyoku, and Y. Sugimoto, "InGaN-Based Multi-Quantum-Well-Structure Laser Diodes," Japanese Journal of Applied Physics **35,** L74–L76 (1996).

[7] L. Ricci, M. Weidemüller, T. Esslinger, A. Hemmerich, C. Zimmermann, V. Vuletic, W. König, and T. Hänsch, "A compact grating-stabilized diode laser system for atomic physics," Optics Communications **117,** 541–549 (1995).

[8] J. Alnis, U. Gustafsson, G. Somesfalean, and S. Svanberg, "Sum-frequency generation with a blue diode laser for mercury spectroscopy at 254 nm," Applied Physics Letters **76,** 1234–1236 (2000).

[9] U. Gustafsson, J. Alnis, and S. Svanberg, "Atomic spectroscopy with violet laser diodes," American Journal of Physics **68,** 660–664 (2000).

[10] H. Leinen, D. G. ner, H. Metcalf, R. Wynands, D. Haubrich, and D. Meschede, "GaN blue diode lasers: a spectroscopist's view," Applied Physics B **70,** 567–571 (2000).

[11] S. Nakamura, M. Senoh, S. Nagahama, N. Iwasa, T. Yamada, T. Matsushita, H. Kiyoku, and Y. Sugimoto, "InGaN multi-quantum-well structure laser diodes grown on $MgAl_2O_4$ substrates," Applied Physics Letters **68,** 2105–2107 (1996).

[12] S. Shionoya and W. M. Yen, "Phosphor Handbook," pp. 293–306 (1998).

[13] H. Amano, M. Kito, K. Hiramatsu, and I. Akasaki, "P-Type Conduction in Mg-Doped GaN Treated with Low-Energy Electron Beam Irradiation (LEEBI)," Japanese Journal of Applied Physics **12,** L2112–L2114 (1989).

[14] S. Nakamura, T. Mukai, M. Senoh, and N. Iwasa, "Thermal Annealing Effects on P-Type Mg-Doped GaN Films," Japanese Journal of Applied Physics **31,** L139–L142 (1992).

[15] C. Kisielowski, "paper We-01 - Composition and Strain Fluctuations in InN/GaN/AlN Heterostructures: A Microscopic Glimpse below Surfaces," 2nd International Symposium on Blue Laser and Light Emitting Diodes, Chiba, Japan pp. 321–326 (1998).

[16] B. Gil, *Group III nitride semiconductor compounds, physics and applications* (Oxford Science Publications, Oxford University Press, Great Clarendon Street, Oxford OX2 6DP, 1998).

[17] M. A. Clifford, J. Arlt, J. Courtial, and K. Dholakia, "High-order Laguerre-Gaussian laser modes for the studies of cold atoms," Optics Communications **156,** 300–306 (1998).

[18] M. G. Boshier, D. Berkeland, E. A. Hinds, and V. Sandoghdar, "External-cavity frequency-stabilization of visible and infrared semiconductor lasers for high resolution spectroscopy," Optics Communications **85,** 355–359 (1991).

[19] T. Nayuki, T. Fujii, K. Nemoto, M. Kozuma, M. Kourogi, and M. Ohtsu, "Continuous Wavelength Sweep of External Cavity 630 nm Laser Diode without Antireflection Coating on Output Facet," Optical Review **5,** 267–270 (1998).

[20] Y. Narukawa, Y. Kawakami, M. Funato, S. Fujita, S. Fujita, and S. Nakamura, "Role of self-formed InGaN quantum dots for exciton localization in the purple laser diode emitting at 420 nm," Applied Physics Letters **70,** 981–983 (1997).

[21] S. Chichibu, T. Azuhata, T. Sota, and S. Nakamura, "Spontaneaous emission of localized excitons in InGaN single and multiquantum well structures," Applied Physics Letters **69,** 4188–4190 (1996).

[22] Y. Narukawa, Y. Kawakami, S. Fujita, S. Fujita, and S. Nakamura, "Recombination dynamics of localized excitons in $In_{0.20}Ga_{0.80}N$-$In_{0.05}Ga_{0.95}N$ multiple quantum wells," Physical Review B **55,** R1938–R1941 (1997).

[23] S. Nakamura and G. Fasol, *The blue laser diode* (Springer-Verlag, 1997).

[24] H. C. Nägerl, W. Bechter, J. Eschner, F. Schmidt-Kaler, and R. Blatt, "Ion strings for quantum gates," Applied Physics B **66,** 603–608 (1998).

[25] W. Wang, M. M. Fejer, R. H. Hammond, M. R. Beasley, C. H. Ahn, M. L. Bortz, and T. Day, "Atomic absorption monitor for deposition process control of aluminium at 394 nm using frequency-doubled diode laser," Applied Physics Letters **68,** 729–731 (1996).

[26] U. Gustafsson, S. P. lsson, and S. Svanberg, "Compact fiber-optic fluorosensor using a continuous-wave violet diode laser and an integrated spectrometer," Review of Scientific Instruments **71,** 3004–3006 (2000).

Chapter 6

Laser Cooling and Atom Trapping Theory

6.1 Introduction

In this chapter, the important concepts of how light can be used to cool and spatially confine an atomic vapour are introduced. A brief historical overview of the origins of the light-matter interaction is presented. The techniques for slowing atomic beams and subsequently those for cooling and trapping neutral atoms are discussed. The field of laser cooling and atom trapping has expanded considerably since its conception in the mid 1980s and is now of such size that it would be inappropriate to recount every aspect of the field in this thesis. Rather, an overview of relevant concepts and theory aiding in the understanding of work presented in the experimental chapters is given.

6.1.1 Temperature

In thermodynamics, temperature is carefully defined as a parameter of the state of a closed system in thermal equilibrium with its surroundings. This requires that

there is heat exchange between the entity whose temperature is being considered and the environment. This is not the case in laser cooling where atoms are continually absorbing and emitting photons with their ambience. This exchange is not of heat but energy and so the system cannot be considered to be at thermal equilibrium although it may be in a steady state condition. Hence, the assignment of a thermodynamic "temperature" is misplaced. Nevertheless, it is convenient to use the label of temperature for an ensemble of atoms with a well defined velocity distribution whose average kinetic energy, $\langle E_k \rangle$, in one dimension is written as,

$$\langle E_k \rangle = \frac{1}{2} k_B T, \tag{6.1}$$

where k_B is Boltzmann's constant and T is the temperature. Using this definition, Figure 6.1 shows the power of laser cooling techniques when used to cool atomic vapour samples in relation to some well known and familiar thermodynamic temperatures. A linear path is drawn from Edinburgh (0 K) to London (300 K) indicating a linear temperature scale. Along that path points are indicated, in distance from Edinburgh, corresponding to temperatures of various physical systems. It provides an intuitive feel for "temperatures" that can be achieved by the techniques described in this chapter.

6.1.2 Historical Background

It was speculated as early as the seventeenth century that light could exert a pressure on matter. The astronomer Johannes Kepler postulated that the tails of comets pointed directly away from the sun as a result of light pressure, stimulating further work in understanding the effects of light on matter. It was not until James Clark Maxwell formulated his electromagnetic theory of light in 1873 that a suitable theoretical explanation was established. His theory predicted that an electromagnetic field would exert a force, albeit a tiny one, on matter. The next important step in the understanding of the force light could exert, named

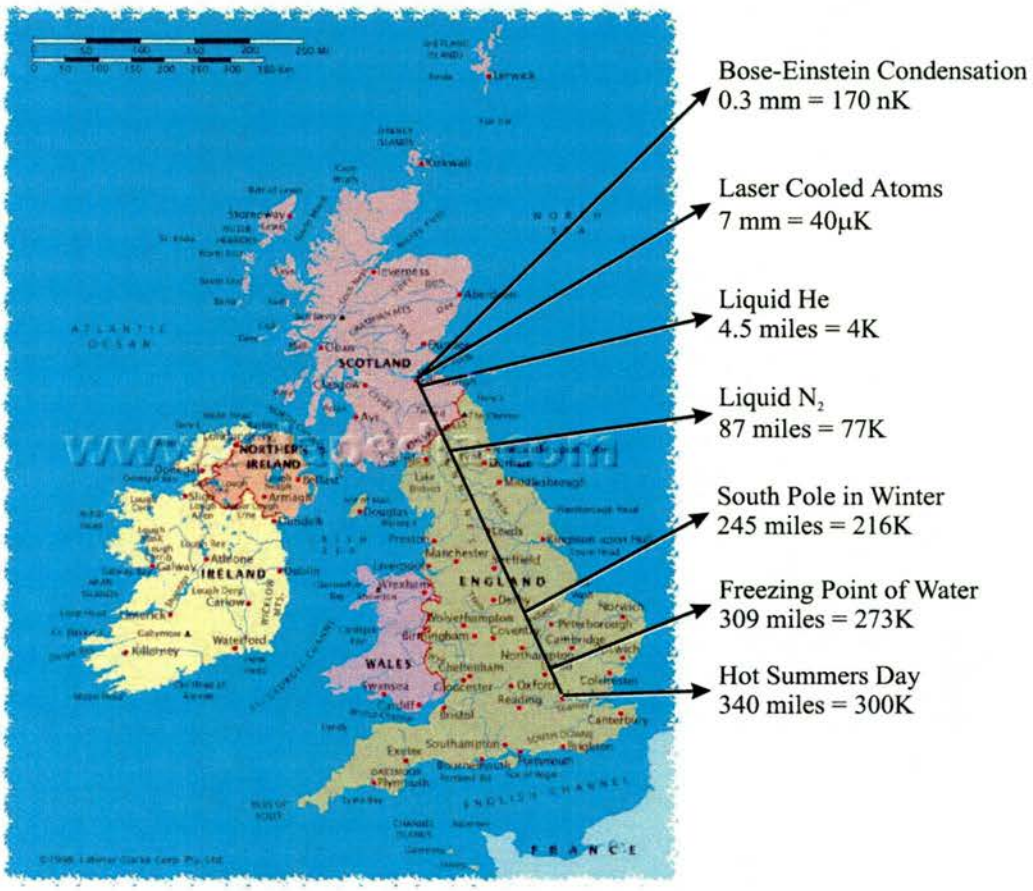

Figure 6.1: (Colour) A map of the UK showing various temperatures measured in distance from the centre of Edinburgh. A line is drawn from Edinburgh to London representing a linear temperature scale with the Scottish capital denoting 0 K while the UK capital denotes 300 K.

the *radiation pressure force*, came with the formulation of quantum theory and the associated quantum mechanical view of light. It was Einstein in 1916 who showed that a quantum of light, or photon, with energy $h\nu$, carries a momentum $h\nu/c$, where h is Planck's constant, ν and c are the frequency and speed of the light respectively [1][1]. The underlying mechanism of radiation pressure is the conservation of momentum during the absorption and emission of photons. A number of years after the theory was formulated, an experiment was conducted which not only showed the quantum nature of light, but also the conservation of momentum in interactions between light and matter. In 1923, Compton observed

[1] A translation of this paper into English can be found in "Sources of Quantum Mechanics" by B. L. Van Der Waerden, North-Holland Publishing Company, Holland, pages 63–77.

the reduction in energy of high-energy photons (X–rays or γ–rays) when scattered by free electrons [2]. He found that photons imparted some of their momentum to the electrons and after scattering, their wavelengths were measured to be longer. The momentum lost from the photon had been imparted to the recoiling electron.

If an atom absorbs a photon, a similar recoil occurs although on a far smaller scale (because of the greater mass of the atom). The first laboratory based experiment to observe radiation pressure on an atomic system was conducted in 1933 by Frisch [3]. In this experiment, a thermal beam of sodium atoms was illuminated from one side by light emitted from a sodium lamp. The photon absorption resulted in a detectable deflection of the atomic beam away from the lamp. It became possible, with time, to observe an increased deflection using narrow linewidth tuneable lasers to enhance the number of absorption-emission cycles within the experimental interaction time [4, 5].

6.2 Primary Cooling Mechanisms

6.2.1 Radiation Pressure Force

In 1970 Ashkin performed preliminary work on the trapping of microscopic particles under the action of the radiation pressure force [6]. Within this initial work, he showed that the radiation pressure force produced by a laser resonant with a strong optical transition in an atom could be formulated mathematically as [7]:

$$F = \frac{\Delta p}{\Delta t} = \frac{\hbar \mathbf{k}}{\tau / f}, \tag{6.2}$$

where $\hbar\mathbf{k}$ is the photon momentum directed along the propagation direction of the light ($\hbar = h/2\pi$ and the wave vector, $\mathbf{k} = 2\pi/\lambda$), τ is the natural lifetime of the excited state, f is the normalised time an atom spends in the excited state and λ is the wavelength of light. The process by which an atom absorbs and then

spontaneously emits a photon is known as the *cooling cycle.*

6.2.2 The Cooling Cycle

If an atom with mass m absorbs a photon with energy $h\nu$, then this quanta of energy will be used to place that atom in an excited state. The atom will also experience a recoil in the same direction to that in which the photon was travelling and as a direct result, the atom experiences a velocity change δv, equal to $\hbar\mathbf{k}/m$. After a characteristic time related to the particular excited state, the atom will de-excite by spontaneously emitting a photon. Because of the conservation of momentum, the atom will experience a second recoil, this time in the opposite direction to which the photon leaves the atom. As spontaneous emission is a random process, the departing photon leaves with no preferred direction over 4π steradians. The atom is then free to absorb another photon of the same energy. The net effect on the motion of the atom is zero when averaged over many absorption-spontaneous emission cycles. In this way, an atom can be accelerated or slowed in one particular direction using light. Figure 6.2 shows how an atom, on average, changes its velocity during one such cycle.

It is important to note that for this technique to work successfully, the atomic transition must be *closed i.e.* a transition where spontaneous emission will always return the atom to the initial ground state level. For efficient cooling, the photon energy must be resonant, or precisely equal to the energy difference between the ground and excited states. However, in reality due to the finite linewidth of cooling lasers used in experiments, off-resonant light allows the possibility that the atom may be raised to a different excited state. Spontaneous emission then confines the atom to a different ground state, terminating the absorption process. A solution to this problem is to use a second laser, called a hyperfine pumping laser, to re-introduce the atom to the cooling cycle by raising it to the excited state of the cooling cycle transition once more where it decays to the correct ground state.

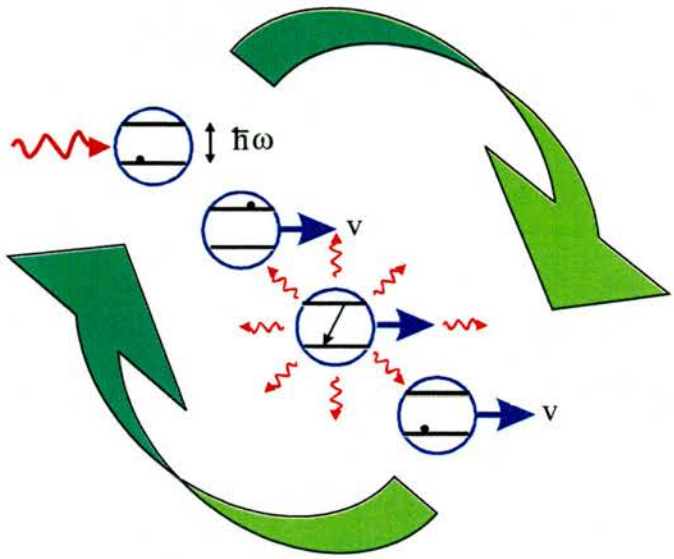

Figure 6.2: (Colour) An atom at rest with an internal energy difference of $\hbar\omega$ has a photon incident on it with energy equal to this. The atom absorbs the photon and is raised to an excited state whilst also receiving a momentum kick equal to $\hbar\mathbf{k}$, causing it to recoil with a velocity, v. The atom spontaneously emits the photon in a direction described by a symmetric probability distribution. Averaging this over several absorption-emission cycles, the net effect on the atom's motion over this part of the cycle is zero. The atom is now in the ground state but is moving with a velocity, v, and can start the cycle again. By inverting this scenario, the atom's kinetic energy can be reduced rather than increased.

6.2.3 Slowing of an Atomic Beam

The first experiments utilizing the radiation pressure force via the cooling cycle was to slow an atomic beam and were conducted in the 1980s. In this scenario, a laser beam tuned below an atomic transition was propagated in the opposite direction to the path of a thermal atomic beam. Absorbed photons slowed the atoms in the beam by imparting their momenta via the cooling cycle. In order to reduce the longitudinal velocity of the atoms from their initial velocities of approximately 10^3 m s^{-1} to near zero, approximately 30,000 photon collisions per atom were required. However, as the atom slowed down, the Doppler shift changed and the laser was tuned effectively out of resonance. In an attempt to overcome this problem a number of solutions were implemented including spatially varying magnetic fields [8], varying the laser frequency or *frequency chirping* [9] or using

broadband spectral sources [10]. A diagram of the first experimental apparatus utilizing light and spatially varying magnetic fields is shown in Figure 6.3. As the atoms are slowed within the solenoid, the changing Doppler shift is exactly compensated for by a Zeeman shift induced on the transition frequency. A source of slow atoms moving with a mean velocity of $\sim$40 m s^{-1} and a spread of 10 m s^{-1} could be obtained [11]. Further work led to the complete stopping of an atomic beam [12].

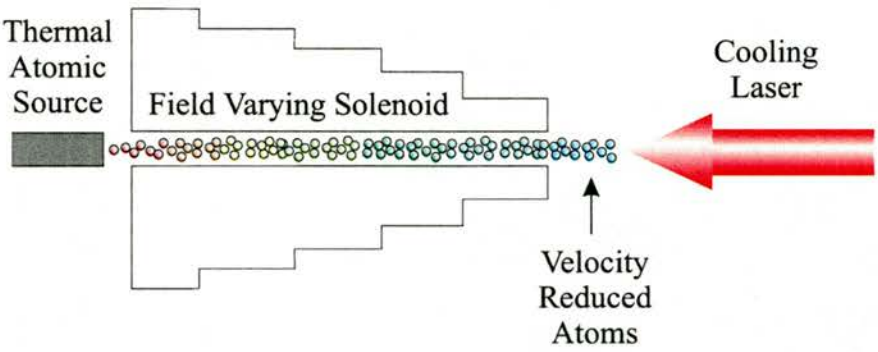

Figure 6.3: (Colour) Functional diagram for Zeeman slowing of a thermal atomic beam. The constantly varying magnetic field compensates for the changing Doppler shift experienced by the slowing atoms. A slow atomic beam is generated at the end of the solenoid.

6.2.4 Doppler Cooling

Although the experiments utilizing spatially varying magnetic fields reduced the velocity spread and mean velocity of the thermal atoms in one dimension, it was not, strictly speaking, cooling. In 1975 two independent proposals that photons could be used to cool particles in three dimensions came from Hänsch and Schawlow [13] with respect to neutral atoms and Wineland and Dehmelt [14] with respect to trapped ions. Their suggestions were to illuminate an ensemble of atoms (or ions) from all directions with light tuned slightly below the atomic resonance frequency. Atoms that were moving towards an oncoming laser beam would be Doppler shifted and preferentially absorb from that beam rather than from a counter-propagating laser beam. Thus, regardless of the direction of mo-

tion of the atom, its kinetic energy would be reduced. Because this technique relies on the Doppler effect, it has been named *Doppler cooling.* A diagram illustrating one dimensional Doppler cooling is shown in Figure 6.4.

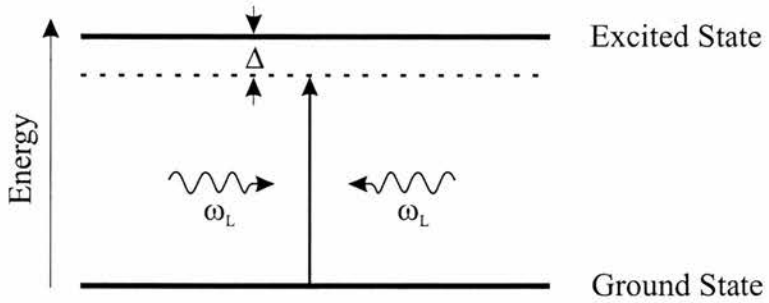

Figure 6.4: One dimensional Doppler cooling. The laser frequency is detuned by a frequency Δ below the atomic resonance. The two counter–propagating beams cause a viscous cooling force around $v = 0$.

The treatment of the atomic motion can be considered classically despite the cooling process being quantum mechanical in nature, as indicated by the discrete momentum jumps. If two opposing beams are treated as independent to each other, then a time averaged interaction can be calculated. This results in a mean cooling term from spontaneous emission and a diffusive term, represented in Equation 6.3 by the first and second terms respectively [15],

$$\begin{aligned} F &= \hbar k \frac{\Gamma}{2} \left[\frac{I/I_{sat}}{4(\Delta + kv)^2/\Gamma^2 + (1 + I/I_{sat})} \right] \\ &- \hbar k \frac{\Gamma}{2} \left[\frac{I/I_{sat}}{4(\Delta - kv)^2/\Gamma^2 + (1 + I/I_{sat})} \right], \end{aligned} \tag{6.3}$$

where $\Gamma = 2\pi \times 6.1\text{MHz}$ is the natural linewidth of the transition, I is the intensity of each beam, $I_{sat} = \pi hc/3\lambda^3\tau$ [16] is the saturation intensity and $\Delta = \omega_{laser} - \omega_0$ is the frequency detuning of the laser from resonance. This produces a force given by Equation 6.4 that varies linearly with velocity near $v = o$ over a velocity capture range as indicated in Figure 6.5. The velocity capture range defines a range of velocities over which the atomic motion is damped effectively.

$$F = -\alpha v, \tag{6.4}$$

where,

$$\alpha = -4\hbar k^2 \frac{I}{I_{sat}} \frac{2\Delta/\Gamma}{\left[4\Delta^2/\Gamma^2 + (1 + I/I_{sat})\right]^2} \tag{6.5}$$

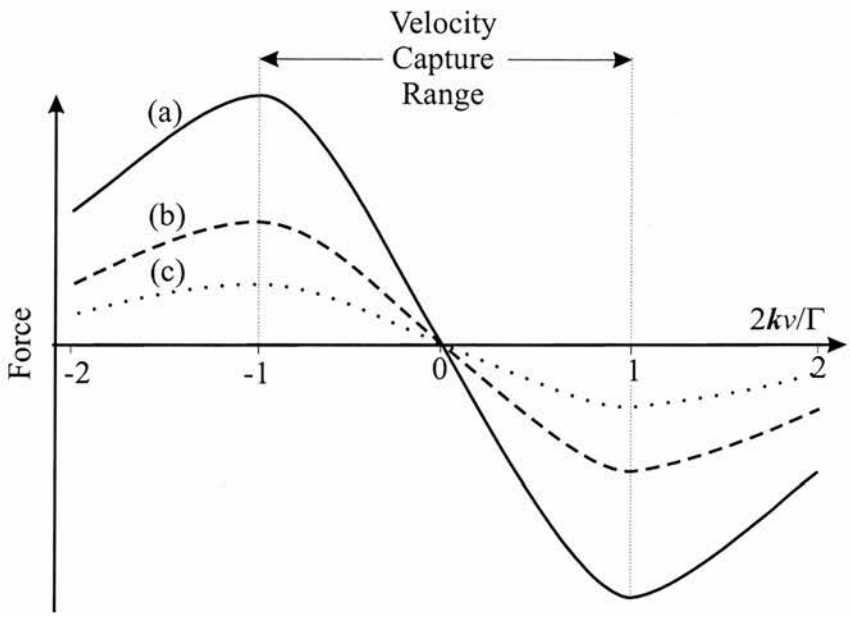

Figure 6.5: The damping force in Doppler cooling. The horizontal axis is normalized atomic velocities where **k** is the wavevector of the laser beams and Γ is the natural linewidth of the atomic transition. Curves are shown for (a) an arbitrary intensity I, (b) $I/2$ and (c) $I/4$. The velocity capture range does not change with intensity, however the viscous cooling force (given by the slope of the curve) increases with increasing intensity.

α is greater than zero for red-detuning of the laser and is referred to as the *friction coefficient.* It is also noted from Figure 6.5 that the friction coefficient is proportional to intensity while the velocity capture range remains independent of intensity. The atomic motion is damped exponentially around $v = 0$ and exhibits similar properties to that of an atom in a viscous medium. The atoms never become completely stationary due to the limiting absorption and spontaneous emission characteristics, however an equilibrium is reached when

the viscous forces equal the diffusion, or heating, forces. Because the velocity of the atoms determine their temperature, an equilibrium temperature is reached as represented by Equation 6.6 [17],

$$k_B T = -\frac{(1+\xi)}{8}\hbar\Gamma\left[\frac{2\Delta}{\Gamma} + \frac{\Gamma}{2\Delta}\left(1 + \frac{2I}{I_{sat}}\right)\right], \tag{6.6}$$

where k_B is Boltzmann's constant, T is the temperature and ξ is a fraction less than 1 determined by the angular distribution of spontaneous emission for a particular transition. For $I \ll I_{sat}$ the minimum temperature is given by Equation 6.7 [18],

$$T_{min} = \frac{\hbar\Gamma}{2k_B}\left(\frac{1+\xi}{2}\right), \tag{6.7}$$

when $\Delta = -\Gamma/2$.

Extrapolation of one dimensional cooling into three dimensions is straightforward using three pairs of mutually orthogonal laser beams converging towards a common centre. The first experiment using this configuration was reported by Chu and co-workers [19] who cooled sodium atoms optically to a temperature of approximately 240 μK. The atoms were subjected to a force opposing their motion regardless of the direction in which they travelled. The phrase *optical molasses* [20] resulted for this regime since it appears that the atoms are confined within a fluid that has the viscosity of molasses or syrup. It is worth noting that this regime is not a trap as the atoms are still free to move, albeit slowly, and if they reach the edge of the laser overlap region then they can escape.

6.3 Further Cooling Mechanisms

Soon after the first optical molasses and atom trapping experiments were conducted, it was observed that the measured atomic temperature was significantly

less than expected from Doppler cooling theory defined by Equation 6.7. There was limited understanding of this phenomenon at the time, even some sighs of disbelief due to the attractive simplicity of Doppler cooling theory and the fact that experiments almost never work better than that predicted by theory! A number of experiments were conducted to verify the low temperatures being measured and a new theory called *sub-Doppler cooling* was unveiled in 1988 by way of explanation and is described in the following section.

6.3.1 Sub-Doppler Cooling

Doppler cooling relied on two independent assumptions. These assumptions required to be investigated and modified in order to correctly explain the newly observed low temperature phenomenon. The first essential step was to revise the opinion that atoms are simple two level systems. The second was that the light was a pure state of polarisation void of interference effects. An atom within a light field undergoes two interactions. The first producing an a.c.–Stark shift in the atomic energy levels and the second, an ability to transfer atoms from one degenerate sub-level to another by way of *optical pumping*. The interference effects produce, what are referred to as, *polarisation gradients*. Details of these two latter phenomena are now discussed.

Polarisation Gradients and Optical Pumping

Interference is present between the cooling beams within the optical overlap region at the centre of a MOT. If this is considered in one dimension then a situation similar to that shown in Figure 6.6 is obtained. Counter-propagating beams with linear but orthogonal polarisations produce a field whose polarisation changes rapidly over one wavelength of the light thereby creating large polarisation gradients. Now consider an atom with sublevels as shown in Figure 6.7. The numbers marked in the figure overlapping the lines denote relative transition probabilities.

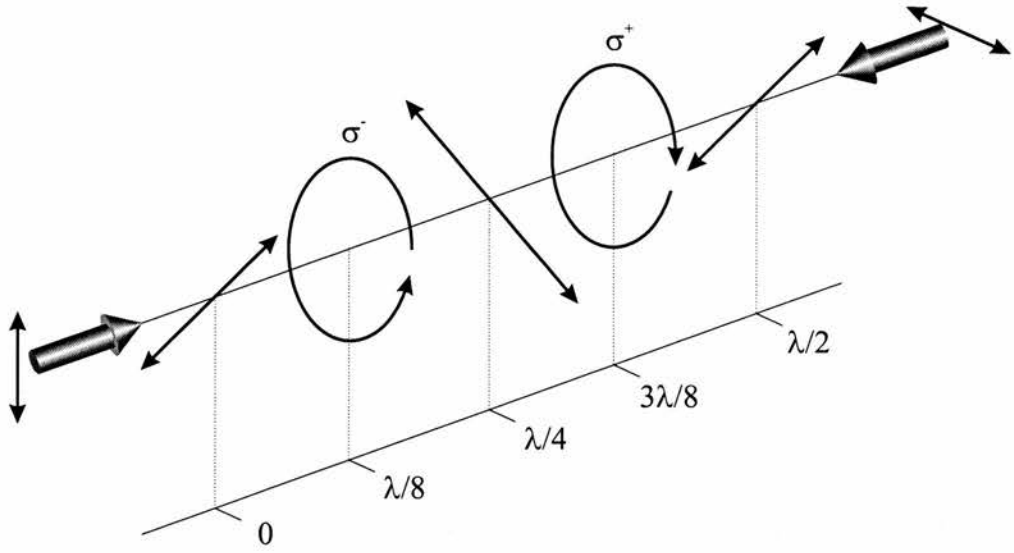

Figure 6.6: Two counter-propagating linearly polarised laser beams produce a field whose polarisation changes every eighth of a wavelength between linearly polarised and circularly polarised.

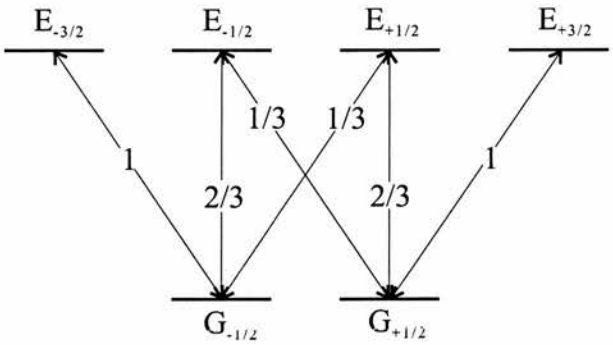

Figure 6.7: The energy levels for an atom in a polarisation gradient. The numbers sitting on top of the lines joining the ground and excited states indicate the relative transition probabilities. E_{m_J} and G_{m_J} represent excited and ground states with total angular momentum, m_J, respectively.

E_{m_J} and G_{m_J} describe excited and ground states of the atom with total angular momentum, m_J respectively. σ^+ and σ^- denote righthand and lefthand circularly polarised light respectively. If the atom is in the ground state, $G_{+1/2}$, with σ^- present then the atom can be pumped through the selection rule $\Delta m_J = -1$, to the excited state, $E_{-1/2}$. Spontaneous de-excitation occurs to the ground state $G_{-1/2}$ or back to $G_{+1/2}$ with probabilities 2/3 and 1/3 respectively. Hence, there is a higher probability of the atom decaying to the $G_{-1/2}$ state than the $G_{+1/2}$. However, if the atom returns to $G_{+1/2}$ then it has a further opportunity to reach the $G_{-1/2}$ with the next stimulated absorption of a photon. From the ground state $G_{-1/2}$, the atom can only be excited to the $E_{-3/2}$ state which can only de-excite back to the $G_{-1/2}$ ground state. It follows that, in the steady state, an atom irradiated with suitably tuned light with σ^- polarisation will be optically pumped into the $G_{-1/2}$ ground state. In a similar fashion, σ^+ polarised light incident on an atom will pumped it into the $G_{+1/2}$ ground state. Therefore an atom present in a light field can be in different ground states depending on the polarisation of the incident light.

Sisyphus Cooling

If we combine the three effects mentioned i.e., the light shifts in atomic energy levels, polarisation gradients and optical pumping then a mechanism can transpire allowing the Doppler cooling limit to be exceeded. The corresponding light shifts that the ground state experiences in conjunction with the effects of optical pumping with displacement along the direction defined by the path of the laser beams, z, are shown in Figure 6.8.

The populations and ground state energies of atoms are strongly related to position along the z direction due to the polarisation gradient. Now consider an atom moving along the z direction. Let us begin where the polarisation is σ^-. If an atom remains in the $G_{-1/2}$ sub–level and meanwhile travels to where the polarisation is σ^+ then it will have climbed a potential "hill" and lost energy. At

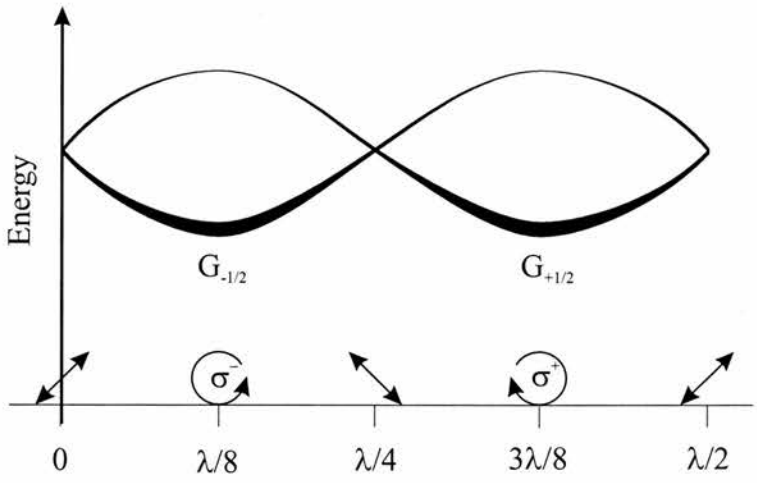

Figure 6.8: The light induced energy shifts of the ground state of an atom placed in the polarisation gradient. The energy and populations vary with polarisation, and therefore position along the z axis. The ground state populations are shown proportional to the thickness of each line.

the top of the "hill" it has a high probability, due to optical pumping effects, that it will be pumped to the bottom of the potential "valley" where the process can then be repeated. A possible path of such an atom is shown in Figure 6.9. One form of polarisation gradient cooling is named *Sisyphus cooling*, after Sisyphus in Greek mythology who, after betraying the secrets of the gods, was condemned to roll a block of stone up a hill, which tumbles down when he reaches the top. The whole process starts again, confining him to this labour for all eternity. The cooling mechanism is most effective when the atom travels a distance of one quarter of one optical wavelength in the average time it takes to be optically pumped to a new ground state. Although this theory was formulated in one dimension, it accounted for many of the features observed in three dimensional optical molasses.

Mathematically the friction coefficient for polarisation gradient cooling can be expressed as [17],

$$\alpha_p = -\frac{24}{17}\hbar\mathbf{k}^2\frac{\Delta}{\Gamma}\frac{1}{4(\Delta/\Gamma)^2+1} \tag{6.8}$$

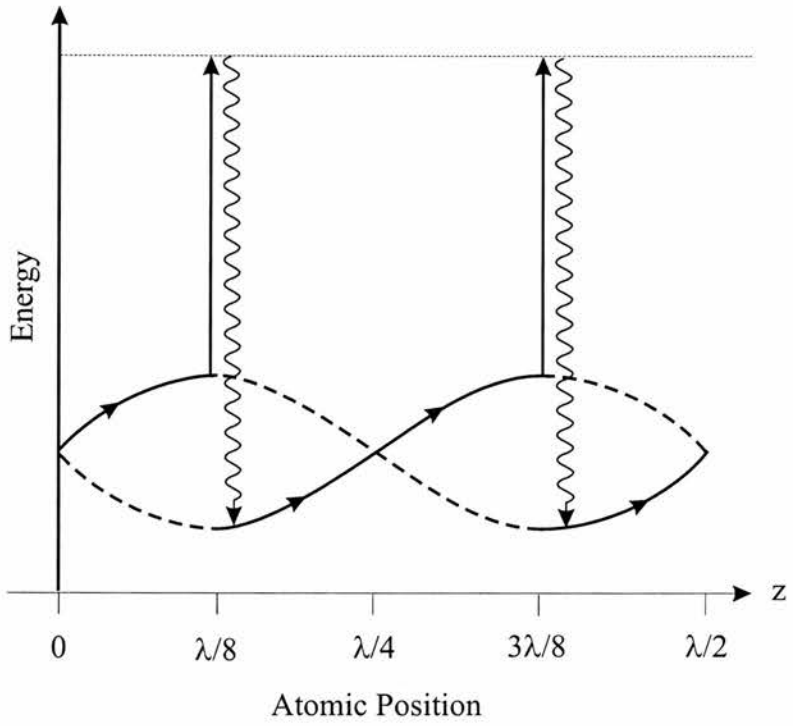

Figure 6.9: Sisyphus cooling in one dimension. An atom moving in a field described by Figure 6.6 experiences a potential hill when it moves away from a potential valley. The atom is then optically pumped back to the foot of another hill. If the time taken to reach the top of a hill from the bottom of a valley is equal to the time taken for the atom to be optically pumped to the alternative ground state then the cooling is at a maximum, as shown in this case, as the atom only experiences uphill gradients.

and the temperature given by,

$$k_B T = \frac{\hbar\Gamma^2}{2|\Delta|}\frac{I}{I_{sat}}\left[\frac{29}{300} + \frac{254}{75}\frac{1}{4(\Delta/\Gamma)^2+1}\right]. \tag{6.9}$$

Using Equation 6.8 to plot the viscous force experienced by an atom as a function of its velocity gives Figure 6.10. It is noted that the friction coefficient is constant for increasing intensities, in contrast with Doppler cooling. Also depicted in Figure 6.10 is the velocity capture range. This is defined as $v_p \approx \lambda/\tau_p$, where τ_p is the optical pumping time. Since τ_p is proportional to I, it follows that the velocity capture range is proportional to I, again in contrast to Doppler cooling where it was independent of intensity.

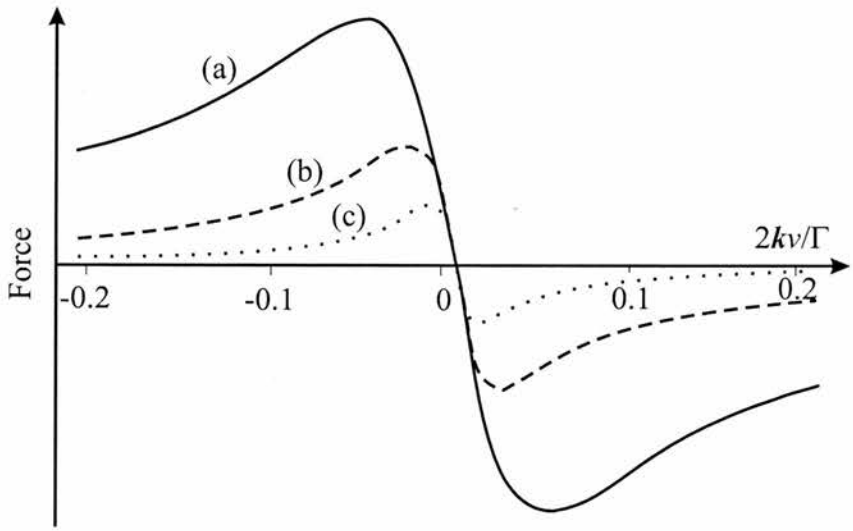

Figure 6.10: The damping force in polarisation gradient cooling. The horizontal axis is normalized atomic velocity where **k** is the wavevector of the laser beams and Γ is the natural linewidth of the atomic transition. Curves are shown for (a) an arbitrary intensity I, (b) $I/2$ and (c) $I/4$. In this case the velocity capture range is not independent of intensity but the viscous cooling force (given by the slope of the curve) is large and independent of intensity. The difference in horizontal axis scales between this figure and Figure 6.5 should be noted.

Equation 6.9 suggests that by lowering the intensity or increasing the detuning an arbitrarily low temperature could be achieved. This is clearly unphysical since this is an optical process and the recoil momentum from emitted photons will define a lower limit for the attainable temperature. There is, therefore, a limit known as the *recoil limit* below which optical cooling methods cannot exceed. While the friction coefficient does not depend on I, the heating rate does. The minimum temperature obtained thus depends on the ratio of viscous cooling to the heating rate and is therefore proportional to laser intensity. With increasing intensity, Doppler cooling provides an unchanging large capture range with increasing viscous damping. In polarisation gradient cooling, the capture range increases while the viscous damping remains unaltered. It is noted that the capture range of Doppler cooling is of the order of 10 to 100 times greater than that in polarisation gradient cooling while the friction coefficient is approximately one order of magnitude smaller. Polarisation gradient cooling therefore takes over when Doppler cooling begins to break down.

The example described above uses linearly polarised, counter-propagating laser beams. However, it can also be achieved with counter-rotating circularly polarised beams. The details of how the cooling operates are slightly different, nevertheless two common features remain: the atoms' ground state energies and population are position dependent. Further details of this and other polarisation gradient cooling schemes can be found elsewhere [17, 21, 22].

6.3.2 Sub-Recoil Cooling

In the 1920s, Bose and Einstein predicted that a gas with sufficiently low temperature and high density would undergo a phase transition that today is called *Bose-Einstein Condensation* (BEC) [23, 24]. The phase transition occurs when the thermal de Broglie wavelength, $\lambda_{dB} = h/(3mk_BT)^{1/2}$, becomes larger than the mean spacing between particles. More precisely, the *phase space density*, $\rho_{ps} = n\lambda_{dB}^3$, must be greater than 2.612 where n is the number density in the gas.

The experimental realization of BEC had been one of the holy grails in physics for a number of years and the development of laser cooling brought with it an air of optimism since this technique led to samples of atoms with low temperature and high densities. For example, laser cooling can increase the phase space density of a vapour of alkali metal atoms by 15 orders of magnitude to $\rho_{ps} \sim 5 \times 10^{-4}$. However, a limit is reached using sub-Doppler cooling methods due to light assisted collisions. This is the mechanism that limits the temperature reached in a magneto-optical trap. If the density of a sample becomes too large, light scattered by one atom is reabsorbed by others close by causing a repulsion between them. If higher densities and lower temperatures are to be obtained then resonant light must be avoided. A more promising approach is to employ *evaporative cooling* [25, 26]. As its name suggests, this technique preferentially removes atoms having higher than average energy from the trap and then rethermalises the remainder through elastic collisions to a new lower temperature. One way to think of evaporative cooling is to consider how a cup of coffee cools. The most ener-

getic molecules escape the surface of the beverage leaving the remaining coffee at a lower temperature. Furthermore, it requires only the evaporation of a small fraction of the coffee to cool it considerably. In practice the most common way of achieving evaporative cooling from an optically cooled ensemble of atoms is to load them into a magnetic trap. This type of trap exploits the forces felt by an atoms placed in a magnetic field gradient and will be discussed in the following section. The trap depth can simply be lowered allowing high energy atoms to escape. Indeed, the success of this method enabled the first experimental realization of a Bose-Einstein condensate [27, 28]. Other techniques to circumvent the sub-Doppler limit include *velocity-selective coherent population trapping* [29] and *Raman cooling* [30].

6.4 Magnetically–Based Traps

While optical molasses provides viscous damping to the motion of atoms contained within it, it is not a trap. There is no spatial dependence imposed on the atoms and as such they are free to move, albeit slowly. If an atom reaches the edge of the overlap region of the cooling laser beams then it can escape to the surrounding environment. The next step is to spatially confine these optically cooled atoms. The idea that scattering forces could be the sole basis for a trap is appealing with one achieving a very simple trap. However, is was shown that a trap based solely on absorption and emission processes from a static arrangement of laser beams would fundamentally be unstable [31]. This is known as the *optical Earnshaw theorem* which is analogous to the theorem in electrostatics which states that it is impossible to trap a charged particle in static electric fields. However, this was shown to be only true if the scattering forces on the atoms are dependent only on laser intensity [32]. If a situation occurred where the proportionality was position dependent then the limitations of the theorem could be lifted and a stable trap formed. The most successful realization of this concept is the magneto-optical trap (MOT) in which the combination of light and

magnetic fields create a position dependent scattering force in three dimensions. This is described in Section 6.4.2.

6.4.1 Magnetic Trap

The principle of a magnetic trap is the same as that in the Stern-Gerlach experiment [33] in which atoms with different magnetic moments experience differing forces in a magnetic field gradient. Purely magnetic traps involve no optical cooling methods but are excellent candidates for spatially trapping optically cooled ensembles of atoms. The first experimental observation of magnetically trapped neutral atoms was reported by Migdall and co-workers in 1985 [34]. An electric current was passed through two coils placed in an anti-Helmholtz configuration (a diagram of an anti-Helmholtz configuration can be found in Section 6.4.2) which generated a spherical quadrupole field pattern with a field zero at its centre. Atoms were loaded into the trap from an optically cooled atomic beam.

An atom with a magnetic moment μ in a magnetic field $\mathbf{B}$ has a potential energy $-\mu \cdot \mathbf{B}$. In the presence of a magnetic field gradient, the atom experiences a force defined by Equation 6.10

$$F = \mu \cdot \nabla \mathbf{B}. \tag{6.10}$$

In such a field, it is only those atoms that have their angular momenta, $\mathbf{F}$, parallel to $\mathbf{B}$ i.e. $m_F > 0$, that are spatially confined to the field minimum. It is impossible to create a field maximum in which $m_F < 0$ atoms can be trapped. Since magnetic traps are spin sensitive, only a fraction of the loaded atoms are trapped without special preparation of atoms into the appropriate ground state beforehand. Magnetic traps are used in trapping and cooling of atoms to temperatures lower than those obtainable in optical traps, as was discussed in Section 6.3.2.

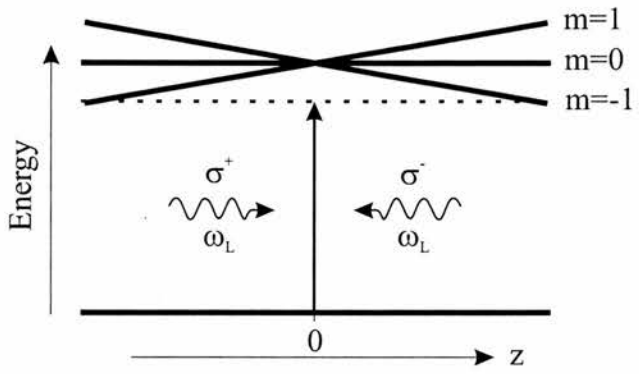

Figure 6.11: The magneto-optical trap in one dimension. For an atom with a positive z-coordinate, the σ^- beam comes into resonance with the Zeeman shifted Δm=-1 transition and pushes the atom back towards $z = 0$. The σ^+ beam has the same effect on the atom if it were to move in the negative z direction.

6.4.2 Magneto-Optical Trap

The first demonstration of simultaneous cooling and trapping was conducted in 1987 by Raab and co-workers [35]. In this experiment, the centre of an optical molasses was overlapped within a magnetic trap, a configuration that became known as a *magneto-optical trap* (MOT). The original idea, conceived by Dalibard *et al.* [36], was to use circularly polarised light for the optical molasses in order that when an atom deviated from the centre of the field zero, the Zeeman effect would shift the m_F sublevel into resonance with the cooling beams. Figure 6.11 demonstrates how this operates in one dimension.

The magnetic quadrupole field varies linearly with distance from the centre, so the $m = +1$ and $m = -1$ sublevels of the atom experience linear Zeeman shifts with position. The cooling laser is tuned to a slightly lower frequency than the atom's transition frequency. Tuning a laser lower in frequency than a resonance is known as red-detuning. Laser beams propagating in the $\pm z$ direction have circular polarisations $\sigma^\pm$ that drive the $\Delta m = \pm 1$ transitions. For example, if an atom moves from the centre of the trap along the positive z axis then it will experience a Zeeman shift, lowering the energy of the $m = -1$ sub-level bringing

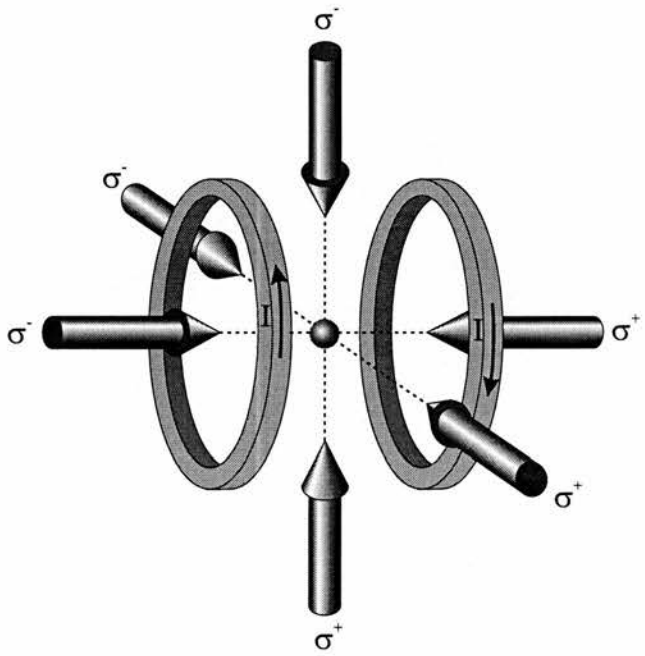

Figure 6.12: Schematic diagram of a MOT. Six mutually orthogonal, circularly polarised beams create three dimensional optical molasses while the anti-Helmholtz coils provide position dependence.

it into resonance with the laser frequency. It can therefore absorb and scatter more σ^- photons than σ^+ photons resulting in a force pushing it back towards $z = 0$. An identical scenario occurs for the $m = +1$ sublevel and an atom moving in the negative z direction. A schematic diagram of a MOT in three dimensions is shown in Figure 6.12. The magnetic field is generated from an anti-Helmholtz coil configuration although the field gradient required is far smaller than that in purely magnetic traps. The convenience and simplicity of this setup has made the MOT the workhorse in obtaining cold ensemble atoms with temperatures and densities of 100 μK and 10^{12} atoms cm^3 typical. At St Andrews, the MOT has a central part in providing a source of cold atoms for several atom guiding experiments. The methods of extracting atoms from within the MOT to form an atomic beam are now discussed.

6.5 Atom Extraction from Magneto-Optical Traps

Thermal atomic beams are well established in atomic physics although improvements in experimental sensitivity require slower, more dense beams. A cold atomic beam is an ensemble of atoms moving with a low longitudinal velocity with a low velocity distribution and minimal transverse kinetic energy. Such beams are important in atom lithography, atom interferometry and studies of wave-particle duality. The first experiments in reducing the longitudinal velocity of thermal atomic beams were accompanied by a serious loss in flux due to the transverse velocities being comparable with the cooled longitudinal velocity causing the atoms to be ejected in all directions. It was possible to collect and recollimate these atoms but this inherently complicated the experiment [37]. Aside from the production of an atomic beam, there must be some level of control or manipulation on the atomic ensemble which has led to atom-optic components such as mirrors, beam splitters and guides being produced. Without doubt the most important factor pushing this research forward is that of atom interferometry [16]. Cooled atoms can be extracted from a MOT by simply switching off the

trapping parameters and allowing the ensemble to fall under gravity. However, there are several instances where one would wish CW extraction in a controlled manner thereby forming a cold atomic beam. Two distinct solutions to this problem emerged from using slow, cool atoms confined in a magneto-optical trap (MOT) as a source and utilizing the radiation pressure force to impose directionality on them namely (i) the *atomic funnel* and (ii) a *low-velocity intense source* (LVIS) of atoms. Each of these in turn will be experimentally described in the subsequent sections.

6.5.1 Atomic Funnel

The first solution was proposed and demonstrated experimentally in 1990 by Riis *et al.* [37]. A diagram of the experimental setup can be found in Figure 6.13.

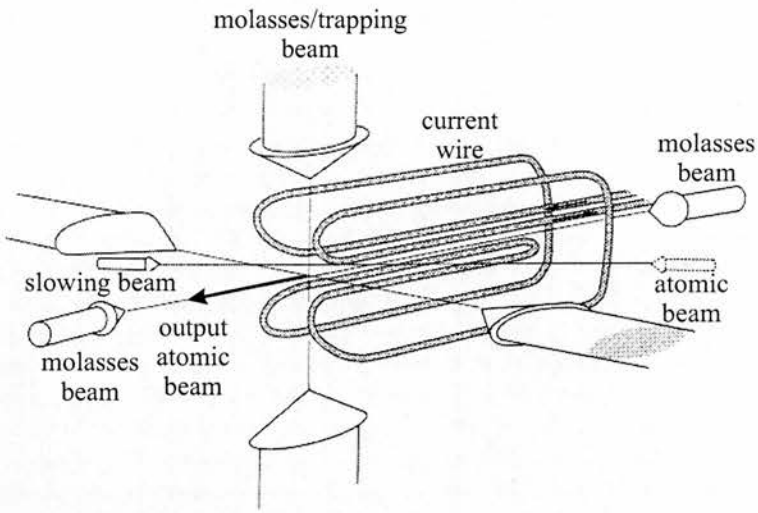

Figure 6.13: Schematic diagram of the atomic funnel. Atoms are loaded from a thermal atomic beam and cooled in an optical molasses. The atomic beam exits along the long axis of the magnetic quadrupole, to the left in the diagram. Reproduced from [37].

In this experiment, which has been termed an atomic funnel, the atoms were loaded into the trapping region from a thermal atomic beam, shown entering from the right in Figure 6.13. A slowing beam opposing the atoms was used

to reduce their velocities before they were cooled in a three dimensional optical molasses. A magnetic quadrupole field was created by four "hairpin" wires that created an elongated zero-field along which the atoms could move. Lateral cooling and guiding was achieved by transverse laser beams with elliptical spatial profiles. The atoms exited the molasses region in the direction indicated in Figure 6.13. Cooling along the zero field axis was provided by a pair of counter-propagating laser beams. To form the atomic beam, a drift velocity was imposed on the atoms along this direction by either introducing a difference in the frequencies or intensities of the two beams. In the latter case the atoms drift at a velocity such that the scattering rates from both beams are equal. In the former case, the atoms drift with a velocity such that the Doppler shift from both beams, as seen by the atom, is the same. In this way, atomic beams with a brilliance of $3\text{x}10^{11}$ atoms sr^{-1} s^{-1} travelling at a velocity of 2.7 m s^{-1} and with a temperature of $\sim$200 μK were obtained.

6.5.2 Low-Velocity Intense Source of Atoms

A second solution using a standard MOT with only minor modifications was reported in 1996 by Lu *et al.* [38]. The experimental setup is shown in Figure 6.14 and produced a low-velocity intense source (LVIS) of atoms. The system was nearly identical to that of a standard MOT using six perpendicular laser beams and a magnetic quadrupole field. The only difference being that one of the six beams had a narrow, dark region at its centre. This was created by drilling a small hole in the reflecting optic for one of the laser beams. Atoms from the background vapour would be cooled and trapped normally, as they would in a conventional MOT, however when the atom reached the very centre of the trap it experienced an imbalance in the radiation pressure force causing it to be forced along the dark central region of the beam and exit through the hole in the retro-reflecting optic. The velocity with which the atoms left the trap was determined by the number of photons scattered from the pushing beam. A key feature of this scheme was that the atoms were continually apertured by the laser light along

the length of the extraction beam. Those atoms whose transverse trajectories take them outwith the dark central region were recycled back to the centre of the cooling and trapping region. In this way, the recycling of diverging atoms makes the transference of trapped atoms to a collimated atomic beam an efficient process.

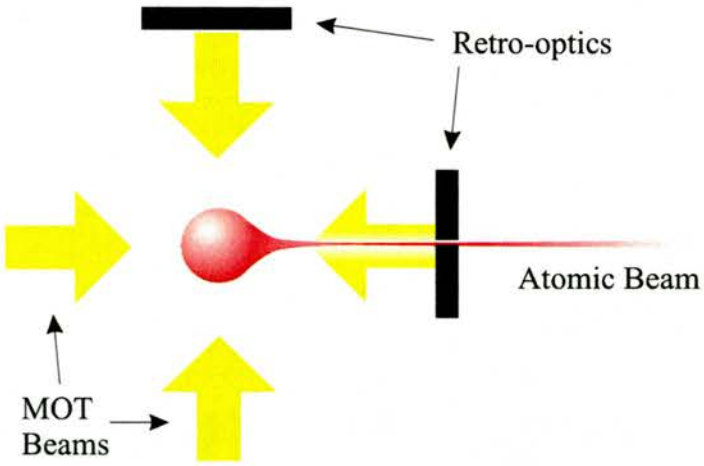

Figure 6.14: (Colour) Schematic of the low-velocity intense source (LVIS) of atoms system. The shaded arrows indicate the cooling and trapping beams. A retro-optic with a small hole drilled in its centre creates an extraction column for the atoms. A detection laser beam, not shown, measures atomic flux further down stream.

Lu and colleagues found the trapping laser frequency that maximised atomic flux was 5Γ below the atomic resonance frequency, where Γ is the natural linewidth of the transition. The frequency detuning that trapped the largest number of atoms in a normal MOT was measured to be 3.2Γ. The discrepancy can be explained by the increased scattering rates of atoms close to exiting the trap. If an imbalance exists in the intensities of the transverse laser beams, this would lead to a deflection in the atomic beam. Increasing the detuning reduced the scattering rates leading to less deflection and increased atom flux. A typical longitudinal velocity of 14 m s^{-1} could be obtained with a full-width-half-maximum (FWHM) distribution of 2.7 m s^{-1}. A narrow velocity distribution is desired in applications with cold atomic beams however the experimentally measured velocity distribution was higher than the expected Doppler cooling limit while taking into account

statistical fluctuations in the number of scattering photons. This was explained by assuming that atoms were not all accelerated out of the trapping region from the same point spatially and therefore were subjected to radiative pressure forces over different distances. Mathematical modelling confirmed this postulate. A further experiment, reported in the same paper by Lu and co-workers, used a conventional retro-reflecting optic and a glass slide onto which an opaque spot had been painted. The glass slide was placed in front of normal, unaltered retro-reflecting optic to produce a dark central spot in the reflected beam. The atomic beam in this case was withdrawn vertically from the trap so that gravity would not pull the atoms out of the extraction column. Similar atomic beam characteristics were observed. A measured brightness of $5\text{x}10^{12}$ atoms sr^{-1} s^{-1} and transverse temperatures of $20\mu\text{K}$ were reported. Atoms were predominately in the repumping ground state upon exit of the trapping region, i.e. the $F = 1$ state for ^{87}Rb and the $F = 2$ state for ^{85}Rb. This can be understood since as the atoms leave the MOT region they are no longer illuminated by the repumping laser and are optically pumped into the repumping ground state. The typical proportion of atoms in LVIS in this state is 90% [39].

An important parameter in the characterisation of any atomic beam is $\Delta v/v$, which expresses a ratio of the spread in longitudinal velocities, Δv, over the mean longitudinal velocity, v. This value describes how "spectrally" pure the beam is in a velocity sense. The atomic funnel and LVIS have $\Delta v/v$ values of 0.1 and 0.2 respectively. The atomic beam generated by the atomic funnel is therefore more monochromatic with a longitudinal velocity 5 times less than that of LVIS. However, the LVIS setup is extremely simple with the only modification needed being one additional optical element that may be placed external to a conventional MOT. This provides an easy, CW atomic source without the need for elaborate intra-vacuum components and high electric currents, as is the case with the atomic funnel. Because of these important considerations, LVIS was chosen to provide an atomic beam for subsequent use in the guiding experiments described in Chapter 9.

6.6 Optical Dipole Traps

An atom in the radiation field of a near-resonant laser experiences two types of force [40]. The first, the *radiation pressure force*, accounts for the viscous cooling and trapping forces described up to this point and occurs as a result of absorption followed by spontaneous emission of photons. A second force, derived from the interaction of an atom with a light field, is the *optical dipole force* and occurs as a result of absorption followed by stimulated emission of photons. This force was proposed in 1970 by Ashkin and has its origins in work conducted on trapping and levitating microscopic particles [6]. By utilizing this force it is possible to either attract or repel atoms from regions of higher light intensity by altering the frequency of the interacting light field either below or above resonance respectively. This force plays an important role in both optical atom traps and atom guiding using light. Atom traps based on this force required the development of efficient cooling techniques as the attainable potential barriers were rather feeble. The shallowness of the trap dictated that atoms needed to be cooled previous to loading, usually from a MOT. Hence it was not until 1986 that the first experimental optical dipole trap was demonstrated by Chu and colleagues [20]. This section outlines the origins of the optical dipole force and documents several red-detuned and blue-detuned optical dipole traps.

6.6.1 Optical Dipole Force

Classically, the dipole force is defined by Equation 6.11

$$F_d = \mathbf{p} \cdot \nabla \mathbf{E}, \tag{6.11}$$

where $\mathbf{p}$ is the dipole moment and $\mathbf{E}$ is the electric field. If placed in an intense optical field, an atom acquires an optically induced dipole moment defined by Equation 6.12

$$\mathbf{p} = \alpha \mathbf{E} \tag{6.12}$$

where α is the polarisability of the atom. For an atom in its ground state, α is dispersive in nature and is positive at frequencies below resonance, zero exactly on resonance and negative above resonance, as shown by the blue curve in Figure 6.15. Mathematically, these two parameters are linked through the Kramers-Kronig relations. This results in a force on the atom, known as the *optical dipole force*, which pulls it into regions of high intensity light for detunings below resonance and pushes it out of such regions for detunings above resonance.

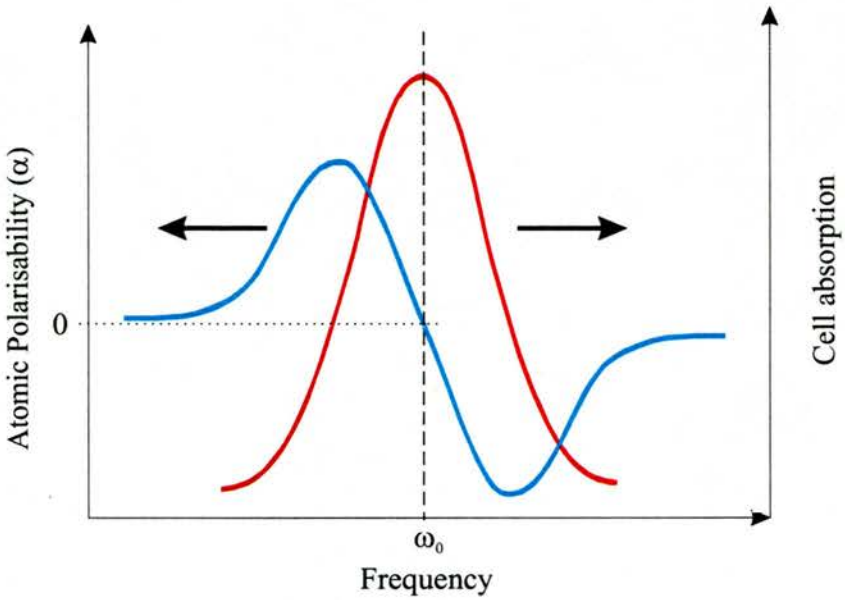

Figure 6.15: (Colour) Classical description of the dipole force. For an atomic transition defined by the red curve, with a characteristic absorption profile as shown, the polarisability of the atom, α, will be positive for laser detunings below resonance, ω_0, and negative for laser detunings above resonance (blue curve) as defined by the Kramers-Kronig relations. The change in sign of the polarisability causes the atom to be either repelled or attracted to regions of light depending on the laser frequency.

6.6.2 Red-Detuned Optical Dipole Trap

The simplest form of an optical dipole trap is a focused Gaussian laser beam detuned red of the atomic transition. The first experiment using this setup was reported in 1986 by Chu and co-workers where a focused laser beam approximately 1000 GHz red of the transition frequency was directed into the centre of a MOT [20]. The dipole trap was loaded by alternating between the cooling beams and the trap beam.

From a quantum mechanical viewpoint, an atom placed in an optical field is subjected to an a.c.–Stark shift of its ground state causing a change in the potential energy of that atom. For an atom with a natural upper state lifetime τ and a saturation intensity I_{sat}, placed in a Gaussian laser beam with a beam waist w_0 $(1/e^2 radius)$, a power P and a detuning from resonance Δ, the potential defining the trap depth is [17],

$$U_0 = -\frac{\hbar P}{4\pi w_0^2 \Delta \tau^2 I_{sat}}. \tag{6.13}$$

If the light is linearly polarised and the laser detuning is greater than the hyperfine splitting of the excited state, the degeneracy of magnetic sublevels allows an atom with an arbitrary spin state to be trapped. The trap depths in optical dipole traps are usually very shallow and spontaneous emission can often be sufficient to "kick" an atom out of the potential. Laser detunings more than a few atomic linewidths dictate a spontaneous scattering rate given by Equation 6.14,

$$\gamma_s = \frac{\omega_R^2 \Gamma}{4\Delta^2}. \tag{6.14}$$

High scattering allows only short trapping lifetimes before heating dissipates the atomic cloud. Miller and co-workers [41] reported a solution to this problem that resulted in improved trap lifetimes. Large laser detunings were used because the trap depth scales with $1/\Delta$ (Equation 6.13) whereas the scattering rate varies

with $1/\Delta^2$ (Equation 6.14). The characteristics of atoms in these *far-off resonance optical dipole traps* have been investigated using laser beams tuned several tens of nanometres from resonance and with high beam powers [42, 43]. Recently, an all optical formation of a rubidium BEC using a dipole trap formed by two crossed CO_2 laser beams (12 W at 10.6 μm) has been reported [44] resulting in essentially no scattering of photons.

The scattering problem occurs only when the laser is detuned red of the transition frequency since it is in this regime where atoms are found in regions of highest light intensity. Blue detuning a laser circumvents the heating mechanisms described by forcing atoms to spatial regions where the light intensity is lowest. Surrounding a spatial region with blue-detuned light allows a trap to be formed.

6.6.3 Blue-Detuned Optical Dipole Trap

In a blue-detuned trap, the atom is confined to low light intensity regions thereby undergoing minimal spontaneous emission. This eradicates viscous heating and allows atoms to remain trapped for longer periods. The first blue detuned optical dipole trap was reported in 1994 using sheets of light from an argon ion laser [45] and resulted from work in creating atom mirrors using evanescent waves [46, 47]. A later refinement came using two crossed sets of V shaped beams [30] and using gravity to confine atoms in the inverted pyramid, as shown schematically in Figure 6.16. To minimise trap losses, care was taken in avoiding interference effects which could lead to a breach in any one of the trapping barriers.

A novel blue-detuned optical trap formed using a Laguerre-Gaussian[2] (LG) beam was reported in 1997 by Kuga and colleagues [48]. In this experiment a blue-detuned LG ($\ell = 3$) was overlapped with the trapping region of a MOT. For three-dimensional confinement of the atoms, two plug beams were used to eradicate movement of atoms along the LG optical axis. A schematic diagram of the setup

[2]Details of Laguerre-Gaussian beams are presented in Section 9.2.2.

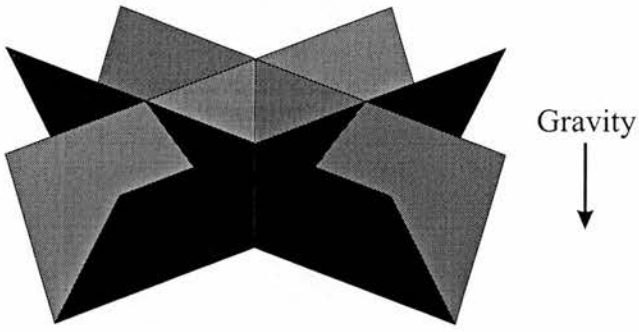

Figure 6.16: Schematic of the blue-detuned optical dipole trap geometry.

is shown in Figure 6.17.

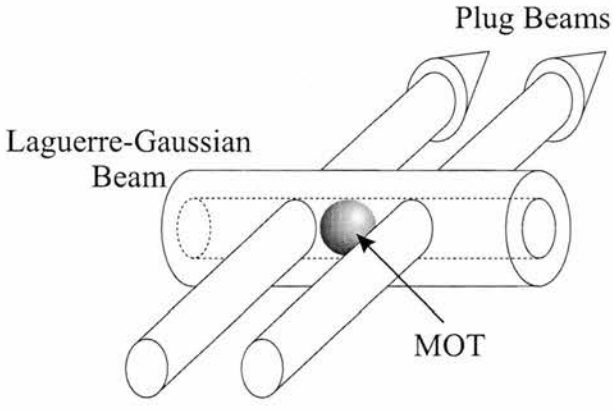

Figure 6.17: Schematic of a blue-detuned optical dipole trap constructed from a Laguerre-Gaussian beam and two Hermite-Gaussian plug beams. Reproduced from [48].

The optical dipole potential formed by the LG mode is given by [49],

$$U(r) = \frac{\hbar\Delta}{2} \ln\left[1 + \frac{I(r)/I_0}{4(\Delta/\Gamma)^2}\right], \tag{6.15}$$

where $\Delta = \omega_L - \omega_0 - kv_z$ denotes laser detuning from resonance with ω_L the laser frequency, ω_0 the atomic resonance frequency and kv_z is the Doppler shift. $I(r)$ denotes the radial intensity variation of the light beam while I_0 and Γ are the saturation intensity and natural linewidth of the atomic transition respectively.

The main disadvantage of early blue-detuned traps was that loading efficiency and tight confinement could not be performed simultaneously. The low loading efficiency resulted from the very different volumes and shapes of the nearly spherical MOT and the highly elongated dipole trap. It is noted that the trap composed of an inverted pyramid had no such loading problems but its reliance on the weak gravitational forces inhibited close confinement of atoms. A solution which enabled both these factors to be addressed was proposed by Ozeri *et al.* [50]. In this work, an optical "bubble" was formed around the MOT by using a binary phase element. This was composed of concentric phase rings with a π-phase difference between neighbouring rings. By focusing the 1st and -1st diffracted orders from a TEM_{00} mode incident on this, an annulus of light was created at the focal plane that closes in on itself both sides of the focal plane owing to the beam divergence to form a dark region completely surrounded by light. Improving the potential mode matching between the dipole trap and the MOT, an increase in the loading efficiency of a factor of 50 was demonstrated. Including a zoom lens system to dynamically alter the dipole trap volume was foreseen as a method of compressing the trapped atoms although this had not been experimentally verified.

6.7 Summary

This chapter has detailed the theory required to perform laser cooling and trapping experiments. Primary cooling mechanisms were discussed and the fundamental forces and processes required to cool and slow an atomic beam presented. These ideas were extended to include three-dimensional cooling, or *optical molasses*, and sub-Doppler mechanisms such as *Sisyphus cooling* which were required to account for experimentally recorded temperatures lower than those predicted by Doppler cooling theory. An introduction to sub-recoil cooling mechanisms was presented with an overview of *evaporative cooling* and its characteristics which directly contributed to the first experimental realization of Bose-Einstein Con-

densation. In combination of cooling techniques with spatially variant magnetic fields, magneto-optical traps (MOTs) were introduced. The generation of a low-velocity intense source (LVIS) of atoms directly from the centre of a MOT was then outlined while experimental applications of this atomic beam within this research are contained in Chapter 9. The optical dipole force experienced by an atom when placed in a near resonant light field was introduced together with the geometric configuration of optical dipole traps for neutral atoms.

Bibliography

[1] A. Einstein, "Zur quantentheorie der strahlung," Mitteilungen der Physikalischen Gesellschaft Zürich **16,** 47 (1916).

[2] A. H. Compton, "Wave–length measurements of scattered x–rays," Physical Review **21,** 715 (1923).

[3] R. Frisch, "Experimenteller nachweis des Einsteinschen strahlungs-rückstosses," Zeitschrift fur Physik **86,** 42–48 (1933).

[4] P. Jacquinot, S. Liberman, J. L. Picqué, and J. Pinard, "High resolution spectroscopic application of atomic beam deflection by resonant light," Optics Communtications **8,** 163–165 (1973).

[5] R. Schnieder, H. Wather, and L. Wöste, "Atomic beam deflection by the light of a tunable dye laser," Optics Communications **5,** 337–340 (1972).

[6] A. Ashkin, "Acceleration and Trapping of Particles by Radiation Pressure," Physical Review Letters **24,** 156–159 (1970).

[7] A. Ashkin, "Atomic–beam deflection by resonance–radiation pressure," Physical Review Letters **25,** 1320–1324 (1970).

[8] W. D. Phillips and H. Metcalf, "Laser deceleration of an atomic beam," Physical Review Letters **48,** 596–599 (1982).

[9] W. Ertmer, R. Blatt, J. L. Hall, and M. Zhu, "Laser manipulation of atomic beam velocities: demonstration of stopped atoms and velocity reversal," Physical Review Letters **54,** 996–999 (1985).

[10] M. Zhu, C. W. Oates, and J. L. Hall, "Continuous high–flux monovelocity atomic beam based on a broadband laser–cooling technique," Physical Review Letters **67,** 46–49 (1991).

[11] J. V. Prodan, W. D. Phillips, and H. Metcalf, "Laser production of a very slow monoenergetic atomic beam," Physical Review Letters **49,** 1149–1153 (1982).

[12] J. Prodan, A. Migdall, W. D. Phillips, I. So, H. Metcalf, and J. Dalibard, "Stopping Atoms with Laser Light," Physical Review Letters **54,** 992–995 (1985).

[13] T. W. Hänsch and A. L. Schawlow, "Cooling of gases by laser radiation," Optics Communications **13,** 68–69 (1975).

[14] D. J. Wineland and H. G. Dehmelt, Bullitin of the American Physical Society **20,** 637 (1975).

[15] P. D. Lett, W. D. Phillips, S. L. Rolston, C. E. Tanner, R. N. Watts, and C. I. Westbrook, "Optical Molasses," Journal of the Optical Society of America B **6,** 2084 (1989).

[16] H. J. Metcalf and P. van der Straten, *Laser Cooling and Trapping* (Springer-Verlag Inc., 175 Fifth Avenue, New York, NY 10010, USA, 1999), pages 219–229.

[17] C. S. Adams and E. Riis, "Laser cooling and trapping of neutral atoms," Progress in Quantum Electronics **21,** 1–79 (1997).

[18] P. D. Lett, R. N. Watts, C. I. Westbrook, and W. D. Phillips, "Obsevation of Atoms Laser Cooled below the Doppler Limit," Physical Review Letters **61,** 169–172 (1988).

[19] S. Chu, L. Hollberg, J. E. Bjorkholm, A. Cable, and A. Ashkin, "Three–dimensional viscous confinement and cooling of atoms by resonance radiation pressure," Physical Review Letters **55,** 48–51 (1985).

[20] S. Chu, J. E. Bjorkholm, A. Ashkin, and A. Cable, "Experimental Observation of Optically Trapped Atoms," Physical Review Letters **57,** 314–317 (1986).

[21] C. N. Cohen-Tannoudji and W. D. Phillips, "New Mechanisms for Laser Cooling," Physics Today pp. 33–40 (1990).

[22] J. Dalibard and C. Cohen-Tannoudji, "Laser cooling below the Doppler limit by polarisation gradients: simple theoretical models," Journal of the Optical Society of America B **6,** 2023–2045 (1989).

[23] S. N. Bose, Z. Phys. **26,** 178 (1924).

[24] A. Einstein, Sitzungsber. Kgl. Preuss. Akad. Wiss. **1924,** 261 (1924).

[25] N. Masuhara, J. M. Doyle, J. C. Sandberg, D. Kleppner, T. J. Greytak, H. F. Hess, and G. P. Kochanski, "Evaporative cooling of spin-polarized atomic hydrogen," Physical Review Letters **61,** 935–938 (1988).

[26] K. B. Davis, M.-O. Mewes, M. A. Joffe, M. R. Andrews, and W. Ketterle, "Evaporative cooling of sodium atoms," Physical Review Letters **74,** 5202–5205 (1995).

[27] M. H. Anderson, J. R. Ensher, M. R. Matthews, C. E. Wieman, and E. A. Cornell, "Observation of Bose-Einstein condensation in a dilute atomic vapor," Science **269,** 198–201 (1995).

[28] K. B. Davis, M. O. Mewes, M. R. Andrews, N. J. van Druten, D. S. Durfee, D. M. Kurn, and W. Ketterle, "Bose–Einstein condensation in a gas of sodium atoms," Physical Review Letters **75,** 3969–3973 (1995).

[29] A. Aspect, E. Arimondo, R. Kaiser, N. Vansteenkiste, and C. Cohen-Tannoudji, "Laser cooling below the one–photon recoil energy by velocity–selective coherent population trapping," Physical Review Letters **61,** 826–829 (1988).

[30] H. J. Lee, C. S. Adams, M. Kasevich, and S. Chu, "Raman Cooling of Atoms in an Optical Dipole Trap," Physical Review Letters **76,** 2658–2661 (1996).

[31] A. Ashkin and J. P. Gordon, "Stability of radiation-pressure particle traps: an optical Earnshaw theorem," Optics Letters **8,** 511–513 (1983).

[32] D. E. Pritchard, E. L. Raab, V. Bagnato, C. E. Wieman, and R. N. Watts, "Light traps using spontaneous forces," Physical Review Letters **57,** 310–313 (1986).

[33] W. Gerlach and O. Stern, "Der experimentelle nachweis des magnetischen moments des silberatoms," Zeitschrift fur Physik **8,** 110–111 (1921).

[34] A. L. Migdall, J. V. Prodan, W. D. Phillips, T. H. Bergeman, and H. J. Metcalf, "First observation of magnetically trapped neutral atoms," Physical Review Letters **54,** 2596–2599 (1985).

[35] E. L. Raab, M. Pretiss, A. Cable, S. Chu, and D. E. Pritchard, "Trapping of neutral sodium atoms with radiation pressure," Physical Review Letters **59,** 2631–2634 (1987).

[36] J. Dalibard, S. Reynaud, and C. Cohen-Tannoudji, "Proposals of stable optical traps for neutral atoms," Optics Communications **47,** 395–399 (1983).

[37] E. Riis, D. S. Weiss, K. A. Moler, and S. Chu, "Atom funnel for the production of a slow, high–density atomic beam," Physical Review Letters **64,** 1658–1661 (1990).

[38] Z. T. Lu, K. L. Corwin, M. J. Renn, M. H. Anderson, E. A. Cornell, and C. E. Wieman, "Low-Velocity Intense Source of Atoms from a Magneto-optical Trap," Physical Review Letters **77,** 3331–3334 (1996).

[39] D. Müller, E. A. Cornell, D. Z. Anderson, and E. R. I. Abraham, "Guiding laser-cooled atoms in hollow-core fibers," Physical Review A **61,** 033411–1–033411–6 (2000).

[40] J. P. Gordon and A. Ashkin, "Motion of atoms in a radiation trap," Physical Review A **21,** 1606–1617 (1980).

[41] J. D. Miller, R. A. Cline, and D. J. Heinzen, "Far–off–resonance optical trapping of atoms," Physical Review A **47,** R4567–R4570 (1993).

[42] D. Boiron, A. Michaud, J. M. Fournier, L. Simard, M. Sprenger, G. Grynberg, and C. Salomon, "Cold and dense cesium clouds in far-detuning dipole traps," Physical Review A **57,** R4106–R4109 (1998).

[43] K. M. O'Hara, S. R. Granade, M. E. Gehm, and J. E. Thomas, "Loading dynamics of CO_2 laser traps," Physical Review A **63,** 3403–1–3403–5 (2001).

[44] M. D. Barrett, J. A. Sauer, and M. S. Chapman, "All–optical formation of an atomic Bose–Einstein Condensate," Physical Review Letters **87,** 010404–1–010404–4 (2001).

[45] N. Davidson, H. J. Lee, C. S. Adams, M. Kasevich, and S. Chu, "Long atomic coherence times in an optical dipole trap," Physical Review Letters **74,** 1311–1314 (1995).

[46] V. I. Balykin, V. S. Letokhov, Y. B. Ovchinnikov, and A. I. Sidorov, "Quantum–state–selective mirror reflection of atoms by laser light," Physical Review Letters **60,** 2137–2140 (1988).

[47] M. A. Kasevich, D. S. Weiss, and S. Chu, "Normal–incidence reflection of slow atoms from an optical evanescent wave," Optics Letters **15,** 607–609 (1990).

[48] T. Kuga, Y. Torii, N. Shiokawa, T. Hirano, Y. Shimizu, and H. Sasada, "Novel optical trap of atoms with a Doughnut beam," Physical Review Letters **78,** 4713–4716 (1997).

[49] J. Yin, Y. Zhu, W. Wang, Y. Wang, and W. Jhe, "Optical potential for atom guidance in a dark hollow laser beam," Journal of the Optical Society of America B **15,** 25–33 (1998).

[50] R. Ozeri, L. Khaykovich, N. Friedman, and N. Davidson, "Large-volume single-beam dark optical trap for atoms using binary phase elements," Journal of the Optical Society of America B **17,** 1113–1116 (2000).

Chapter 7

Review of Atom Guiding Experiments

7.1 Introduction

This chapter aims to outline the reasons and impetus behind research conducted in cold atom guiding while also presenting some of the experimental techniques that have been employed in achieving this to date. Atom guiding can be achieved by two main methods. The first utilizes the force felt by an atom when placed in a magnetic field gradient and the second employs the optical dipole force as discussed in Chapter 6. Three different methods of atom guidance will be discussed, namely magnetic field guiding; hollow optical fibre guiding and free-space light beam guiding although the latter two methods both rely on the optical dipole force. Entwined within research conducted in atom guiding is that of splitting an atomic beam. This has serious repercussions in atom interferometry. Within each of the guiding sections in this chapter, references will be made to pertinent results concerning atomic beam splitting. This chapter does not aim to recount rigorously all research conducted in this field but rather reviews some of the important results achieved to date.

7.1.1 Application to Atom Interferometry

The considerable progress made in the field of laser cooling in the past decade has opened a number of new avenues in atomic physics, such as atom optics and atom interferometry. In these disciplines, matter-waves behave much like light-waves in conventional optics and as such there is a requirement for atom-optic elements such as lenses, mirrors and beam splitters. One of the most important goals is the realization of an efficient, large angled atomic beam splitter for use in atom interferometers.

An atom interferometer is, in essence, identical to its optical analogue. A coherent source of atoms with a well defined de Broglie wavelength is spatially split along separate paths before being recombined. Upon recombination, interference between atoms occur allowing a fringe pattern to be observed. Any phase difference between the two paths will alter the fringe pattern. A promising application of atom interferometry is in precise measurements in a non-inertial reference frame *e.g.* rotating. For example, laser gyroscope interferometers determine changes in orientation by measuring the phase shift experienced due to the Sagnac effect [1]. The phase shift of the fringes is defined as [2]:

$$\Delta\Phi = \frac{4\pi\vec{\Omega}\cdot\vec{A}}{\lambda v} \tag{7.1}$$

where $\mid \vec{\Omega} \mid$ is the rotation frequency, λ is the wavelength of the interfering entity and v is the velocity of propagation. $\vec{A}$ is a vector whose magnitude is equal to the area of the plane enclosed by the two paths of the interferometer and whose direction is normal to this plane. For an optical interferometer $v = c$ and for and atom interferometer, $\lambda = h/p = h/mv$, where c is the speed of light in vacuum, h is Planck's constant and m is the mass of the atom. It therefore follows that the Sagnac phase shift is larger for atoms by a factor $mc^2/\hbar\omega$, which is typically 10^{10}, where $\hbar = h/2\pi$ and ω is the angular frequency of the interfering entity. This huge factor is somewhat compromised by optical interferometers having $|\vec{A}|$

hundreds of times larger than atomic analogues and better signal-to-noise ratios. Nevertheless, there exists the possibility of realizing atomic gyroscopes and other inertial sensors with new higher sensitivities. This would be of particular use for navigational purposes in space where the motion of the atoms would not be affected by gravity.

Atomic beam splitters have been experimentally demonstrated using both magnetic fields and optical means. Large deviation angles and high splitting efficiencies are characteristics preferred by atom interferometers. Magnetic fields generated from current carrying patterned substrates have led to guiding and splitting with large deviation angles but are restricted in efficiency due to only certain non-zero magnetic moment atomic levels being guided [3]. Splitting as a result of photon momentum transfer from transverse laser beams have allowed only small angle deviation [4] while implementing an optical standing wave Bragg grating resulted in multiple diffracted orders [5]. Other optical methods include using the optical dipole force generated from focused laser beams to guide and split ensembles of cold atoms with high efficiency and large splitting angles [6]. The aim of current research is to implement improved guiding geometries for larger splitting angles and more compact apparatus. Just as optical waveguides play a central role in modern optics, such as in the communication industry, atom waveguides are likely to become an expanding sector for future atom-optics based science.

7.2 Magnetic Field Guiding

Generating a source of cold atoms directly from the centre of a MOT has been outlined in Chapter 6. A means of transporting them over distance using guiding forces is then required if they are to be used in an experiment at a different spatial location or as part of an atom interferometer. Initial work on the transportation of atoms was conducted utilizing the interaction between the magnetic moment possessed by an atom and magnetic field gradients.

7.2.1 Wire Guiding

The first experiment to transfer neutral atoms by way of magnetic fields was proposed and, shortly afterwards, demonstrated by Schmiedmayer [7, 8]. A radially symmetric magnetic field was generated by a current carrying wire which resulted in an attractive force for atoms whose magnetic moment was parallel to the magnetic field. Atoms were kept spatially separate from the wire in order to avoid loss of atoms due to collisions with it. This was achieved naturally by the atoms motioning around the wire in Kepler-like orbits thereby attaining a centripetal potential barrier. The magnetic field pattern and guiding potential is shown in Figure 7.1(a) while the experimental setup is shown in Figure 7.2. In this scheme, a thermal beam of sodium atoms was overlapped with a 1 m long length of wire. A hot wire detector and a channeltron counted the number of sodium atoms at the far end of the apparatus. This detector operated by first surface-ionising atoms incident on the hotwire and having the channeltron subsequently count electons. The entire system was mounted within a vacuum. A bend of less than 10^{-3} rad was introduced in the wire to help demonstrate the guiding effect. The experimental results confirmed that guiding had taken place. A raw data set from the experiment is shown in Figure 7.3. A current of 1 A was passed through the wire with a bend of 0.5 mrad present. The current was switched off completely between 3.5 and 7.2 seconds.

This scheme was advanced and adapted through the addition of homogeneous magnetic bias fields perpendicular to the wire allowing atoms to be guided approximately 1 mm away from the wire, parallel to it. A schematic diagram of the field pattern is shown in Figure 7.1(b). This is known as a *side guide*. An experiment demonstrating guiding in this geometry, as well as in the previous unbiased magnetic field design, from the centre of a MOT was conducted by Denschlag and co-workers [9]. This side guide represented a new and promising way of guiding in future applications of atom optics since a current carrying wire could be incorporated onto the surface of a substrate with atoms capable of being guided above it. Then, the ability to load atoms close to a substrate becomes important.

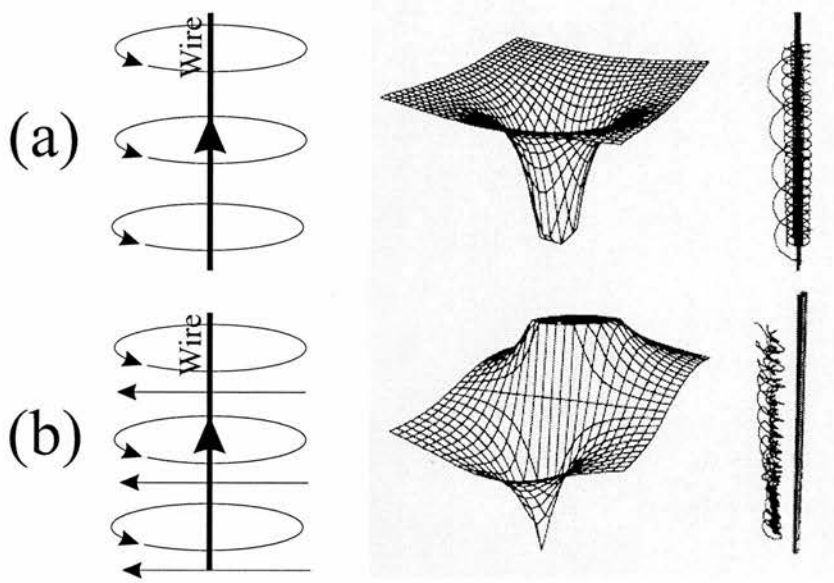

Figure 7.1: Configurations for magnetic guiding of neutral atoms. The left images show the wire and the magnetic field potentials, the centre images show the guiding potentials whilst the right images show typical trajectories of guided atoms. (a) is for when only a wire is used and (b) for when a wire and a bias field is applied to produce *side guiding*. Reproduced from [9].

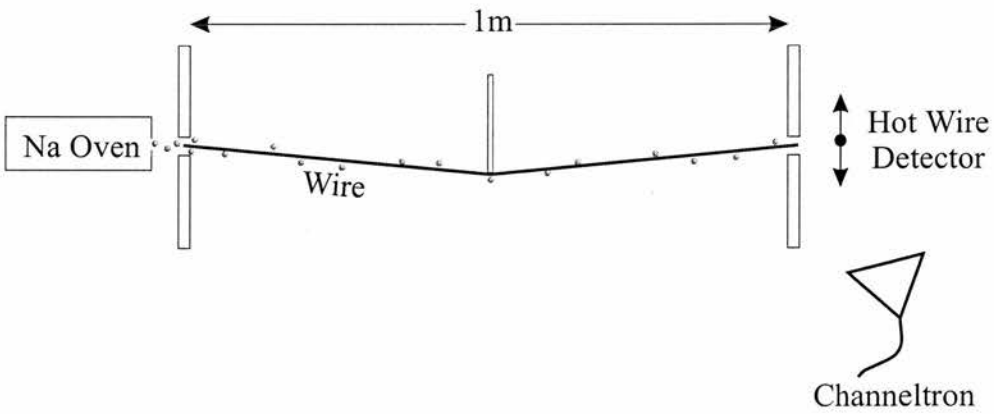

Figure 7.2: Functional diagram of the wire guiding experiment. Sodium atoms are emitted from an oven, guided by a field minimum around the bent current carrying wire and then detected by the translatable hot wire detector and channeltron. Reproduced from [7].

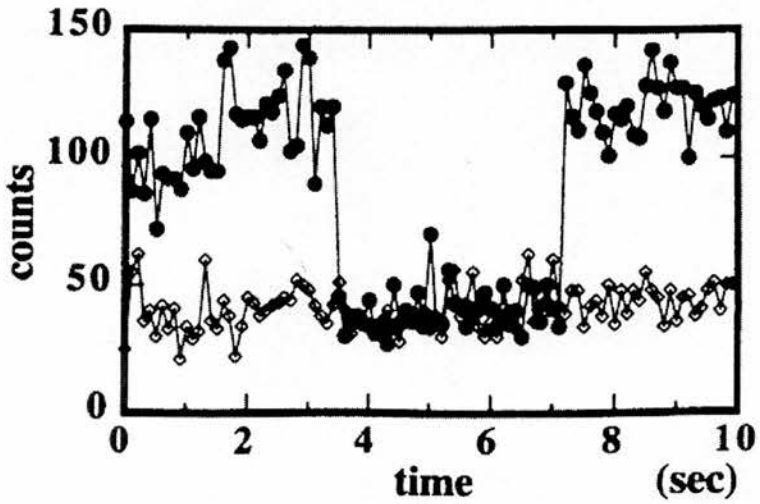

Figure 7.3: Raw data from the experimental setup shown in Figure 7.2 with a current of 1 A and a bend of 0.5 mrad. Measurements were taken alternately with the current on for 100 ms (•) and off for 100 ms (◇). The current was turned off completely between 3.5 and 7.2 seconds. Reproduced from [7].

This has been addressed during the work undertaken at St Andrews with the placement of a MOT approximately 1 mm above a surface. This is detailed in Section 8.3.

Indeed, it was not long before an experiment of magnetically guiding atoms above a substrate was demonstrated. The experimental setup for this is shown in Figure 7.4. Laser cooled atoms from a LVIS were overlapped with two parallel wire tracks grown on a substrate and guided around three curves each with a 15 cm radius of curvature over a distance of 10 cm [10]. The tracks consisted of dimensions 100 x 100 μm with a separation of 100 μm between them. The resulting magnetic field was zero in the centre between the wires. This is known as a *centre guide.* After exiting the guide at the end of the apparatus, the atom flux was detected using a hot wire and channeltron. A beam block placed line-of-sight from LVIS to the detection region obstructed any atoms not guided from reaching the hot wire. This experiment again showed conclusively guiding of neutral atoms but more so displayed the potential of this technique in building not only individual

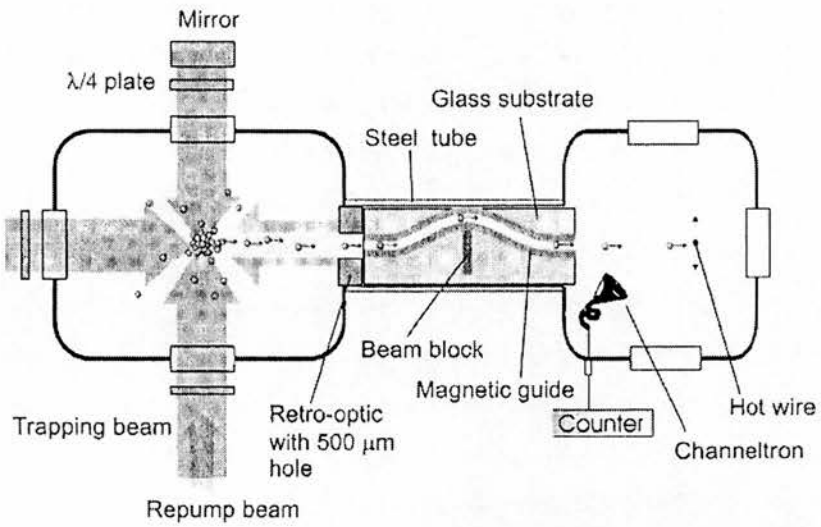

Figure 7.4: Experimental setup for magnetic guiding above the surface of a substrate. A LVIS provides a beam of atoms that are coupled into the magnetic guide. Atoms are guided around a barrier and are then ionised with a hot wire and counted using a channeltron. Reproduced from [10].

optical elements but multicomponent arrays on a single substrate for use in atom optics.

7.2.2 Magnetic Atomic Beam splitters

Atomic beam splitters are pivotal in any atom interferometer. Whereas the original beam splitter was probably the Stern-Gerlach experiment [11], modern free-space beam splitters rely on optical or mechanical means for spatial separation. Small splitting angles characterise these apparatus and because the sensitivity is defined by the enclosed area of both interferometer arms, experiments are particularly bulky in order to split and the recombine both beams. By extending the ideas used in magnetic atom guides described in Section 4.3.1, waveguide atomic beam splitters and atom switches have been constructed on a substrate enabling arbitrary splitting angles to be realized.

Müller and co-workers constructed an atom switch [3] based on earlier work they

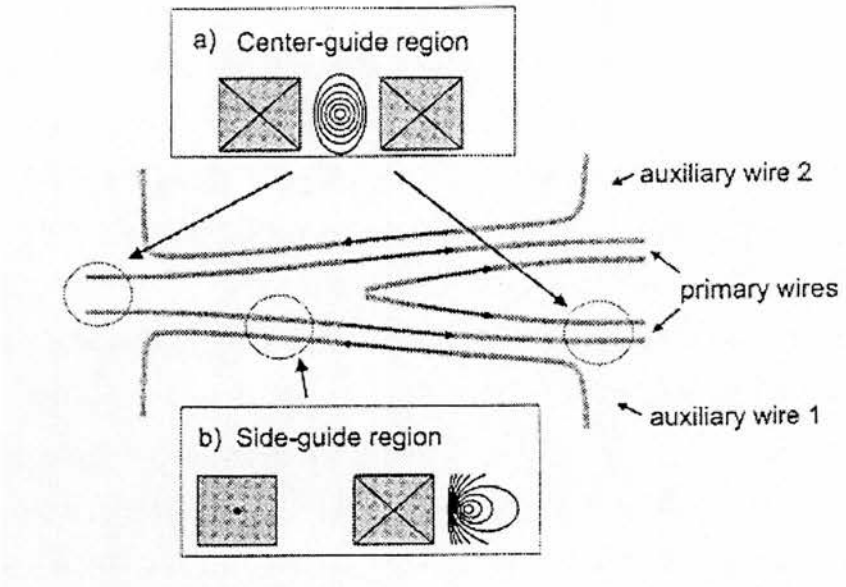

Figure 7.5: Experimental realization of a substrate magnetic atom switch. Insets (a) and (b) show the magnetic field contour lines at two separate regions. The contour lines are separated by 10 Gauss. A centre guide forks into one of two side guides depending on which auxiliary wire is turned on before returning back to a centre guide. Reproduced from [3].

had performed in the manufacture of an atomic beam splitter [12]. The experimental setup for the atom switch is shown in Figure 7.5. Atoms enter the apparatus from the left and travel along a centre guide for 1 cm before the wires begin to separate slowly. The guiding potential reduces as the wires diverge with each wire now each arm of the switch. A side guide is created by passing an electric current through either one of the auxiliary wires. The side guide extends over 4 cm before merging back into a centre guide over the next 4 cm, reversing the above process. Passing current through auxiliary wire one or auxiliary wire two dictates along which arm the atoms are guided. Approximately $5\text{x}10^4$ atoms s^{-1} could be observed exiting either arm of the apparatus spatially separated by 8 mm.

7.2.3 Summary of Magnetic Field Guiding

The experiments described within this section demonstrate that magnetic guiding is successful in achieving the transference of neutral atoms over a distance comparable to that demanded by a compact atom interferometer. Several atom-optic components have been demonstrated experimentally and the potential has been shown clearly in combining several of these to produce a multi-element device. However, there exist several undesirable characteristics with these systems:-

(i) The atoms need to be loaded into the guiding potential generated by the wires. This requires the careful alignment of the guiding apparatus to the atomic beam before the trap is assembled. In some setups this is more straightforward but in all, changes in this alignment once the experiment has been constructed is extremely difficult, if not impossible.

(ii) Large currents are required to generate sufficiently large field gradients because the magnetic moments of neutral atoms are small. The small diameter wires used in many of these experiments are unable to pass large currents continuously and therefore the experiment must be operated in a pulsed mode.

(iii) It is only atoms occupying specific m_F sublevels that will be attracted to the field zero and guided unless specific population pumping is applied. All other atoms are lost. Therefore only a small percentage (usually $< 25\%$) of the initial atom flux incident on the guide can be observed at the detection region.

7.3 Hollow fibre Light Beam Guiding

A solution to items (ii) and (iii) listed in Section 7.2.3 above was found in using the optical dipole force described in Chapter 6, where atoms, regardless of their

spin states, can be either attracted or repelled from regions of light intensity. This can be employed by having light propagate within a hollow optical fibre or in free-space. This provides a method of guiding that is complimentary to magnetic guiding. In the following two sections, hollow optical fibre guiding and free-space guiding will be explored respectively.

By coupling light into the hollow core or the surrounding glass fibre of a hollow-core optical fibre and detuning it correctly, the optical confinement coupled with the dipole force can allow atoms to be guided along the hollow core. A diagram illustrating the cross section of a hollow-core optical fibre and also the regions of light intensity when the fibre is used both in the red-detuned and blue-detuned geometries is shown in Figure 7.6.

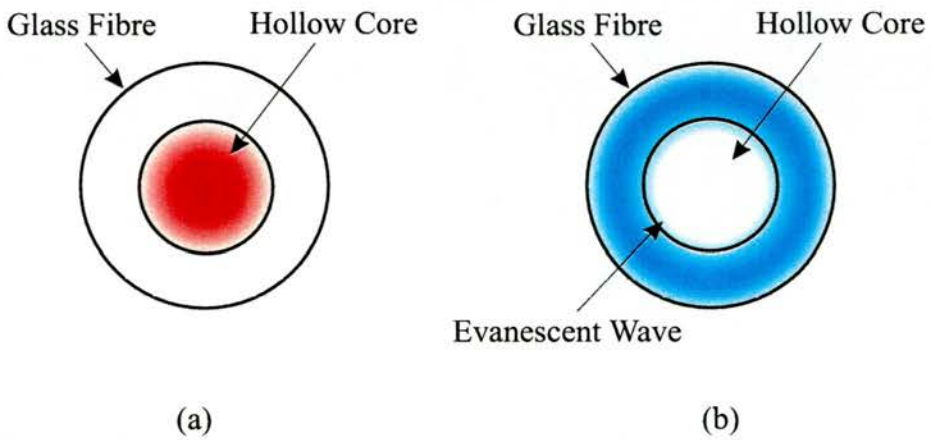

Figure 7.6: (Colour) Diagram illustrating light fields in hollow-core optical fibre guiding when (a) using red-detuned light and (b) blue-detuned light.

This was first proposed by Ol'Shanii and co-workers in 1993 for a red-detuned laser beam [13] and by Marksteiner *et al.* for blue-detuned light [14]. There are a number of advantages in using hollow optical fibres:-

(i) Atoms can be transported from one vacuum chamber to another while the outside surface of the fibre is subject to atmospheric pressure.

(ii) There is the ability to guide around bends and by varying the radius of curvature of the bend one can obtain a velocity selective element.

(iii) Optical access through the fibre walls allow atoms to be probed and manipulated without the constraints of cumbersome vacuum equipment.

It would be naïve to assume that one could couple atoms into the centre of such a fibre and expect to measure an atomic flux exiting. In the absence of any optical potentials, the atoms are attracted to the fibre walls due to the attractive van der Waals interaction which, if the curvature of the walls is ignored and the fibre is treated as a dielectric slab, is given by [15],

$$U_{vdW} = -\frac{1}{4\pi\epsilon_0}\left(\frac{\epsilon-1}{\epsilon+1}\right)\frac{\langle g|d^2|g\rangle}{8k_B x^3}, \tag{7.2}$$

where ϵ is the dielectric constant of the material, ϵ_0 is the absolute permittivity of free space [1], $\langle g|d^2|g\rangle$ is the matrix element of the square of the dipole operator and x is the distance from the wall.

An atom injected into the hollow core would soon become attached to the inside wall of the fibre. Only when the optical potential is greater than this attractive potential can atoms be guided. For two-level atoms, the potential from the optical dipole force is [16]

$$U(r) = \frac{\hbar\Delta}{2}\ln\left(1+\frac{I(r)/I_0}{1+4\Delta^2/\Gamma^2}\right), \tag{7.3}$$

where $\Delta = \omega - \omega_0$ is the detuning of the laser frequency ω from the atomic transition frequency ω_0, $I(r)$ is the field intensity, I_0 is the atomic saturation intensity and Γ is the natural linewidth of the transition. In this way, red-detuned light can propagate within the hollow core of the fibre thereby attracting atoms toward the centre of the core region away from the walls. Alternatively, blue-detuned light can be totally internally reflected within the glass fibre resulting in a small evanescent wave "leaking" into the hollow core. In this case the optical

[1] Otherwise known as the electric constant.

potential is repulsive therefore rebuffing atoms that come too close to the fibre walls.

7.3.1 Red-Detuned Guiding

Guiding of neutral atoms along a hollow-core optical fibre using light was pioneered experimentally by Renn *et al.* in 1995 [17]. The setup used is shown in Figure 7.7. A 3.1 cm long capillary fibre with an outside diameter of 144 μm and

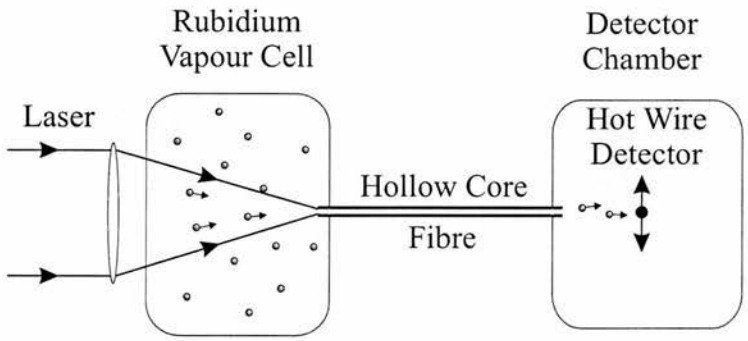

Figure 7.7: Experimental setup for red-detuned guiding in a hollow optical fibre. Laser light is coupled into the centre of the hollow fibre. Low transverse velocity atoms from the background vapour are coupled into the fibre and guided to the detector chamber. Reproduced from [17].

a hollow core diameter of 40 μm was used. Typically 45 mW of light from a titanium sapphire laser was focused into the central hollow. The grazing incidence modes decay exponentially as they propagate thus limiting the distance over which guiding could be achieved to a few centimetres. This is a grave limitation with red-detuned guiding in fibres but is remedied by using blue-detuned light as shall be discussed in Section 7.3.2. Atoms entered the fibre from the background rubidium vapour in the first chamber and were measured as they exited the fibre by a hot wire and channeltron. The experimental results, shown in Figure 7.8, were similar to those found in wire guiding. Atom guiding could be observed with the laser detuned from 1 to 30 GHz red of the rubidium D2 resonance lines with a maximum flux observed at 3 GHz. This experiment demonstrated the ability to guide atoms along either a straight or curved hollow optical fibre using a coupled

red-detuned Gaussian beam.

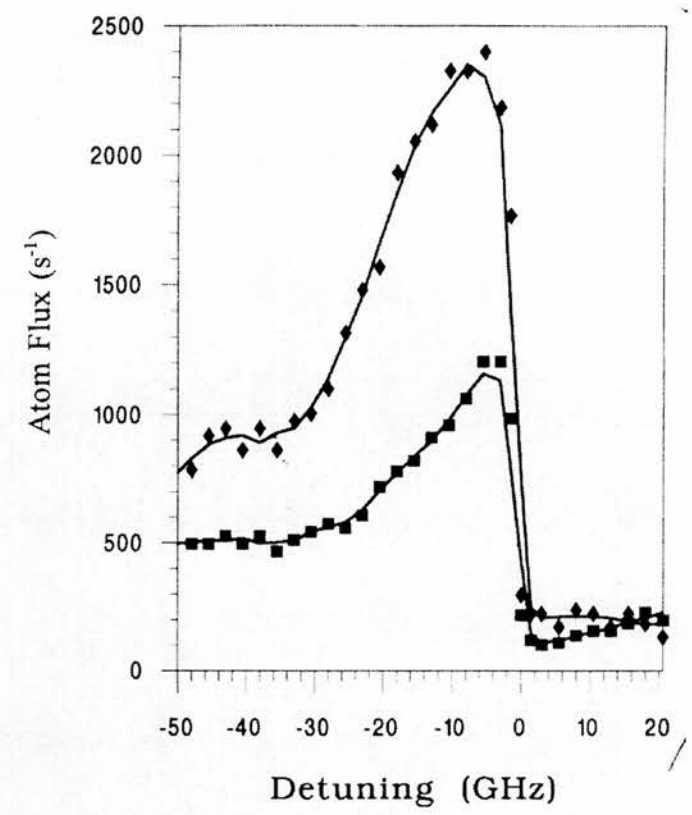

Figure 7.8: Guided atom signal versus laser detuning from resonance. The upper and lower curve relate to higher and lower guide laser intensities respectively. The data show a sharp increase in the number of guided atoms when the laser is tuned slightly to the red of the resonance line. Reproduced from [17].

Further studies revealed that the atomic flux was not solely dependent on the detuning but the intensity of light also. In 1997, Renn *et al.* [18] reported that at higher guide laser intensities, heating of the atoms due to spontaneous emission led to a "hole" being burnt in the flux spectrum. A graph of such a flux spectrum is shown in Figure 7.9. The interplay between a.c.-Stark shifts within the optical guide, spatial variation of the atom and spontaneous emission processes resulted in this "hole". At low intensities the dipole force is conservative and leads to a sharply peaked, roughly dispersion shaped flux spectrum, as can be seen in Figure 7.8. However, at higher intensities viscous heating forces became more apparent imparting transverse kinetic energy to the atoms. The "hole" arises

due to the heating forces at low and high detunings decreasing faster than the dipole potential. A more thorough and rigorous description can be found in literature [18].

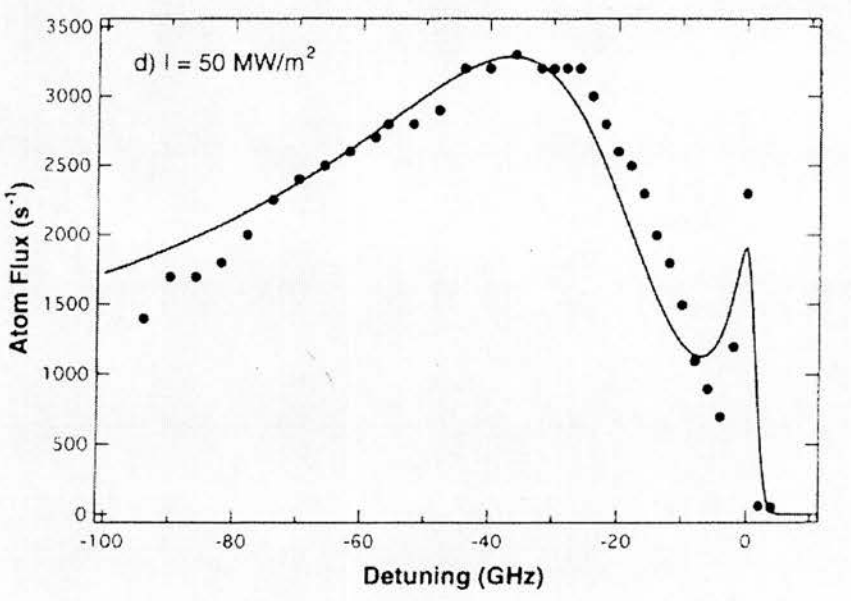

Figure 7.9: Guided atom flux versus laser detuning from resonance for a high laser intensity of 50 MW m^{-2}. A spike near zero detuning is observed due to the rapid turn off of the heating mechanism relative to the guiding potential as the detuning tends to zero. Reproduced from [18].

7.3.2 Blue-Detuned Guiding

The limitations of using red-detuned Gaussian beams when close to resonance and in hollow optical fibres are twofold. Firstly, random scattering of photons by atoms within the guide causes viscous heating thereby reducing atomic flux. This is not particular only to hollow fibres but to all red-detuned optical guiding. Secondly, the high coupling of the free-space laser mode into the surrounding fibre limits the distance over which guiding can be accomplished. A solution surmounting both of these problems is to use a blue-detuned guide beam coupled into the glass fibre region. In this way atoms are confined to low intensity regions

where spontaneous emission is minimised while the light propagates in modes along the fibre resulting in guiding over extended distances.

The first step taken in realizing blue-detuned hollow-core optical fibre guiding came experimentally in 1995 when Ito and co-workers [16] investigated the coupling of light from a laser into a hollow-core optical fibre. It should be noted that the fibre used by Ito *et al.* is different to that used by Renn *et al.*, as described in Section 7.4.1. Whereas Renn *et al.* used a simple capillary, Ito and colleagues used an actual hollow-core optical fibre complete with cladding. Modelling the propagation of supported modes in a fibre Ito and colleagues determined that, like any other optical waveguide, an exponentially decreasing field "leaked" into the surrounding cladding regions. Such quickly diminishing fields in such circumstances are known as *evanescent waves.* Approximately 100-200 nm from the hollow-core–glass-fibre boundary, the evanescent field for experimentally attainable laser powers, was calculated to be sufficient for guiding. Because the van der Waals interaction is extremely short ranged (it is inversely proportionally to the seventh power of the distance between atoms or molecules), the evanescent wave induced optical dipole force is large enough to surmount this attractive force at these modest distances.

Blue-detuned guiding of rubidium atoms was reported a year later in 1996 by Renn and colleagues [15]. The experimental setup was similar to that of Figure 7.7 with the exception that a second red-detuned escort laser was used to help couple atoms into the 6 cm long fibre. This laser was required because difficulty in coupling the blue-detuned laser field into the fibre created scattered light in the hollow core. To circumvent this mode-matching problem the second escort laser was red-detuned and focused into the hollow core of the fibre. Since both potentials generated by the scattered and the escort light in the hollow core decayed exponentially within the first few centimetres of the fibre, atoms were escorted through the entrance region to where the evanescent potential was dominant. As the escort laser decayed, the evanescent potential was present to guide atoms over the remainder of the fibre distance. Both beams were coupled

to the fibre via a polarising beam splitting cube. Experimentally 500 mW of blue-detuned guide light was focused into the beginning of the fibre while 10 mW was sufficient as the escort power. Optimum detunings from resonance of -1.6 GHz red-detuned for the escort laser and +3 GHz blue-detuned for the evanescent wave laser resulted in a factor of 4 increase in atomic flux measured at the hot wire. Qualitatively, the guiding was different from implementing red-detuned grazing incidence modes. Whereas in red-detuned guiding the atom was confined to the centre of the hollow core and interacted weakly with the van der Waals forces, the atoms in blue-detuned evanescent guiding interacted significantly more strongly resulting in an intensity threshold for guiding. This "turn-on" of guiding where the evanescent potential equals that of the van der Waals potential can be seen clearly in Figure 7.10.

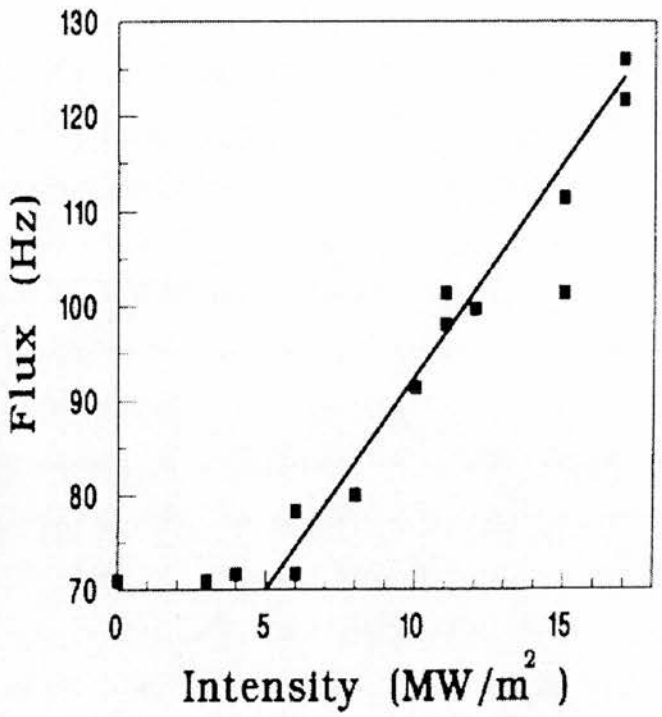

Figure 7.10: Intensity dependence of the evanescent-wave-guided atom flux. The threshold for the commencement of guiding can clearly be seen to be $\simeq$5 MW/m^2 and also that above threshold the atomic flux increases linearly with intensity. Reproduced from [15].

For inclusion into atom interferometers any form of guiding process must preserve

the coherence of the atomic states. Cold atomic ensembles are therefore required to be guided with minimal heating. An elegant experiment to investigate the effect of evanescent guiding on the kinetic motion of atoms extracted from a MOT was conducted by Müller and colleagues in 2000 [19]. Atoms from a LVIS were injected into the centre of a hollow core optical fibre bridging two separate vacuum chambers. The first vacuum chamber contained the MOT and cold atomic beam whilst the second housed the detection equipment. Blue-detuned light from a Ti:Sapphire laser was focused into the end of the fibre allowing evanescent guiding to take place. The fibres used ranged from 17 to 30.5 cm in length. The experiment analysed the spontaneous emission occurring during guiding by probing the internal states of the atoms exiting the fibre. This was achieved by introducing a probe laser perpendicular to the direction of the atomic flux upon exit from the optical fibre and tuned to the cooling transition. 90% of atoms exiting a LVIS are originally in the repumping ground state [19] and so with the probe laser present those atoms in the cooling cycle ground state absorb photons from the probe beam and are deflected allowing only those atoms in the repumping ground state to be counted. Figure 7.11 shows the atomic flux as a function of guiding laser frequency detuned from the hyperfine repumping transition.

At small detunings the internal states of the atoms have been pumped to that of the cooling cycle ground state indicating that a significant number of spontaneous absorption/emission processes have occurred. The overall flux is also lowered at these small detunings implying that the spontaneous heating mechanism increased the transverse kinetic energies of the atoms until they were no longer guided. At increased detunings the internal states of the atoms remained the same as those which they entered the fibre with i.e. the repumping ground state.

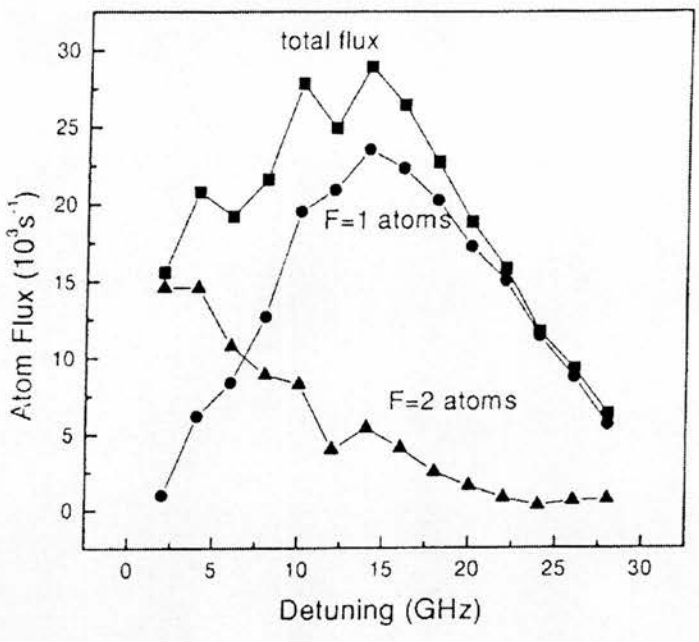

Figure 7.11: Detuning dependence of the guided atoms' internal states. At small detunings the atoms are optically pumped into the cooling cycle ground state as they are reflected off the evanscent light field (triangles). At large detunings the total flux (squares) consists of 90% of atoms in the hyperfine ground state (circles) which indicates suppression of spontaneous emission during the guiding process. Reproduced from [19].

7.4 Free-Space Light Beam Guiding

Much of the early work associated with atomic beams and guiding using light was carried out in conjunction with research in the field of laser cooling and trapping of neutral atoms. There are certain benefits to using light beams propagating in free-space as atomic guides over both previously mentioned schemes. The simplicity in focusing a laser into the trap region is in stark contrast to the preparation, manufacture and physical alignment of either a wire guide or a hollow fibre setup where an intra-vacuum element is always required. Also, there are no attractive forces such as the van der Waal's force to reduce the guided atomic flux although the ability to guide round bends is lost.

7.4.1 Red-Detuned Guiding

One of the earliest experiments concerning the free-space guiding of an atomic beam was reported in 1978 when Bjorkholm *et al.* [20] demonstrated the focusing, defocusing and steering of sodium atoms using a laser beam tuned close to resonance. In their experiment, a functional diagram of which is shown in Figure 7.12, a 50 mW focused laser beam propagated co-axially with a thermal atomic beam. A hot wire detector was used to record the flux and profile of the

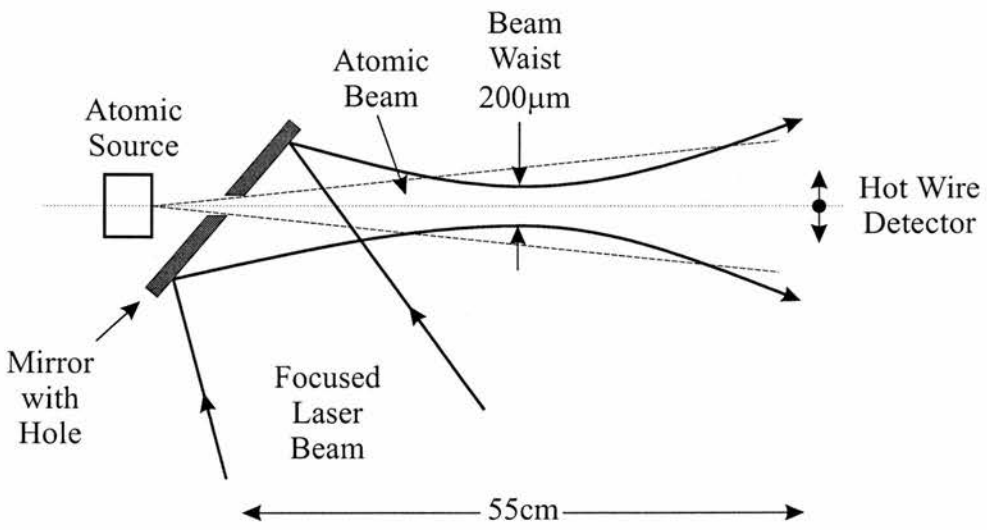

Figure 7.12: Schematic diagram of focusing of a thermal atomic beam using a red-detuned Gaussian beam. Note the differences in scales between the longitudinal and transverse directions. Reproduced from [20].

atomic beam. The guide beam was typically focused to 100 μm beam radius approximately halfway between the mirror and the detector using a 750 mm focal length lens. The laser was detuned, in turn, both red and blue the atomic transition frequency. The results they achieved, reproduced in Figure 7.13, show clearly the effect of the optical dipole force. When the laser was red-detuned the atoms were attracted to the areas of highest intensity i.e. the centre of the Gaussian beam, whereas when it was blue-detuned, they were repelled from the laser beam. Subsequent work by the same group improved red-detuned guiding by implementing higher guide powers and narrower beam waists [21] while

determining the minimum obtainable atomic beam spot size for a given guide power [22]. Again the spontaneous emission associated with red-detuned guiding was present. One method of overcoming this, as discussed in Chapter 6 and the previous section, is to use a high power guide beam that has been significantly red-detuned from resonance thereby reducing spontaneous emission whilst still providing a high guiding potential. Such a scheme has been experimentally demonstrated by Szymaniec *et al.* [23] in which a far-off resonance red-detuned beam was used to guide an atomic funnel from the centre of a MOT region to a second UHV chamber. The important feature of this experiment was that the phase space density of the atomic funnel was preserved. Therefore, the beam allowed confinement and guiding without heating.

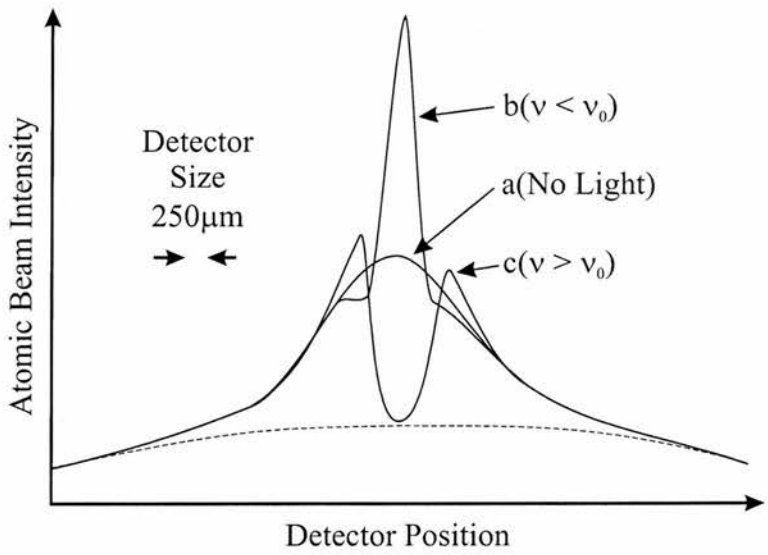

Figure 7.13: The atomic beam flux at the detector as a function of transverse detector position. ν is the frequency of the laser while ν_0 is the atomic transition frequency. The dashed line shows the approximate background intensity. Peak beam current is approximately 2×10^8 atoms s^{-1}. Reproduced from [20].

7.4.2 Blue-Detuned Guiding

To eradicate the the problem of spontaneous emission and heating effects without the need for high power far-off-resonance guide beams, atoms can be confined to

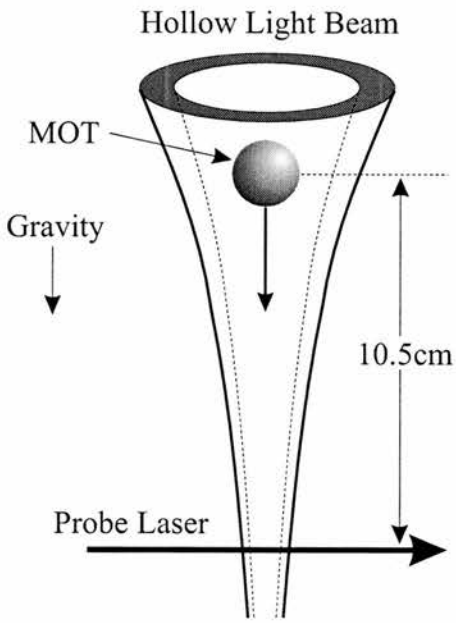

Figure 7.14: Functional diagram for the guiding of cold Rb atoms directly from a MOT within the centre of a hollow light beam. The beam can either be incident from above the trap, in which case it is co-propagating with gravity, or from below, in which case it is counter-propagating with gravity. The probe laser induces atomic fluorescence to allow the atoms to be counted. Reproduced from [24].

regions of low intensity by detuning the laser frequency blue of resonance. A beam suitable for this purpose would have a circularly symmetric intensity profile with zero light intensity at its centre. Balykin *et al.* [25] first evaluated the properties of an atomic laser lens that consisted of an atomic beam passing through the central zero intensity region of a Laguerre-Gaussian (LG) beam. Further publications extended these ideas [26] and provoked interest in higher-order LG beams as well as high order Bessel beams [27]. A description of the production and properties of LG beams can be found in Section 9.2.2. Experimentally, blue-detuned guiding using a "hollow" laser mode was realized in 1998 by focusing ultracold neon atoms within the centre of a LG ($\ell = 1$) beam [28, 29]. The following year, Song and co-workers [30] and Xu and colleagues [31] reported the guiding of atoms released directly from a MOT within a dark hollow beam. The setup for both experiments is shown in Figure 7.14. In the first of these experiments [30], the hollow light beam was generated by passing a TEM_{00} mode output from a diode

laser through a series of axicons to produce a thin annulus of light intensity in the far field. It should be noted that this annulus is not a laser mode and thus will not propagate over long distances in contrast to a LG beam. This annulus was then superimposed vertically, propagating either with or against gravity, over the trapping region. The atomic cloud was dropped and guided within the central dark region of the beam. It was shown that even though the atoms only interacted with the light field over a short period, this time was sufficient for the velocity of the atoms and the centre of mass of the falling cloud to be altered significantly by the detuning of the guide laser.

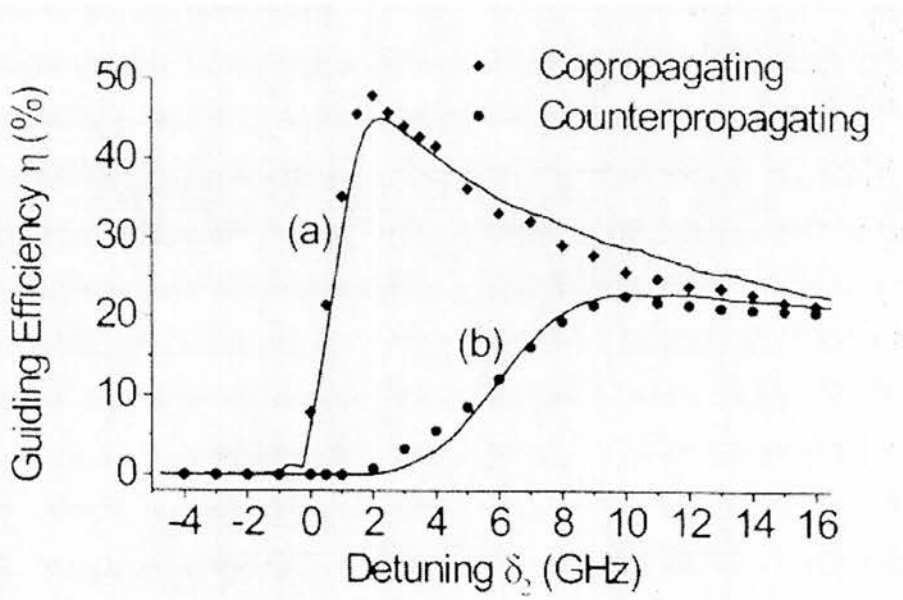

Figure 7.15: The guiding efficiency as a function of the detuning, δ_2, in the co-propagating (a) as well as the counter-propagating (b) scheme. The solid curves represent numerical simulations. Reproduced from [24].

The second experiment [31] had fundamentally an identical setup to the first but with the hollow light beam being generated from illuminating a micron-sized hollow optical fibre with the output from a Ti:Sapphire laser. Data from this experiment, shown in Figure 7.15, concluded that there existed a detuning for which optimal guiding occurred. Optimal guiding was defined by two parameters, the loading efficiency η_l which determined the fraction of atoms entering the guide and the guide efficiency η_g which quantified the fraction of those atoms detected

as an atomic flux after guiding. The loading efficiency, η_l, is expressed as,

$$\eta_l = \frac{N_{load}}{N_{MOT}}, \tag{7.4}$$

where N_{load} is the number of atoms that enter the guide and N_{MOT} is the total number of atoms in the MOT while the guide efficiency, η_g, is expressed as,

$$\eta_g = \frac{N_{guide}}{N_{load}}, \tag{7.5}$$

where N_{guide} is the number of atoms measured after guiding. The loading efficiency was determined by the relative radii of the MOT cloud and the guide beam while the guiding efficiency was determined by the intensity and detuning of the beam as well as the initial temperature of the atoms before loading. If the radius of the guide beam was increased in order to increase the number of atoms coupled into the guide, i.e. the loading efficiency increased, a decrease in intensity of the beam and therefore a reduction in the potential wall of the guide would occur reducing the guiding efficiency. Therefore optimal conditions exist for which a maximum flux of atoms can be guided. Experimentally it was observed that maximum guiding occurred with a laser detuning of 6 GHz. Detuning closer to resonance caused viscous heating to become important while further from resonance reduced the guiding potential.

7.4.3 All Optical Atomic Beam Splitters

In 2000, Houde *et al.* [6] reported the coupling of cold rubidium atoms released directly from a MOT into a far-off-resonance red-detuned beam splitter. The experimental setup is shown in Figure 7.16. The dipole guides were provided by a 15 W TEM_{00} CW Nd:YAG laser with a detuning from atomic resonance of approximately $-10^7\Gamma$, where Γ is the natural linewidth of the transition. Initially the guide beam was directed vertically through the centre of the MOT

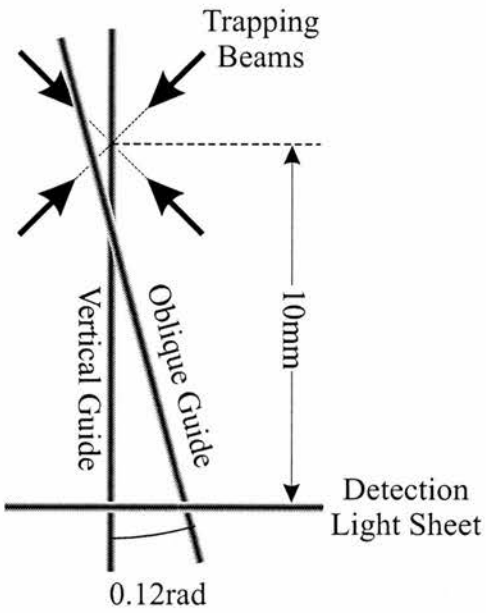

Figure 7.16: Experimental scheme for cold atom guiding using a far-off-resonance red-detuned laser. The MOT is represented by four trapping beams while the coils and remaining two beams have been omitted for clarity. Reproduced from [6].

region before being reflected and refocused to provide the second, oblique guide. The potential depths of the vertical and oblique guides were 30 and 10 μK respectively. Once a cold atomic ensemble of ^{87}Rb atoms had been produced, the trapping lasers were switched off and the atoms allowed to fall naturally due to gravity. Approximately 10% of the total number of atoms were captured within the vertical guide. When the atoms reached the intersection of the vertical and oblique beams, the oblique guide was switched on suddenly. In this way, the timing sequence allowed the atoms to be first guided by the vertical guide before being split by the second, oblique guide. The splitting was analysed 10 mm below MOT centre by a weak resonant light sheet, slightly red detuned, retroreflected and perpendicularly linear-linear polarised permitting reliable imaging without any transverse atom displacement.

Experimental results are shown in Figure 7.17. In this Figure, atomic density cross sections imaged at the light sheet are shown for (i) when only the vertical guide is present, (ii) when both guides are present and (iii) a numerical subtraction

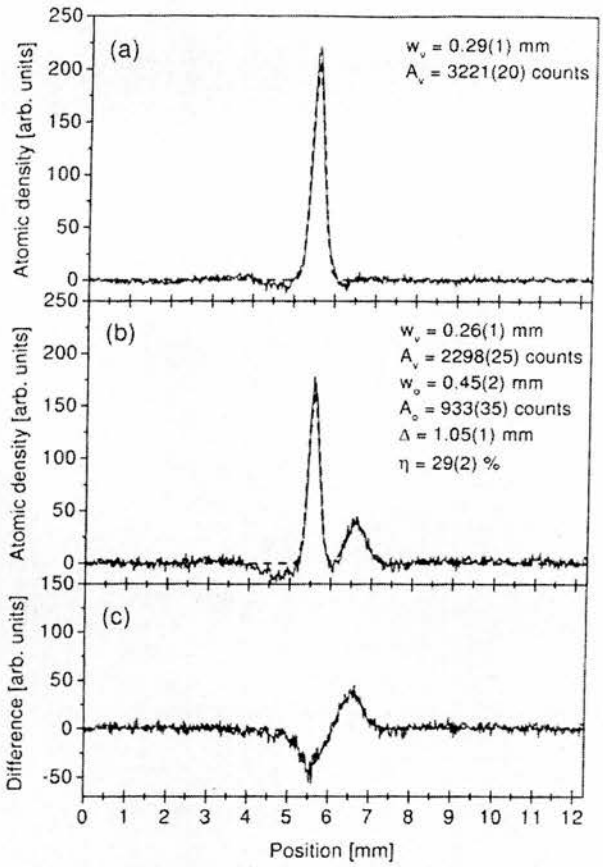

Figure 7.17: Results gained from the experimental apparatus shown in Figure 7.16. Atomic density cross-sections for (a) the vertical guide only, (b) two guides and (c) (b)-(a). Gaussian fits are shown by dotted lines. The letters in the figure refer to the peak areas, A_v for atoms in the vertical guide and A_o for atoms in the oblique guide, w_v andw_o are the $1/e^2$ beam radii, Δ the atomic peak separation and η the efficiency. Reproduced from [6].

of these two graphs. The important features of this experiment are that a high coupling efficiency from one guide to the other was achieved, typically up to 40%. Since minimal spontaneous emission occurred, the coherent properties of a BEC guided in such a manner could be preserved. Further, the large splitting angle, 0.12 rad, allowed an atomic splitting greater than the individual diameters of the atomic beams. From this it would be possible to produce an atomic interferometer in a reduced-size apparatus.

An interesting result obtained by Yan *et al.* [32] reported that atoms had been

directly coupled into and guided along a blue-detuned L-G beam crossing a LVIS. During the course of this project an experiment very similar in nature was performed in which their results could not be reproduced. As such, a discussion of this experiment shall be postponed to coincide with the reported experimental findings in Chapter 9.

7.5 Summary

This chapter has highlighted atom guiding and splitting as necessary elements in any atom interferometer. The experiments detailed outlined the three primary methods for guiding cold atomic beams, namely magnetic fields, hollow optical fibres and free-space light beams. Magnetic guiding has allowed the fabrication of a number of atom-optic elements directly onto a substrate permitting the possibilities of constructing small, compact atom interferometers. However, the small magnetic moment of an atom restricts the operation of these devices to a pulsed format and only certain atomic spin states can be guided. Utilizing the optical dipole force overcomes these problems in both hollow optical fibre and free-space light beam guiding. Red-detuning confines atoms to regions of highest light intensity while the opposite is true for blue-detuning. A disadvantage of red-detuning is the inherent viscous heating effect on the atoms due to them being spatially present in high intensity light fields. There are two generally acknowledged solutions to this problem. One is to use a far-off-resonance red-detuned beam to reduce spontaneous emission while providing an optical guiding potential. However, high powers are required to achieve the necessary guiding potential. The second is in implementing a blue-detuned laser beam with a zero intensity region at its centre thereby minimising spontaneous emission while providing high guiding potentials for modest beam powers. This final solution seems the most promising with respect to the preservation of atomic coherence in creating an all-optical atomic interferometer. It is along this avenue that research at St Andrews is currently progressing with Chapter 9 detailing experiments

performed during this research project in the guiding of cold atomic beams using laser beams.

Bibliography

[1] M. Sagnac, "L'éther lumineux démontré par léffet du vent relatif d'éther dans un interfèromètre en rotation uniforme," Compt. Rend. Acad. Scien. **157,** 708 (1913).

[2] H. J. Metcalf and P. van der Straten, *Laser Cooling and Trapping* (Springer-Verlag Inc., 175 Fifth Avenue, New York, NY 10010, USA, 1999), pages 219–229.

[3] D. Müller, E. A. Cornell, M. Prevedelli, P. D. D. Schwindt, Y. Wang, and D. Z. Anderson, "Magnetic switch for integrated atom optics," Physical Review A **63,** 041602–1(R)–041602–3(R) (2001).

[4] M. Kasevich and S. Chu, "Atomic interferometry using stimulated Raman transitions," Physical Review Letters **67,** 181–184 (1991).

[5] E. Rasel, M. Oberthaler, H. Batelaan, J. Schmiedmayer, and A. Zeilinger, "Atom wave interferometry with diffraction gratings of light," Physical Review Letters **75,** 2633–2637 (1995).

[6] O. Houde, D. Kadio, and L. Pruvost, "Cold Atom Beam Splitter Realized with Two Crossing Dipole Guides," Physical Review Letters **85,** 5543–5546 (2000).

[7] J. Schmiedmayer, "Guiding and trapping a neutral atom on a wire," Physical Review A **52,** R13–R16 (1995).

[8] J. Schmiedmayer, "A wire trap for neutral atoms," Applied Physics B **60,** 169–179 (1995).

[9] J. Denschlag, D. Cassettari, and J. Schmiedmayer, "Guiding neutral atoms with a wire," Physical Review Letters **82,** 2014–2017 (1999).

[10] D. Müller, D. Z. Anderson, R. J. Grow, P. D. D. Schwindt, and E. A. Cornell, "Guiding Neutral Atoms Around Curves with Lithographically Patterned Current-Carrying Wires," Physical Review Letters **83,** 5194–5197 (1999).

[11] W. Gerlach and O. Stern, "Der experimentelle nachweis des magnetischen moments des silberatoms," Zeitschrift fur Physik **8,** 110–111 (1921).

[12] D. Müller, E. A. Cornell, M. Prevedelli, P. D. D. Schwindt, A. Zozulya, and D. Z. Anderson, "Waveguide atom beam splitter for laser-cooled neutral atoms," Optics Letters **25,** 1382–1384 (2000).

[13] M. A. Ol'Shanii, Y. B. Ovchinnikov, and V. S. Letokhov, "Laser guiding of atoms in a hollow optical fiber," Optics Communications **98,** 77–79 (1993).

[14] S. Marksteiner, C. M. Savage, P. Zoller, and S. L. Rolston, "Coherent atomic waveguides from hollow optical fibers: quantized atomic motion," Physical Review A **50,** 2680–2690 (1994).

[15] M. J. Renn, E. A. Donley, E. A. Cornell, C. E. Wieman, and D. Z. Anderson, "Evanescent-wave guiding of atoms in hollow optical fibers," Physical Review A **53,** R648–R651 (1996).

[16] H. Ito, K. Sakaki, T. Nakata, W. Jhe, and M. Ohtsu, "Optical potential for atom guidance in a cyindrical-core hollow fiber," Optics Communications **115,** 57–64 (1995).

[17] M. J. Renn, D. Montgomery, O. Vdovin, D. Z. Anderson, C. E. Wieman, and E. A. Cornell, "Laser-Guided Atoms in Hollow-Core Optical Fibers," Physical Review Letters **75,** 3253–3256 (1995).

[18] M. J. Renn, A. A. Zozuluya, E. A. Donley, E. A. Cornell, and D. Z. Anderson, "Optical-dipole-force fiber guiding and heating of atoms," Physical Review A **55,** 3684–3696 (1997).

[19] D. Müller, E. A. Cornell, D. Z. Anderson, and E. R. I. Abraham, "Guiding laser-cooled atoms in hollow-core fibers," Physical Review A **61,** 033411–1–033411–6 (2000).

[20] J. E. Bjorkholm, R. R. Freeman, A. Ashkin, and D. B. Pearson, "Observation of Focusing of Neutral Atoms by the Dipole Forces of Resonance-Radiation Pressure," Physical Review Letters **41,** 1361–1364 (1978).

[21] D. B. Pearson, R. R. Freeman, J. E. Bjorkholm, and A. Ashkin, "Focusing and defocusing of neutral atomic beams using resonance–radiation pressure," Applied Physics Letters **36,** 99–101 (1980).

[22] J. E. Bjorkholm, R. R. Freeman, A. Ashkin, and D. B. Pearson, "Experimental observation of the influence of the quantum fluctuations of resonance–radiation pressure," Optics Letters **5,** 111–113 (1980).

[23] K. Szymaniec, H. J. Davies, and C. S. Adams, "An atomic fountain guided by a far-off resonance laser beam," Europhysics Letters **45,** 450–455 (1999).

[24] X. Xu, K. Kim, W. Jhe, and N. Kwon, "Efficient optical guiding of trapped cold atoms by a hollow laser beam," Physical Review A **63,** 063401–1–063401–4 (2001).

[25] V. I. Balykin and V. S. Letokhov, "The possibility of deep laser facusing of an atomic beam into the Å–region," Optics Communications **64,** 151–156 (1987).

[26] J. J. McClelland and M. R. Scheinfein, "Laser focusing of atoms: a particle-optics approach," Journal of the Optical Society of America B **8,** 1974–1986 (1991).

[27] J. Arlt, T. Hitomi, and K. Dholakia, "Atom Guiding along Laguerre-Gaussian and Bessel light Beams," Applied Physics B **71,** 549–554 (2000).

[28] S. Kuppens, M. Rauner, M. Schiffer, K. Sengstock, W. Ertmer, F. E. V. Dorsselaer, and G. Nienhuis, "Polarization-gradient cooling in a strong doughnut-mode dipole potential," Physical Review A **58,** 3068–3079 (1998).

[29] M. Schiffer, M. Rauner, S. Kuppens, M. Zinner, K. Sengstock, and W. Ertmer, "Guiding, focusing, and cooling of atoms in a strong dipole potential," Applied Physics B **67,** 705–708 (1998).

[30] Y. Song, D. Milam, and W. T. H. III, "Long, narrow all-light atom guide," Optics Letters **24,** 1805–1807 (1999).

[31] X. Xu, V. G. Minogin, K. Lee, Y. Wang, and W. Jhe, "Guiding cold atoms in a hollow laser beam," Physical Review A **60,** 4796–4804 (1999).

[32] M. Yan, J. Yin, and Y. Zhu, "Dark-hollow-beam guiding and splitting of a low-velocity atomic beam," Journal of the Optical Society of America B **17,** 1817–1820 (2000).

Chapter 8

Experimental Realization of Magneto-Optical Traps

M. A. Clifford, G. P. T. Lancaster, R. H. Mitchell, F. Akerboom and K. Dholakia, "Realization of a mirror magneto-optical trap"
Journal of Modern Optics **48**, 1123–1128 (2001).

8.1 Introduction

This chapter will detail the assembly and operation procedure of an ultra high vacuum (UHV)[1] system required for any atom trapping experiment. A number of magneto-optical traps (MOTs) have been custom built, tested and evaluated for their suitability in atom trapping throughout this Ph.D.. Each will be described and the choice of the individual geometries explained. The three traps described here are:

(i) Prototype MOT - The first "conventional" trap designed and built at St Andrews used to capture cold rubidium atoms. As well as describing the

[1]UHV is defined to be a system whose pressure is less than 10^{-7} mbar.

steps in its construction, the method for obtaining the first neutral atom cloud and all associated problems will be outlined.

(ii) Mirror MOT - A MOT in which the atom cloud can be placed close to a surface and requires only four instead of six trapping beams.

(iii) Ten-Way Cross MOT - This trap has the spatially confined trap region placed in the centre of a ten-way cross UHV piece. The extra viewports give improved visual access to the cloud and additional flexibility for experiments. This trap is used currently in all ongoing research.

This list describes the chronological order in which the traps were built. The overall objective of this work was to obtain guiding of cold atoms. The initial prototype trap was built simply as a proof-of-principle experiment for obtaining a functioning MOT. Some elementary guiding results were taken while using this trap in addition to polarisation spectroscopy experiments. These are reported in Chapters 3 and 9 respectively. The mirror MOT was constructed as a way of trapping an ensemble of atoms using only two input beams and of extracting and guiding atoms vertically downwards through a hole drilled in one of the optics. Instead of allowing a passage through which the atoms could leave, the hole prohibited the formation of an atomic cloud placed directly above it. Nevertheless, the trap was successful in obtaining an atomic cloud in close proximity to a reflecting surface which is of importance in certain magnetic guiding experiments, as discussed in Section 7.2. Finally, the ten-way cross trap was chosen because of its flexibility in allowing different guiding geometries, improved access for guiding beams and viewing. This is currently the operational trap in the laboratory and has provided guiding data for a number of different lightbeams.

8.2 Prototype MOT

8.2.1 Construction

A photograph of the prototype MOT used initially in proof-of-principle experiments is shown in Figure 8.1. The trap was mounted on a standard UHV six-way cross. The trap consisted of a glass cross (80 mm x 80 mm x 120 mm with five 25 mm diameter windows) blown in-house by the School's glassblower, Fritz Akerboom. The five windows, through which the trapping beams pass, were of optical quality. The sixth optic in the setup was a viewport placed on the bottom of the six-way cross. The base of the cross was blown and affixed to a blank flange that had a 36 mm diameter hole drilled in it. The hole facilitates access of one of the trapping beams to trap centre. A background vapour of rubidium (Rb) must be present for trapping. One conventional method of doing this is by using a *cold finger* in which alkali metal is released into the apparatus and is allowed to settle on the inner surfaces. To release the vapour pressure the outside of the vacuum chamber is heated. Another method is to insert a glass enclosed ampule of the specific alkali metal within the vacuum, break the glass and use a heating element to provide the background vapour. In the work described within this chapter, relatively new and little used getter ovens (SAES Getters, UK) were implemented to generate the background vapour required for trapping. These are metal enclosed capsules which split and release alkali vapour when an electrical current is passed through them. Getter ovens have a number of advantages over the previously mentioned systems including the ease in which they can be integrated into UHV apparatus and that the vapour release can be localised within the vacuum. These ovens were connected via an electrical feedthrough on one arm of the six-way cross. A 40 ℓs^{-1} ion pump (Varian, VacIon Plus 40 Triode, Model 919-0201) kept the vacuum within the apparatus at $\sim 10^{-9}$ mbar. A blank flange is also included on one of the arms as well as a T-piece which can be connected to a turbo pump (Varian, Turbo-Dry 70) taking the trap system from air pressure to 10^{-6} mbar. All flanges were bolted with copper gaskets between them, except

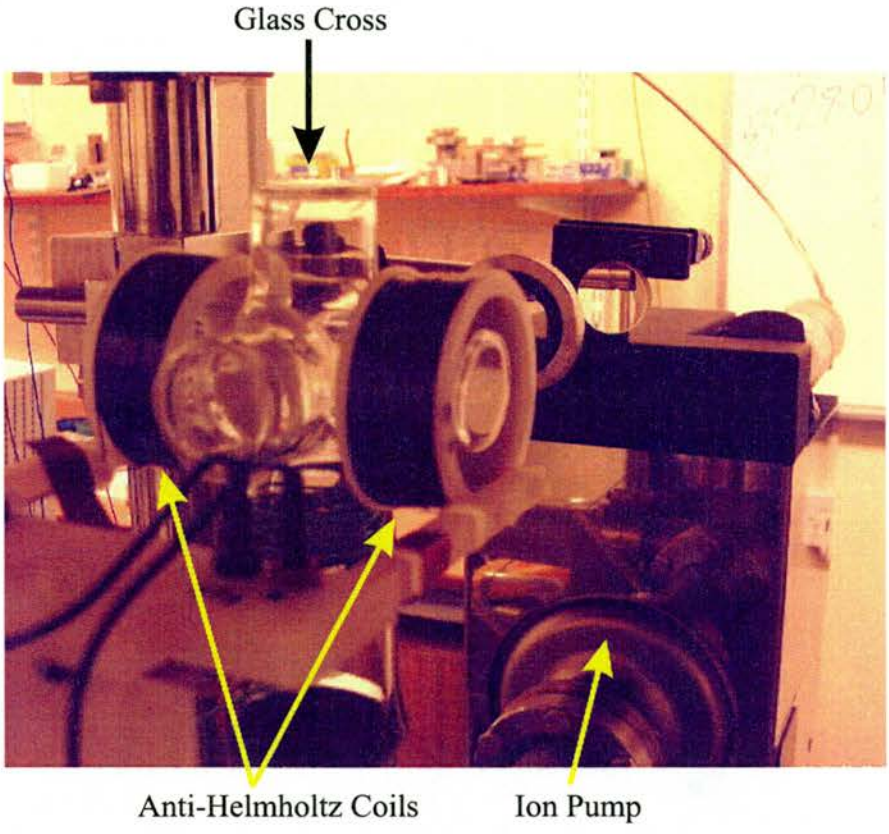

Figure 8.1: (Colour) A photograph of the prototype atom trap.

in the case of the viewports which required annealed copper gaskets to alleviate stress on the windows. Care was required when handling all parts of the vacuum system and disposable latex gloves were worn at all times to avoid contaminating any of the surfaces with oil or dirt from skin contact. It is good practice therefore to keep all component parts in their packaging until immediately before use. It should also be noted that when joining flanges, opposite bolts should be tightened in pairs to avoid undue stress on the metal and to ensure a high quality seal.

8.2.2 Bakeout

The primary concern in the construction of an atom trap is that UHV is required. Although atoms can be observed at pressures of 10^{-7} mbar [1], excess collisions with hot background atoms/molecules result in decreased trap lifetimes. For most

cold atom experiments a vacuum pressure of less than 10^{-8} mbar is needed. In order to reach these pressures the vacuum apparatus was required to be baked to high temperatures to rid the interior surfaces of contaminants, especially water vapour, which are detrimental to trap operation. This subsection details the procedure implemented before any of the trap configurations discussed in this chapter were used experimentally.

Several thermocouples were placed at different areas on the apparatus to monitor the temperature during bakeout. The vacuum system, including the ion pump, was wrapped as evenly as possible with two electrical heating cables and any viewports or optical elements covered entirely in aluminium foil. The whole apparatus was then wrapped in aluminium foil for insulation purposes and placed in a metal oven. The turbo pump was connected to the T-piece, started and the heating cables switched on. The temperature was raised to $\sim 150^{o}$C and left for approximately 48 hours. The heating tapes were reduced in current and temperature allowed to cool to $\sim 75^{o}$C before the turbo pump was switched off and the ion pump started. The bakeout continued at this temperature for another 24 hours before the heating tape was switched off. On cooling, the pressure measured by the ion pump current gauge was approximately 10^{-9} mbar. This is sufficiently low for use in atom trapping experiments. The rubidium in the ovens is protected from the atmosphere by being enclosed in a protective, metal case. The case has a score along one side and in order that rubidium be released this has to be split by heating the oven until it fractures. Passing a high current through the ovens is the usual method of achieving this. Before the trap can be used, the rubidium getter ovens needed to be degassed and opened. This was done by carefully turning up the drive current to the ovens. Contaminants evaporated off the ovens and surrounding area surfaces and entered the vacuum. The ion pump then swept these out although monitoring the ion pump current was required as too high a current would result in the safety switch in the ion pump tripping. The current to the ovens was slowly ramped upwards with rest periods when it was switched off to allow the vacuum to recover. As the ovens degassed, the current could be increased. Typically with ~ 5 A the ovens were degassed and

anything above this up to 9 A broke the seal[2]. To confirm when the seal had been broken required observing the Rb vapour using a charge coupled device (CCD) camera while the trapping lasers were tuned to one of the Rb transitions. On rubidium being released, a line of fluorescence could be observed as the laser induced spontaneous emission in the vapour.

8.2.3 Trap Operation

The anti-Helmholtz magnetic field was generated by winding 57 turns of 0.6 mm diameter insulated wire onto two plastic drums (40 mm inside diameter) and placing these round the glass trapping region. These parameters were calculated to give a field gradient of 10 G cm^{-1} at trap centre from a computer program written in Mathematica. The program is contained in Appendix B. The coils were wired to a variable current power supply allowing the magnitude of the magnetic field to be controlled.

The output from an extended-cavity diode laser (ECDL) described previously in Chapter 3 was used as the cooling laser and passed through a beam expanding telescope consisting of a f=-25 mm and a f=+300 mm lens separated by 275 mm. This enlarged the beam to ~20 mm in diameter. The beam was then split at a 70/30 beam splitter and also a 50/50 beam splitter to give three beams of approximately equal power. The total power in the beams was measured to be 12 mW. Beam steering mirrors of 1 inch diameter (silver coated, 99% reflective @ 780 nm) were then used to direct the beams into the trapping region. Before entering the trap, each of the three beams passed through a quarter-wave plate orientated correctly which depended on the geometry of the anti-Helmholtz coils. Figure 8.2 shows the handedness of the circularly polarised light relative to the anti-Helmholtz coils. Each of the three beams was then retro-reflected by means of three dielectric mirrors (99.9% reflective @ 780 nm) with a quarter-wave

[2]When the seal is broken, the current should be reduced immediately to 1 or 2 Amps or switched off entirely.

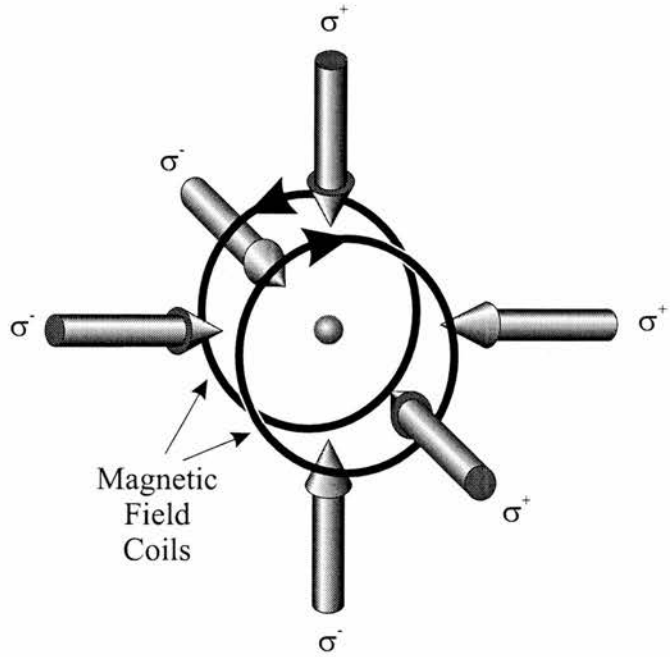

Figure 8.2: Schematic of the MOT. Laser beams are incident from all six directions and have angular momenta as shown. The coils have current flowing in the direction of the arrows which produces a zero magnetic field in the centre which varies linearly along all three mutually perpendicular axes.

plate placed in front of each of them. This generated six mutually orthogonal beams with correct handedness of circular polarisation at the trap centre. The orientation of the retro-reflecting wave plates was unimportant. The hyperfine laser output was focused gently into the trapping region using a f=+300 mm lens ~100 cm from trap centre. A CCD camera sensitive in the infrared (IR) was orientated towards the trapping region to observe the fluorescence of the trapped cloud and the image viewed on a TV monitor.

At this point it is worth noting that several weeks were lost when trapping could not be conducted in the prototype trap because of an unknown error in the experimental setup. After ensuring that rubidium was present in the vacuum, the lasers had a narrow enough linewidth and were tuned to the correct frequencies, the beam alignment through the trap was good and that the coils were operating in the correct anti-Helmholtz configuration it was eventually discovered that one

of the input quarter-wave plates had its fast and slow axes defined in a manner opposite to the other five. All six were purchased from the same supplier and so, with good faith, it was assumed that each would have their fast or slow axis defined identically with respect to the chord cut on the optic. An experiment was conducted to determine the optical properties of the six quarter-wave plates. Two wave plates were placed together with the chords defining either their slow or fast axis aligned. This unit now performed as a half-wave plate. Placing this in a linearly polarised laser beam with the fast/slow axis aligned at 45^o to the beam polarisation would result in a 90^o rotation of the beam's polarisation. Through testing of all six wave plates in pairs it was found that one had its fast axis defined the same way that all of the others had their slow axis defined. By bad luck, this particular wave plate happened to be placed on the input side of the trap where the orientation was important (if it had been placed in front of one of the retro-reflectors then the trap would have worked regardless of the ill-defined quarter-wave plate. It is likely, however, that the problem would have reared its ugly head at some inopportune moment in the future!). Personally, this was an invaluable lesson in experimental physics early on in my Ph.D. and made me aware that no part of an experiment, however simple it may appear to be, should be nonchalantly overlooked. The moral of this story is: never take anything for granted!

Trapped atoms were obtained in this MOT by the following means. Firstly it was ensured that all wave-plates were orientated correctly and that the six beams were well overlapped in the centre of the trap. The trapping laser was tuned and locked approximately 2Γ, where Γ is the natural linewidth of the cooling transistion, lower in frequency than the $5S_{1/2}F = 3 \rightarrow 5P_{3/2}F' = 4$ transition for ^{85}Rb (or the $5S_{1/2}F = 2 \rightarrow 5P_{3/2}F' = 3$ transition for ^{87}Rb) while the hyperfine pumping laser was tuned and locked[3] to the $5S_{1/2}F = 2 \rightarrow 5P_{3/2}F' = 3$ transition for ^{85}Rb (or the $5S_{1/2}F = 1 \rightarrow 5P_{3/2}F' = 2$ transition for ^{87}Rb). In

[3]While locking of the hyperfine laser was not absolutely necessary for operation of the trap, drifting of the frequency over tens of seconds or a minute affected cloud size and if any reproducible results were to be taken then the locking of this laser was a prerequisite.

our initial experiment approximately 12 and 6 mW of trapping and hyperfine pumping power, respectively, were used. The rubidium getter ovens were turned on by passing a few amperes of current through them. In practice, the current required to sustain a reasonable background vapour varied depending on the actual ovens used. This ranged typically between 2.5 and 5 A. As the time the ovens had been in use increased, the current needed to be increased to generate the same vapour pressure such that the background vapour should be visible in the trapping region at all times . To generate the magnetic quadrupole, current was passed through the field coils. For the size of coils and number of turns of wire described previously, 2 A of current was sufficient to provide 10 G cm^{-1}. A Mathematica program was written to model the current required to achieve this field gradient with this being reproduced in Appendix B. If this procedure is followed as described then at this stage a cloud of trapped atoms should be seen on the TV monitor. An image of an cold atomic cloud captured using the CCD camera is shown in Figure 8.3.

8.2.4 Trap Characterisation

In a MOT, the cooling mechanism results in spontaneous re-emitted photons being ejected over 4π steradians from the cloud region. By collecting and measuring fluorescence from a cloud over a solid angle and dividing by the photon emission rate from a single atom in the trap, the number of atoms in that cloud can be calculated. The number of atoms trapped in a typical sized cloud, which was obtained on a regular basis, was measured in the following fashion. A 1 inch diameter f=+38.1 mm focal length lens was used to image the cloud through the glass trap onto a photodiode. The lens was placed in a black cardboard tube to eliminate any stray light from outwith the trapping region entering the photodiode. The experimental setup is shown in Figure 8.4.

The lens was placed 100 mm away from the cloud and 60 mm from the photodiode. To make a reliable measurement of the number of atoms, it was crucial to

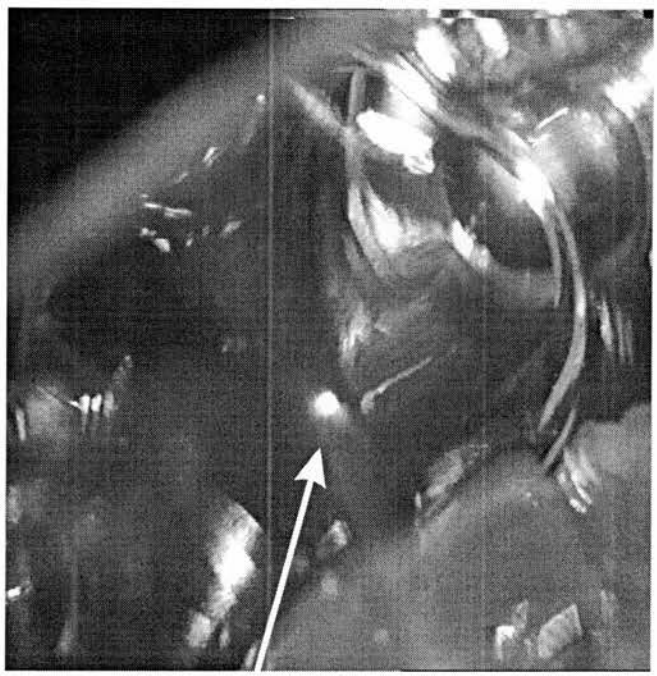

Figure 8.3: Captured image using an infrared sensitive CCD camera of trap centre showing a cloud of cooled and trapped rubidium atoms.

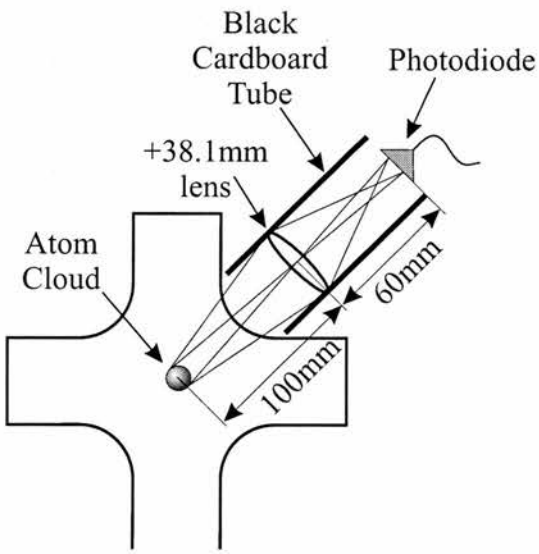

Figure 8.4: Diagram of the setup used to measure the number of atoms in the trap.

differentiate accurately between the fluorescence signals from the cloud of trapped atoms and the background fluorescence and scattered light from the trap apparatus. This was done by comparing the photodiode voltages when the cloud was present and when it was absent. The trap must therefore be disabled in such a way as to have negligible impact on the background fluorescence. The method used was to turn the magnetic field coils off. Although the fluorescence of the background vapour changed slightly, the change was small in comparison to the fluorescence emitted from the cloud.

Calibration of the photodiode was achieved by illuminating it with a fraction of the trapping beam when it had been removed from the experimental setup. By carefully monitoring the incident laser intensity on the photodiode, a difference in power could be measured relating to the recorded difference in voltage between when the cloud was present and when it was not. This was the power radiating from the cloud over the measured solid angle and by a simple calculation the total power emanating from the cloud could be calculated along with the total number of photons per second.

The scattering rate (i.e. the number of photons scattered per second per atom)is

defined as Equation 8.1 [2]:

$$R = \frac{(I/I_S)\Gamma/2}{1 + (I/I_S) + 4(\Delta/\Gamma)^2} \tag{8.1}$$

where I is the total intensity of the six trapping beams, I_S is the saturation intensity for rubidium (1.63 mW/cm^2) [3], Γ is the natural linewidth of the transition ($2\pi \times 6.1$ MHz) and Δ is the detuning of the trapping laser from resonance. With 9 mW of laser power at the trap $\sim$ 8x10^7 atoms were obtained.

An experiment was also conducted to measure the trap filling time. If the trap is suddenly turned on at time t=0 then the number of atoms , N, in the trap will increase in a similar fashion to that of a charging capacitor and is described by:

$$N(t) = N_0(1 - e^{-t/\tau}) \tag{8.2}$$

where τ is the time constant for the trap to fill to its steady state[4] and N_0 is the steady state number of trapped atoms. The experimental setup was identical as was used for measuring the number of trapped atoms except a digital oscilloscope (Tektronix TDS360) was used to output a time dependent cloud intensity. The lasers were locked and the magnetic field switched off momentarily before being turned back to the original level again. The recorded intensities for different background vapour pressures are shown in Figures 8.5 and 8.6.

[4] τ is also the average time an atom will remain trapped

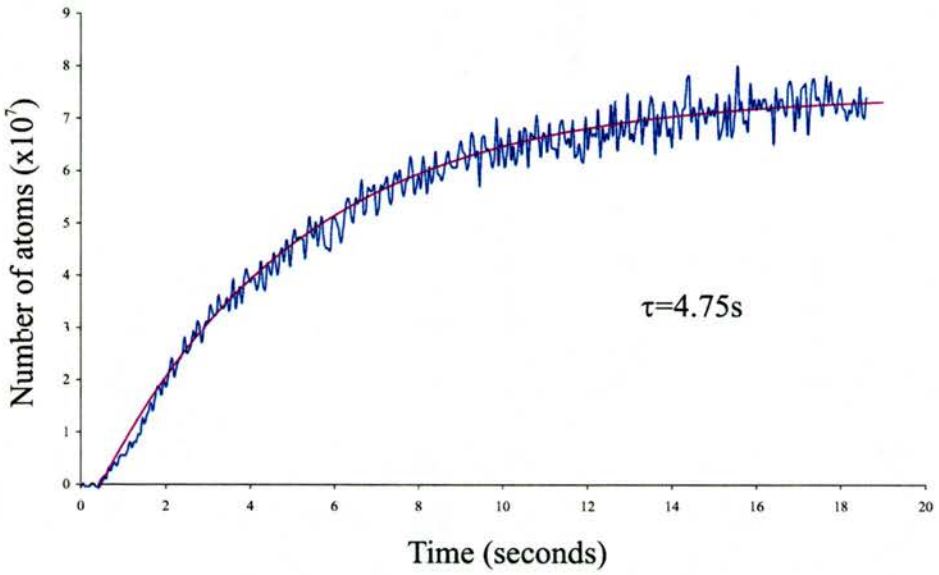

Figure 8.5: (Colour) Number of trapped atoms verses time after the trap is turned on at 0.45s. The recorded photodiode voltage is shown in dark blue while the pink line is a theoretical fit of Equation 8.2 with $\tau = 4.75$s.

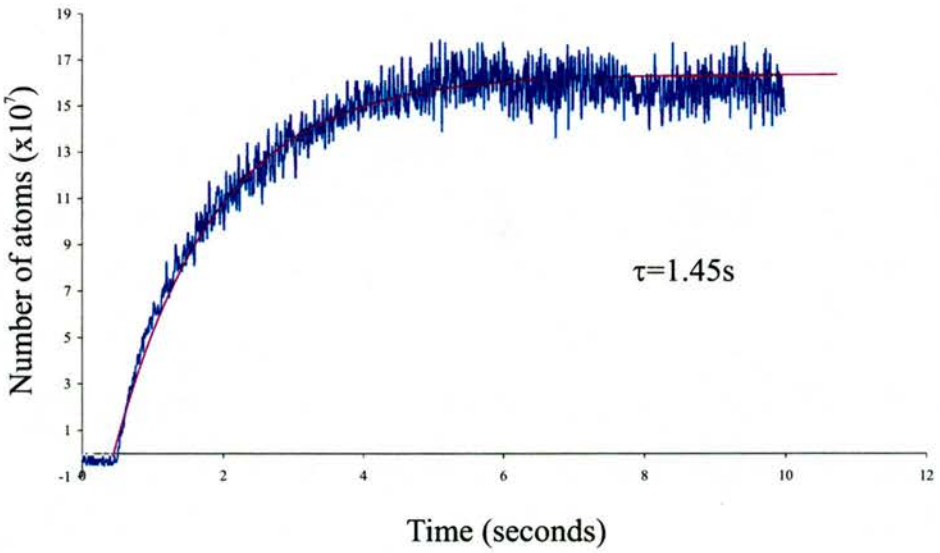

Figure 8.6: (Colour) Number of trapped atoms verses time after the trap is turned on at 0.43s. The recorded photodiode voltage is shown in dark blue while the pink line is a theoretical fit of Equation 8.2 with $\tau = 1.45$s.

8.3 Mirror MOT

8.3.1 Motivation

The ability to cool and trap neutral atoms close to a metallic or dielectric surface is of relevance in two main research areas in atomic physics. Firstly, the investigation of atom-surface interactions once the thermal motion of the atom has been minimised can reveal additional structure to atomic energy levels due to effects such as the contribution of the van der Waals interaction [4]. Also, as outlined in Section 7.3, manipulating atomic motion utilizing magnetic fields has important consequences in the guiding and transportation of cold atoms. Novel methods of guiding atoms a fraction of a millimetre above the surface of a substrate using thin wires etched into the surface is bringing forth the realization of atom-optic components [5], "atom chips" [6] and atomic waveguides [7]. If the atoms are to be loaded into these structures from a MOT then it is clear that the trap must be placed close to the substrate surface. Furthermore, the mirrored surface enables trapping to be achieved with only two cooling beams in contrast to three that are necessary in a conventional MOT. Pyramidal and conical traps can also provide a sample of cold atoms near a surface whilst only requiring one cooling beam but these can be commercially expensive to manufacture [8]. In this section a mirror MOT is constructed allowing cold atoms to be placed approximately 1 mm above a mirrored surface.

8.3.2 Construction

This trap was mounted on one flange of a standard six-way UHV cross-piece. Figure 8.7 shows a picture of the assembled mirror MOT. The whole apparatus was held at a base pressure of 10^{-9} mbar by a 25 ℓs^{-1} ion pump (Varian, VacIon Plus 25 Triode, Model 911-5030). A blank vacuum flange was bored with a 25 mm hole. A metallic cylindrical holder was placed on this hole (2 cm in

length) upon which a right-angled metal-coated prism was attached. Two small holes on one side of the flange were drilled to allow placement of a rubidium getter oven (SAES Getters, UK). The getter oven is an alkali metal dispenser that releases rubidium vapour when sufficient current flows through it. The rubidium source was placed in close proximity (~2 cm) to the trapping region. Further, the walls of the vacuum vessel acted as pumps for any excess rubidium vapour present and thus the remainder of the vacuum system (notably the ion pump) was not contaminated by rubidium. It was experimentally found that it was advantageous to have an unobstructed path between the Rb oven and the trapping region, although this need not be a direct line of sight. The Rb oven was connected, using kapton wire, to an electrical feedthrough placed on one arm of the six-way arm of the cross. Typically a current of a few amperes were passed through the oven to generate sufficient rubidium at the trap region. Placed over this was a right-angled prism with a mirrored surface at 45^o to the horizontal. Note that a hole has been drilled through the centre of the mirror this setup. This was to facilitate the possible extraction of cold atoms directly from the mirror MOT. A quartz cuboid was placed over the right-angled prism and rubidium getter and was affixed to the flange[5] using a low vapour pressure torr seal (Caburn, UK). An inexpensive commercially available cuboid (Hellma, England) having outer dimensions 40 mm x 40 mm x 70 mm and a wall thickness of 4 mm was used. The cuboid had one open end and was fused on all other sides. The glass was of optical quality, the typical use for such a cuboid being in spectrometry. Several of these cells have been used and found to serve as excellent and very inexpensive cells for atom traps. The position of the Rb getter oven is indicated. Two coils were placed around the trap in an anti-Helmholtz configuration. Each had 100 turns and carried a current of approximately 1.5 A in typical experimental conditions yielding a field gradient of ~10 G cm^{-1}. It should be noted that experimentally we found that careful positioning of these trap coils was critical due to the relatively small trapping region above the mirror

[5]Initially a groove was machined into the flange into which the cuboid was placed but due to difficulties experienced when baking the trap the cuboid was subsequently affixed directly to the flat flange surface. See Section 8.3.3 for further details.

surface.

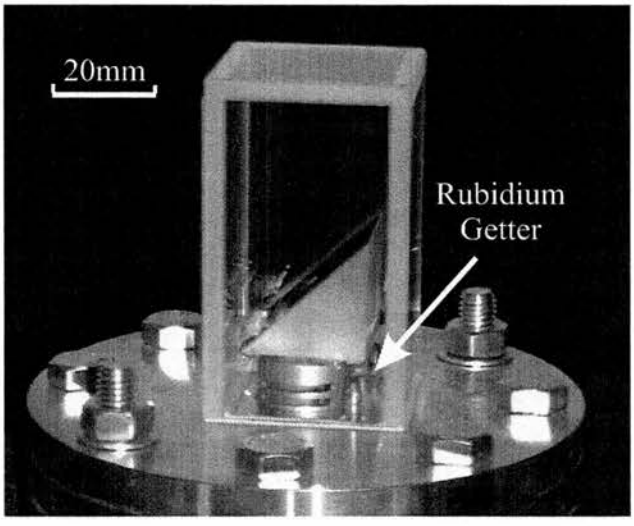

Figure 8.7: (Colour) A photograph of the assembled mirror MOT. The Rb getter is located behind the right-angled mirror. Although the Rb is pumped by the walls of the trap, the gap of a few millimetres between the mirror and the wall is enough to allow sufficient Rb vapour to reach the trapping region.

8.3.3 Bakeout

The bakeout was carried out in exactly the same manner as described in Section 8.2.2 apart from the initial bake only being allowed to reach 110°C. This was to to the epoxy restrictions. However, the first attempt at baking resulted in the quartz cube cracking along one of its faces. Initially the cube was epoxied into a 1 mm deep machined groove on the surface of the flange. The quartz cube cracked because, on baking, a mismatch existed between the expansion coefficients of the metal flange and the quartz causing a stress fracture along one of the cube faces. Subsequently a new quartz cuboid was epoxied directly onto the surface of a vacuum flange without a groove being present This new cuboid did not suffer the same stress fracture that terminated the first attempt on baking.

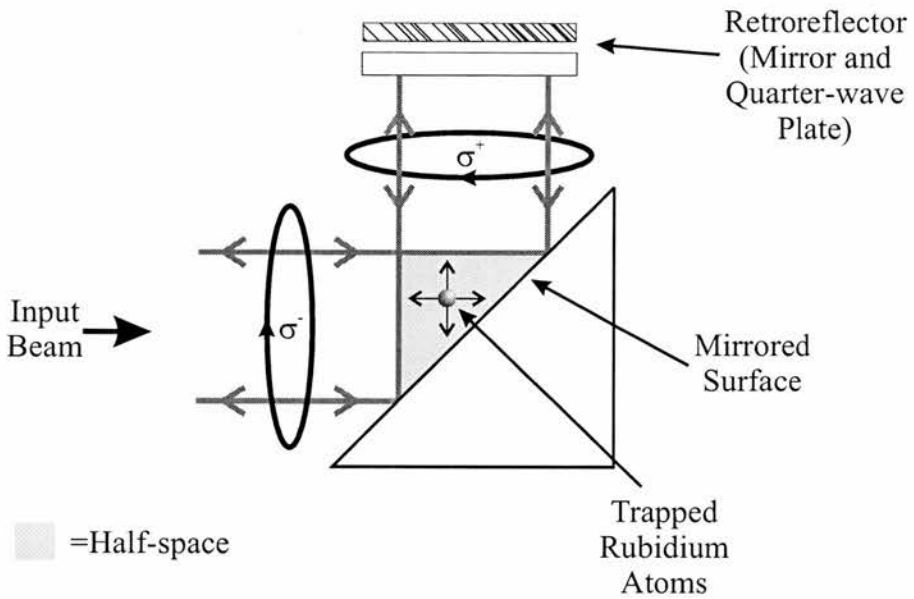

Figure 8.8: A layout showing the polarisations and laser orientation requirements for trapping. σ^+ denotes right handed circular polarisation and σ^- denotes left handed circular polarisation. The arrows in the overlap region show how a single incident beam can generate two orthogonal trapping beams by reflection above the mirror surface. The overlap region here also denotes what is termed the "half-space" above the mirror surface (shaded area). Note here there is a further beam in and out of the plane of the page that is not shown.

8.3.4 Trap Operation and Characterisation

Only two mutually orthogonal laser beams are required to operate the mirror MOT. One beam is reflected at 45^o by the mirror and is retroreflected. In the half-space defined by the mirror, see Figure 8.8, this creates four orthogonal overlapping beams. The term half-space here refers to the region of overlap above the mirror surface created by this first beam and its retroreflected counterpart. A second beam (also retroreflected) is sent in at grazing incidence to the mirror surface. Figure 8.9 shows the directions of the two required input cooling beams for this trap and also the magnetic field coil placements.

The ECDL systems used in this experiment are detailed in Chapter 4. These take form of two novel ECDLs operating at 780 nm and having 40 mW output power but which have a virtual point microlens attached immediately in front of the

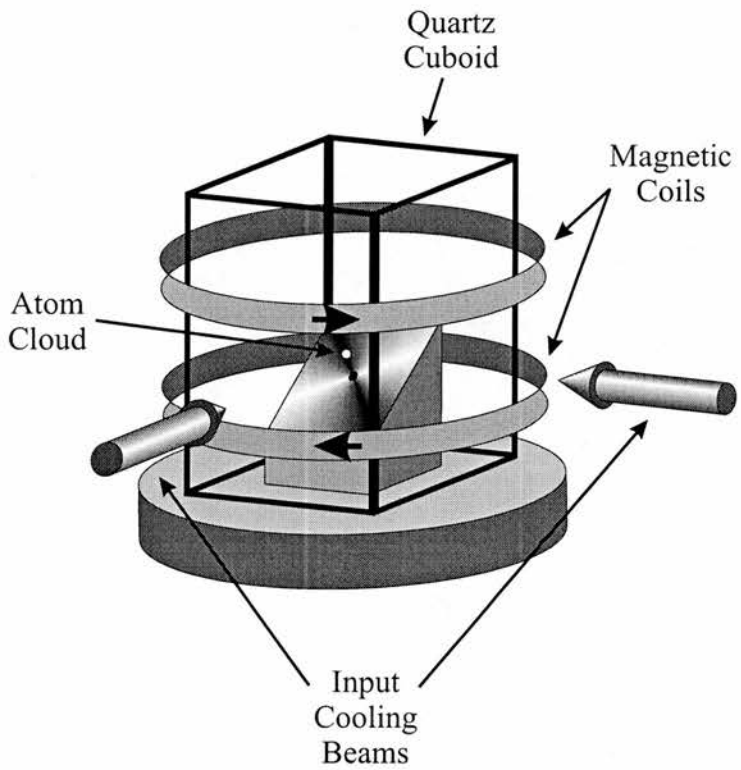

Figure 8.9: Schematic diagram of the mirror MOT. The trap requires only two input cooling beams, the directions of which are shown. The anti-Helmholtz coils are positioned around the quartz cuboid with the arrows indicating the direction of current flow.

output facet of the diode. This produces a circular divergent laser beam without the need for extraneous beam shaping optics thereby simplifying the experimental setup. The outputs from two such lasers were expanded using a telescope consisting of a f=-25 mm focal length lens and a f=+300 mm focal length lens separated by 275 mm. This produced a beam with diameter of approximately 20 mm suitable for trapping. Before entering the trap region, the polarisation of the light was changed into the correct right-hand or left-hand polarisation by way of correctly orientated quarter-wave plates. The lasers were used unlocked initially because of their inherent stability characteristics, as discussed in Chapter 4. For long trap times the lasers were stabilized using polarisation spectroscopy [9] and readers are referred to Section 3.3.1 where the this technique is presented.

Clouds of atoms could only be observed when the trap centre was located a few millimetres above the mirror surface. It is worthy to note that the operation of the trap was very sensitive to the positioning of the field coils. With incorrect coil heights offset from the optimum value by as little as 5 mm, trapping could not be observed. By varying the relative currents in the coils, the cloud could be translated vertically in a controlled fashion. A series of images showing this is shown in Figure 8.10(a)–(c). As the cloud neared the mirror surface, however, its size reduced dramatically until it vanished completely. Scattered light can be seen emanating from a hole drilled vertically through the mirrored prism. This hole was originally included in the design to allow cold atoms to be either dropped or guided through it. However, it was found that due to the proximity of the atomic cloud to the surface and the fact that a zero intensity region was present in the centre of the reflected beam, trapping could not be achieved directly above the hole. A possible solution to this would be to drill the hole at an arbitrary angle from the vertical and rotate the entire trap respectively.

Beginning from a pair of magnetic coils with equal current flowing in each, the measured movement of the atom cloud was approximately 1 mm per 10^{-4} Tesla difference induced between the coils. This was to be expected considering that the field gradient in the vicinity of the trap centre is 10 G cm^{-1}. Careful alignment

of the trapping beams maximised their overlap. Approximately 10^8 atoms were recorded from atomic fluorescence measurements taken by a photodiode using 21 mW of trapping power. Trap lifetime was determined by monitoring the trap fluorescence versus time and fitting the resultant curves to extract the characteristic time constant[6]. This is done in a similar fashion to the experiment detailed in Section 8.2.4. The measured lifetime was approximately 0.2 s for typical operating parameters of the Rb oven. It should be noted that in comparison with the prototype trap, an equivalent number of atoms could be observed.

8.4 Ten-way Cross MOT

The ten-way cross was chosen as the next trap to construct in order to create a trap that would give flexibility for subsequent guiding experiments. The increased number of viewports gave improved visual access to the trapping region over the prototype trap and allowed the guiding geometry to be altered easily.

8.4.1 Construction

A functional diagram of the trap is shown in Figure 8.11. This trap consisted of a ten-way cross UHV piece, the centre of which was the trapping region. It had six 70 mm diameter flanges and four 35 mm diameter flanges. Four of the larger flanges had viewports attached and were used as access for the cooling beams. One of the other flanges was attached to a UHV cube (70 mm x 70 mm x 70 mm) which had five viewports and was included as a probe region. The probing area was 115 mm from trap centre. Between the cube and the ten-way cross was a flange with a 26 mm diameter hole drilled in it. After drilling, the flange was cleaned manually to the best of one's abilities and then cleaned in an ultrasonic bath filled with methanol for 30 minutes. The four smaller arms

[6]Also known as 'Trap Lifetime'

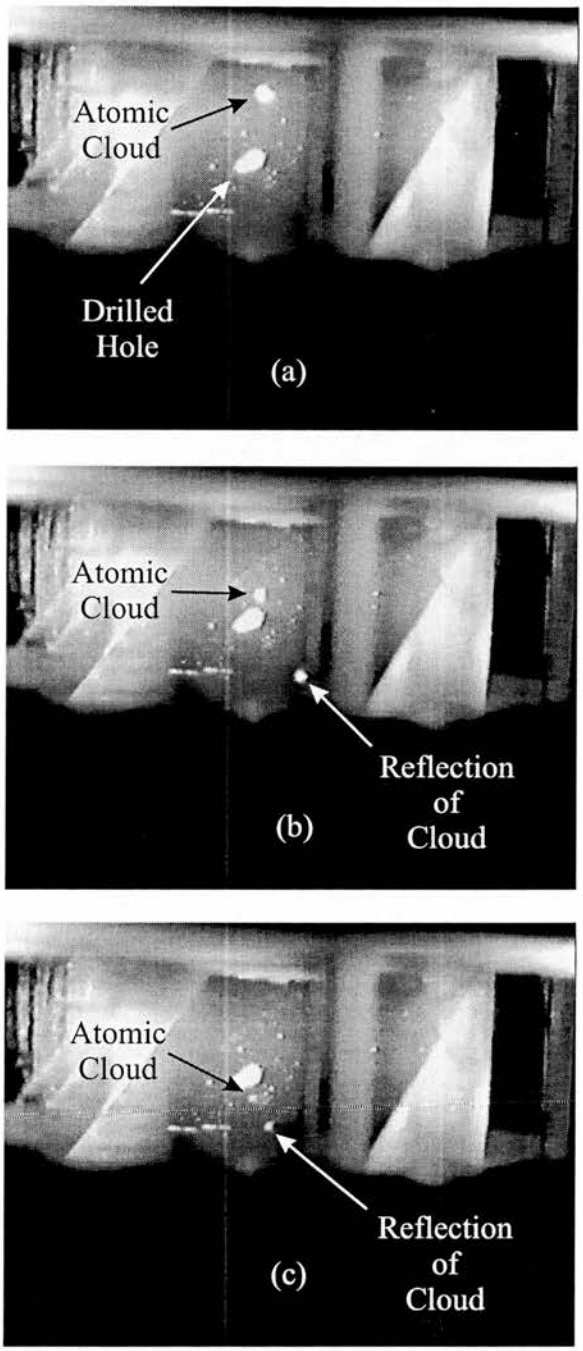

Figure 8.10: A series of images showing the vertical translation of an atomic cloud within the mirror MOT. Scattered light illuminates the position of the hole drilled through the prism. As the cloud is moved closer to the mirrored surface, the atom-surface interaction becomes significant reducing the number of trapped atoms. Also as the cloud is lowered, reflections come into view of the CCD camera as indicated in (b) and (c). In the final image, (c), the cloud is 1.2 mm above the mirror surface.

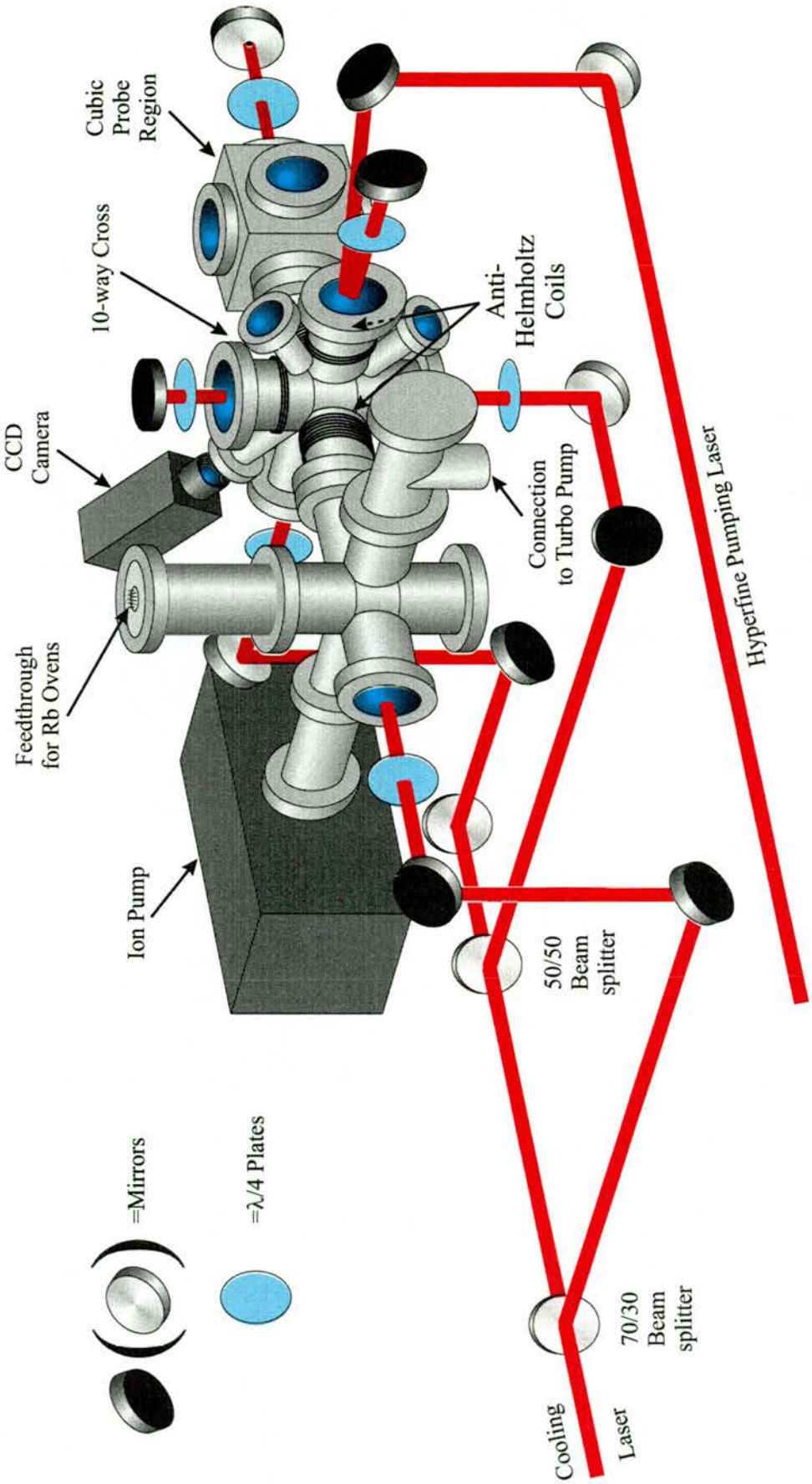

Figure 8.11: (Colour) A functional diagram of the ten-way cross trap.

had viewports attached and were used for viewing the trapped cloud with CCD cameras. The last large flange on the ten-way cross was attached to a standard six-way cross. Rubidium vapour was provided by getter ovens that have been described earlier in this chapter. These operated by passing a current through them and were connected via an electrical feedthrough on one of the arms of the six-way cross. A turbo pump (Varian, Turbo-Dry 70) was connected via a T-piece to the apparatus in order to reduce the pressure from atmospheric pressure to $\sim 10^{-6}$ mbar. A 40 ℓs^{-1} ion pump (Varian, VacIon Plus 40, Triode Model 919-0201) reduces the vacuum pressure to 10^{-9} mbar required for atom trapping. Again copper gaskets were used between flanges to achieve a UHV seal except when viewports were required and then annealed copper gaskets were used to minimise stress on the windows.

8.4.2 Bakeout

The bakeout for this trap was carried out in an identical manner to that described in Section 8.2.2.

8.4.3 Trap Operation

The magnetic quadrupole field was achieved by winding two sets of 70 turns of 0.6 mm diameter insulated wire directly onto the arms of the ten-way cross as shown in Figure 8.11. Shim coils were made in the same manner by winding 25 turns of wire each onto orthogonal arms. This gave three dimensional movement of trap centre by varying all of the currents to the coils. The shim coils were included in this trap design since this particular trap was made primarily to investigate the guiding of cold atoms directly from trap centre and the means to move the cloud spatially in three dimensions would ease alignment of the cloud with respect to the optics.

The cooling beams were introduced to the trapping region in the same manner as described previously for earlier traps, with the actual physical setup highlighted in Figure 8.11. The hyperfine pumping beam was expanded gently over the trap centre and could be introduced experimentally either along the axis of the field coils or perpendicular to this. No difference in trapping was observed between these two scenarios although the orientation did make a difference when atom guiding was conducted but this matter will be discussed in due course.

The ovens were cleaned and made operational in the same way described for previous traps and for trapping, a current of typically a current of 2.5 A was passed through the ovens for trapping. To generate the required field gradient, a minimum of ~0.8 A was needed but equal currents of 1.2 A in each quadrupole coil gave better trapping. As before, the lasers were tuned and locked to their respective transition lines in rubidium and trapping commenced.

8.5 Discussion and Summary

Three separate atom trapping apparatus have been constructed, tested and used to trap both neutral ^{85}Rb and ^{87}Rb atoms. The first consisted of a simple, glass five-way cross as the trapping region. Approximately 8x10^7 atoms were trapped using 9 mW and 6 mW of cooling and hyperfine repumping light respectively. At this time, frequency stabilization of the lasers was provided by a polarisation spectroscopy lock, details of which can be found in Section 3.3.1. Typical trap lifetimes were measured as a characterisation of the apparatus. The second trap, a mirror MOT, used a mirror surface at 45^o to generate a trapping region ~1 mm from the surface. Only two input cooling beams were required due to the geometry of the trap. Approximately 10^8 atoms could be trapped close to the mirrored surface using 21 mW of trapping power from circularized diode lasers in an extended-cavity which are detailed in Chapter 4. The ability to place a cold ensemble of atoms such a distance from a surface is of direct importance in magnetic guiding where current carrying wires or structures are written onto a

substrate surface. The third and final trap used a ten-way cross. This trap was built primarily to generate a low velocity source of cold atoms for subsequent experiments. Shim coils allowed three dimensional manipulation of the atom cloud.

The construction techniques of each trap and associated problems have been outlined. By highlighting these it is hoped that readers contemplating building a trapping experiment in the future can avoid time-consuming problems experienced throughout the development contained within this chapter.

Bibliography

[1] C. Wieman, G. Flowers, and S. Gilbert, "Inexpensive laser cooling and trapping experiment for undergraduate laboratories," American Journal of Physics **63,** 317–330 (1995).

[2] H. J. Metcalf and P. van der Straten, *Laser Cooling and Trapping* (Springer-Verlag Inc., 175 Fifth Avenue, New York, NY 10010, USA, 1999), pages 219–229.

[3] C. S. Adams and E. Riis, "Laser cooling and trapping of neutral atoms," Progress in Quantum Electronics **21,** 1–79 (1997).

[4] M. Chevrollier, E. G. Lima, O. D. Lorenzo, A. Lezama, and M. Oriá, "Magneto-optical trap near a surface," Optics Communications **136,** 22–26 (1997).

[5] J. Reichel, W. Hänsel, and T. W. Hänsch, "Atomic Micromanipulation with Magnetic Surface Traps," Physical Review Letters **83,** 3398–3401 (1999).

[6] R. Folman, P. Krüger, D. Cassettari, B. Hessmo, T. Maier, and J. Schmiedmayer, "Controlling Cold Atoms using Nanofabricated Surfaces: Atom Chips," Physical Review Letters **84,** 4749–4752 (2000).

[7] D. Müller, D. Z. Anderson, R. J. Grow, P. D. D. Schwindt, and E. A. Cornell, "Guiding Neutral Atoms Around Curves with Lithographically Patterned Current-Carrying Wires," Physical Review Letters **83,** 5194–5197 (1999).

[8] K. I. Lee, J. A. Kim, H. R. Noh, and W. Jhe, "Single-beam atom trap in a pyramidal and conical hollow mirror," Optics Letters **21,** 1177–1179 (1996).

[9] G. P. T. Lancaster, R. S. Conroy, M. A. Clifford, J. Arlt, and K. Dholakia, "A polarisation spectrometer locked diode laser for trapping cold atoms," Optics Communications **170,** 79–84 (1999).

Chapter 9

Experimental LVIS Generation And Cold Atom Guiding

G. P. T. Lancaster, R. S. Conroy, M. A. Clifford, J. Arlt and K. Dholakia, "Channeling of cold atoms along a Laguerre-Gaussian light beam"
Conference paper presented at *Quantum Electronics and Laser Science*, San Francisco, 2000.

D. P. Rhodes, G. P. T. Lancaster, J. Livesey, J. Arlt and K. Dholakia, "Guiding a cold atomic beam along a co-propagating and oblique hollow light guide"
Submitted for publication to *Physical Review A*.

9.1 Introduction

The significant progress made in atomic guides and coherent atomic beam splitters in recent years has been reviewed in Chapter 7. Two of the most important goals in the realization of an atomic beam splitter are high efficiency and large deviation angles. To date, magnetic means have prevailed as the most promising methods due to optical splitting suffering from small deviation angles. However, several optical splitting experiments have been conducted recently that overcome

this weakness and provide both of the preferred characteristics. This chapter describes experimental work carried out in St Andrews that augments and complements such research. The generation and characterisation of a low-velocity intense source (LVIS) of atoms by two independent methods is outlined. Further, co-linear blue-detuned Laguerre-Gaussian guiding is demonstrated experimentally. Preliminary experiments into promising methods of an all optical splitting of a LVIS beam in the future are also introduced.

9.2 Generation of a Low-Velocity Intense Source of Atoms

The importance of a cold, brilliant atomic beam in precise atomic physics experiments has been stressed in Chapter 7. One such beam is known as LVIS and a more detailed description of the experimental setup can be found in Section 6.5.2. Briefly, a LVIS can be constructed by forming a region of zero light intensity in the centre of the intensity profile of one trapping beam in a conventional magneto-optical trap (MOT). This causes an imbalance in the radiation pressure forces allowing atoms to be propelled along the centre of the dark region, thereby exiting the trap in a controlled manner. A simple diagram showing the underlying principle is shown in Figure 9.1. This section describes a pilot study performed in the generation of LVIS by two different methods. The first method is a repetition of work carried out by Lu and colleagues [1] where the zero intensity region was formed by obscuring one of the trapping beams with a small, opaque spot. The second implements a Laguerre-Gaussian (LG) beam replacing one of the six trapping beam.

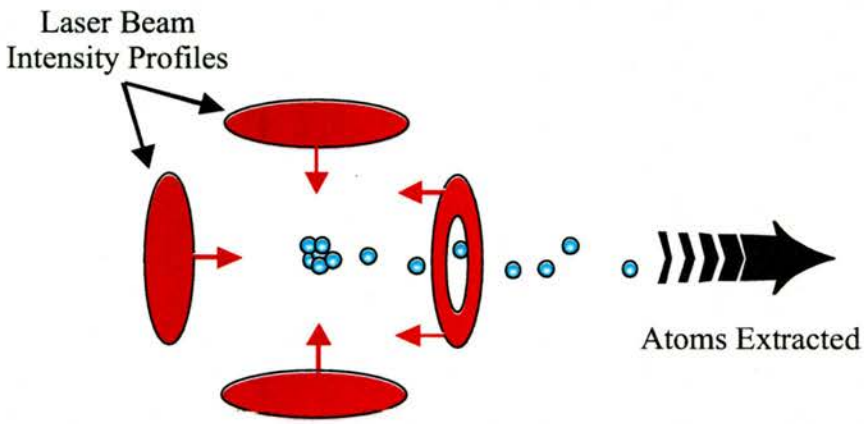

Figure 9.1: (Colour) A diagram showing the basic principle behind the formation of a low-velocity intense source (LVIS) of atoms. It is identical to that for a conventional MOT other than one of the trapping beams has a dark region in the centre of its intensity profile. The additional two trapping beams in and out of the page have been omitted for clarity.

9.2.1 Opaque Spot LVIS

The first experiment performed in St Andrews for obtaining a LVIS of atoms directly from the centre of a MOT was undertaken with the prototype trap described in Section 8.2. A spherical, cold atomic cloud was initially obtained in the manner described in Section 8.2.3. The cloud was imaged using a charged-coupled device (CCD) camera and viewed on a TV monitor. A glass coverslide 25.4 mm x 76.2 mm was affixed to an x-y translator using non-permanent universal bonding compound and located approximately 20 mm from one of the optical input windows of the trap. Onto the coverslide had been painted black spots of approximate diameters 0.2 mm, 0.7 mm, 1.0 mm and 1.5 mm. When correctly aligned and illuminated with a TEM_{00} mode laser beam, the required dark central region surrounded by an annulus of light was observed directly behind the coverslide. This dark region extended for a number of centimeters but diffraction filled in the central region the further one travelled behind the obstruction. Experimentally, the coverslide was placed approximately 40 mm from the centre of the MOT. The largest spot was initially inserted but upon alignment was found to completely ablate the atomic cloud. This was due to a reduction in the loading

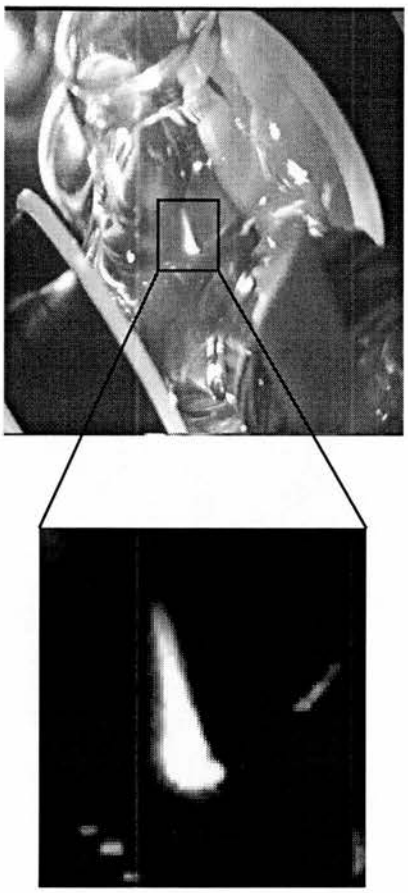

Figure 9.2: An image captured using a CCD camera of a low-velocity intense source (LVIS) of atoms exiting the centre of a MOT produced by the insertion of a 1 mm diameter spot into the path of one of the trapping beams. In this instance the spot was placed over the window that can be seen at the top of the first image causing the atoms to be extracted vertically upwards. The cloud is 3 mm in diameter with the LVIS tail extending over approximately 10 mm.

mechanism efficiency of the MOT. It is in the outer regions of the beam overlap volume where atoms are firstly cooled and captured before being loaded into the centre of the trap. A beam with a large, zero intensity at its centre will therefore reduce this efficiency. Smaller spots were inserted subsequently and found to produce a cold atomic flux directly output from the MOT centre with the spots with diameters of approximately 0.7 mm and 1.0 mm producing the best results. A typical imaged captured using the CCD camera is shown in Figure 9.2.

Figure 9.2 shows clearly the direction of travel of atoms from the centre of the MOT. The MOT cloud is approximately 2 mm in diameter with the LVIS ex-

tending 5 mm in length

9.2.2 Laguerre-Gaussian LVIS

A different method of generating LVIS was proposed at this time and consisted of replacing the altered cooling beam with a Laguerre-Gaussian (LG) beam. This was felt worthy of study due to the lack of diffraction associated with the propagation of the LG beam. One of the characteristics of using an opaque spot as a means of generating a dark region in the centre of the beam intensity profile is that during propagation light will fill the "dark hole" as a result of diffraction. A pure laser mode that has the desired annular intensity profile, such as a LG beam, will propagate over all distances preserving its intensity profile and thus the "dark hole".

Laguerre-Gaussian Beams – Theory

Within any laser cavity, a number of boundary conditions must be met for oscillation to be possible. Longitudinally, and in the steady state, there is a requirement that the phase of the light must reproduce itself after one round trip. This leads to the familiar equation describing the frequency spacing between longitudinal laser modes:

$$\Delta\nu = \frac{c}{2\eta L}, \tag{9.1}$$

where c is the speed of light in vacuum and ηL is the optical path length in one round trip of the cavity. Similarly, the necessity that the electromagnetic field must fall to zero away from the axis of the laser cavity leads to transverse laser modes that define the intensity profile of the laser output. These can be rectangularly symmetric, Hermite-Gaussian (HG), or circularly symmetric, Laguerre-Gaussian (LG), in nature. In the vast majority of cases, a laser output

oscillating in the fundamental HG, or TEM_{00}, mode is desirable but utilizing the special characteristics of LG modes has made their generation popular of late. LG beams have created interest in the fields of atom optics and macroscopic particle manipulation for two reasons. First, the $LG_{p\ell}$ beams have orbital angular momentum of $\ell\hbar$ per photon along the direction of the optical axis when $\ell \neq 0$, where p and ℓ describe the radial and azimuthal indices of the mode respectively [2]. The azimuthal index refers to the number of 2π phase cycles around the circumference of the mode and $(p+1)$ describes the number of nodes in the mode profile. Orbital angular momentum transfer from the beam to an absorptive macroscopic particle can result in the particle rotating [3]. Second, the $LG_{p\ell\neq 0}$ beam has a spiral phase structure causing its phase to be undefined on its optical axis, hence at this point it has zero intensity. A class of LG beams, $LG_{0\ell\neq 0}$, are referred to as doughnut beams since the intensity profile cross-section is a dark spot surrounded by an annulus of light. Figure 9.3 illustrates the effect ℓ has on the intensity profile. The intensity distribution of a generalised $LG_{p\ell}$ beam propagating in the Z direction is [4],

$$\begin{aligned} I(r,z) &= \frac{2p!}{\pi(p+|\ell|)!}\frac{P_0}{w^2(z)} \\ &\times \exp\left[\left(-2\frac{r^2}{w^2(z)}\right)\left(\frac{2r^2}{w^2(z)}\right)^{|\ell|}\left\{L_p^{|\ell|}\left(\frac{2r^2}{w^2(z)}\right)\right\}^2\right], \end{aligned} \tag{9.2}$$

where the beam waist at any position along the z axis is,

$$w(z) = w_0\sqrt{1+\left(\frac{\lambda z}{\pi w_0^2}\right)^2}. \tag{9.3}$$

z is the distance travelled along the optical axis from beam waist, w_0, r is the radius from centre of the beam, P_0 is the power of the beam, $w(z)$ is the radius at which the Gaussian term falls to $1/e^2$ of its on-axis value, $L_p^{|\ell|}$ is the generalised Laguerre polynominal and λ is the wavelength of light. A more thorough and detailed discussion of LG beams can be found elsewhere [5]. Methods for the generation of these beams and their inclusion in the experimental work will now be addressed.

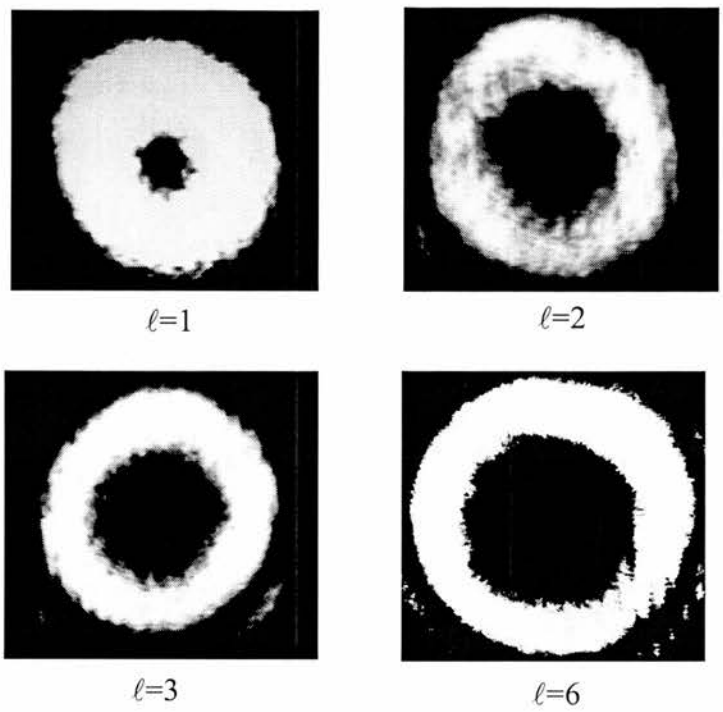

Figure 9.3: Experimental intensity profiles for Laguerre-Gaussian laser modes with the azimuthal index term, ℓ, shown for each. $p = 0$ in all cases. As ℓ increases so the radius of the dark central region increases.

Laguerre-Gaussian LVIS – Experiment

Experimentally, LG beams were formed from illuminating a computer generated hologram with a TEM_{00} mode laser beam. In the far field of the first diffracted order, a LG mode is generated. A more indepth discussion of the methods used in the fabrication process of these holograms can be found elsewhere [6].

The output from an extended-cavity diode laser (ECDL), as detailed in Chapter 3, was passed through anamorphic prisms and then a beam expanding telescope consisting of a f=-25 mm and a f=+300 mm focal length lenses separated by 275 mm. It was then split into three equal intensity beams. One of these beams was split further using a 50/50 beam splitter with one of the subsequent beams being incident on the computer generated hologram. The intensity profile of the first diffracted order was viewed approximately 2 m behind the hologram

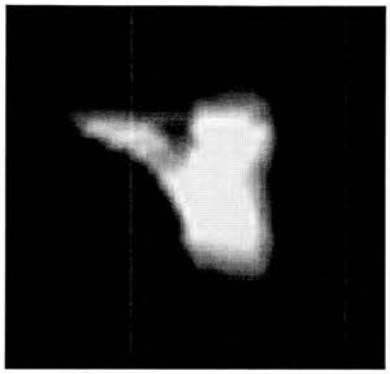

Figure 9.4: An image captured using a CCD camera of a (LVIS) exiting the centre of a MOT produced by the insertion of a LG_{01} ($p = 0, \ell = 1$) beam as one of the six cooling and trapping beams. The LG beam was incident from the upper left portion of the image. The fluorescence from the extracted atoms extends approximately 6 mm.

and the hologram aligned to give the best LG mode profile. The LG beam was introduced into the trap as one of the six cooling and trapping beams. LVIS structures could only be observed using LG beams with $\ell < 4$, presumably due to the dark region diameter in beams with higher azimuthal indexes being too large thereby lowering the loading efficiency from the outer overlap regions, as previously discussed. Hence, LG beams with $\ell = 1$ and $\ell = 2$ would be expected to be better. A typical observed cloud shape is shown in Figure 9.4.

Figure 9.4 shows two distinct lobes at trap centre with a tail of exiting atoms leaving along the central hollow region of the LG beam. Other cloud structures were witnessed when using a LG beam with azimuthal index, $\ell = 3$, and are shown in Figure 9.5. These images show a central spherical cloud surrounded by a two dimensional ring of atoms. To exclude the possibility that this was an artifact of distortion due to the CCD camera observing through sculptured regions of glass, the camera was moved to different viewing locations. The same cloud shapes could be observed. These forms have been reported previously by Walker and co-workers and were attributed to radiation pressure forces within trap centre providing repulsive forces between atoms [7]. In this published work, a slight misalignment of one of the six TEM_{00} trapping beams led to the transition from

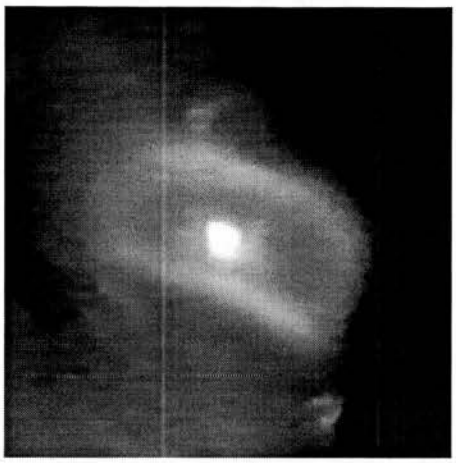

Figure 9.5: Cloud shape seen when a LG_{03} was introduced as one of the six trapping beams. A ring of atoms can be seen orbiting the central cloud.

a spherical cloud shape to a form similar to that which can be seen in Figure 9.5. The ring of atoms were found by Walker and colleagues to be either a stable ring of orbiting atoms or, through strobe experiments, clumps of atoms rotating about the central cloud. The difference between these two regimes were attributed to the number of atoms and the degree of misalignment. Strobe experiments were not undertaken at St Andrews since the discovery of these effects was an unexpected and unwanted artefact not relevant to the generation of a LVIS for guiding purposes. Atoms have also been induced into orbital motion from the intentional misalignment of trapping beams in a racetrack geometry by de Araujo *et al.* [8].

9.2.3 Laser Detuning of LVIS

Lu *et al.* reported that the maximum flux measured from a LVIS occurred at a laser cooling frequency detuned 5Γ below the atomic resonance [1]. This was in contrast to the detuning of 3.2Γ below resonance for a maximum number of atoms trapped in a conventional MOT. The difference in frequency was attributed to transverse heating of atoms as they exited the trap region as a result of any imbalances in the transverse cooling laser powers. A preliminary study was con-

ducted in St Andrews to investigate the effect laser detuning had on the atomic cloud shape and LVIS both when it was generated from an opaque spot and a LG beam.

The experiment was carried out using the ten-way cross trap described in Chapter 8. The two methods described in the previous sections were used to produce a LVIS. Utilizing the newly built ten-way cross trap allowed increased and non-distorted visual access to the trapping region. It should be noted that the hyperfine pumping laser was sent into the trap co-linear with the direction of LVIS thereby keeping the extracted atoms in resonance with the cooling beams. Once a satisfactory LVIS had been obtained, the cooling and trapping laser was tuned in incremental steps of 8 MHz below the cooling transition frequency. This was achieved using a polarisation spectroscopy lock (details of which can be found in Chapters 2 and 3) and an electronic d.c. offset. At each detuning, a short period of video footage was recorded for analysis purposes. Using an opaque spot to generate LVIS, Figure 9.6 shows false colour images captured from video alongside normalised intensity plots taken horizontally through each cloud centre. Figure 9.7 and Figure 9.8 show similar data for when LVIS is generated using a LG_{01} beam. The intense regions seen below the central cloud occur as a result of scattered light from internal surfaces of the vacuum chamber.

Compilation of the unnormalised data in both types of LVIS generation are shown in Figure 9.9. It was observed that a distinct difference existed between the spatial LVIS characteristics of the two schemes with respect to laser detuning. With a spot generated LVIS, Figure 9.9(a), a noticeable deformation of the cloud with detuning was observed, presumably as a result of diffraction of light into the "dark hole" forming a weak two dimensional trap. With a LG generated LVIS, Figure 9.9(b) shows a maximum cloud size was achieved with a trapping laser detuning of -36 MHz agreeing with literature [1]. The fluorescence seen at this detuning in the LVIS was a maximum and led to the conjecture that the flux was a maximum also. However, no direct measurements were taken of the atomic flux although this is a point worthy of future investigation. This could be achieved by

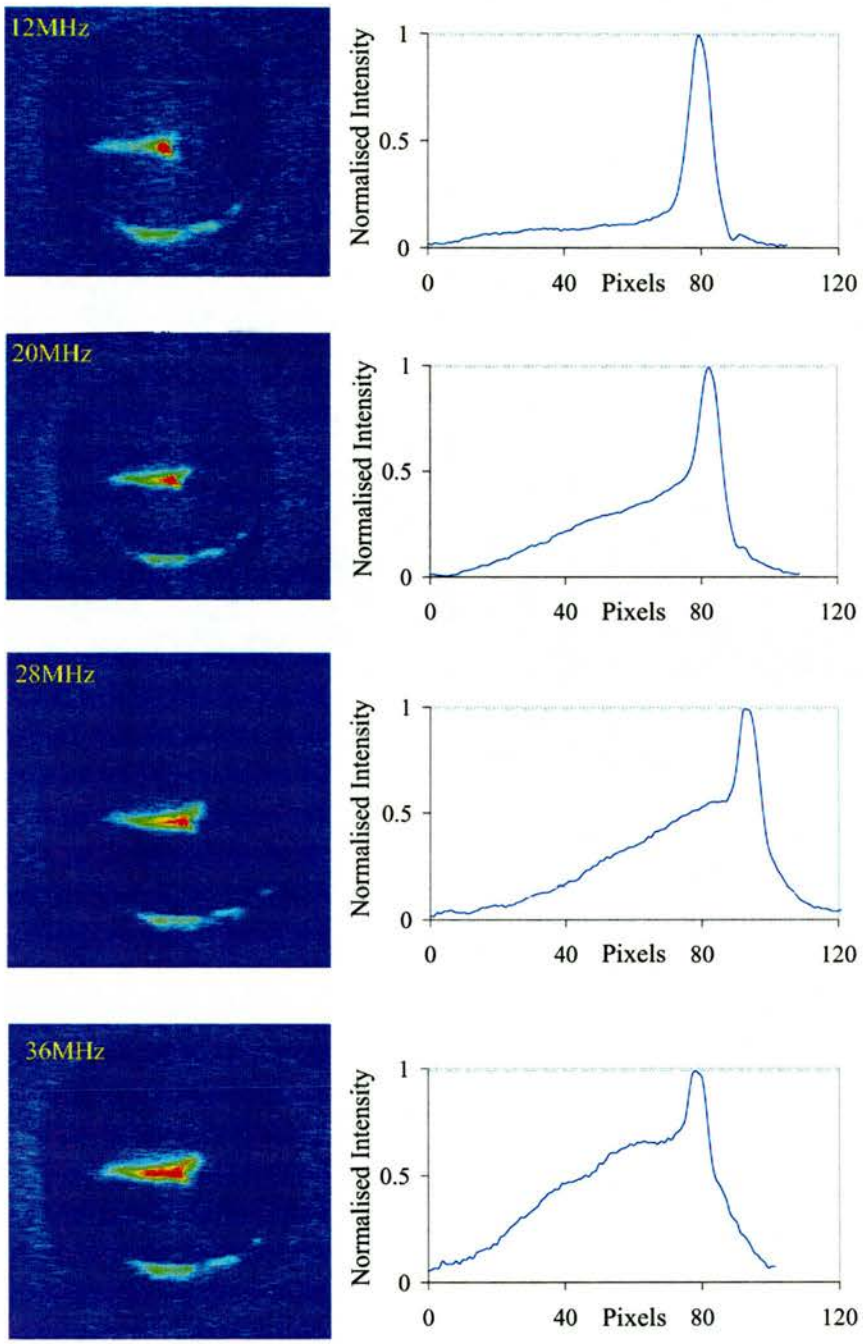

Figure 9.6: (Colour) On the left are seen false colour images of an opaque spot generated LVIS exiting the central region of a MOT. The frequency detunings of the cooling and trapping beams below atomic resonance are indicated by the values in the top left hand corner of the image. On the right are normalised intensity plots taken horizontally through the centre of the MOT and LVIS. Scattered light reflecting off the interior surfaces of the vacuum chamber can be seen directly below the central cloud. 1 pixel equals 100 μ m.

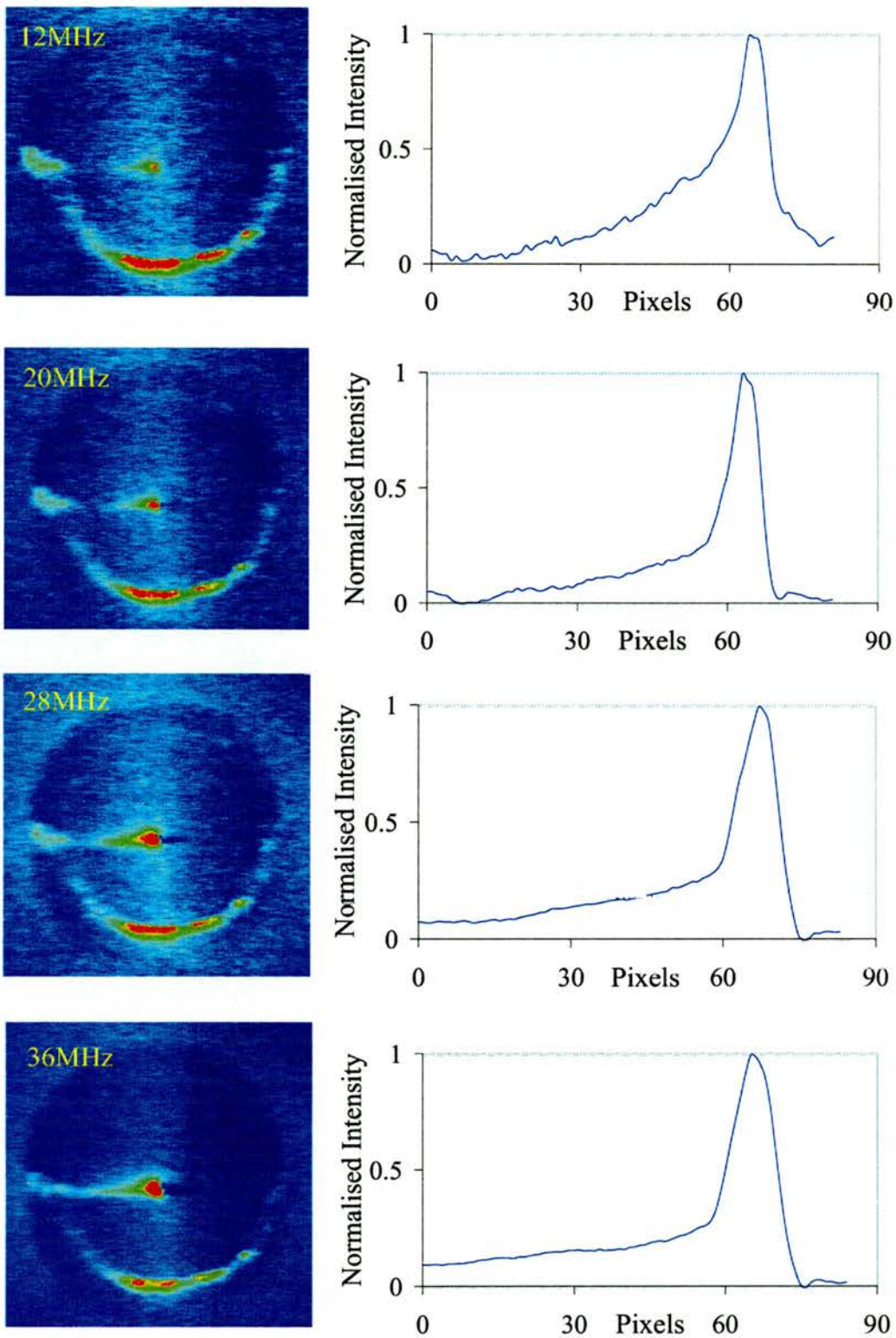

Figure 9.7: (Colour) On the left are seen false colour images of a LG_{01} beam generated LVIS exiting the central region of a MOT. The frequency detunings of the cooling and trapping beams below atomic resonance are indicated by the values in the top left hand corner of the image. On the right are normalised intensity plots taken horizontally through the centre of the MOT and LVIS. Scattered light reflecting off the interior surfaces of the vacuum chamber can be seen directly below the central cloud. 1 pixel equals 100 μ m. Data continued in Figure 9.8.

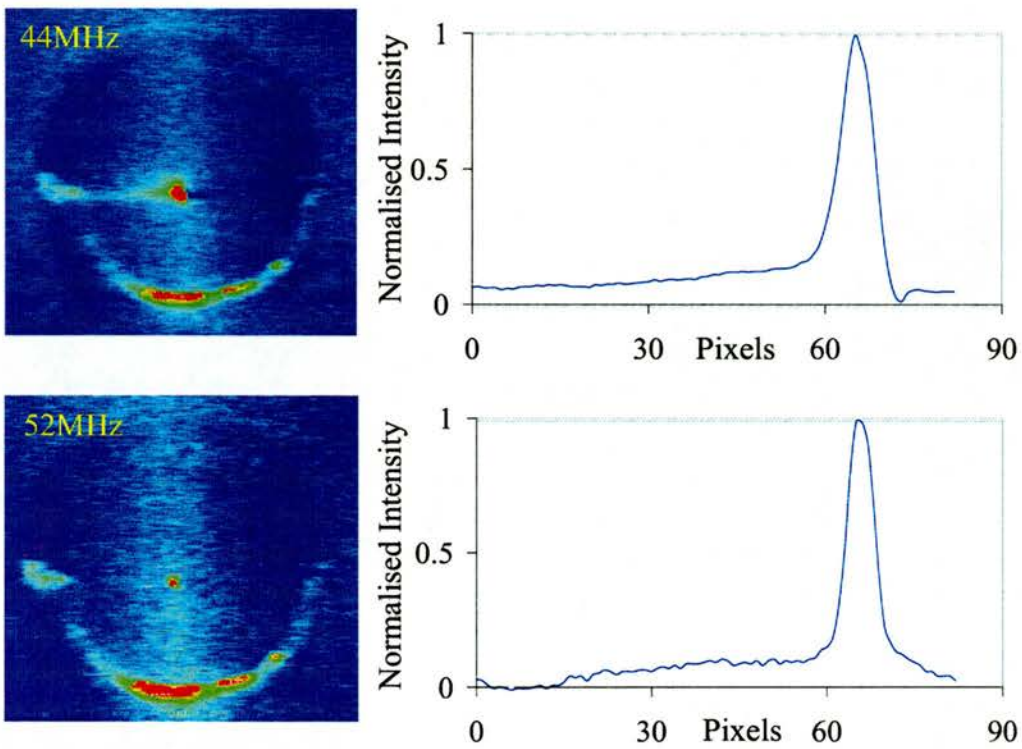

Figure 9.8: (Colour) On the left are seen false colour images of a LG_{01} beam generated LVIS exiting the central region of a MOT. The frequency detunings of the cooling and trapping beams below atomic resonance are indicated by the values in the top left hand corner of the image. On the right are normalised intensity plots taken horizontally through the centre of the MOT and LVIS. Scattered light reflecting off the interior surfaces of the vacuum chamber can be seen directly below the central cloud. 1 pixel equals 100 μ m.

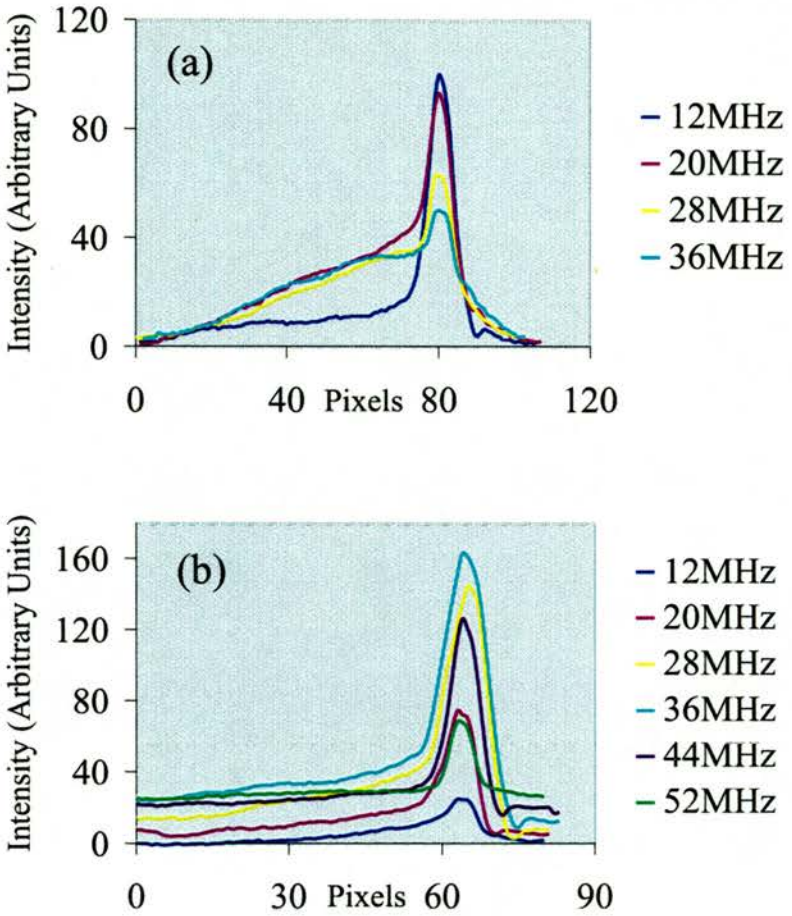

Figure 9.9: (Colour) Composite data of unnormalised intensity profiles through a LVIS beam generated from (a) an opaque spot and (b) a LG_{01} beam. The different graphs refer to different laser detunings below resonance, as indicated in the legend. 1 pixel equals 100 μ m.

inducing fluorescence at a spatially separated probe region away from trap centre using a weak laser beam tuned to resonance and incident perpendicularly on the atomic flux. A photodiode would record a signal proportional to the number of atoms in a region absent of other forms of fluorescence.

9.3 Guiding of a LVIS

A preliminary investigation into the optical guiding of a LVIS was undertaken by two different methods. Both utilized the dipole force experienced by an atom when placed in a light field. The theory describing this force can be found in Chapter 6. The first of these methods used a red-detuned near-resonant Gaussian beam while the second used a blue-detuned LG beam.

9.3.1 Red-Detuned Gaussian Beam Guiding

A LVIS was generated by means of an opaque spot. Along the direction of the LVIS beam, a red-detuned Gaussian TEM_{00} mode laser beam was directed. This was provided by a Spectra Physics Nd:YVO_4 pumped titanium sapphire laser which gave 1 W around 780 nm, as detailed in Section 3.2.2. This shall be known as the *guide beam*. The guide beam was focused into the trap using a f=+500 mm focal length lens which gave an approximate beam waist size of 300 μm at trap centre. The guide beam axis and LVIS beam axis did not overlap completely since optical access problems made this impossible. Rather, an angular deviation occurred between the LVIS beam and the guide beam and was measured to be 16 mrad. The guide beam was tuned to resonance and reduced in intensity using a neutral density (ND) filter wheel to approximately 100 mW. The beam was then aligned through the cloud by observing a black line where spontaneous emission effects heated the atoms out of the LVIS. The lower power was required in order to avoid completely ablating the atomic cloud. Once alignment was satisfactory, the ND filter was removed and the titanium sapphire laser detuned, $\Delta = -7$ GHz, below the cooling transition. Images were captured using two CCD cameras placed perpendicular to one another, with and without the guide beam present. Images were also recorded of the trap centre with the magnetic coils switched off to allow background scatter to be subtracted. Figure 9.10 show typical results of two captured raw images from one of the cameras of the atomic cloud with (a) no guide beam present and (b) 700 mW with $\Delta = -7$ GHz red-detuned guide

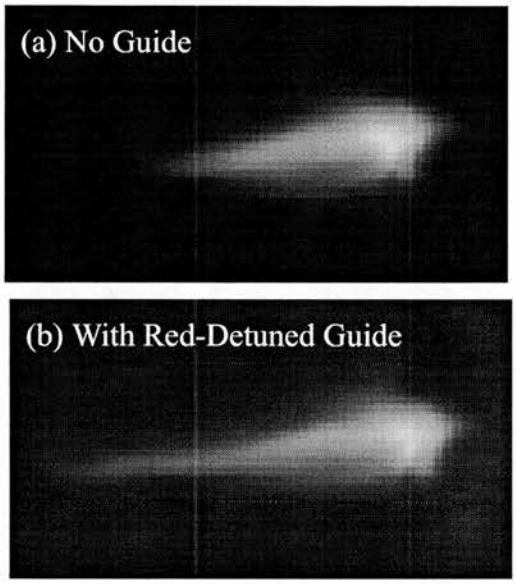

Figure 9.10: Captured images from one CCD camera of an atomic LVIS with (a) no guide beam present and (b) 700 mW of 7 GHz of red-detuned guide beam present. The intensity profile along the LVIS axis was measured in each image and presented in the graphs in Figure 9.11.

beam present. Figure 9.11(a) shows intensity plots measured horizontally along the LVIS axis of each image after subtraction of background scatter while, in the same figure, (b) shows the subtraction of intensity plots from (a).

Visually comparing images (a) and (b) from Figure 9.10 as well as that shown by the data in Figure 9.11, the extension in fluorescence of the LVIS beam can be seen clearly. However, this could not be attributed entirely to guiding as the detuning is relatively close to resonance and the power of the guide beam generated a scattering rate of 1.48×10^6 photons atom^{-1} s^{-1}. This was comparable to the scattering as a result of the cooling processes within a MOT which was typically 2.5×10^6 photons atom^{-1} s^{-1}. It was therefore unclear as to which process contributed a greater extent to the extension of LVIS and without a direct measurement of the atomic flux a conclusion could not be reached.

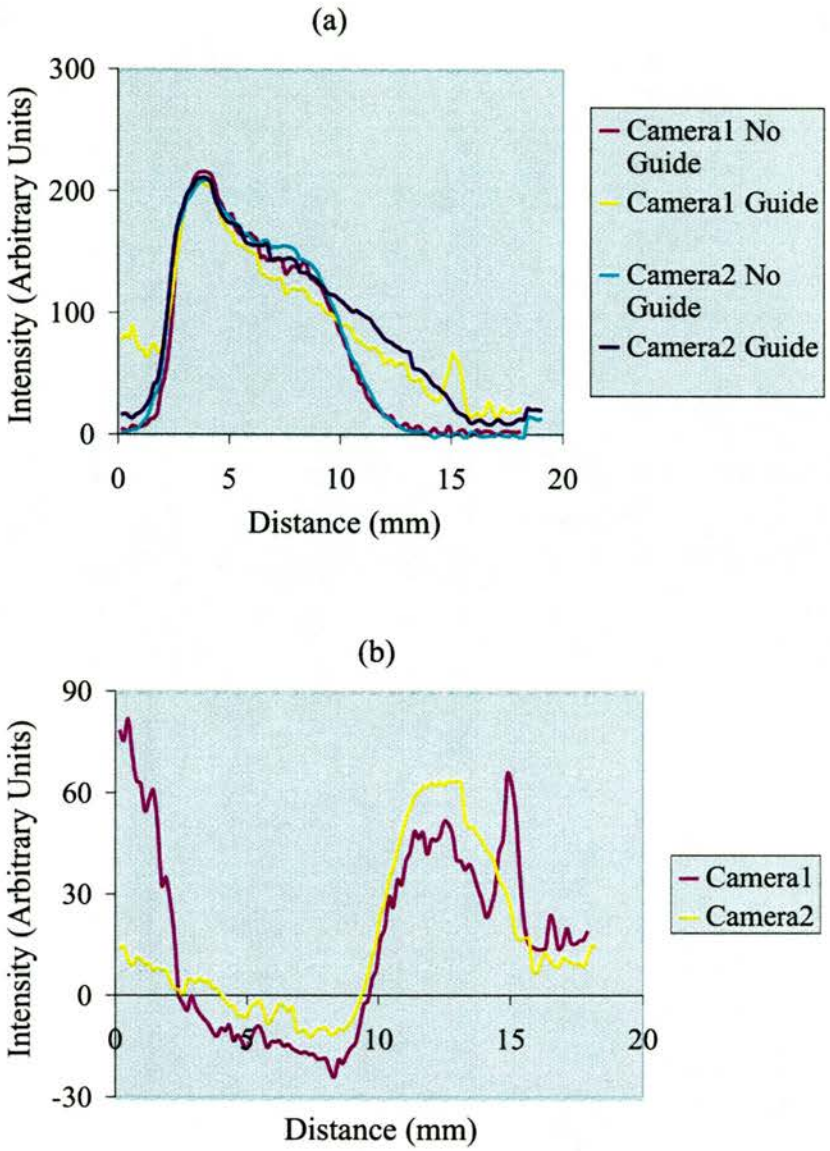

Figure 9.11: (Colour) Intensity profiles measured along the LVIS axis are plotted in (a) after the subtraction of background scattering. Graph (b) is a subtraction of the "guide" and "no guide" plots from (a). Extension of LVIS fluorescence can be observed. If this is as a result of increased spontaneous emission or increased guiding cannot be determined from this experiment.

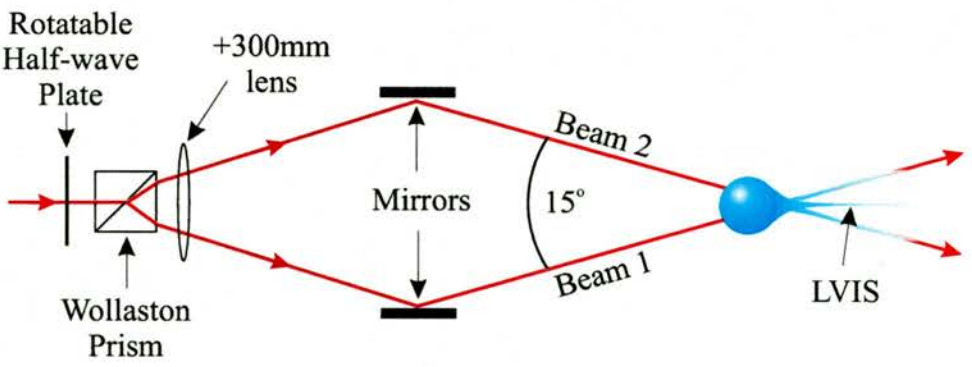

Figure 9.12: (Colour) Schematic diagram for an all-optical switch. The linearly polarised Gaussian guide beam is incident on a linear polariser that can be rotated allowing any arbitrary linear polarisation to be incident on the Wollaston prism. The beam is split with relative powers depending on the angle of polarisation of the incident beam. A lens focuses the beams to a waist of 100 μm at trap centre.

9.3.2 Future Red-Detuned Guiding

A method to eliminate spontaneous emission is to use a high power, far-off resonant guide beam. In this way, the optical potential is preserved while the spontaneous emission is reduced dramatically. An experiment currently being conducted at St Andrews is investigating replacing the titanium sapphire laser guide beam with a 10W Nd:YAG laser emitting at 1064 nm with new results being submitted for publication[1]. This is similar in nature to work done by Houde *et al.* on the splitting of a dropped MOT cloud using a similar laser system in which spontaneous emission was less than 0.1 photons atom^{-1} s^{-1} [9].

A pilot study currently in progress is the realization of a novel atomic beam splitter and optical switch. Initial results are promising with the concept being proven in a proof-of-principle experiment. The experimental setup is shown in Figure 9.12.

The guide beam was a red-detuned Gaussian obtained from a titanium sapphire

[1]D. P. Rhodes, J. Livesey, J. Arlt and K. Dholakia, "Guiding of a low-velocity intense source of atoms along a far-off resonance guide beam".

(a) (b) (c)

Figure 9.13: Results from the optical switch experiment using 550 mW of guide power detuned -12 GHz from resonance. Image (a) shows the effect of having 550 mW in Beam 1 , (b) shows 550 mW in Beam 2 only and in (c) there is approximately 225 mW in each beam. Splitting can be seen in all cases.

laser emitting at 780.3 nm. The linearly polarised output was incident on a half-wave plate before being split at a Wollaston prism and each of the two paths focused into trap centre using a f=+300 mm focal length lens. Using a Wollaston prism enabled the cross-over-point of the beams in the trap to be achieved with relative ease since each beam originated from a common point within the prism. The power in each beam could be varied between zero and 650 mW by rotation of the half-wave plate. Each beam was aligned to cross the LVIS beam at an angle of 7.5^o [9]. Initial experimentation has shown encouraging results, see Figure 9.13. Each arm of the optical beam splitter can be resolved illustrating the future promise of this setup. Indeed, the addition of a second Wollaston prism and guide beam setup to reverse this process could be envisaged enabling a simple atom interferometer to be realized.

9.3.3 Blue-Detuned Laguerre-Gaussian Beam

The ability to eradicate spontaneous emission and heating is important if an optical guide is to be used for the transport of a coherent ensemble of atoms. An alternative method of suppressing spontaneous emission, other than implementing far-detuned guide beams, is to confine atoms within low intensity regions such as

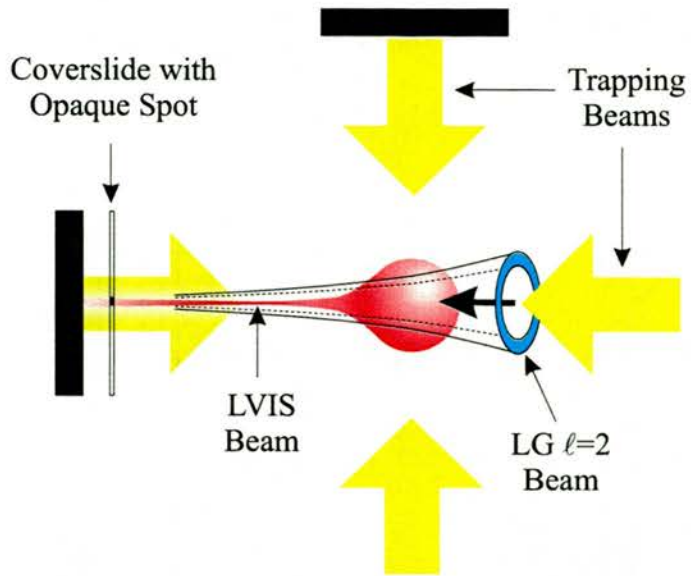

Figure 9.14: (Colour) Schematic diagram of co-linear blue-detuned Laguerre-Gaussian guiding of LVIS.

the centre of a Laguerre-Gaussian mode laser beam. By detuning the laser blue of the atomic resonance, atoms can be confined within the dark central region of the beam. A number of experiments were outlined in Chapter 7 in which guiding and focusing had been accomplished with thermal atoms [10, 11]. In this section, the first experimental demonstration of guiding an atomic LVIS beam using a co-linear blue-detuned LG beam is described.

Blue-Detuned Laguerre-Gaussian Guiding of LVIS

A schematic diagram of the guiding setup is shown in Figure 9.14. A LVIS was generated using an opaque spot as prescribed in Section 9.2.1. A LG_{02} beam was then directed through the centre of the MOT co-linearly with LVIS and in a co-propagating manner. The experimental setup for the generation of the required LG guide beam from the output of a titanium sapphire laser is shown in Figure 9.15. The rubidium cell was used as a crude method of determining when the guide laser was on or near an atomic resonance and the apertures were included to block the residual diffracted orders from reaching the trapping region.

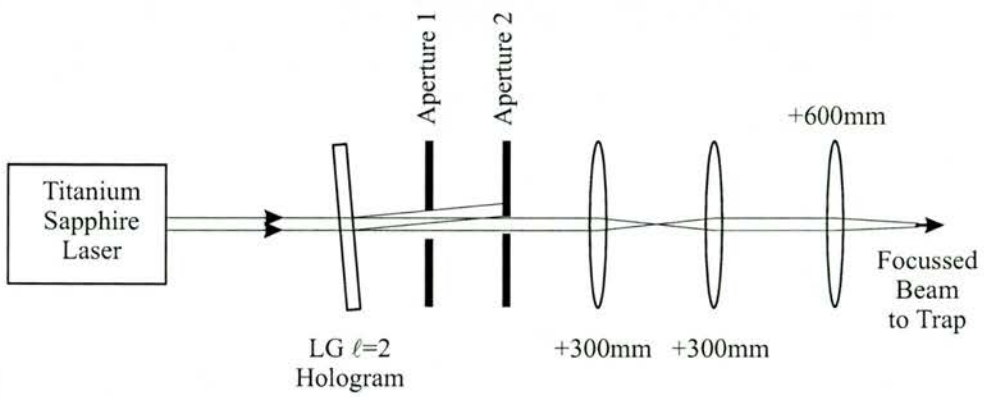

Figure 9.15: Experimental setup for the production of a Laguerre-Gaussian guide beam.

A collimation telescope consisting of two f=+150 mm focal length lenses separated by 300 mm and a f=+600 mm focal length lens to focus the guide beam to a waist of approximately 450 μm were also included. The measured power available at trap centre was 250 mW. With a laser detuning of $\Delta = +5$ GHz blue-detuned from the cooling transition resonance, the optical guiding potential was 7 mK. The transverse temperature of atoms in LVIS are typically tens of microKelvin. The potential walls of the guide beam are therefore approximately an order of magnitude greater in height.

Images of LVIS with no guide and with the guide beam present are shown in Figures 9.16(a) and (b) respectively while (c) indicates the position and relative size of the LG guide beam used in the experiment. The yellow, numbered lines correspond to where intensity profiles were taken for analysis purposes. Line 1 is a longitudinal profile along the LVIS axis, line 2 is a transverse profile through the cloud centre and line 3 is a transverse profile taken at a point towards the end of LVIS. The data from these profiles are shown in Figure 9.17(a)–(c).

From these data it can be seen clearly that LVIS is extended in length while the centre of the MOT is widened. Since there was zero guide beam intensity along the length of LVIS, spontaneous emission was eliminated inferring atom guidance. The widening of the cloud seen in Figure 9.17(b) is due to the repulsive nature of the LG beam within the MOT repelling atoms from their normal equilibrium

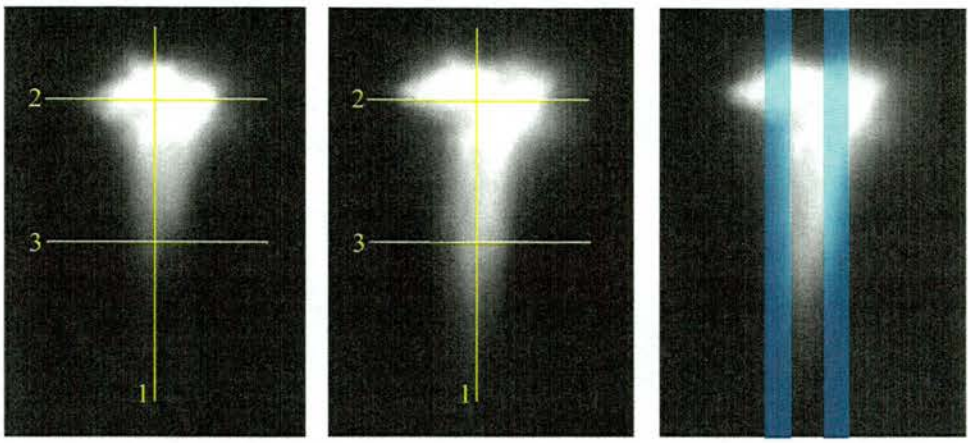

Figure 9.16: (Colour) Captured images of LVIS with (a) no guide and (b) a co-linear, co-propagating, 250 mW, $\Delta = +5$ GHz blue-detuned LG_{02} guide beam present. Yellows lines indicate axes along which intensity profiles were taken. These data are shown in Figure 9.17. Image (c) is a duplicate of (b) but indicates the position and relative size of the guide beam.

positions. Over a 100% increase in the fluorescence is noted towards the end of LVIS, see Figure 9.17(c) . This is in contrast to Yan *et al.* who, using a similar scheme but using an axicon generated hollow beam, reported an increase in fluorescence of 25% [12]. Also in contrast to this paper, transverse compression of LVIS was not observed although this can be accounted for by the different guide beam parameters. This is the first experimental demonstration of CW guidance of an atomic LVIS using a blue-detuned LG beam. A logical progression from co-linear guiding of a LVIS is to split a LVIS using similar physical principles. If an oblique guide were to be realized, then this would be the first step in constructing a blue-detuned all-optical atom interferometer.

Blue-Detuned Laguerre-Gaussian splitting of LVIS

In 2000, Yan and colleagues reported the splitting and guiding of an atomic LVIS beam using a blue-detuned hollow laser beam [12]. This was not a LG beam but rather a thin annulus of light generated using a pair of axicons in combination with a spherical lens [13]. A titanium sapphire laser was used to produce 200 mW

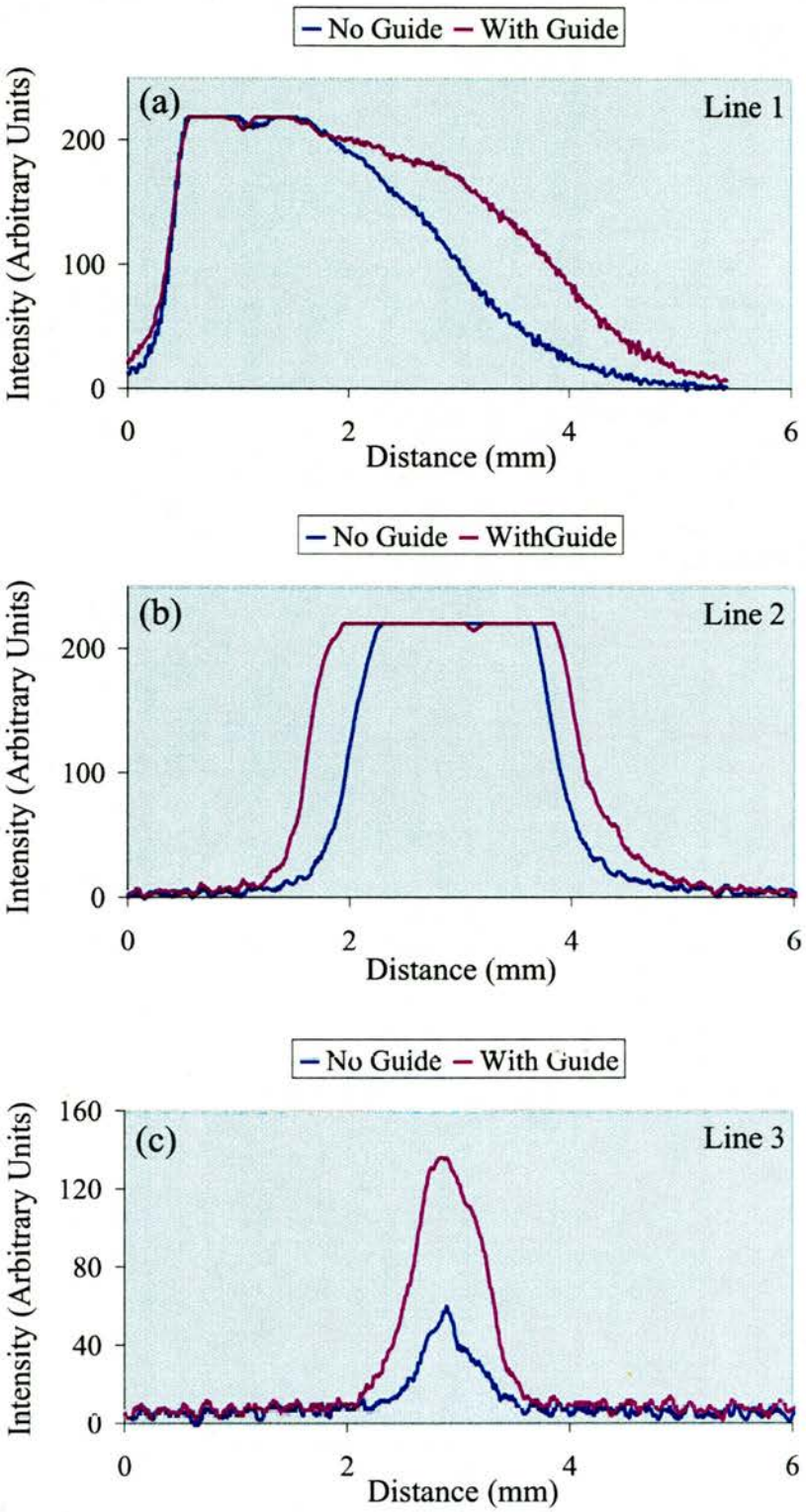

Figure 9.17: (Colour) Intensity profiles taken along yellow lines indicated in Figure 9.16. Plot (a) is from data measured longitudinally along LVIS (Line 1), (b) is measured transversely through the centre of the trapped cloud (Line 2) and (c) is measured transversely towards the end of LVIS (Line 3). The flat tops present in both (a) and (b) are due to saturation of the CCD camera.

of guide power at trap centre. This was overlapped with a LVIS beam generated by inserting a 0.8 mm diameter opaque spot in front of one of the retro-reflecting optics. A schematic diagram of the experimental setup is shown in Figure 9.18. Both the LVIS and the guide beam propagate in the direction of gravity. The angle of overlap between the LVIS and the hollow beam, α could be changed with results being recorded for $\alpha = 0^o$ (co-linear) and $\alpha = 8^o$ (oblique). Their results concluded that with a co-linear guide, a focusing of LVIS occurred with a 25% increase in flux intensity and a 20% reduction in spatial width. This is compared with the 100% increase in flux measured by ourselves for a similar scheme which was described above. With the guide beam present with $\alpha = 8^o$, a fraction of the LVIS beam was observed to be split from the vertical, along the direction of the guide beam. The literature concluded that atoms were coupled from the LVIS into the hollow blue-detuned guide beam. A similar experiment was conducted at St Andrews in order to verify these observations. However, it was found that some of their results were not replicated and, indeed, were markedly different from those obtained at St Andrews. This line of research is still ongoing but a number of interesting effects have already been observed and new theories proposed.

The largest concern came from understanding how atoms present within a LVIS beam can be coupled effectively into the centre of an oblique hollow guide. The potential walls that are there to confine atoms within it should also inhibit atoms from entering in the first instance. It was this dilemma that provided the motivation for further investigation.

The experimental setup at St Andrews was almost identical to that of Yan and colleagues. The only exceptions being that LVIS was generated in a horizontal direction and that a LG_{03} beam was used as the guide beam. The guide beam setup is shown in Figure 9.15. A guide beam of 180 mW with a detuning of +5 GHz was used. Figure 9.19 shows images taken (a) without and (b) with a blue-detuned LG guide beam present.

From Figure 9.19 (b) two distinct lines of fluorescence can be seen . These two

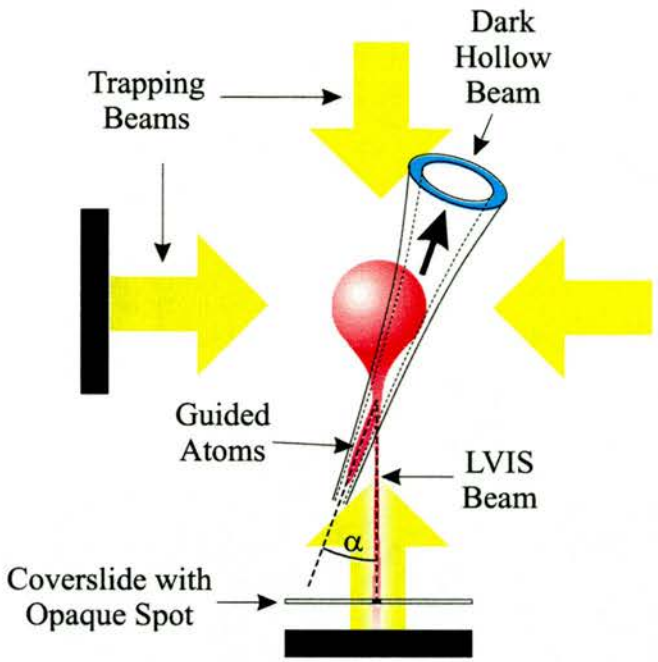

Figure 9.18: (Colour) Schematic diagram of the blue-detuned dark hollow beam guiding experiment conducted by Yan *et al.* [12].

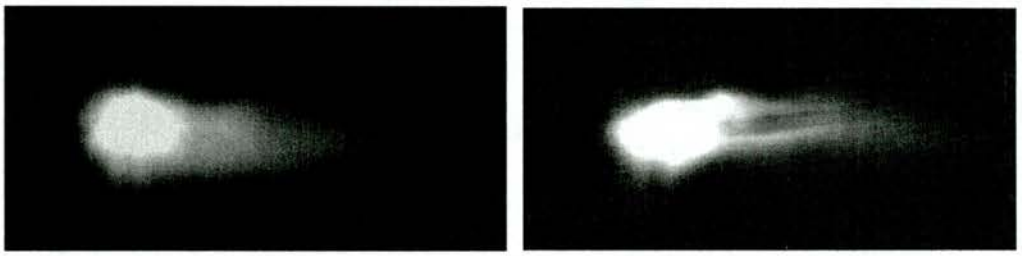

(a) No Guide (b) LG_{03}, +5 GHz, 180 mW

Figure 9.19: Images of an atomic LVIS with (a) no guide beam present and (b) 180 mW of $\Delta = +5$ GHz blue-detuned LG_{03} oblique guide beam present. Two lines of fluorescence can be observed at a small angle above LVIS in (b). This is as a result of the recycling nature of LVIS which is discussed in the body of the text. A thin line of fluorescence may be seen between these two other lines and shows a small number of atoms being guided within the LG beam.

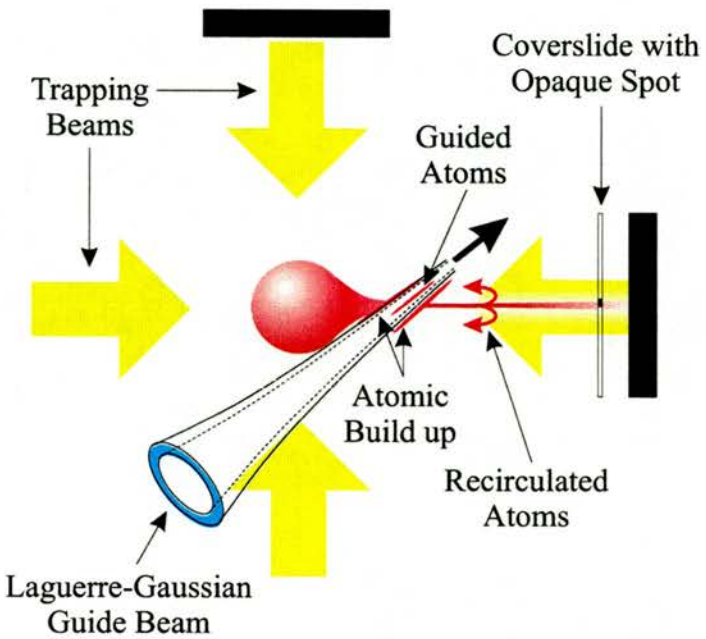

Figure 9.20: (Colour) Diagram showing the formation of the two observable lines in Figure 9.19. Atoms exiting along LVIS can accumulate either at the first potential barrier presented by the Laguerre-Gaussian guide beam or, after passing over both potential barriers and exiting the LVIS transversely, be recirculated and accumulate on the opposite side of the guide.

lines are believed to be the compression of atoms as they accumulate against the guide walls. This can be explained further with the aid of Figure 9.20. Atoms exiting along LVIS encounter two potential barriers of the LG beam of equal heights. Slow atoms will not possess sufficient kinetic energy to traverse the first barrier and so build up along the base of the potential hill. The first line closest to the MOT is therefore a result of slow atoms in LVIS meeting the optical barrier of the blue-detuned LG beam and being deflected or "sliding" along the side of the guide. Atoms therefore accumulate at this barrier causing the increase in fluorescence. Atoms with high kinetic energy surmount both barriers and form an LVIS on the other side of the guide beam. As detailed in Section 6.5.2, there is a continuous recycling process returning atoms exiting the LVIS beam transversely back to the centre of the MOT region. It is this mechanism along with the potential barrier encountered on their return journey that accounts for and explains the second line seen furthest from the MOT. It is difficult for an atom to surmount the first barrier while being repelled by the second. In this way it is difficult to envisage the mechanism which allows atoms to be loaded into the guide through one of its potential walls.

9.4 Future Work

The work presented in this chapter is preliminary in many respects. A number of further experiments could be performed in order to characterise and clarify generation and optical guiding of a LVIS. In the case of the generation of a LVIS using both an opaque spot and an LG beam, useful studies would include the measurement of atomic flux with detuning, the effects of an opaque-spot-LVIS versus a LG-LVIS in terms of the longitudinal and transverse atomic velocities and separately detuning the LVIS generating beam with respect to the 5 other trapping beams. There has been no characterisation of guiding with respect to beam size or whether the guide beam is co-propagating or counter-propagating with LVIS and these are areas that are deserving of future study. For the ma-

jority of these investigations a direct measurement of the atomic flux outwith the guide region is required. This would most likely take the form of a hotwire detector, which was mentioned in Chapter 7, or a weak, resonant laser beam interacting "down stream" and perpendicularly to the atomic flux. This would give unambiguous flux measurements regardless of laser detuning.

Initial steps taken in red-detuned guiding has led onto far-off resonance guiding. Further studies in this area would lead to splitting of a LVIS with minimal spontaneous emission. The ideas encompassed within the Wollaston prism optical atomic beam splitter show potential for success in future experimentation. A characterisation is required of this system to determine its applicability in the field of atom-optics.

Improvements in coupling atoms from LVIS into the centre of an oblique blue-detuned LG guide beam are currently being investigated at St Andrews. The scheme involves placing a small dark hole in the side of the LG guide beam so as to allow atoms to enter the central region. This has been done by obstructing part of the LG beam with an opaque spot. Careful placement allows diffraction to partially refill the gap in the wall thereby confining atoms once they have been coupled inside.

9.5 Discussion and Summary

The area of cold atom guiding using only optical methods is young both in St Andrews and around the world. The experiments described in this chapter complement and further work performed in this field. The spatial characteristics of LVIS have been investigated both when LVIS is generated by means of placing an opaque spot in the centre of one of the trapping beams or replacing this beam entirely with a Laguerre-Gaussian beam. Red-detuned guiding of atoms exiting along a LVIS has been conducted including a proof-of-principle experiment in which an all-optical beam splitter was realized. Further, investigation into the

coupling of cold atoms into a blue-detuned optical guide revealed that considering the optical potentials in relation to coupling atoms into the guide is an important factor and one that has possibly been overlooked to date in literature. A solution has been proposed and is currently under experimental verification in St Andrews.

A number of avenues have been broached during this research with several showing promise for the future. This chapter has described the research that has provided a cold atomic beam directly from a MOT, optical guiding of a LVIS in a blue-detuned LG beam and a base from which further work in this area can be built.

Bibliography

[1] Z. T. Lu, K. L. Corwin, M. J. Renn, M. H. Anderson, E. A. Cornell, and C. E. Wieman, "Low-Velocity Intense Source of Atoms from a Magneto-optical Trap," Physical Review Letters **77,** 3331–3334 (1996).

[2] L. Allen, M. W. Beijersbergen, R. J. C. Spreeuw, and J. P. Woerdman, "Orbital angular momentum of light and the transformation of Laguerre-Gaussian laser modes," Physical Review A **45,** 8185–8189 (1992).

[3] N. B. Simpson, K. Dholakia, L. Allen, and M. J. Padgett, "Mechanical equivalence of spin and orbital angular momentum of light: an optical spanner," Optics Letters **22,** 52–54 (1997).

[4] J. Arlt, T. Hitomi, and K. Dholakia, "Atom Guiding along Laguerre-Gaussian and Bessel light Beams," Applied Physics B **71,** 549–554 (2000).

[5] M. Padgett, J. Arlt, N. Simpson, and L. Allen, "An experiment to observe the intensity and phase structure of Laguerre-Gaussian laser modes," American Journal of Physics **64,** 77–82 (1996).

[6] J. Arlt, Ph.D. Thesis, School of Physics and Astronomy, University of St Andrews, St Andrews, Fife, Scotland., 1999.

[7] T. Walker, D. Sesko, and C. Wieman, "Collective behaviour of optically trapped neutral atoms," Physical Review Letters **64,** 408–411 (1990).

[8] M. T. de Araujo, R. J. Horowicz, D. Milori, A. Tuboy, R. Kaiser, S. C. Zilio, and V. S. Bagnato, "Time of flight technique to determine temperature of atoms in a ring-shaped trap," Optics Communications **119,** 85–89 (1995).

[9] O. Houde, D. Kadio, and L. Pruvost, "Cold Atom Beam Splitter Realized with Two Crossing Dipole Guides," Physical Review Letters **85,** 5543–5546 (2000).

[10] S. Kuppens, M. Rauner, M. Schiffer, K. Sengstock, W. Ertmer, F. E. V. Dorsselaer, and G. Nienhuis, "Polarization-gradient cooling in a strong doughnut-mode dipole potential," Physical Review A **58,** 3068–3079 (1998).

[11] M. Schiffer, M. Rauner, S. Kuppens, M. Zinner, K. Sengstock, and W. Ertmer, "Guiding, focusing, and cooling of atoms in a strong dipole potential," Applied Physics B **67,** 705–708 (1998).

[12] M. Yan, J. Yin, and Y. Zhu, "Dark-hollow-beam guiding and splitting of a low-velocity atomic beam," Journal of the Optical Society of America B **17,** 1817–1820 (2000).

[13] I. Manek, Y. B. Ovchinnikov, and R. Grimm, "Generation of a hollow laser beam for atom trapping using an axicon," Optics Communcations **147,** 67–70 (1998).

Chapter 10

Conclusions

10.1 Summary of the Thesis

In this thesis, two distinct but inter-linked areas have been investigated. First, the development of novel diodes lasers and their associated frequency stabilization for use in laser cooling and atom trapping experiments. Secondly, the construction, testing and characterisation of several magneto-optical traps (MOTs) for use in the generation and subsequent guiding of a cold atomic beam.

A number of extended-cavity diode lasers (ECDLs) have been constructed. These are in the Littrow geometry and have proven to be reliable and robust tools tailored for use in laser cooling and atom trapping experiments. Commercially available diode lasers at 780 nm with 50 mW output power have been integrated into such geometries yielding 40 mW of single longitudinal mode output tuneable continuously over 8 GHz and discontinuously over 4 nm. Through a heterodyne experiment, the linewidth of the laser was measured to be 135 kHz. Polarisation spectroscopy was utilized as a means of providing a locking signal to frequency stabilize such an ECDL. This technique was incorporated into an atom trapping experiment for the first time providing an improved locking scheme over saturated absorption spectroscopy with very little additional complexity. Dichroic-atomic

vapour laser lock (DAVLL) was investigated as an improvement on polarisation spectroscopy. The increased locking range (800 MHz in comparison to polarisation spectroscopy's 100 MHz) and insensitivity to laser power fluctuations or alignment made this a more attractive scheme. Further, the non-mechanical tuning of the laser frequency whilst locked by altering the magnetic field through the vapour cell was demonstrated. Both these schemes are limited by the sole feedback mechanism being the piezoelectric transducer (PZT). Although not novel, a dual current/PZT locking technique was integrated to the existing experimental equipment to significantly improve the frequency stability of the lasers. This is the method by which all current ECDLs in St Andrews are stabilized.

A commercially available circularized diode was discovered to possess qualities advantageous in the area of spectroscopy and atomic physics. These were completely unaltered semiconductor diode lasers except for the inclusion of a small microlens that had been epoxied close to the front facet. This produced a circular output beam directly from the laser can. In addition to this spatial improvement, a small amount of feedback occurred causing the laser linewidth to be reduced. Furthermore, the ability to tune continuously over 100 GHz by varying the current was experimentally observed. A marked reduction in drift of the frequency of the laser was also noted. Free-running, this laser was used as a tool to perform Doppler-free saturated spectroscopy on rubidium. It was also included in an atom trapping experiment as the hyperfine pumping laser. When placed in an extended-cavity, this circularized laser presented a simplification of the trapping experiment since beam shaping optics were not required. However, a reduction in the continuous tuning was observed. An inherent improvement in the stability of this laser resulted in atoms being trapped for a number of minutes with no active frequency stabilization. In conclusion to the work conducted with this circularized laser, a circularized diode laser in an extended-cavity was used successfully to injection lock a free-running circularized laser. This allowed 60 mW of laser power to be present at the MOT. It is noted that all current atom trapping experiments at St Andrews use the circularized diode laser in one form or another.

A commercially available Nichia diode laser based on gallium nitride has been placed in an extended-cavity and characterised. Either 3.5 mW or 1.5 mW of tuneable, single longitudinal mode output was extracted depending on the particular grating used. An upper linewidth of 5 MHz was placed on the laser although this was instrument limited. The emitted light was at 392 nm and continuously tuneable over 6 GHz and discontinuously over 2.7 nm. The tunability of this laser is less than observed for red and near infrared diodes in the same geometry. This is believed to be as a result of compositional fluctuations in the multi-quantum-well structure. Due to the reduced tuning, a judicious choice of laser diode is necessary if it is to be used in an extended-cavity for spectroscopic purposes.

Three separate MOTs have been designed, constructed, tested and evaluated for use in trapping either ^{85}Rb or ^{87}Rb. The first, a prototype trap, was built as a proof-of-principle trap and consisted of a simple glass five-way cross. Approximately 8×10^7 atoms were trapped and the trap lifetimes characterised. The second trap, a mirror MOT, used a mirrored surface at 45^o to enable trapping to be conducted with only two beams. The geometry of the setup also allowed a cloud of cold atoms to be trapped 1 mm above the surface of the mirror. A similar number of atoms was observed as in the first trap. The third trap was constructed using a metallic ten-way cross as the trapping region. This trap was designed with the intention of generating and guiding a cold atomic beam. An increased number of viewports allowed easier access for viewing and also for insertion of guiding beams. Shim coils enabled three-dimensional manipulation of the atomic cloud.

The culmination of work in this research project was the realization of atomic guiding. Experiments in the generation of a low-velocity intense source (LVIS) of atoms revealed a spatial difference in LVIS beams generated either by an opaque spot or a Laguerre-Gaussian (LG) beam. This was believed to be due to the dark centre of the beam created by the opaque spot filling with light due to diffraction while the LG beam is a pure mode and suffers no such degradation in its intensity

profile. Preliminary guiding of LVIS was conducted using either a near-resonant, red-detuned Gaussian beam or a blue-detuned LG beam. Guiding could not be corroborated conclusively, in the red-detuned regime, since inclusion of the guide beam through LVIS itself increased fluorescence by spontaneous emission. A more definitive result was obtained by guiding with a blue-detuned LG beam. Over 100% increase in the fluorescence of the LVIS was observed. Splitting of a LVIS using either red-detuned or blue-detuned light was investigated. Preliminary results in blue-detuned guiding have been markedly different from those reported in literature. New theories have been proposed to explain observations to aid a complete understanding of the mechanisms involved.

10.2 Future Work

There are many avenues open for the continuation of work presented in this thesis. However, I believe there are three main paths which hold the greatest intrigue. The first, is the completion of work performed on the Circulaser. An investigation into whether the frequency of the free-running laser can be stabilized sufficiently to allow it to be used as the cooling laser in an atom trapping experiment would be warranted. If this were to be proved true, then atom trapping could be taken to a new realm of simplification without the need for ECDLs.

The second involves the gallium nitride violet diode laser. This laser has been characterised in a Littrow geometry but not in a Littman-Metcalf geometry. This would be an interesting and worthwhile study. As would the insertion of an anti-reflection (AR) coated diode laser in an extended-cavity in order to investigate the continuous tuning characteristics. AR coated diode lasers in the red and near-infrared show increased tunability when placed in an extended-cavity and this would be an interesting investigation to make regarding violet emitting diode lasers. The circularization of a Nichia diode laser is also a possibility worthy of study. Indeed, recently a grant has been awarded at St Andrews which aims to address a number of these questions regarding violet diode lasers thereby contin-

uing this line of research.

Last, but by no means least, is atomic guiding. The atomic guiding results presented in this thesis are, as stated, preliminary. Indeed, over the last few months, during the writing of this thesis, a number of experiments have been performed at St Andrews to elaborate on and consolidate some of the results presented in Chapter 9. These include far-off resonance red-detuned guiding at 1064 nm, a novel method of enabling atoms to enter into the centre of a blue-detuned LG guide beam by placing a hole in the side of the beam and refinement of an all-optical beam splitter utilizing a Wollaston Prism. This work is not yet completed. Once a means of splitting a cold atomic beam optically has been reached, the next obvious step is to recombine the two parts again. This represents more of a challenge for the experimentalist. However, methods alluded to in this thesis could help make a compact, all-optical atom interferometer possible.

The final area of optical guiding of atoms which I think shows considerable promise for the future is in the use of Bessel beams. These are light beams that can have zero intensity in the centre of their intensity profiles, much like $\mathrm{LG}_{p\ell\neq 0}$ beams. However, one of the distinguishing characteristics of Bessel beams is that they are non-diffracting. Therefore, these can provide thin, narrow, optical guides, with constant diameters of the order of the wavelength of a cold, de Broglie atom. Atomic speckle patterns and the propagation of atoms in a single mode then become interesting and intriguing notions.

Appendix A

Laser Frequency Stabilization Electronics

A.1 Introduction

This appendix details the circuit diagram and operational details of the dual current/PZT locking electronics used in the latter half of this research for the frequency stabilization of extended-cavity diode lasers (ECDLs). A detailed description of the lasers that were stabilized is provided in Chapters 3 and 4.

A lock box was purchased from the University of Oxford in May 1999. This was to replace the simple locking circuits that had been used up to this point as their performance was limited due to the feedback loop solely acting on the PZT attached to the grating. The limitations of corrective feedback loops are discussed in Section 2.4.1. The electronics had been designed and built by David T. Smith in November 1998 in the Central Electronics Group under project number EW1225.

A.2 Circuit Description

The system enables a laser frequency to be stabilized, or locked, to an atomic transition or an external cavity. It operates by applying a small dither (or modulation) to the laser frequency and implementing corrective feedback to keep the mean laser frequency at the peak of the resonance. A block diagram of the circuit is shown in Figure A.1. The reference oscillator from the *Oscillator Board* applies a dither signal to the laser diode driver current supply resulting in a small frequency modulation. The level of dither can be controlled and monitored by the *Reference Dither* and the *Dither* socket respectively. The same oscillator is used to supply the reference input of a phase sensitive detector via a squarer and phase shifter. The phase shift is included to compensate for the total phase shift lags in the complete system and to give the correct polarity for the feedback loop. The input from a photodiode[1] placed in a saturated absorption setup (see Section 2.4.2) is fed to an amplifier tuned to the dither frequency. The amplified signal becomes the signal input to the phase shift detector. The d.c. output from this is fed to the current integrator on the *Integrator Board* which provides corrective feedback to the laser current driver. This is a defined to be the "fast" loop. A second "slow" loop is provided by integrating the current integrator output and applying this signal to a PZT controlling the extended-cavity grating. Having this second feedback control minimises the d.c. component on the current signal.

A.3 Modifications

A number of modifications and improvements were made to the electronics to suit our particular experimental setup. Firstly, the 20 Hz oscillator found on the *Inte-*

[1]It is important to ensure that the photodiode and any associated electronics have a large enough bandwidth to detect and pass signals at the dither frequency. This is an important consideration when 100 kHz dither is used.

grator Board was disconnected and an additional BNC socket (*Ramp In*) installed so that an external wavefunction generator could be used to drive the PZT scan. This was required as it was observed experimentally that several PZTs used had individual resonance frequencies. Secondly, an additional 741 operational amplifier was included, also in the *Integrator Board*, to allow the signal from *Ramp In* to be varied in amplitude and also offset by the addition of a d.c. voltage. This gave added flexibility when tuning the ECDL to the appropriate atomic transition. The circuit diagrams, incorporating all modifications are shown in Figure A.2, Figure A.3, Figure A.4 and Figure A.5.

The internal links of the box are listed below.

- **Tuned Amplifier Board**

  Fit Link (LK) 1 and LK2 for minimum a.c. gain.

  Fit LK1 only for medium gain. (min. $\times 10$)

  Fit LK2 only for maximum gain.(min. $\times 100$)

  Fit LK3 for untuned operation (not normally used).

  Fit LK4 for operation at 100 kHz.

  Fit LK5 for operation at 30 kHz.

  Fit LK6 for operation at 10 kHz.

- **PSD Board**

  Fit LK1 for 30 kHz and 100 kHz operation but omit for 10 kHz.

  LK2 and LK3 are 90^o and 180^o phase links.

  Fit LK 4 and 7 for 33μs amplifier time constant.

  Fit LK 5 and 8 for 10μs amplifier time constant.

  Fit LK 6 and 9 for 3.3μs amplifier time constant.

  RV1. This is the zero adjustment for the signal inverter. Remove signal input, turn signal gain to minimum. Connect d.c. reading digital multimeter between pins 9 and 16 of IC7 and set RV1 for zero volts.

- **Integrator Board**

  Short LK1 forwards (towards the front of the box) for full offset range and

rearwards for offset range ÷10.

LK2 is shorted to suit polarity of PZT feedback loop.

Fit LK3 to reduce the d.c. gain of the current feedback loop.

Fit LK4 to reduce the d.c. gain of the PZT feedback loop.

RV1 sets the 1st amplifier zero. Remove signal input and turn signal gain to minimum. Connect d.c. digital multimeter between pin A and ground and set RV1 for zero volts.

RV4 sets the 2nd amplifier zero. Set current gain to zero and current reset switch to off. Connect digital multimeter to current output socket and set RV4 for zero volts.

- **Oscillator Board**

  Fit LK1 for 10 kHz operation.

  Fit LK2 for 30 kHz operation.

  Fit LK3 for 100 kHz operation.

A.4 Experimental Locking of an ECDL and Circuit Diagrams

Below outlines the procedure for obtaining a lock using the electronics detailed in Section A.3.

(i) Initially before any attempt could be made at locking an ECDL, certain internal links of the box needed to be shorted. The status of the internal links are detailed below.

- **Tuned Amplifier:** LK2 fitted for maximum gain and LK4 fitted for amplification at 100 kHz.
- **PSD Board:** LK1 fitted, LK2 not fitted, LK3 fitted, LK6 and LK9 fitted. LK4, LK5, LK7 and LK8 not fitted.

- **Integrator Board:** LK1 is fitted forwards. LK2 is set arbitrarily at this stage, later it will be found whether it is correct or not. LK3 is fitted. LK4 is not fitted.
- **Oscillator Board:** LK3 fitted for 100 kHz.

(ii) The correct connections need to be made to/from the input/output BNC sockets.

- The output from a wavefunction generator is connected to *signal input.* Obviously the frequency has to be slow enough that the PZT can respond, in practise $\sim$ 200 Hz was used. Peak-to-peak voltage of 20 V was typical. The particular PZTs used within this project could be driven directly by the voltage output from this box and so no voltage amplification was required. If voltage amplification is needed then this should be incorporated into the apparatus using the *PZT Output* signal as the input to the amplifier.
- The signal from the photodiode in the saturated absorption spectroscopy setup is viewed on an oscilloscope and also fed to the *Signal Input.*
- The dispersive locking signal produced by the PSD board is monitored by viewing the *Signal Monitor* output on an oscilloscope.
- The *PZT Output* is connected to the PZT.
- The *Current Output* is connected to the external dither connection on the current diode driver.
- If need be, the dither signal supplied to the current driver can be monitored by viewing *Dither Monitor* on an oscilloscope. This was not normally used.

(iii) With the *Dither* and *Signal Gain* set to a minimum, the atomic transition of interest is found using the laser current and the *Ramp Gain* and *Offset* knobs. The laser is made to scan, using the PZT, over the transition frequency.

(iv) Monitoring the *Signal Monitor*, a small amount of dither is applied by turning up the *Dither* knob and at the same time the *Gain* knob. A dispersive signal should then be seen for every hyperfine feature in the scan. In practice I have found that the best way to optimise this signal is by rotating the *phase* knob until the *lock* LED ceases illumination. The phase is turned back and the strongest signal located by viewing the *Signal Monitor* output, if need be by either inserting or removing the 90^o phase link in the PSD Board. It should be noted that the dispersive locking signal should cross at 0 V and hence this should be accounted for by viewing the *Signal Monitor* with a d.c. setting on the oscilloscope. The d.c. offset can be changed by altering the phase or RV1 on the PSD board. A strong locking signal is found by altering the *Phase*, *Dither* and *Gain* knobs however, it should be noted that minimal dither is desirable since this provides the strongest lock.

(v) By reducing the *Ramp Gain* and changing the *Offset*, the laser is made to "zoom in" on the transition which it should be locked to. With the *Current Gain* set to zero, the current lock switch is switched on resulting in a blue LED being illuminated. The *Current Gain* is then increased slowly until feedback either causes the noisy *Signal Monitor* signal to become flat and tend towards 0 V or it is forced from 0 V in which case the 180^o link on the PSD Board should be inserted or removed depending on its current status. In practice the *Current Gain* was usually kept very low, between 0.5 and 1.5 on the ten-turn potentiometer dial.

(vi) To complete the lock, the PZT lock switch is switched on with the *PZT Gain* set to zero. Again a blue LED is illuminated to show when the integrating circuit is closed. The *PZT Gain* is slowly increased until the flat *Signal Monitor* remains unaltered or the laser is forced to jump from current lock. In the latter case, the internal link on the Integrator Board (LK2) should be reversed to change the polarity of the PZT feedback and steps (v) and (vi) repeated. In practice the *PZT Gain* was set to maximum. If, when the PZT lock is switched on, a slight d.c. offset is seen on the *Signal Monitor* this can be corrected for by varying RV4 on the Integrator Board. At this

stage both the current and PZT locks are closed.

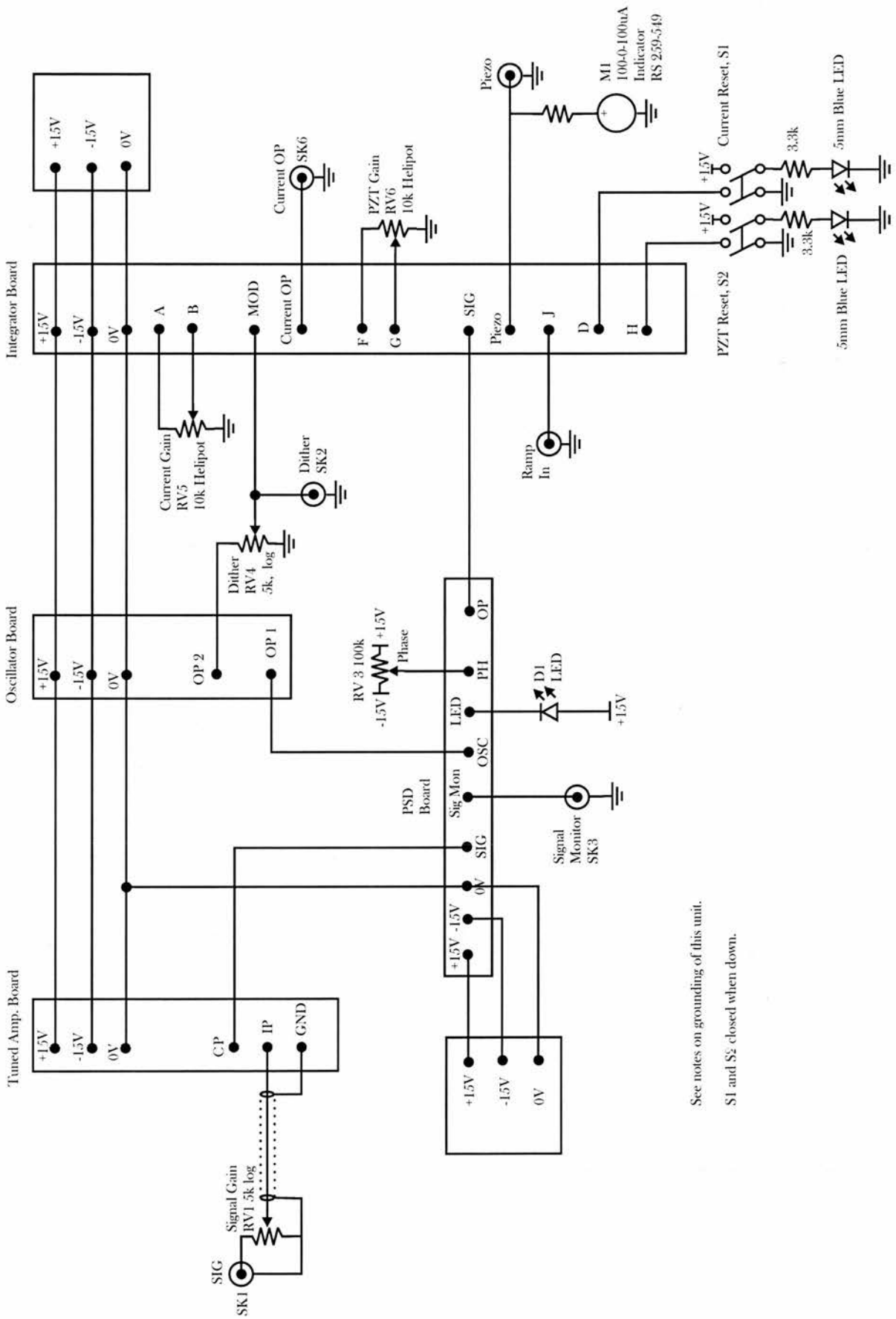

Figure A.1: A block diagram of the laser stabilization electronics.

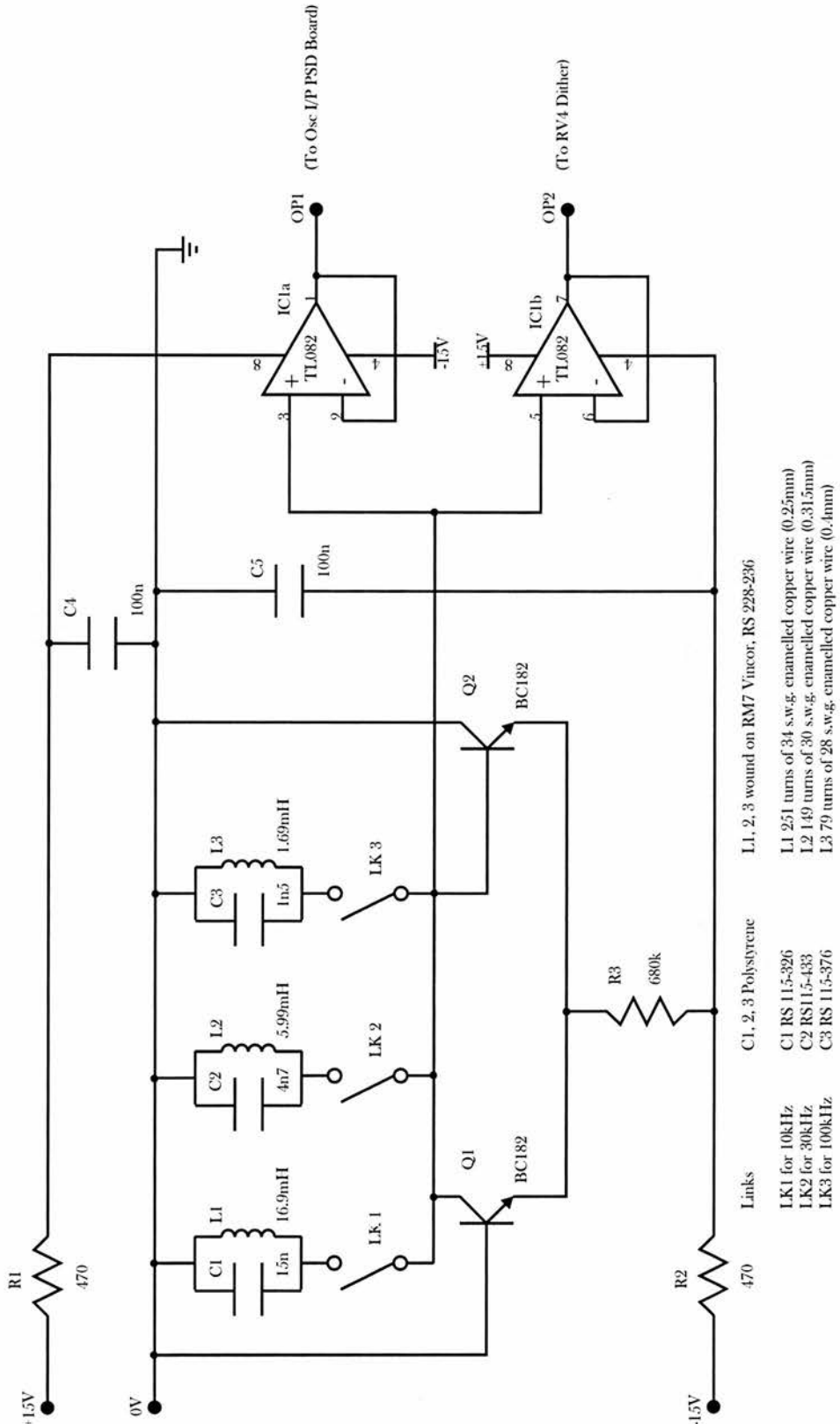

Figure A.2: Circuit diagram of the oscillator board.

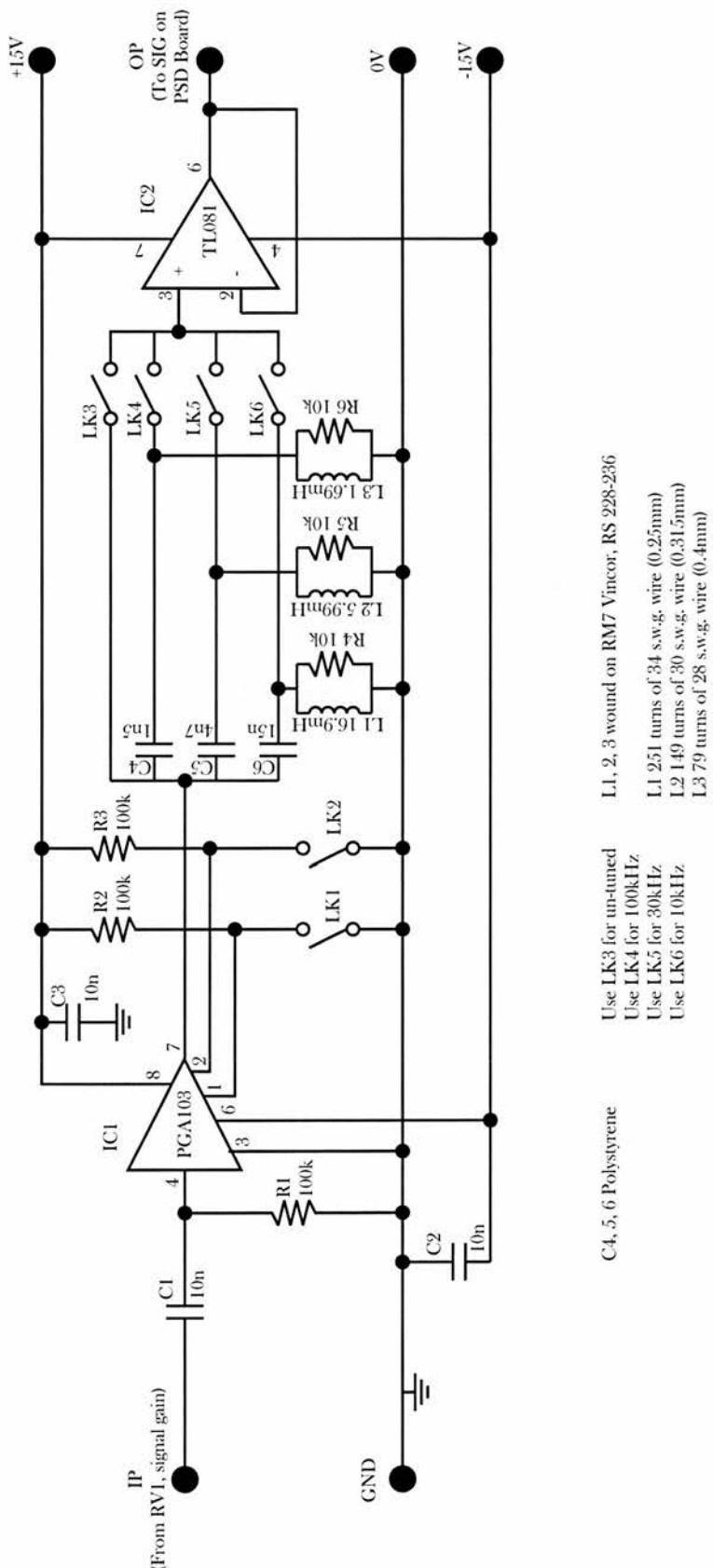

Figure A.3: Circuit diagram of the tuned amplifier board.

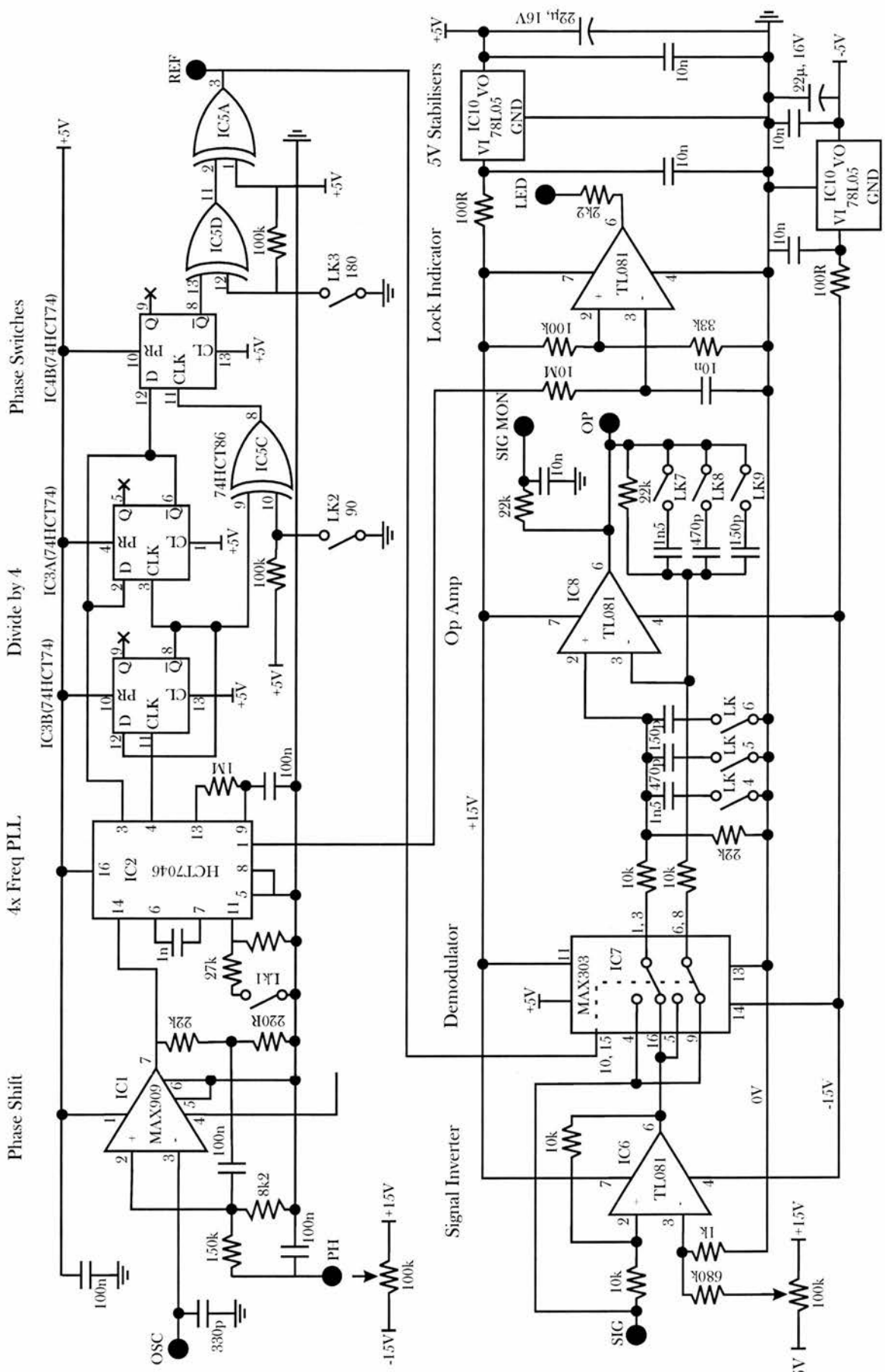

Figure A.4: Circuit diagram of the phase sensitive detection board.

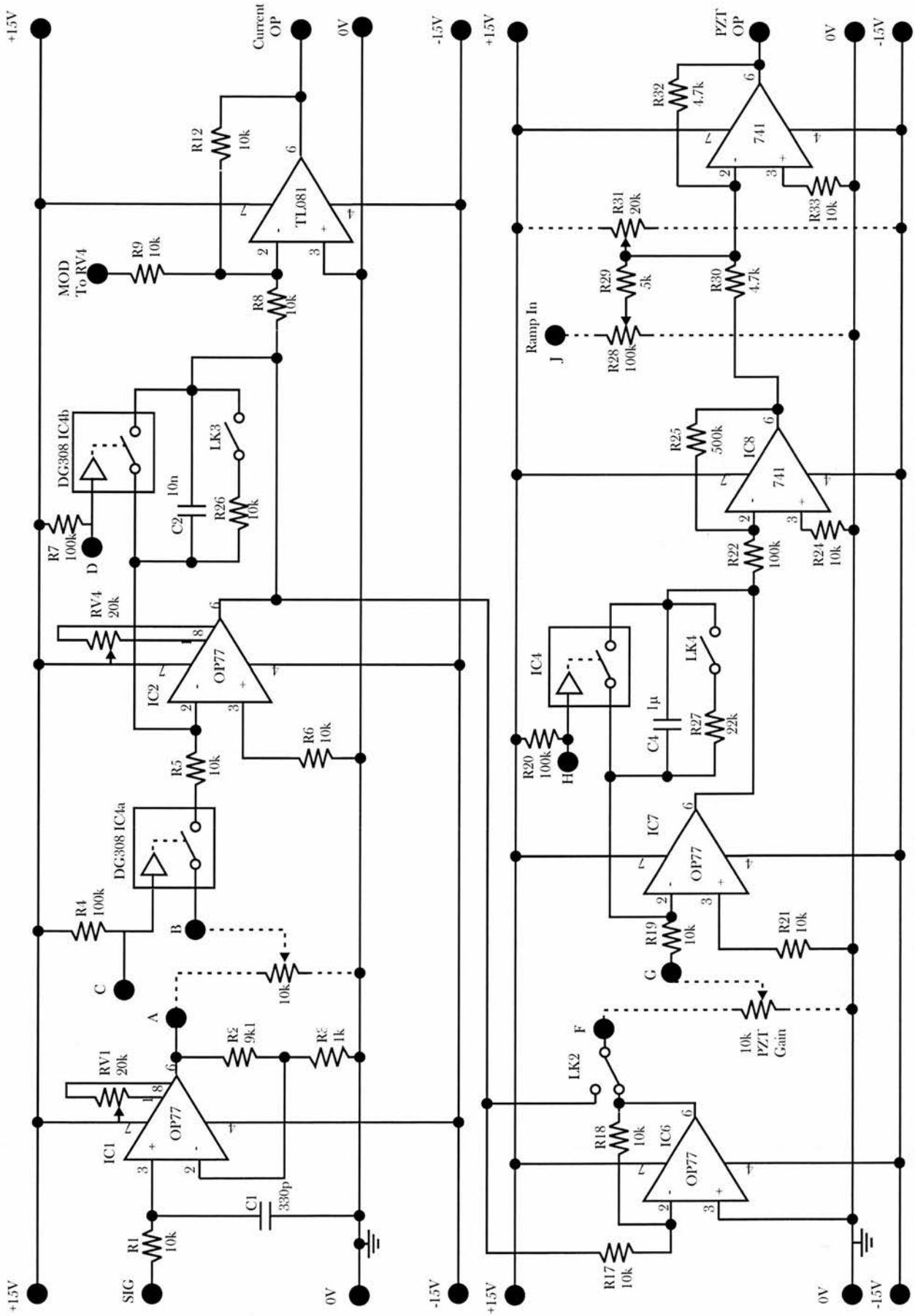

Figure A.5: Circuit diagram of the integrator board.

Appendix B

MOT Field Gradient Modelling

B.1 Introduction

This appendix is a reproduction of a program written in Mathematica to model the magnetic field pattern and field gradient of various anti-Helmholtz coil configurations for use in magneto-optical traps as outlined in Chapter 8. It is a two dimensional representation of the field along the coil axis (i.e. the axis connecting the centre of both coils) although since an anti-Helmholtz configuration generates a quadrupole field, the field will be spherically symmetric. The program is written in a logical, progressive manner with suitable explanations inserted in appropriate positions. What is presented is what is seen when viewing the Mathematica file and all text is included to enable any person to easily reproduce these results.

Anti-Helmholtz Configuration

■ Infinitely Narrow Coils

Assuming 2 coils of wire arranged in a Helmholtz configuration with radius, R, current through them, i and number of turns, n. Then the field produced at a distance, z, from the midpoint between the coils which are separated by 2d, is B.

```
R = 0.02;
i = 2.5;
μ = 4 Pi * 10^-7;
n = 57;
d = .025;
B1 = μ*i*n*R^2 / (2 ((Z - d)^2 + R^2)^3/2) (*the field prduced
   by only one coil set 2.5 cm to right of origin*);
Plot[1000 B1, {Z, -.1, .1}, AxesLabel ->
   {"Z (Metres)", "B (Gauss)"}];
B2 = μ*i*n*R^2 / (2 ((Z + d)^2 + R^2)^3/2) (*field produced by
   other coil set 2.5 cm to left of origin*);
Plot[-1000 B2, {Z, -.1, .1},
  AxesLabel -> {"Z (Metres)", "B (Gauss)"}];
Print["These two graphs show the field produced
    from each infinitely narrow coil separated by the
    distance d from the origin, which is taken to be
    the middle of separation distance detween them."];
B3 = 10000 * ( μ*i*n*R^2 / (2 ((Z - d)^2 + R^2)^3/2) - μ*i*n*R^2 / (2 ((Z + d)^2 + R^2)^3/2) );
Plot[B3, {Z, -.1, .1}, AxesLabel -> {"Z (Metres)", "B (Gauss)"}];
Print["And this is the cumulative
    field seen along the axis of the coils"];
B4 = 0.01 Dt[B3, Z];
Plot[B4, {Z, -.1, .1},
  AxesLabel -> {"Z (Metres)", "dB/dZ (Gauss/cm)"}];
Print["This shows the field gradient
    associated with the above set up."];
```

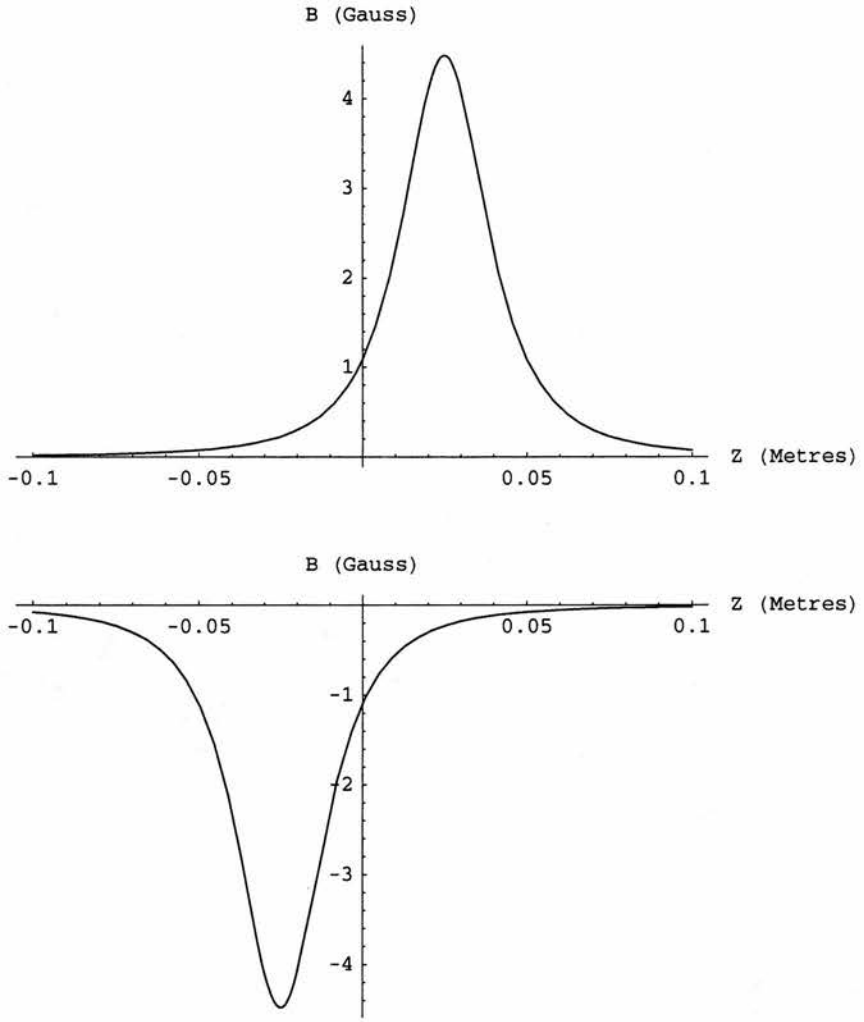

These two graphs show the field produced from each infinitely narrow coil separated by the distance d from the origin, which is taken to be the middle of separation distance detween them.

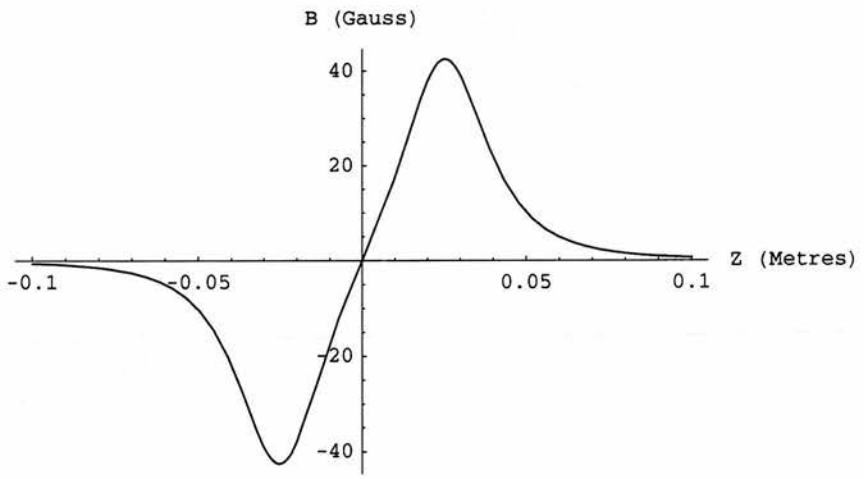

And this is the cumulative field seen along the axis of the coils

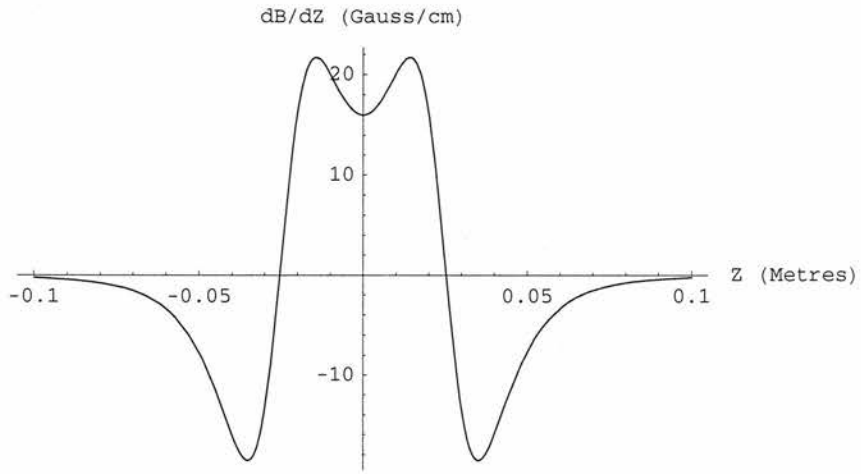

This shows the field gradient associated with the above set up.

■ Finite Width Coils

If we now do not assume that the width of the coils are infinately narrow then we must assign a width to them. We must also integrate the field produced at a distance,z, from the origin to obtain the total field at that point. Let the width of the windings be 1cm and assuming that there are 57 turns over the 1cm distance then there is a density of nn=n/2a turns per metre giving:

```
R = 0.02;
a = 0.005;
i = 2.5;
μ = 4 Pi * 10^-7;
nn = 57 / 0.01;
d = .025;
```

$$\text{B21[z\_]} := \frac{\mu * nn * i * R^2}{2} \int_{z+a}^{z-a} (z^2 + R^2)^{-3/2}\, dz$$

$$\text{Integrate}\left[\frac{\mu * nn * i * R^2}{2} * (z^2 + R^2)^{-3/2},\ \{z,\ z+a,\ z-a\}\right]$$

$$\frac{-0.0000447677 + 0.00895354\, z}{\sqrt{0.0004 + (-0.005 + z)^2}} - \frac{0.0000447677 + 0.00895354\, z}{\sqrt{0.0004 + (0.005 + z)^2}}$$

$$\text{B22} := -10000 * \left(\frac{-0.00004476769531365456 52` + 0.00895353906273091304` z}{\sqrt{0.0004` + (-0.005` + z)^2}} - \frac{0.00004476769531365456 52` + 0.00895353906273091304` z}{\sqrt{0.0004` + (0.005` + z)^2}} \right)$$

```
Plot[B22, {z, -.1, .1}]
```

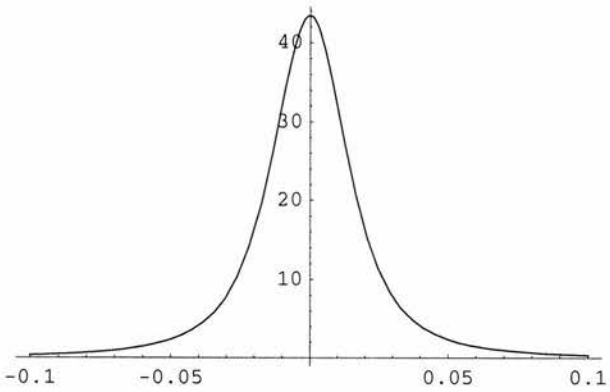


```
- Graphics -
```

Translating this by 2.5cm to the right of the origin gives:

$$B23 := -10000 * \left(\frac{-0.00004476769531365456 52` + 0.00895353906273091304` (z - d)}{\sqrt{0.0004` + (-0.005` + (z - d))^2}} - \frac{0.00004476769531365456 52` + 0.00895353906273091304` (z - d)}{\sqrt{0.0004` + (0.005` + (z - d))^2}} \right)$$

```
Plot[B23, {z, -0.1, 0.1}]
```

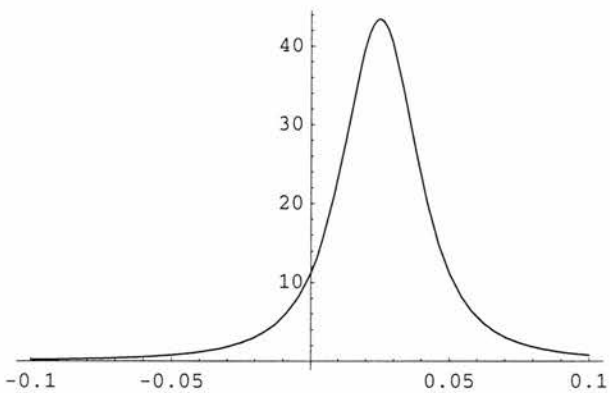


```
- Graphics -
```

Now plotting the other coil with a translation of 2.5cm to the left gives:

$$B24 := 10000 * \left(\frac{-0.00004476769531365456 52` + 0.00895353906273091304` (z + d)}{\sqrt{0.0004` + (-0.005` + (z + d))^2}} - \frac{0.00004476769531365456 52` + 0.00895353906273091304` (z + d)}{\sqrt{0.0004` + (0.005` + (z + d))^2}} \right)$$

```
Plot[B24, {z, -0.1, 0.1}]
```

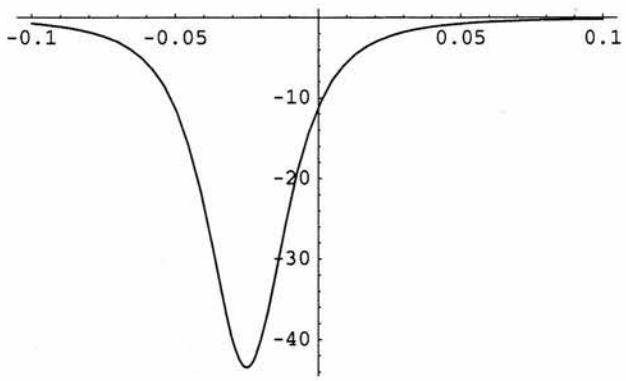


```
- Graphics -
```

Combining we have:

```
Plot[(B23 + B24), {z, -.1, 0.1},
 AxesLabel -> {"Z (Metres)", "B (Gauss)"}]
```

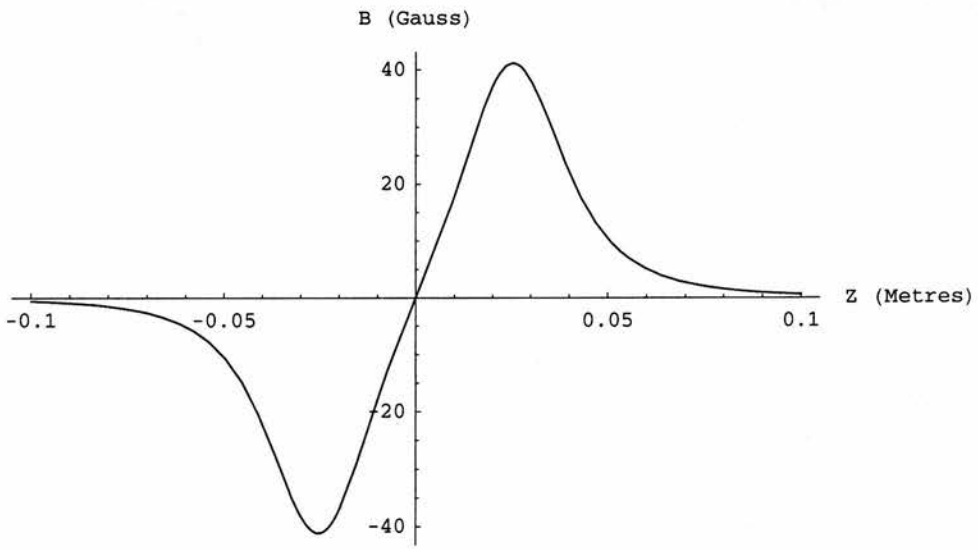


```
- Graphics -
```

The the graph above is the field produced from the set of coils positioned 5cm apart with a diameter of 4cm and a width of 1cm.

If we now differentiate this to obtain the field gradient :-

```
Dt[(B23 + B24), z]
```

$$
\begin{aligned}
&-10000\left(\frac{0.00895354}{\sqrt{0.0004+(-0.03+z)^2}}-\frac{0.00895354}{\sqrt{0.0004+(-0.02+z)^2}}-\right.\\
&\quad\frac{(-0.0000447677+0.00895354\,(-0.025+z))\,(-0.03+z)}{(0.0004+(-0.03+z)^2)^{3/2}}+\\
&\quad\left.\frac{(0.0000447677+0.00895354\,(-0.025+z))\,(-0.02+z)}{(0.0004+(-0.02+z)^2)^{3/2}}\right)+\\
&10000\left(\frac{0.00895354}{\sqrt{0.0004+(0.02+z)^2}}-\right.\\
&\quad\frac{(0.02+z)\,(-0.0000447677+0.00895354\,(0.025+z))}{(0.0004+(0.02+z)^2)^{3/2}}+\\
&\quad\frac{(0.03+z)\,(0.0000447677+0.00895354\,(0.025+z))}{(0.0004+(0.03+z)^2)^{3/2}}-\\
&\quad\left.\frac{0.00895354}{\sqrt{0.0004+(0.03+z)^2}}\right)
\end{aligned}
$$

```
% / 100
```

$$
\begin{aligned}
&\frac{1}{100}\left(-10000\left(\frac{0.00895354}{\sqrt{0.0004+(-0.03+z)^2}}-\frac{0.00895354}{\sqrt{0.0004+(-0.02+z)^2}}-\right.\right.\\
&\quad\frac{(-0.0000447677+0.00895354\,(-0.025+z))\,(-0.03+z)}{(0.0004+(-0.03+z)^2)^{3/2}}+\\
&\quad\left.\frac{(0.0000447677+0.00895354\,(-0.025+z))\,(-0.02+z)}{(0.0004+(-0.02+z)^2)^{3/2}}\right)+\\
&10000\left(\frac{0.00895354}{\sqrt{0.0004+(0.02+z)^2}}-\right.\\
&\quad\frac{(0.02+z)\,(-0.0000447677+0.00895354\,(0.025+z))}{(0.0004+(0.02+z)^2)^{3/2}}+\\
&\quad\frac{(0.03+z)\,(0.0000447677+0.00895354\,(0.025+z))}{(0.0004+(0.03+z)^2)^{3/2}}-\\
&\quad\left.\left.\frac{0.00895354}{\sqrt{0.0004+(0.03+z)^2}}\right)\right)
\end{aligned}
$$

```
Plot[%, {z, -.1, .1},
 AxesLabel -> {"Z (Metres)", "dB/dZ (Gauss/cm)"}]
```

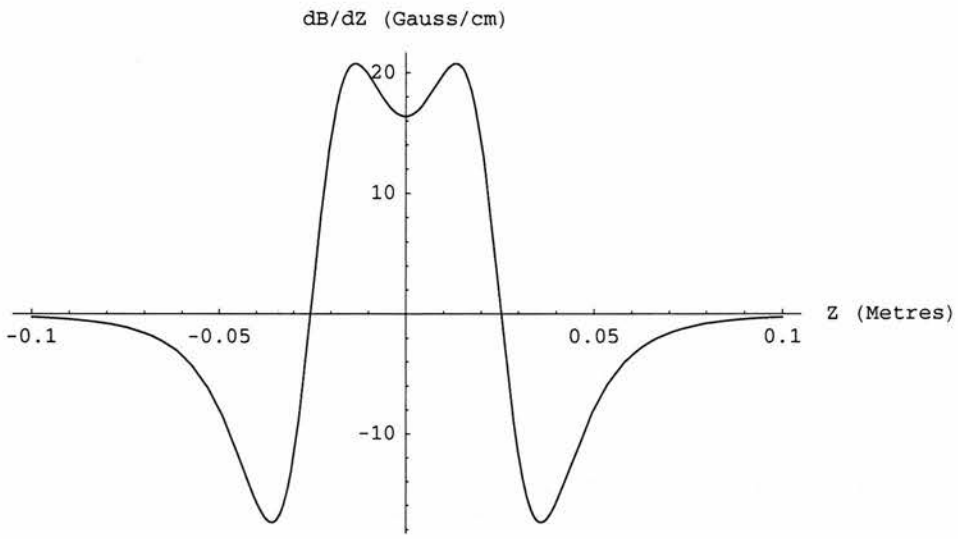


```
- Graphics -
```

The above graph is the field gradient for coils of diameter 4cm, width 1cm and with a separation of 5cm.

■ Axicon Trap Coils

■ Equal Currents

If we now look at a pair of coils with a diameter of 2R, width 2a, nu number of turns , i Amps going throught them and a separation of 2d set in the anti-helmholtz configuration then we get the graphs of field from a single coil, the total field produce and the field gradient.

```
R = 0.0325;
a = 0.005;
i = 1.8;
μ = 4 Pi * 10^-7;
nu = 120;
d = .025;
nn = nu / 0.01;
Integrate[ μ*nn*i*R^2/2 * (z^2 + R^2)^(-3/2), {z, z + a, z - a}];
B31 =
  -10000 Integrate[ μ*nn*i*R^2/2 * (z^2 + R^2)^(-3/2), {z, z + a, z - a}];
Plot[B31, {z, -0.1, 0.1}, AxesLabel → {"Z (Metres)", "B (Gauss)"}];
Print["This graph plots the field of one coil with the
   parameters described above along the axis of the coil."]
B32 = -10000 Integrate[ μ*nn*i*R^2/2 * ((z - d)^2 + R^2)^(-3/2),
    {z, z + a, z - a}];
B33 = 10000 Integrate[ μ*nn*i*R^2/2 * ((z + d)^2 + R^2)^(-3/2),
    {z, z + a, z - a}];
Plot[(B33 + B32), {z, -.1, .1}, AxesLabel ->
   {"Z (Metres)", "B (Gauss)"}];
Print["This shows the field along the coil axes of
   two coils set in the anti-helmholtz configuration
   with parameters as described above."]
B34 = 1 / 100 Dt[(B32 + B33), z];
Plot[B34, {z, -.1, .1},
  AxesLabel -> {"Z (Metres)", "dB/dZ (Gauss/cm)"}];
Print["This is the field gradient of the
   above anti-helmholtz conguration"]
```

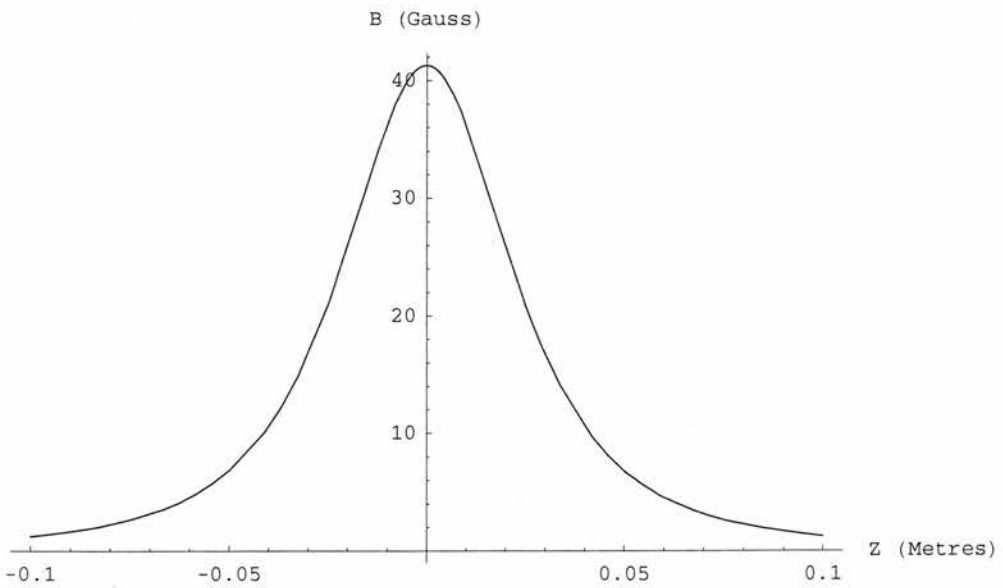


```
This graph plots the field of one coil with
  the parameters described above along the axis of the coil.
```

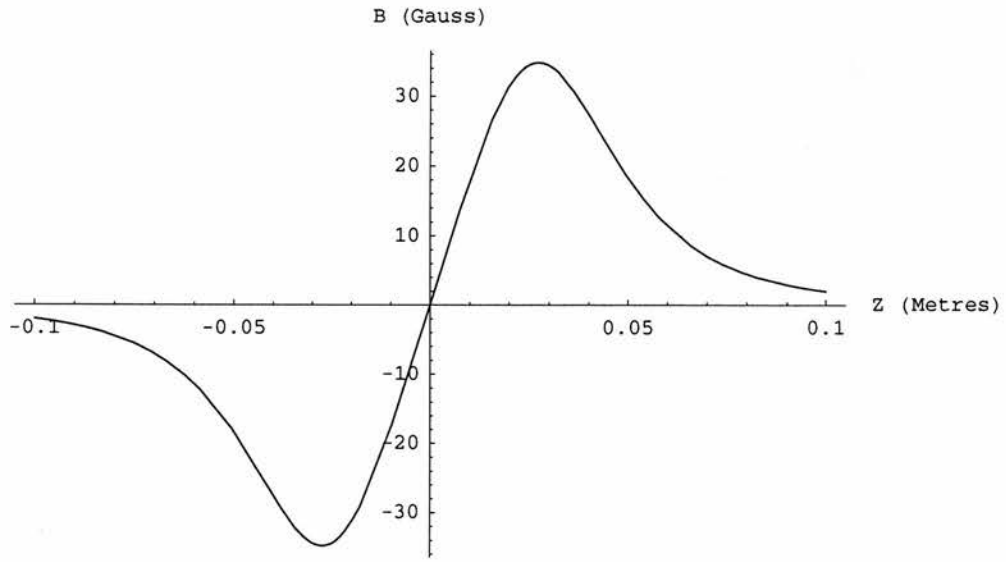

This shows the field along the coil axes of two coils set in the anti-helmholtz configuration with parameters as described above.

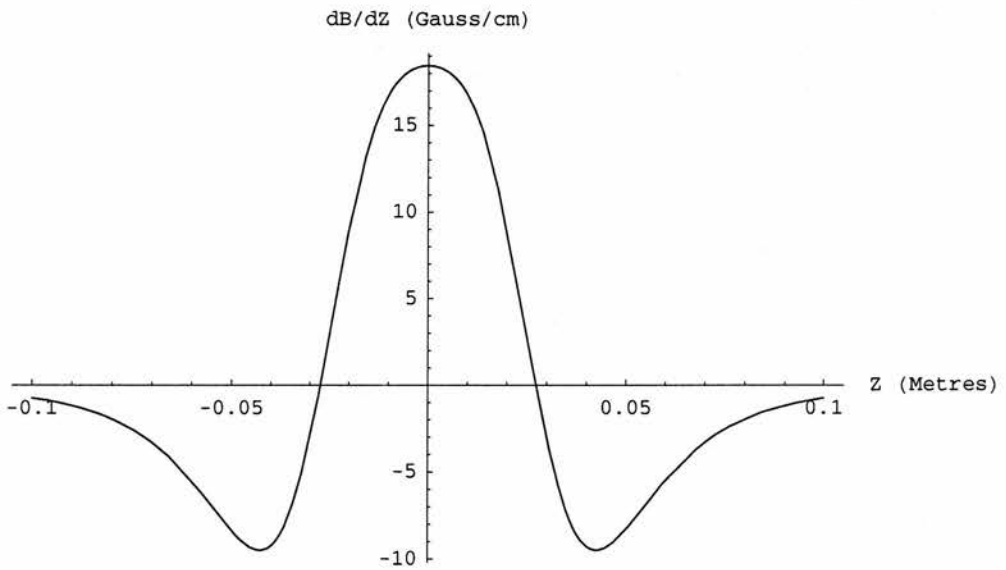

This is the field gradient of the above anti-helmholtz conguration

■ Field Zero Point Variation with asymmetric currents

If we now put different currents through each coil separately then the point of zero field would move a distance away from middle of the two coils.Having the same values for the coils as before but putting a prefactor,p,in one of the expressions,we get:

```
R = 0.0325;
a = 0.005;
i = 1.8;
μ = 4 Pi * 10^-7;
nu = 120;
d = .025;
nn = nu / 0.01;
z =.;
p =.;
B101 = -10000 Integrate[
    (μ * nn * p * i * R^2)/2 * ((z + d)^2 + R^2)^(-3/2), {z, z + a, z - a}];
B100 = 10000 Integrate[(μ * nn * i * R^2)/2 * ((z - d)^2 + R^2)^(-3/2),
    {z, z + a, z - a}];
B102 = (B100 + B101);
P = Solve[B102 == 0, p];(*This solves the equation
  for p and defines the solution as an array called P*)
l = Table[{z * 1000, p /. P[[1]]}, {z, 0, 0.01, 0.0001}];
(*The line "p/. P[[1]]" defines that we want to only
  use the first element of the array P.  Otherwise
  the propramme will try and plot the graph using
  the number as an array, which it doesn't like! *)
ListPlot[l, AxesLabel → {"Distance from centre (mm)",
    "Prefactor for second coil"}];
Print["This shows the expected movement of the zero field
   point along the field coil axis when each of the coils is run
   separately.  The prefactor is how much the current through
   one coil is more than through the other, ie. when p=1.5, then
   there is 1.5 times more current in one coil than in the other."]
```

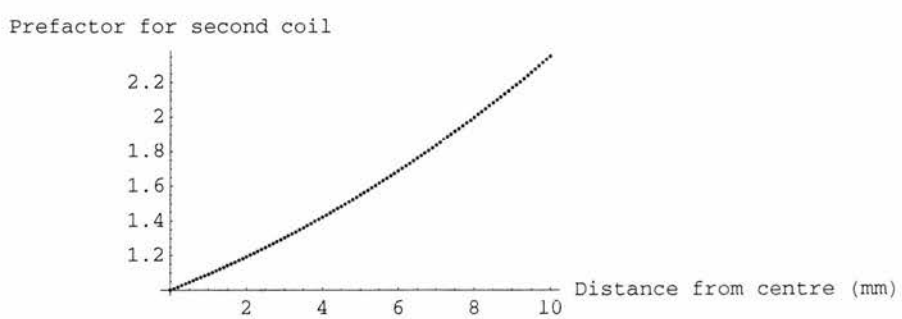

```
This shows the expected movement of the zero field
  point along the field coil axis when each of the coils is run
  separately.  The prefactor is how much the current through
  one coil is more than through the other, ie. when p=1.5, then
  there is 1.5 times more current in one coil than in the other.
```

■ Field Gradient Variation with:-

■ Coil separation

Now we shall assign values for all parameters associated with the coils apart from their separation and calculate the field gradient produced exactly half way between them. We shall give the coils a diameter of 6.5cm, a width of 1cm with 57 turns in that distance and a current of 2.5Amps.

```
μ = 4 Pi * 10^-7;
n = 57 / 0.01;
i = 2.5;
R = 0.0325;
a = 0.005;
d =.
    z =.
```

$$B41 := \frac{\mu * n * i * R^2}{2} \int_{z+a}^{z-a} (z^2 + R^2)^{-3/2}\, dz$$

$$\text{Integrate}\left[\frac{\mu * n * i * R^2}{2} * (z^2 + R^2)^{-3/2},\ \{z,\ z+a,\ z-a\}\right]$$

$$\frac{-0.0000447677 + 0.00895354\, z}{\sqrt{0.00105625 + (-0.005 + z)^2}} - \frac{0.0000447677 + 0.00895354\, z}{\sqrt{0.00105625 + (0.005 + z)^2}}$$

Now the total field for an anti-helmholtz pair is:-

$$B42 := -\left(\left(\frac{-0.00004476769531365453 85` + 0.00895353906273090771` (z - d)}{\sqrt{0.0010562500000000013` + (-0.005` + (z - d))^2}} - \frac{0.00004476769531365453 85` + 0.00895353906273090771` (z - d)}{\sqrt{0.0010562500000000013` + (0.005` + (z - d))^2}}\right) - \left(\frac{-0.00004476769531365453 85` + 0.00895353906273090771` (z + d)}{\sqrt{0.0010562500000000013` + (-0.005` + (z + d))^2}} - \frac{0.00004476769531365453 85` + 0.00895353906273090771` (z + d)}{\sqrt{0.0010562500000000013` + (0.005` + (z + d))^2}}\right)\right)$$

Differentiating to calculate the field gradient gives:-

```
z =.
```

```
100 * D[B42, z]
 (*the "100" puts the gradient in the correct units of Gauss/cm*)
```

$$
\begin{aligned}
100 \Bigg(& -\frac{0.00895354}{\sqrt{0.00105625 + (-0.005 - d + z)^2}} + \\
& \frac{(-0.005 - d + z)\,(-0.0000447677 + 0.00895354\,(-d + z))}{(0.00105625 + (-0.005 - d + z)^2)^{3/2}} - \\
& \frac{(0.005 - d + z)\,(0.0000447677 + 0.00895354\,(-d + z))}{(0.00105625 + (0.005 - d + z)^2)^{3/2}} + \\
& \frac{0.00895354}{\sqrt{0.00105625 + (0.005 - d + z)^2}} + \frac{0.00895354}{\sqrt{0.00105625 + (-0.005 + d + z)^2}} - \\
& \frac{(-0.005 + d + z)\,(-0.0000447677 + 0.00895354\,(d + z))}{(0.00105625 + (-0.005 + d + z)^2)^{3/2}} + \\
& \frac{(0.005 + d + z)\,(0.0000447677 + 0.00895354\,(d + z))}{(0.00105625 + (0.005 + d + z)^2)^{3/2}} - \\
& \frac{0.00895354}{\sqrt{0.00105625 + (0.005 + d + z)^2}} \Bigg)
\end{aligned}
$$

```
DB4 := 100 (-0.00895353906273090771` /
     Sqrt[0.00105625000000000013` + (-0.005` - d + z)^2] +
   ((-0.005` - d + z) (-0.000044767695313654538` +
       0.00895353906273090771` (-d + z))) /
    (0.00105625000000000013` + (-0.005` - d + z)^2)^(3/2) - ((0.005` - d + z)
      (0.000044767695313654538` + 0.00895353906273090771` (-d + z))) /
    (0.00105625000000000013` + (0.005` - d + z)^2)^(3/2) +
   0.00895353906273090771` /
    Sqrt[0.00105625000000000013` + (0.005` - d + z)^2] +
   0.00895353906273090771` /
    Sqrt[0.00105625000000000013` + (-0.005` + d + z)^2] - ((-0.005` + d + z)
      (-0.000044767695313654538` + 0.00895353906273090771` (d + z))) /
    (0.00105625000000000013` + (-0.005` + d + z)^2)^(3/2) + ((0.005` + d + z)
      (0.000044767695313654538` + 0.00895353906273090771` (d + z))) /
    (0.00105625000000000013` + (0.005` + d + z)^2)^(3/2) -
   0.00895353906273090771` /
    Sqrt[0.00105625000000000013` + (0.005` + d + z)^2])
  z = 0;
Plot[DB4, {d, 0.001, 0.1},
 AxesLabel -> {"d (Metres)", "dB/dZ (Gauss/cm)"}]
```

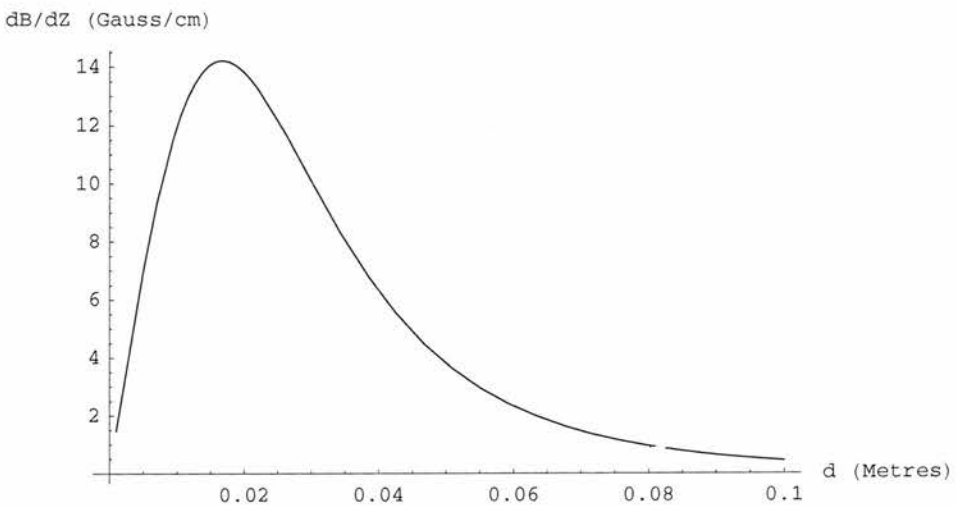


```
- Graphics -
```

■ Current

We now only change the current through the coils and keep all other parameters the same.

```
μ = 4 Pi * 10^-7;
n = 57 / 0.01;
i =.
R = 0.0325;
a = 0.005;
d = 0.015;
    z =.
```

$$\text{Integrate}\left[\frac{\mu * n * i * R^2}{2} * (z^2 + R^2)^{-3/2},\ \{z,\ z+a,\ z-a\}\right]$$

$$\frac{0.00358142\, i\, (-0.005 + z)}{\sqrt{0.00105625 + (-0.005 + z)^2}} - \frac{0.00358142\, i\, (0.005 + z)}{\sqrt{0.00105625 + (0.005 + z)^2}}$$

This integral defines the field produced by one coil of the above given parameters. The total field produced for the total anti-helmholtz pair is then:-

$$\begin{aligned} B5 := \Bigg(& \frac{0.00358141562509236432`\, i\, (-0.005` + (z - d))}{\sqrt{0.00105625000000000013` + (-0.005` + (z - d))^2}} - \\ & \frac{0.00358141562509236432`\, i\, (0.005` + (z - d))}{\sqrt{0.00105625000000000013` + (0.005` + (z - d))^2}} - \\ & \Bigg(\frac{0.00358141562509236432`\, i\, (-0.005` + (z + d))}{\sqrt{0.00105625000000000013` + (-0.005` + (z + d))^2}} - \\ & \frac{0.00358141562509236432`\, i\, (0.005` + (z + d))}{\sqrt{0.00105625000000000013` + (0.005` + (z + d))^2}} \Bigg) \Bigg) \end{aligned}$$

Differentiating to calculate the field gradient gives:-

```
100 * D[B5, z]
 (*the "100" puts the gradient in the correct units of Gauss/cm*)
```

$$\begin{aligned} 100 \Bigg(& \frac{0.00358142\, i}{\sqrt{0.00105625 + (-0.02 + z)^2}} - \frac{0.00358142\, i}{\sqrt{0.00105625 + (-0.01 + z)^2}} - \\ & \frac{0.00358142\, i\, (-0.02 + z)^2}{(0.00105625 + (-0.02 + z)^2)^{3/2}} + \frac{0.00358142\, i\, (-0.01 + z)^2}{(0.00105625 + (-0.01 + z)^2)^{3/2}} + \\ & \frac{0.00358142\, i\, (0.01 + z)^2}{(0.00105625 + (0.01 + z)^2)^{3/2}} - \frac{0.00358142\, i}{\sqrt{0.00105625 + (0.01 + z)^2}} - \\ & \frac{0.00358142\, i\, (0.02 + z)^2}{(0.00105625 + (0.02 + z)^2)^{3/2}} + \frac{0.00358142\, i}{\sqrt{0.00105625 + (0.02 + z)^2}} \Bigg) \end{aligned}$$

```
DB5 := -100 ( 0.0035814156250923643`i / Sqrt[0.0010562500000000013` + (-0.02` + z)^2] -
  0.0035814156250923643`i / Sqrt[0.0010562500000000013` + (-0.0099999999999999822` + z)^2] -
  0.0035814156250923643`i (-0.02` + z)^2 / (0.0010562500000000013` + (-0.02` + z)^2)^(3/2) +
  0.0035814156250923643`i (-0.0099999999999999822` + z)^2 / (0.0010562500000000013` + (-0.0099999999999999822` + z)^2)^(3/2) +
  0.0035814156250923643`i (0.0099999999999999822` + z)^2 / (0.0010562500000000013` + (0.0099999999999999822` + z)^2)^(3/2) -
  0.0035814156250923643`i / Sqrt[0.0010562500000000013` + (0.0099999999999999822` + z)^2] -
  0.0035814156250923643`i (0.02` + z)^2 / (0.0010562500000000013` + (0.02` + z)^2)^(3/2) +
  0.0035814156250923643`i / Sqrt[0.0010562500000000013` + (0.02` + z)^2] )

z = 0;
Plot[DB5, {i, 1, 10},
 AxesLabel -> {"I (Amps)", "dB/dZ (Gauss/cm)"}]
```

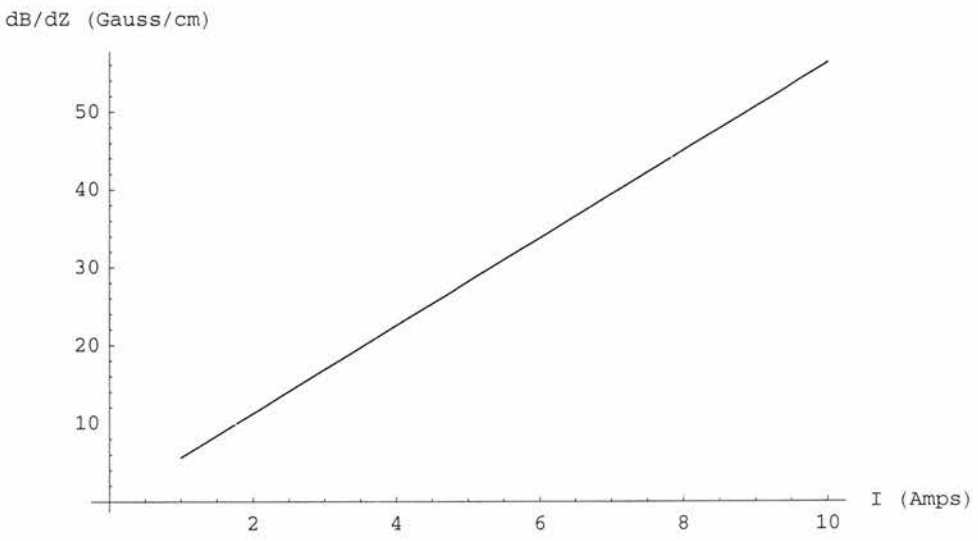

- Graphics -

■ Coil Width

```
μ = 4 Pi * 10^-7;
n = 57 / 0.01;
i = 2.5;
R = 0.0325;
a =.
d = 0.05;
    z =.
    Integrate[ μ*n*i*R^2 / 2 * (z^2 + R^2)^-3/2, {z, z+a, z-a}]
```

$$\frac{-0.00895354\,a + 0.00895354\,z}{\sqrt{0.00105625 + (a-z)^2}} - \frac{0.00895354\,(a+z)}{\sqrt{0.00105625 + (a+z)^2}}$$

Now,as before, the total field produced by the pair of coils is:-

```
B6 := ( (-0.00895353906273090771` a + 0.00895353906273090771` (z - d)) /
      Sqrt[0.00105625000000000013` + (a - (z - d))^2] -
    (0.00895353906273090771` (a + (z - d))) /
      Sqrt[0.00105625000000000013` + (a + (z - d))^2] ) -
  ( (-0.00895353906273090771` a + 0.00895353906273090771` (z + d)) /
      Sqrt[0.00105625000000000013` + (a - (z + d))^2] -
    (0.00895353906273090771` (a + (z + d))) /
      Sqrt[0.00105625000000000013` + (a + (z + d))^2] )

100 * D[B6, z]
 (*the "100" puts the gradient in the correct units of Gauss/cm*)
```

$$100\left(-\frac{0.00895354}{\sqrt{0.00105625 + (-0.05 + a - z)^2}} + \frac{0.00895354}{\sqrt{0.00105625 + (0.05 + a - z)^2}} + \frac{(-0.00895354\,a + 0.00895354\,(-0.05 + z))\,(0.05 + a - z)}{(0.00105625 + (0.05 + a - z)^2)^{3/2}} - \frac{(-0.05 + a - z)\,(-0.00895354\,a + 0.00895354\,(0.05 + z))}{(0.00105625 + (-0.05 + a - z)^2)^{3/2}} + \frac{0.00895354\,(-0.05 + a + z)^2}{(0.00105625 + (-0.05 + a + z)^2)^{3/2}} - \frac{0.00895354}{\sqrt{0.00105625 + (-0.05 + a + z)^2}} - \frac{0.00895354\,(0.05 + a + z)^2}{(0.00105625 + (0.05 + a + z)^2)^{3/2}} + \frac{0.00895354}{\sqrt{0.00105625 + (0.05 + a + z)^2}}\right)$$

```
DB6 := -100 (-0.00895353906273090771`/
     Sqrt[0.00105625000000000013` + (-0.05` + a - z)^2] +
   0.00895353906273090771`/
     Sqrt[0.00105625000000000013` + (0.05` + a - z)^2] +
   ((-0.00895353906273090771` a +
       0.00895353906273090771` (-0.05` + z)) (0.05` + a - z))/
    (0.00105625000000000013` + (0.05` + a - z)^2)^(3/2) -
   ((-0.05` + a - z) (-0.00895353906273090771` a +
       0.00895353906273090771` (0.05` + z)))/
    (0.00105625000000000013` + (-0.05` + a - z)^2)^(3/2) +
   0.00895353906273090771` (-0.05` + a + z)^2/
    (0.00105625000000000013` + (-0.05` + a + z)^2)^(3/2) -
   0.00895353906273090771`/
     Sqrt[0.00105625000000000013` + (-0.05` + a + z)^2] -
   0.00895353906273090771` (0.05` + a + z)^2/
    (0.00105625000000000013` + (0.05` + a + z)^2)^(3/2) +
   0.00895353906273090771`/
     Sqrt[0.00105625000000000013` + (0.05` + a + z)^2])

z = 0;
Plot[DB6, {a, 0.005, 0.045},
 AxesLabel -> {"a (Metres)", "dB/dZ (Gauss/cm)"}]
```

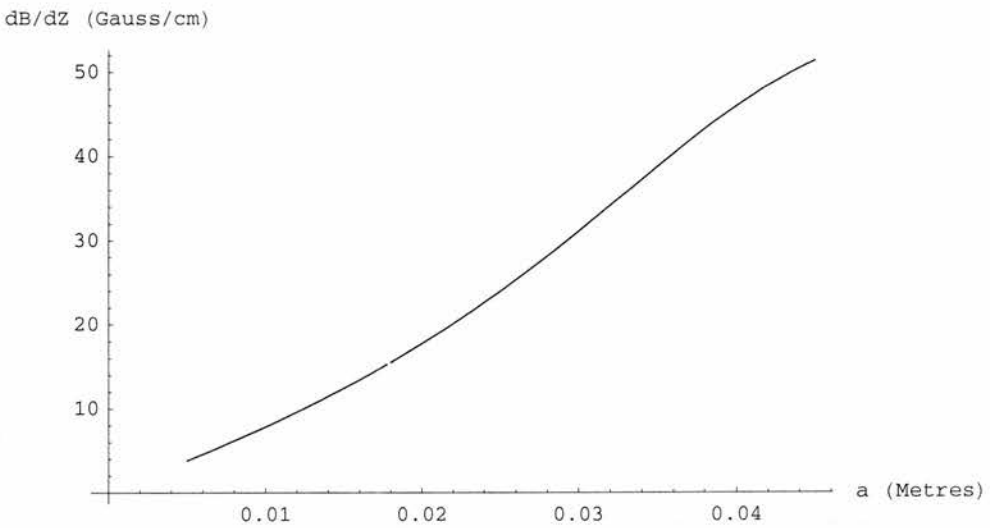


```
- Graphics -
```

Appendix C

Publications And Publicity

C.1 Publications

M. A. Clifford, G. P. T. Lancaster, R. H. Mitchell, F. Akerboom and K. Dholakia, "Realization of a mirror magneto-optical trap"
Journal of Modern Optics **48**, 1123–1128 (2001).

G. P. T. Lancaster, W. Sibbett and K. Dholakia, "An extended-cavity diode laser with a circular output beam"
Review of Scientific Instruments **71**, 3646–3647 (2000).

M. A. Clifford, G. P. T. Lancaster, R. S. Conroy and K. Dholakia, "Stabilization of an 852 nm extended cavity diode laser using the Zeeman effect"
Journal of Modern Optics **47**, 1933–1940 (2000).

R. S. Conroy, J. J. Hewett, G. P. T. Lancaster, W. Sibbett, J. W. Allen and K. Dholakia, "Characterisation of an extended cavity violet diode laser"
Optics Communications **175**, 185–188 (2000).

G. P. T. Lancaster, R. S. Conroy, M. A. Clifford, J. Arlt and K. Dholakia, "A polarisation spectrometer locked diode laser for trapping cold atoms"

Optics Communications **170**, 79–84 (1999).

D. P. Rhodes, G. P. T. Lancaster, J. Livesey, J. Arlt and K. Dholakia, "Guiding a cold atomic beam along a co-propagating and oblique hollow light guide"
Submitted for publication to *Physical Review A*.

G.P.T. Lancaster, W. Sibbett and K. Dholakia, "A circularized laser diode for high-resolution spectroscopy of rubidium"
To be submitted.

UK Patent no. C455.00/U.

C.2 Conference Papers

G. P. T. Lancaster, R. S. Conroy, M. A. Clifford, J. Arlt and K. Dholakia, "Channeling of cold atoms along a Laguerre-Gaussian light beam"
Presented at *Quantum Electronics and Laser Science*, San Francisco, 2000.

G. P. T. Lancaster, "Trapping and Channeling Cold Atoms"
Presented at *Aspects of Spectroscopy*, Manchester, 1999.

R. S. Conroy, G. P. T. Lancaster, M. A. Clifford and K. Dholakia, "Frequency stabilisation of an 852 nm diode laser using the Zeeman effect in Cs vapour"
Presented at *Quantum Electronics and Photonics Conference 14*, Manchester, 1999.

R. S. Conroy, G. P. T. Lancaster, W. Sibbett, and K. Dholakia, "Single Frequency, violet laser diode and its applications"
Presented at *Quantum Electronics and Photonics Conference 14*, Manchester, 1999.

R. S. Conroy, G. P. T. Lancaster, M. A. Clifford and K. Dholakia, "A compact high-performance extended-cavity diode laser at 635 nm"

Presented at *LEOS Chapter*, Heriot Watt University, 1999.

G. P. T. Lancaster, R. S. Conroy, M. A. Clifford, J. Arlt and K. Dholakia, "Trapping and Channeling of Cold Rb Atoms"
Presented at *ATMOP 25*, Manchester, 1999.

G. P. T. Lancaster, M. A. Clifford, and K. Dholakia, "Atom Guiding with Lithographic Applications"
Presented at *Industrial Materials for the 21st Century: Electronics and Displays Symposium*, Royal Society of Edinburgh, Edinburgh, 1999.

C.3 Lectures

February 2001: Open Day lecture for potential students, St Andrews, UK.

October 2000: Open Day lecture for potential students, St Andrews, UK.

August 2000: Represented the UK at the *International Conference for Physics Students*, Zadar, Croatia.

March 2000: Lecture at the *Institute of Physics Annual Physics Congress*, Brighton, UK.

February 2000: Lecture to Cupar Round Table, Cupar, UK.

November 1999: First year talk, St Andrews, UK. Runner-up Arthur Maitland Prize.

November 1999: Nexus Lecture Competition, Winner–Postgraduate Section at *Young Physicists Conference*, York, UK.

In my end is my beginning.

Mary, Queen of Scots 1542–87